KU Leuven
Biomedical Science Group
Faculty of Medicine
Department of Development and Regeneration
Prometheus - the division of Skeletal Tissue Engineering
Skeletal Biology and Engineering Research Center

KU LEUVEN

DOCTORAL SCHOOL
BIOMEDICAL SCIENCES

MODULAR TISSUE ENGINEERING FOR REGENERATION OF BONE AND CARTILAGE

ASSEMBLIES OF DEVELOPMENTALLY ENGINEERED CARTILAGINOUS BUILDING BLOCKS

Gabriella NILSSON HALL

Supervisor:	Prof. Dr. Frank P. Luyten
Co-supervisor:	Prof. Dr. Ioannis Papantoniou
	Prof. Dr. Liesbet Geris
Chair examining committee:	Prof. Dr. John Creemers
Chair public defense:	Prof. Dr. Rik Lories
Jury members:	Prof. Dr. Jérôme Guicheux (FR)
	Prof. Dr. Carlos Mota (NL)
	Prof. Dr. Stefan Giselbrecht (NL)
	Prof. Dr. Maurilio Sampaolesi (BE)
	Prof. Dr. Jean-Marie Aerts (BE)

Dissertation presented in partial fulfilment of the requirements for the degree of Doctor in Biomedical Sciences

Leuven 2020

Thesis submitted in partial fulfillment of the requirements for the degree of "*Doctor in Biomedical Sciences*" (KU Leuven)

All rights reserved. Except in those cases expressly determined by law, no part of this publication may be multiplied, saved in an automated data file or made public in any way whatsoever without the express prior written consent of the authors.

Acknowledgments

We're finally reaching a big milestone, the last step on my journey towards a PhD degree and it's "we" because I couldn't have done it without all the amazing people that I've met over the past years! I'm really looking forward to a diploma but it's the journey that has been the most rewarding. Even though the last months have been challenging with a world pandemic, the COVID-19 quarantine did give me some calm to write…

First of all, I would like to thank my promotors, without you there would not be a PhD thesis. Prof. Luyten, Frank, you have always been there for guidance and with excitement positioning the research towards application with a clinical as well as commercial viewpoint. Prof. Papantoniou, Ioannis, you have followed my journey on the floor from a master student to a PhD student. Throughout, you've had an inexhaustible number of ideas which has boosted my thesis project and maintained my explorative interest. During the inevitable low and sceptic periods of a PhD, you have talked me into the positive aspects which motivated me to continue and our improvised corridor meetings generated many ideas. Prof. Geris, Lies, you have been a kingpin to get strategic advice regarding both science and carrier choices throughout my time in the lab. I also want to express my gratitude to my external jury members Prof. Jérôme Guicheux, Prof. Stefan Giselbrecht and Prof. Carlos Mota for reviewing my PhD manuscript and giving valuable comments. Thanks to Prof. Maurilio Sampaolesi and Prof. Jean-Marie Aerts for giving feedback on my doctoral project from the start and much appreciated comments on my PhD manuscript.

The warm and helpful atmosphere between colleagues has been more than amazing and has contributed to my scientific knowledge and made both science and life even more fun. My first years started with a Friday beer tradition with the "old" TE gang: Hiroki (we started the same day as lonely lost souls and became best bench buddies – nioki nioki), Maarten and Toon (taught me everything in the lab the first year), Luis (always there for valuable discussions), Abhi (always made the day happy), Johanna (Svenska stabiliteten i labbet), Wai (introduced me to the iPSC world), Dennis, Yoke Chin, Veerle, Jeroen and Liliana... Next, more people joined and we entered an era of travel with Marjorie in the lead – I will never forget all our travels together and I'm expecting more. I want to thank everyone in the TE-lab for generating

such an amazing work environment that reached outside the lab: Carlos M and Louca my fellow PhD students who've been great support along the way, Priyanka, Sébastien, Raphaëlle, Niki, Thomas, Paulo, Rezmi, Delia and the "new" strong team Hannah, Tim, Isaak, Angela. An important thanks to the incredible lab-tech team for your help and positive spirits: Inge, Samuel, Kathleen, Janne, Carla, Orely and Melanie. Also big thanks to Jenny for all the daily help in organizing the lab-environment and answering questions. But it's not only the TE-team, I also want to thank everyone in Prometheus who have enabled good collaborations and good times during the retreats: Yann, Bart, Maxim, Guillaume, Steve, Shauni… Additionally, the whole SBE team has aided in keeping us moving by organizing sports as well as board game nights. An extra thanks to Marion for our improvised coffee breaks about everything!

BT-brudarna! Trots att vi är i olika länder så har våran kontakt med meddelanden som lyser upp dagen, möhhippor, disputationer, baby-showers, bröllop m.m funnits där. Detta har betytt massor for mig och jag ser fram emot flera fantastiska möten (när Corona lagt sig…). Min kontakt till Sverige under Belgien vistelsen har också hållits igång av de (nästan) årliga besöken av Eve. Tack for din vänskap och dina och Daniel's besök, nu börjar nya äventyr!

Jag vill såklart också tacka min kära familj: mamma, pappa och Rebecka, som alltid funnits där när det behövts. Ni har stöttat mig till tusen under denna period! Finalement, je voudrais remercier la personne dans mon cœur : Carlos (Calle 😉). Tous les jours, tout le temps tu étais là pour me supporter. Te amo.

List of Abbreviations

2D	two dimensional
3D	three dimensional
4D	four dimensional
ACAN	aggrecan
ACs	articular chondrocytes
ATMP	advanced therapy medicinal product
BMP	bone morphogenetic protein
BMSCs	bone marrow stromal cells
CaP	calcium phosphate
CM	chondrogenic media
COL10A1	collagen type a1(X)
COL2A1	collagen type II, α1
CT	computed x-ray tomography
DMEM	Dulbecco's modified eagle medium
DMP1	dentin matrix protein1
ECM	extracellular matrix
EMA	European medicines agency
EO	endochondral ossification
FGF2	fibroblast growth factor 2
FN	fibronectin
FOXA	forkhead box A
GAG	glycosaminoglycan
GF	growth factor
HA	hydroxyapatite
hASCs	human adipose derived stromal cells
hBMSCs	human bone marrow stromal cells
HH	hedgehog
HUVEC	human umbilical vein endothelial cell
hiChon	human induced chondrogenic cells

hPDCs	human periosteum-derived cells
hiPSCs	human induced pluripotent stem cells
IGF	insulin-like growth factor
IHH	indian hedgehog
iPSCs	induced pluripotent stem cells
MEF2C	myocyte enhancer factor 2C
MMP	matrix metalloproteinase
N-CAM	neural cell adhesion molecule
OA	osteoarthritis
OSX/SP7	osterix
PCL	poly(ε-caprolactone)
PDCs	periosteum derived cells
PEG	poly(ethylene glycol)
PLGA	poly(lactic-co-glycolic acid)
PLLA	poly (l-lactic acid)
POC	primary ossification center
Prx1	paired related homeobox 1
PTHrP	parathyroid hormone-related protein
RANKL	receptor activator of NF-kappa B ligand
rhBMP-2	recombinant human bone morphogenetic protein 2
RNA	ribonucleic acid
RUNX2	runt-Related Transcription Factor 2
scRNAseq	single cell ribonucleic acid sequencing
SOC	secondary ossification center
SOX9	SRY-Box Transcription Factor 9
SPP1	secreted phosphoprotein 1 / osteopontin
TE	tissue engineering
TFs	transcription factors
TGF-β	transforming growth factor beta
TNF-α	tumor necrosis factor alpha
TRAP	tartrate-resistant acid phosphatase
VEGF	vascular endothelial growth factor
WNT	wingless-related integration site

Table of Contents

ACKNOWLEDGMENTS ..... **V**

LIST OF ABBREVIATIONS ..... **VII**

TABLE OF CONTENTS ..... **IX**

LIST OF FIGURES AND TABLES ..... **XI**

CHAPTER 1. INTRODUCTION AND RATIONALE **1**

1.1. THE SKELETAL TISSUE – *ITS IMPORTANCE AND STRUCTURE* 5

1.1.1. Bone structure *5*
1.1.2. Joint surface structure *7*

1.2. BONE AND CARTILAGE DEVELOPMENT AND REPAIR 8

1.2.1. Endochondral ossification during limb development *8*
1.2.2. Long bone fracture healing *10*
1.2.3. Synovial joint development *12*
1.2.4. The importance of periosteum *13*
1.2.5. Cell signaling pathways during skeletal development and maintenance *13*
1.2.6. Molecular markers for cell fate specification in long bone *14*

1.3. CLINICAL HURDLES FOR BONE AND OSTEOCHONDRAL DEFECTS 16

1.3.1. Long bone fractures - current clinical treatments *16*
1.3.2. Osteochondral defects - current clinical treatments *17*
1.3.3. Advanced Therapy Medicinal Products *18*

1.4. CLASSICAL SKELETAL TISSUE ENGINEERING 19

1.4.1. Biocompatible scaffolds *19*
1.4.2. Bioactive molecules *20*
1.4.3. Cell source *21*

1.5. DEVELOPMENTAL ENGINEERING - TOWARDS BIOLOGICAL MANUFACTURING 23

1.5.1. Bone developmental engineering - recapitulate endochondral ossification *24*
1.5.2. Osteochondral developmental engineering *25*

1.6. ASSEMBLY OF DEVELOPMENTALLY ENGINEERED MODULES 27

1.6.1. 3-dimensional spheroid culture *27*

CHAPTER 2. HYPOTHESIS, OBJECTIVES AND METHODOLOGY **31**

2.1. GENERAL HYPOTHESIS AND PROJECT AIM 33

2.2. SPECIFIC OBJECTIVES AND HYPOTHESES 33

2.3. EXPERIMENTAL METHODOLOGY 35

2.3.1. Cell types *35*
2.3.2. Cell culture set-up *35*
2.3.3. Media formulation *36*
2.3.4. In vitro assays *36*
2.3.5. In vivo assays *36*

CHAPTER 3. DEVELOPMENTALLY ENGINEERED CALLUS ORGANOID BIOASSEMBLIES EXHIBIT PREDICTIVE *IN VIVO* LONG BONE HEALING 37

CHAPTER 4. PATTERNED, ORGANOID-BASED OSTEOCHONDRAL IMPLANTS RESULT IN ZONE-SPECIFIC FUNCTIONALITY *IN VIVO* 77

CHAPTER 5. DESIGN CONSIDERATIONS FOR SPHEROID-BASED IMPLANTS FOR ENDOCHONDRAL OSSIFICATION: TOWARDS ROBOTIC-DRIVEN BIOMANUFACTURING ... 105

CHAPTER 6. GENERAL DISCUSSION, FUTURE PERSPECTIVE AND APPLICATIONS 133

6.1. PROJECT STRATEGY AND RESULTS OVERVIEW 135
6.2. BIOLOGICAL AUTONOMY DEPICTS FUNCTIONALITY 136
6.3. CELLULAR BUILDING BLOCKS AS "BIOINK" – ALONE OR WITH BIOMATERIAL? 138
6.4. APPLICABILITY FOR CLINICAL TRANSLATION 139
6.5. TOWARDS BUILDING BLOCK MANUFACTURING AND ASSEMBLY 141
6.6. DISEASE MODEL AND DRUG SCREENING PLATFORM 142

CHAPTER 7. GENERAL CONCLUSIONS 143

PROJECT SUMMARY 147

REFERENCES 149

SCIENTIFIC ACKNOWLEDGEMENT 160
PERSONAL CONTRIBUTION 160
CONFLICTS OF INTEREST 160

CURRICULUM VITAE 161

PERSONAL INFORMATION 161
EDUCATION 161
SCIENTIFIC TRAINING 161
BIBLIOGRAPHY 162

List of Figures and Tables

Figure 1.1. Overview of introduction chapters. 4

Figure 1.2. The skeleton is divided into the axial (grey) and appendicular (blue) skeleton. 5

Figure 1.3. a) The long bone comprises multiple tissues to build up a functional organ. 6

Figure 1.4. Joint surface structure. 7

Figure 1.5. Endochondral ossification during long bone development 9

Figure 1.6. Fracture healing can be divided into four overlapping phases 11

Figure 1.7. Synovial joint development. 12

Figure 1.8. Simplified schematic of important cell signaling pathways during skeletal development. 14

Figure 1.9. Cell fate specification during the process of endochondral ossification. 15

Figure 1.10. Number of publications per year including "Tissue Engineering" (black line), "Bone Tissue Engineering" (green dashed line) or "Cartilage Tissue Engineering" (red dotted line).. 19

Figure 1.11. Knowledge from in vivo development represents guidelines and quality control for the in vitro process. 24

Figure 1.12. Schematic visualization of different living building blocks to be applied for assembly into larger tissues. 27

Figure 1.13. Number of publications containing the key words "cell spheroid", "microtissue" or "organoid" have increased the last decade. 28

Figure 2.1. Thesis CHAPTER overview 34

Figure 3.1. Long-term culture of periosteal microspheroids 43

Figure 3.2. Microspheroids follow endochondral ossification patterns toward pre-hypertrophic callus organoids able to form bone in vivo 45

Figure 3.3. Assembly of cartilage intermediate microtissues into larger bone forming constructs 48

Figure 3.4. Histological assessment after ectopic implantation 50

Figure 3.5. RNA sequencing analyses of spheroids and Macropellet 52

Figure 3.6. Healing of murine critical-sized long bone defect 55

Figure 4.1. Hierarchical micromodule implant derived from adult hPDCs. 84

Figure 4.2. Formation of cartilage microtissues from hiPSC derived chondrocytes (hiChon). 87

Figure 4.3. Creation of integrated osteochondral tissues through assembly of hPDC- and hiChon-derived building blocks 88

Figure 4.4. In vivo functionality of integrated dual constructs after 4 weeks implantation ...90

Figure 5.1. Chondrogenic maturation of cellular building-blocks.....111

Figure 5.2. Dual fusion of building-blocks with different maturity.....113

Figure 5.3. Spreading assay on adherent surface 115

Figure 5.4. Assembly of building-blocks of different chondrogenic maturity into mesotissues with a total culture time of 22 days.....116

Figure 5.5. Assembly of building-blocks of different chondrogenic maturity into mesotissues without necrotic core.....118

Figure 5.6. Image-driven robotic spheroid handling.....119

Figure 7.1. Developmentally engineered bioassemblies for healing of critical-sized murine defect.....145

Figure 7.2. Assembly of distinct cellular building blocks in vitro matured into osteochondral-like tissues in vivo.....145

Figure 7.3. Spheroids assays to quantify fusion and spreading capacity of cellular building blocks to define design limitations for future robotic manufacturing of spheroid-based tissue engineering.....146

Table 1. List of growth factors present in the differentiation media and their knockout phenotype. 36

Table S1. Genes significantly up-regulated D14-21 and associated with endochondral ossification……...72
Table S2. Genes significantly up-regulated D14-21 and associated with angiogenesis…….73

1

CHAPTER 1.

Introduction and rationale

The skeletal system plays a vital role in our daily life by giving support to our body and protect inner organs. The long bones, present in limbs such as arms and legs, are connected to each other with articular joints to allow everyday movement. The connecting bone surfaces in the articular joints are covered with a dense cartilage tissue that works as a lubricant to generate smooth joint movement and withstand impact forces to protect the underlying bone tissue. Hence, the maintenance of both bone and cartilage tissue is of great importance for the human body and daily life.

Although skeletal bone has the ability to regenerate without scar tissue formation, 5-10% of long bone fractures are unable to heal successfully resulting in delayed and non-unions, bone defects that fail to heal. Despite treatment options, such as allografts or distraction osteogenesis, large long bone defects, in particular of the lower limbs, remain an unmet medical need. In addition to large bone defects, damages of the joint surface penetrating through the articular cartilage and deep into the underlying bone, called osteochondral defects, remain problematic to treat. Untreated osteochondral defects lead to osteoarthritis, a joint disease linked with pain and restricted movement associated with both social and economic impact. Current clinical treatments are limited by either tissue availability or incapacity to regenerate the tissues to their original functionality. Regenerative medicine, and more specifically tissue engineering (TE), shows great potential to meet this clinical need by creating *in vitro* implants able to heal *in vivo* large bone and osteochondral defects.

Despite 30 years of research, few tissue engineered products (categorized as Advanced Therapy Medicinal Products – ATMPs in Europe) have reached clinical translation. Encountered problems include limited scalability of the manufacturing, lack of/limited process quality controls, poor survival due to diffusion limitations and insufficient tissue integration. The first TE strategies involved seeding of cells onto scaffolds to mimic the structure of adult bone/cartilage tissue which often resulted in inhomogeneous cell seeding and low cell density. To improve the creation of TE constructs, researchers currently aim at mimicking the process of tissue development – a concept named “Developmental Engineering”. Consequently, knowledge learned from developmental biology is used as guidelines and quality controls to engineer *in vitro* processes.

The “Developmental Engineering” principle has been demonstrated for bone formation but diffusion limitations and scalability still poses a great hurdle for future clinical translation. **This thesis focused on the characterization of micrometer sized building-blocks**

(micromodules) and their subsequent *in vitro* assembly into larger intermediate constructs for regeneration of bone and osteochondral tissue in murine animal models. This modular "bottom-up" approach was hypothesized to circumvent diffusion limitations and pave the way towards a scalable process for the manufacturing of complex tissue engineered tissues. The introduction contains information regarding the skeletal tissues (1.1), bone and cartilage development (1.2), regeneration (1.2.2) and clinical hurdles (0). These chapters are of importance to understand the rationale of bone and cartilage tissue engineering (0) and most importantly developmental engineering (0) (**Figure 1.1**).

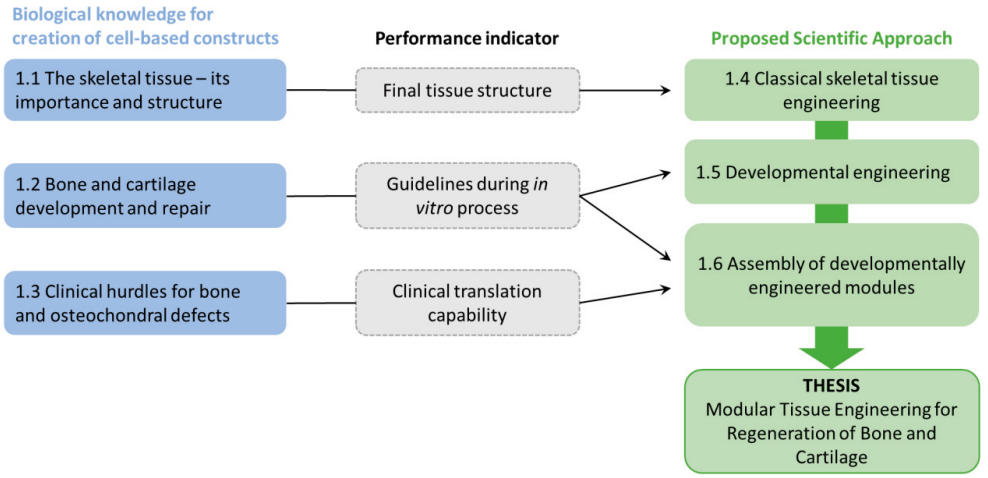

***Figure 1.1. Overview of introduction chapters**. Chapter 1.1.-1.2 describes the biology which will act as guidelines and quality control of the in vitro process as well as the final product. Chapter 1.3 describes current clinical treatments and hurdles for healing of bone and osteochondral defects. Finally, chapter 1.4-1.6 introduce the field of bone and cartilage tissue engineering and developmental engineering.*

1.1. The skeletal tissue – *its importance and structure*

The skeletal system account for approximately 20% of the human body weight and consists of bones and other connective tissues, including cartilage, tendons and ligaments. Ligaments link different bones with each other while tendons connect muscles with bone to enable smooth movement of joints with articular cartilage as a protective layer on the ends of long bones. The skeleton can be divided into the axial skeleton which include the skull, facial bones, ribs and vertebrae and the appendicular skeleton which comprises limbs, pelvis and shoulders (**Figure 1.2**) [1,2]. Although the most obvious purposes of the skeleton is to stabilize the body, allow movement and protect inner organs, the bone also functions as storage of minerals (*i.e.* calcium and phosphorus) as a source of energy and hosts the bone marrow for blood cell production (hematopoiesis) [3]. Since the skeletal tissues have multiple purposes, it is important that damages within each tissue regenerate towards their native tissue state /or restore full functional capacity. The structure and composition of bone and cartilage are very distinct with bone being a hard tissue for support while cartilage conforms a dense structure to enable absorption of high impact.

1.1.1. Bone structure

The long bones (*e.g.* femur and tibia) consist of dense cortical bone, also known as compact bone, with a medullary channel in the center containing the bone marrow with hematopoietic cells (**Figure 1.3**a-b). The cortical bone is present as an outer protective shell with trabecular bone, also known as cancellous or spongy bone, in the center. The periosteum covers the cortical bones as a highly vascularized fibrous layer [4]. Periosteum is the cell source used in this thesis and the importance of periosteum for bone maintenance and fracture healing is described in more detail in chapter 1.2.4.

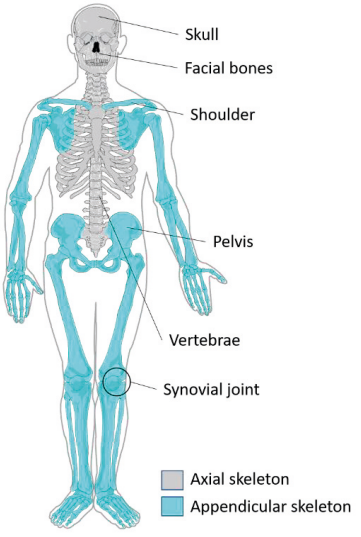

Figure 1.2. *The skeleton is divided into the axial (grey) and appendicular (blue) skeleton. Figure adapted from [1].*

The mechanical strength of bone comes from its complex structure of mineralized collagen fibrils that together with water, non-collagenous proteins (e.g. osteocalcin, osteopontin and bone sialoprotein) and proteoglycans arrange in a hierarchical structure. The collagenous fibrils consist mainly of collagen type I (>90%) which form triple helices that are

stacked together to create a network containing holes where intrafibrillar crystals of carbonated hydroxyapatite (HA) reside (**Figure 1.3**c). Consecutively, the fibrils are organized into fiber arrays which build up a lamellae structure to form the two different bone tissue types present in long bones, namely the cortical bone and trabecular bone[5].

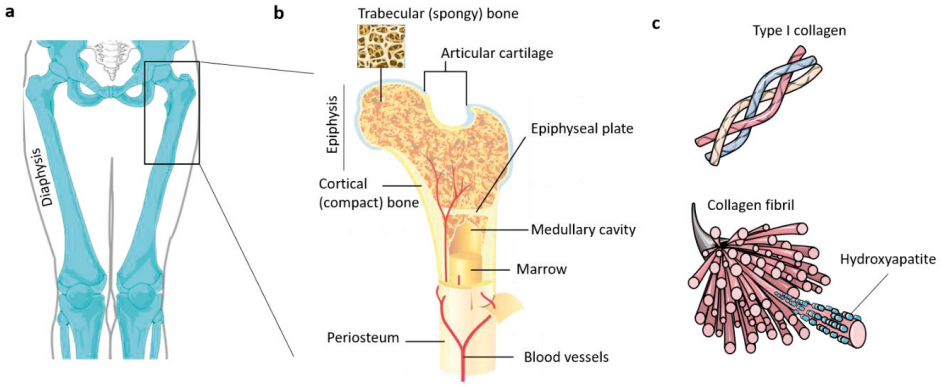

***Figure 1.3**. a) The long bone comprises multiple tissues to build up a functional organ. b) Periosteum covers the bone surface of cortical bone with bone marrow in the medullary cavity. Trabecular bone is present in the epiphysis and the bone ends are covered with articular cartilage c) The main component of the bone tissue is collagen type I fibrils with hydroxyapatite. Figure adapted from Wikimedia Commons[1]. The schematic was produced using Servier Medical Art (https://smart.servier.com). Servier Medical Art by Servier is licensed under a Creative Commons Attribution 3.0 Unported License (https://creativecommons.org/licenses/by/3.0/).*

Although bone is a mineralized tissue and appear static, it is continuously undergoing turnover throughout an individual's lifetime. This remodeling process increases the bone strength by formation of new bone to meet mechanical changes as well as to repair microfractures resulting from normal daily activity and exercise [6]. The engine to these events is the cellular composition of bone which includes osteoblasts (bone-forming), osteocytes (bone-sensing) and osteoclasts (bone-resorbing). During a remodeling cycle, osteoblasts secrete receptor activator of NF-kappa B ligand (RANKL) which bind to the receptor RANK on osteoclast precursors which are activated. Osteoclast precursors differentiate into osteoclasts which dissolve bone minerals and degrade the collagen type I rich bone matrix through acidification and secretion of metalloproteinases [7,8]. After matrix resorption, osteoblast precursors and osteoblasts are recruited to secrete new organic bone matrix. Osteoblasts are subsequently embedded in their bone matrix and differentiate into osteocytes which possess mechanosensory properties enabling activation of bone remodeling [7]. Although the sequential steps of bone remodeling are relatively well known, the cross-talk between osteoblasts and osteoclasts is still under investigation [9,10]. The described bone structure represents important parameters for the quality control of the final product of long bone in CHAPTER 3.

1.1.2. Joint surface structure

In contrast to bone, the articular (hyaline) cartilage has high viscoelastic properties to function as a protective layer providing low friction during joint movement as well as absorption and transmission of load towards the subchondral bone. The 2-4 mm thick avascular cartilage is built up by multiple highly organized layers of cells (chondrocytes) and extracellular matrix (ECM) mainly consisting of water, collagen type II and proteoglycans (mainly aggrecan) containing highly negatively charged glycosaminoglycans (GAGs). The organized network of collagens and proteoglycans allows retention of water within the cartilage tissue (80% wet weight) contributing to the capacity to withstand high cyclic loads [11,12]. Collagen orientation in combination with chondrocyte stage contribute to the different zones found within the mm thick articular cartilage: superficial (10-20% of the thickness), transition (40-60%), deep (30%) and calcified zone (**Figure 1.4**). The superficial zone is characterized by horizontally aligned cells expressing hyaluronan and PRG4 (lubricin) to generate a surface allowing movement with low friction [13]. The transition zone contains larger chondrocytes with more round shape embedded in collagen type II collagen fibers with alternative orientation. In the deep zone, the collagen fibers are aligned perpendicular to the surface with chondrocytes organized in columns [14]. The mineralized cartilage, linking the non-mineralized cartilage with the underlying subchondral bone, contain a mineralized ECM of mainly collagen type II and X and glycosaminoglycans (GAGs) which embed relatively large chondrocytes. The deep zone and mineralized cartilage are separated from the non-mineralized cartilage by the tidemark, an important interface for maintenance of joint homeostasis (**Figure 1.4**b) [12]. The structure described here represents the quality control of the final product of an osteochondral unit which will be presented in CHAPTER 4.

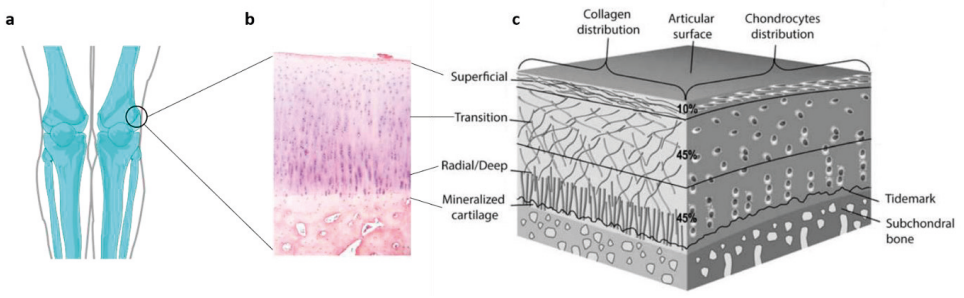

Figure 1.4. Joint surface structure*. a) Articular cartilage covers the ends of long bone in synovial joints. b) Hematoxylin and eosin staining demonstrate the layered structure of articular cartilage which comprises of c) multiple zones from non-mineralized cartilage, mineralized cartilage to subchondral bone. Figure adapted from Di Luca et al. [15] and Wikimedia Commons[1].*

1.2. Bone and cartilage development and repair

The development of skeletal elements is initiated by mesenchymal condensation followed by two distinct bone formation pathways i) intramembranous ossification (direct bone formation) and ii) endochondral ossification (indirect ossification) [16,17]. The flat bones which comprise the skull and medial clavicles are developed through intramembranous ossification while the majority of bones, the appendicular skeleton, vertebrae and facial bones develop through endochondral ossification (EO) (**Figure 1.2**) [18,19]. While intramembranous ossification involves direct differentiation of embryonic mesenchymal cells to bone forming osteoblasts, EO comprises differentiation into chondrocytes that create a cartilage template which subsequently is remodeled into bone [17]. Since a majority of bones develop and heal through EO and long bones is the focus of this thesis, endochondral ossification (EO) and its molecular regulation is described in more detail (chapter 1.2.1). During mesenchymal condensation of limb development, release of signaling molecules leads to the formation of an interzone, dividing the condensed mesenchyme into two parts giving space to formation of the joint and articular cartilage which is described in chapter 1.2.2 [20].

1.2.1. Endochondral ossification during limb development

Endochondral ossification during limb development is initiated by condensation of *Prx1*+ skeletal progenitor cells derived from the mesoderm [21]. The cellular condensation is regulated by multiple signaling molecules to direct the initiation of condensation (transforming growth factor beta - TGF-β, fibronectin - FN, neural cell adhesion molecule - N-CAM), proliferation (fibroblast growth factor 2 – FGF2) and subsequent onset of differentiation (bone morphogenetic proteins – BMPs, SRY-Box Transcription Factor 9 - SOX9) (**Figure 1.5**a) [16]. Differentiation of skeletal progenitor cells into early stage chondrocytes is promoted by the transcription factor (TF) SOX9, together with SOX5 and 6 [22,23]. The SOX trio further regulate secretion of the structural proteins collagen type II, α1 (COL2A1) and aggrecan (ACAN) resulting in the formation of a cartilage template with a surrounding perichondrium of fibroblastic cells. The fibrous perichondrium provides progenitor cells to support endochondral bone development and provide signaling cues for the chondrocytes within the cartilage template [24–26]. While the SOX trio is important for chondrogenic differentiation, BMPs in combination with their receptors play a crucial role in both proliferation and regulation of chondrogenic differentiation during skeletal development [27].

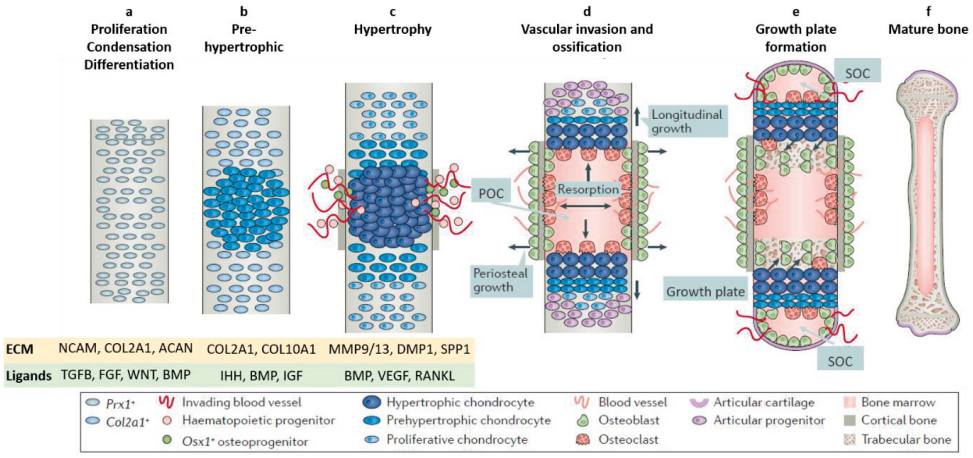

Figure 1.5. Endochondral ossification during long bone development*. a) Mensenchymal cells condense and differentiate towards b) hypertrophic chondrocytes which is followed by vascular invasion and b) bone formation. Important ECM proteins (yellow bar) and ligands (green bar) involved in chondrocyte maturation are mentioned below figure a-c. POC: primary ossification center, SOC: secondary ossification center. Figure adapted from Salazar et al.*[27]

Chondrocytes in the central cartilage template mature into prehypertrophic chondrocytes regulated by SOX9, MEF2C and FOXA2/3 which drive further maturation towards hypertrophic chondrocytes (**Figure 1.5**b) [22,28–30]. The hypertrophic chondrocytes are characterized by a larger cell size and expression of specific ECM molecules such as collagen type α1(X) (COL10A1), osteopontin (SPP1) and dentin matrix protein1 (DMP1) [28]. In addition, the hypertrophic chondrocytes secrete matrix metalloproteinases 9/13 (MMP9/13), to degrade the collagen type II rich ECM, vascular endothelial growth factor (VEGF) to attract blood vessel invasion and RANKL to stimulate osteoclastogenesis (**Figure 1.5**c) [31]. The blood vessels provide access for multiple progenitor cells important for bone formation: osteoblast-, ECM degrading osteoclast-, blood vessel forming endothelial- and pericyte progenitor cells [32,33]. These events, in combination with transdifferentiation of hypertrophic chondrocytes, give rise to the primary ossification center (POC) (**Figure 1.5**d) [34,35]. Secondary ossification centers (SOC) are later formed in the epiphysis leading to the formation of the growth plate (**Figure 1.5**e).

The growth plate, shown in **Figure 1.5**e, consists of a gradient of cells from resting, proliferating, prehypertrophic to hypertrophic chondrocytes which drive longitudinal bone growth until adulthood [36]. This cell gradient is maintained by a distinct negative feed-back loop between parathyroid hormone-related protein (PTHrP) expressed by proliferative chondrocytes and indian hedgehog (IHH) secreted by prehypertrophic and hypertrophic chondrocytes [36,37]. IHH promotes PTHrP, which in turn promotes chondrocyte proliferation and delays

hypertrophy while blocking Ihh, hence generating a continuous supply of chondrocytes for EO. While the growth plate with ongoing EO contributes to the lengthening of the bone, intramembranous ossification of periosteal cells regulates the thickening of the cortical bone forming the bone shaft (**Figure 1.5**d-e) [38].

The process of endochondral ossification during limb development is relatively well studied with regards to chondrocyte maturation which is linked with specific secretion of signaling molecules and ECM constituents. The described information contributes as a guideline as well as quality control for each consecutive step in the process of engineering cartilage intermediates *in vitro*.

1.2.2. Long bone fracture healing

Fracture healing of the appendicular skeleton involves both endochondral and intramembranous ossification, and although a combination of both processes occur, EO is the primary process for the majority of clinically relevant fractures [39]. The stability of the fracture is a dominant factor directing the ossification process [40] where a more stable fracture directs cells towards intramembranous ossification while unstable microenvironments and micro-movements promote EO [40,41]. Hence, the cellular differentiation cascade of EO during limb development (1.2.1) are also recapitulated during postnatal fracture healing with the main differences of an initial inflammatory response and hematoma formation [42,43]. The fracture healing process can be divided into four partially overlapping phases (**Figure 1.6**): **i) Acute inflammation response and hematoma (blood clot) formation** are promoted directly after fracture when tissue and vasculature damage occur [40]. Blood from ruptured vessels coagulate to form the hematoma (fibrin clot) creating an environment with low oxygen tension (0.1-2 %). Inflammatory cells including neutrophils are recruited to the defect followed by macrophages to remove damaged tissue [39]. Pro-inflammatory cytokines (*e.g.* TNF-α, IL-1 and IL-6), angiogenic cytokines (*e.g.* FGF2, VEGF and PDGF) and transforming growth factors (*e.g.* BMP-2, BMP-4 and BMP-6) are secreted to promote blood vessel formation and attract mesenchymal progenitor cells from adjacent tissues including the periosteum, endosteum and bone marrow [40,44,45].

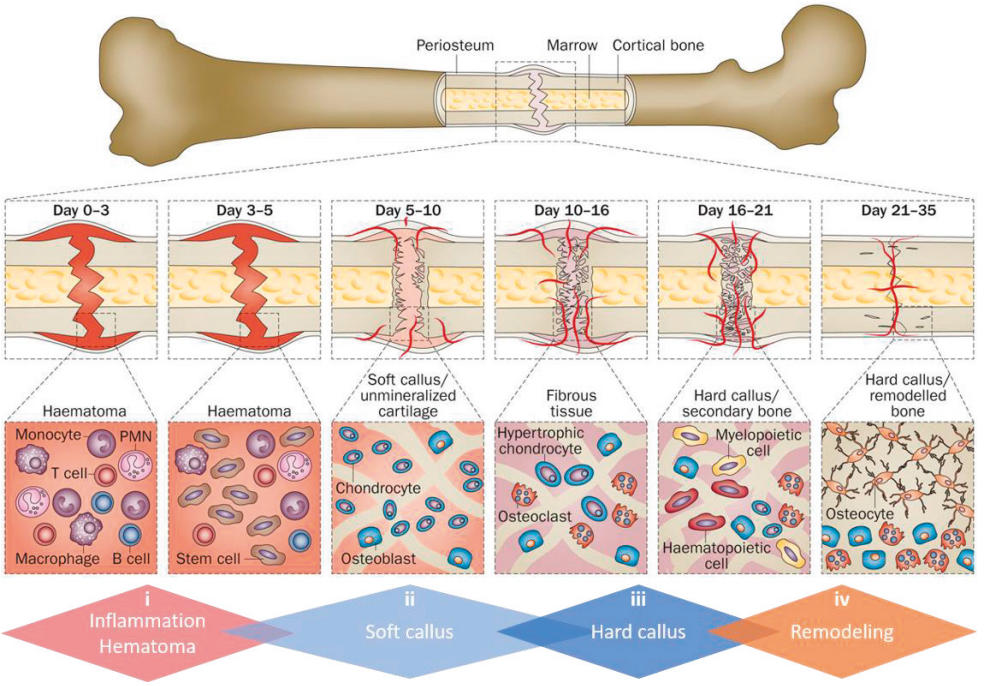

Figure 1.6. Fracture healing can be divided into four overlapping phases. *i) Acute inflammation and haematoma formation are followed by the formation of ii) soft callus containing hypertrophic chondrocytes. The soft callus matures and remodel into a bony iii) hard callus which further is iv) remodeled into lamellar bone. Adapted figure Einhorn, 2014* [43]

The subsequent phase **ii) soft callus formation**, is driven by mostly periosteum-derived osteochondral progenitor cells which proliferate and differentiate towards the chondrogenic lineage and form a cartilaginous template (soft callus) which provides some mechanical stability of the fracture [45,46]. The cartilaginous soft callus is then remodeled into bone to form the **iii) hard callus**. This phase recapitulates major events of the EO process during limb development (1.2.1) including chondrocyte maturation into hypertrophic chondrocytes and subsequent bone formation in coordination with vascularization [47]. In addition, intramembranous ossification occurs close to the fracture, along the bone surface leading to further stabilization. The newly formed bone in the defect is woven and requires remodeling. **iv) The remodeling phase** is driven by the balance of osteoclasts and osteoblasts which remodel the newly formed woven bone into mature lamellar bone. The remodeling phase results in bone with restored mechanical properties, homeostasis and shape [39].

1.2.3. Synovial joint development

Initiation of joint development is apparent in the cartilage template where a separation called the interzone is formed (**Figure 1.7**a). The interzone defines the location of the synovial joint and is characterized by condensed, flattened cells which are *Gdf5* positive but *Col2a1* negative [13]. The origin of the *Gdf5* positive cells in the joint is not fully understood but data suggest that these cells originate from both i) the cartilage template chondrocytes and ii) areas surrounding the interzone [20]. Additionally, recent studies demonstrate a continuous invasion of Gdf5 positive cells into the interzone during joint development creating the full joint, including the articular cartilage [48]. The interzone further develops into the joint cavity which is characterized by an increased amount of hyaluronan and the development of the joint cavity has also been associated with presence of mechanical movement (**Figure 1.7**c) [13]. Subsequently, cells forming the articular cartilage expand and rearrange to create the zonal structure of adult articular cartilage (see 1.1.2) [49]. Moreover, *Prg4* positive cells from the superficial layer have been shown to proliferate and contribute to the deeper regions of the articular cartilage postnatally during aging [50]. Nevertheless, adult articular cartilage has limited tissue turnover and very limited repair after damage [51].

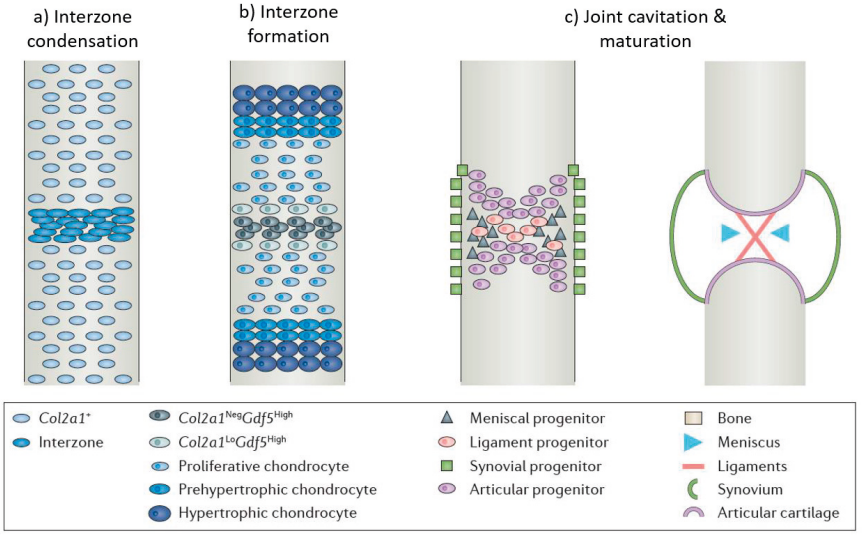

Figure 1.7. Synovial joint development *is initiated with a) interzone condensation and b) formation associated with Gdf5 positive cells. c) The joint cavitation is further developed to form the synovial joint with bone, articular cartilage, ligaments and synovium. Figure adapted from Salazar et al.* [27].

1.2.4. The importance of periosteum

The perichondrium surrounds the cartilage intermediate during development and matures into the periosteum along the bone shaft (**Figure 1.3**). The periosteum is a thin (approximately 100 μm) membrane consisting of an outer fibrous layer and an inner cellular cambium layer containing progenitor cells (stem cells, osteoblasts and endothelial pericytes) [52]. Its vasculature supply blood to neighboring bone and muscles while nerve fibers permit pain sensation in bone [53]. These components of periosteum generate a potent tissue that plays an important role in skeletal tissue during the entire lifetime by involvement in cortical bone maintenance/ thickening [54,55] as well as fracture healing [56].

The importance of periosteum during fracture healing has long been described and it was shown that damaged periosteum or removal of the periosteum results in delayed fracture healing [57,58]. Periosteal grafting has also been applied clinically for the repair of non-healing fractures and cartilage defects [59,60]. It has later been demonstrated that cells in the periosteum (compared with bone marrow or endosteum) contributes to the majority of cells within the fracture callus in murine long bone defects [56]. Upon fracture, cells within the periosteum are activated and proliferate to create the callus which was attribute to the recently identified skeletal stem cells (SSCs) within the periosteum [38,61–63]. These characteristics strongly motivate the use of periosteum as a cell source for the development of TE cell-based constructs.

1.2.5. Cell signaling pathways during skeletal development and maintenance

As described, the development of the skeleton involves an orchestrated combination of cellular and molecular interactions to form a fully functional bone organ. An important driving force are the cell secreted growth factors which bind to cell receptors activating signaling pathways to induce transcription of cell specific genes. Important signaling pathways in skeletal development include the TGFβ family (BMP, GDF, TGFβ), FGF, WNT, IGF and HH signaling pathways as demonstrated in **Figure 1.8**. Their importance has been demonstrated in multiple mouse models by genetic deletion of either ligands, receptors or signaling transducers. For example, genetic deletion of *Smad3* (signaling transducer of TGFβ) resulted in progressive degeneration of articular cartilage and accelerated chondrocyte hypertrophy while cartilage-specific (*Col2A1–Cre*) knockout of *Smad1* and *Smad5* (signaling transducer of BMPs and GDF) resulted in disruption of growth plate signaling and severe chondrodysplasia [64,65]. Double deletion of *Lrp5* and *Lrp6* in the embryonic mesenchyme resulted in limited osteoblasts and

bone formation, demonstrating the importance of WNT signaling for osteogenic differentiation [66]. Furthermore, genetic deletion of either *Ihh* or *PTHrP* resulted in skeletal defects and inhibition of Ihh eliminated the formation of SOC in mice [67,68].

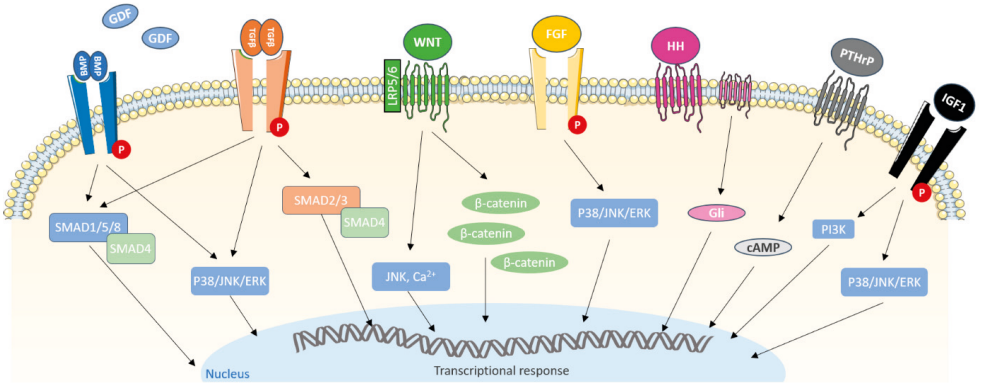

Figure 1.8. Simplified schematic of important cell signaling pathways during skeletal development. *Members of the TGFβ-family (BMPs, GDFs and TGFβs) bind to type I and II receptors, which phosphorylate (P) and recruit SMAD1/5/8 or SMAD2/3. The SMADs translocate into the nucleus together with SMAD4 to regulate gene expression. BMP, GDF and TGFβ ligands can also signal via non-canonical pathways (p38/JNK/ERK). WNT ligands bind to a frizzled receptor and LRP leading to stabilization and nuclear translocation of β-catenin. BMP: bone morphogenetic growth factor, GDF: growth/differentiation factor, TGF: transforming growth factor, WNT: wingless-related integration site, FGF: fibroblast growth factor, HH: hedgehog, PTHrP: parathyroid hormone-related protein, IGF1, insulin-like growth factor. Components of this figure were created using Servier Medical Art templates, which are licensed under a Creative Commons Attribution 3.0 Unported License; https://smart.servier.com*[69].

1.2.6. Molecular markers for cell fate specification in long bone

The major steps of endochondral ossification were outlined already a century ago by applying histological staining which demonstrated the distinct patterning in the growth plate[70]. Specific cell identity and fate specification during development and in adulthood has made major steps forward but is not yet fully elucidated. The last years, multiple research groups have identified markers for skeletal stem cells (SSCs) in different skeletal tissues regulating tissue turnover as well as repair. Identification of dedicated SSCs in different skeletal environments is therefore emerging. Cell surface markers for murine and human SSCs and progenitor cells were recently identified in skeletal tissue [71,72]. This was followed by identification of SSC niches in the growth plate, periosteum as well as SSCs in the fracture callus [38,61–63,73,74].

In addition to identification of SSCs, novel technologies such as single cell RNA sequencing (scRNAseq) have enabled a more precise description of gene regulation of limb development and growth plate cells from proliferating to hypertrophic chondrocytes [28,75]. Transcriptional regulation of chondrocyte maturation includes co-regulation of multiple transcription factors (TFs) from *Sox9* and *Gli1* in proliferating chondrocytes to *Mef2c*, *Runx2*/3 and *Sp7* in

hypertrophic chondrocytes (**Figure 1.9**) [30,76]. **This cell specific characterization of the hierarchically differentiated cells in the growth plate enables improved quality control measures for the development of skeletal cell-based therapies**.

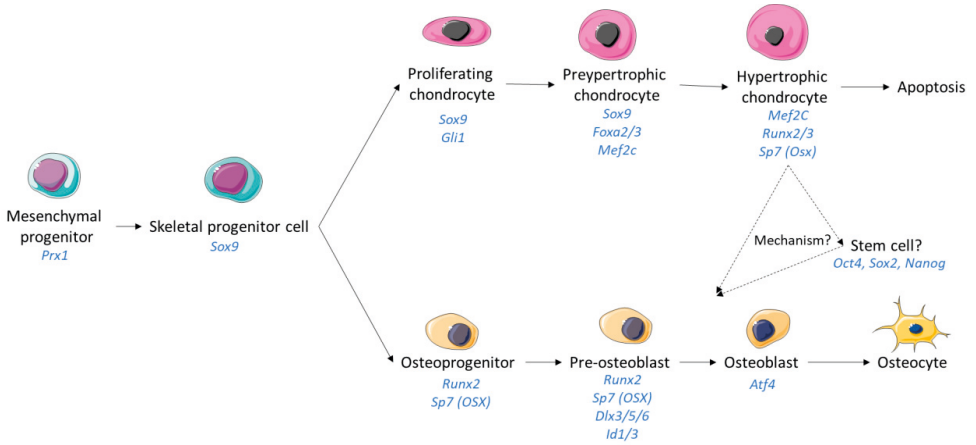

Figure 1.9. Cell fate specification during the process of endochondral ossification. *Components of this figure were created using Servier Medical Art templates, which are licensed under a Creative Commons Attribution 3.0 Unported License; https://smart.servier.com*

The main fate of hypertrophic chondrocytes was generally accepted to be apoptosis and that bone forming osteoblasts originate from cells via the blood vessels. Although osteoprogenitor cells are recruited via blood vessels and differentiate into osteoblasts (**Figure 1.9**) [33], emerging data also demonstrates that hypertrophic chondrocytes transdifferentiate into osteoblasts [77]. Even though transdifferentiation of chondrocytes into osteoblasts was described during the 90's [78–80], it was never fully accepted as a physiological phenomenon during EO *in vivo* until recently. With technical advancements allowing lineage tracing, multiple groups have redefined the fate of hypertrophic chondrocytes *in vivo* and described the occurrence of hypertrophic chondrocytes that transdifferentiate into osteoblasts during both long bone development and fracture repair [34,35,81]. The understanding of this cell plasticity is of interest for the development of cell-based *in vitro* constructs and highlights the importance of appropriate chondrogenic maturation. However, the mechanism of chondrocyte-osteoblast transdifferentiation is not fully clarified and one hypothesis includes dedifferentiation into a stem cell-like phenotype before osteoblast differentiation (**Figure 1.9**) [47,77,82]. The described cell specification and signaling factors affecting both development and repair of skeletal tissues have been studied over decades resulting in valuable information for clinical applications. However, a substantial amount of research has been performed using mouse models and care should be taken when transferring this knowledge to a human setting.

1.3. Clinical hurdles for bone and osteochondral defects

The bone tissue is remarkable with both mechanical strength and ability to self-renew without creating scar tissue. Despite these properties, bone diseases and traumatic injuries cause widespread problems leading to large bone defects that are unable to regenerate [83,84]. Bone fractures are one of the most common traumatic large-organ injuries and 5-10% of fractures do not heal properly, a prevalence that increases up to 50% for open tibia fractures [85,86]. These so called non-unions are associated with trauma, tumor, infection, metabolic bone diseases or genetic diseases [87]. In addition, age, diabetes and smoking are factors associated with delayed fracture healing [88].

In contrary to bone, cartilage is healing poorly and osteochondral defects will therefore result in substantial functional disability, pain, swelling and onset of the joint disease osteoarthritis (OA) leading to significant implications for life quality as well as burden on the healthcare system[89]. Post-traumatic OA is estimated to attribute approximately 12% of symptomatic OA of the hip, knee and ankle which corresponds to approximately 5.6 million individuals in the United States[90]. Unfortunately, an increase in skeletal defects is probable since the currently aging population is associated with fractured hips, osteoporosis and osteoarthritis [91].

1.3.1. Long bone fractures - current clinical treatments

The gold standard for treatment of bone defects is autografts where bone from the patient is transplanted to the defect site. Autografts have demonstrated good results also for treatment of non-unions but entails drawbacks, *e.g*. limited amount of healthy bone tissue and/or risk of infection as well as the requirement for additional surgeries to retrieve healthy bone tissue [92,93]. The use of allografts (donor derived tissue), typically for larger defects, is also a common treatment but is associated with limited graft integration and vascularization. Distraction osteogenesis, where a fracture is introduced to enable slow movement over a long time to allow healing, is applied to non-unions and large long bone defects. Although this technique is well established, it requires extended healing time and entail high infection risks [87]. To overcome these treatment limitations, bone graft substitutes have and are being developed. These include biomaterials based on decellularized bone matrix and ceramics *e.g*. calcium phosphate cement, tri-calcium phosphate and hydroxyapatite [94]. Addition of bioactive molecules have shown promise with the combination of BMP-2 and collagen type I sponge but adverse effects have been reported with the off-label use of supra-physiological BMP-2 concentrations [95].

Additional growth factor based and cell-based treatments (orthobiologics) are currently studied in clinical trials [96].

Finally, the type of fracture with regard to size and location as well as the surrounding environment are important parameters for the choice of treatment. Smaller fractures are able to heal on their own and biomaterial-based substitutes exist for non-compromised fractures but healing of large long bone defects and non-unions requires a biological alternative. **Suitable cell-based products, which would circumvent autograft shortage, are still lacking**.

1.3.2. Osteochondral defects - current clinical treatments

An osteochondral defect is defined as a local damage of the joint surface which includes both the articular cartilage and the underlying subchondral bone [97]. The cartilage has strong mechanical properties to sustain load, but unlike bone, it has poor regenerative capacity partially attributed to the tissues' avascular nature [98]. Consequently, osteochondral defects are also slow healing and regenerated cartilage tissue is often of a fibrocartilaginous nature which lack the biomechanical properties of native cartilage [98,99]. If left untreated, osteochondral defects results in the joint disease osteoarthritis (OA) [89]. OA is characterized by progressive remodeling of the joint including degradation of articular cartilage, bone and adjacent tissues[100].

Pharmacological strategies have been suggested to prevent post-traumatic OA by targeting inflammatory response but these methods should be implemented in combination with surgical methods to enable regeneration of the osteochondral defect [100]. Current surgical methods for treatment of deep osteochondral defects (>8 mm) include osteochondral autograft/allograft transplantation and autologous bone grafting in combination with autologous chondrocyte implantation (ACI), named "ACI sandwich technique" [101–103]. These techniques entail drawbacks since autografts are restricted by limited tissue availability and expansion of articular chondrocytes for ACI is associated with chondrocyte dedifferentiation [102,104]. Conclusively, improved techniques for regeneration of deep osteochondral defects are needed to enable joint function after damage. **This PhD project focused on the development of cell-based constructs that will enable formation of both articular cartilage and subchondral bone**.

1.3.3. Advanced Therapy Medicinal Products

The field of regenerative medicine aims to develop methods and products to repair/restore the function of damaged tissues or organs. In Europe, the European Medicine Agency (EMA) defines these products as "Advanced therapy medicinal products" (ATMPs) which include medicines based on a) gene therapy, b) somatic cell therapy or c) tissue engineering with the purpose to treat acute or chronic diseases in a long-term or permanent manner. More specifically, a) gene therapy entails insertion of recombinant genes with a therapeutic or diagnostic effect while b) somatic cell therapy contains manipulated cells/tissues which changes their biological characteristics to cure, diagnose or prevent diseases and finally, c) tissue engineered medicines, focus in this thesis, contain modified cells/tissues able to repair, regenerate or replace human tissue[105]. The last decade, twenty-six ATMPs were submitted for market authorization (EMA) in Europe, of which only fourteen received authorization (January 2020)[106]. Three of the approved products involved tissue engineered products for treatment of articular cartilage defects (ChondroCelect®, MACI® [autologous cultured chondrocytes on porcine collagen membrane] and Spherox®) however ChondroCelect® and MACI® were withdrawn from the market for commercial reasons. Notably, no tissue engineered ATMP for bone defects has been accepted up to date (January 2020).[106,107]

In addition to limited acceptance of submitted applications, only a limited number of products in clinical trial are presumed to go further to marketing authorization application submission at EMA. Search on "fractures, bone" and "cells" at clinicaltrials.gov results in 124 clinical studies whereof 54 are European studies while search on "cartilage defect" and "cells" resulted in 40 registered trials worldwide of which 16 were registered in Europe [108,109]. Although ATMPs have promise to obtain successful organ/tissue repair, only a few products are available. Improvements regarding robustness and scalability are required already at an early stage of product development to enable future clinical application[110,111].

1.4. Classical skeletal tissue engineering

The term "tissue engineering" (TE) was introduced during the late 80s and described in different meeting proceedings [112]. However, TE advanced as a general research field after a review paper by R. Langer and J. P. Vacanti in 1993 (**Figure 1.10**) where TE was described as "an interdisciplinary field that applies the principles of engineering and the life sciences toward the development of biological substitutes that restore, maintain, or improve tissue function" [113]. Since 1994, publications involving "Tissue Engineering" went from 26 to 4900 in 2019 of which bone and cartilage TE represent approximately half of the publications (**Figure 1.10**). With the introduction of TE, two dimensional (2D) monolayer cultures were adapted towards three dimensional (3D) constructs to mimic the structure of native tissues. This entailed the combination of biocompatible scaffolds (1.5.1), bioactive molecules (1.5.2) and progenitor/osteogenic cells (1.5.3) to create a 3D tissue similar to the adult tissue structures (see 1.1). For bone, this strategy mainly involved the formation of a mineralized 3D construct with focus on direct bone formation (intramembranous ossification, see 1.2) [114].

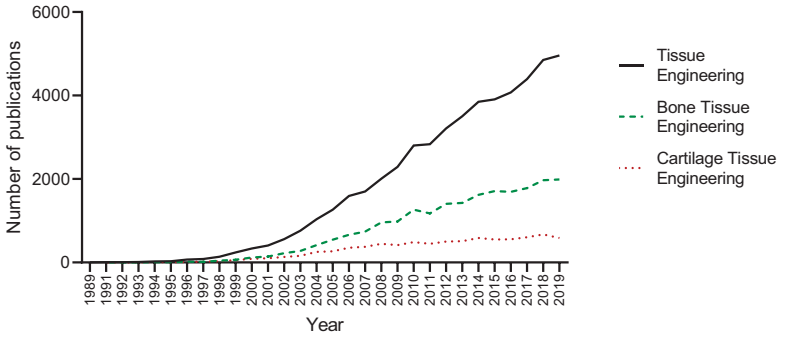

Figure 1.10. *Number of publications per year including "Tissue Engineering" (black line), "Bone Tissue Engineering" (green dashed line) or "Cartilage Tissue Engineering" (red dotted line). Certain data included herein are derived from Clarivate Web of Science. © Copyright Clarivate 2019. All rights reserved.*

1.4.1. Biocompatible scaffolds

Scaffolds for skeletal tissue engineering aim to generate structural stability and guide functional tissue regeneration followed by degradation to allow replacement by *de novo* tissue. Regarding bone, scaffolds with strong mechanical stability and inclusion of ceramic components have commonly been applied to render strength and mimic the native bone structure (1.1.1). These biomaterials include calcium phosphates (CaP), synthetic polymers (PCL, PLGA, PLLA), as well as biomaterials derived from native tissues such as decellularized bone and collagen [115]. Multiple scaffolds based on decellularized bone, ceramics and/or

collagen have already been commercialized as products for bone regeneration, including NuOss™ (Ace Surgical), Bio-Oss® (Geistlich), chronOS® (Synthes), CERAFORM® (Teknimed). While scaffolds alone can be sufficient to heal smaller non-loading bone defects, larger segmental defects require cellular constructs to permit full tissue regeneration.

Concerning cartilage TE, hydrogel-based scaffolds have been in focus to render a suitable environment for chondrocytes and ECM secretion. Both natural hydrogels (agarose, alginate, fibrin, gelatin, hyaluronic acid) and synthetic hydrogels (polyethylene glycol, polylactic acid) have been applied alone or in combinations to generate scaffolds with mechanical and structural properties similar to native cartilage (1.1.2) [116,117]. Scaffolds based on collagen (Chondro-Gide® - Geistlich and Novocart® Basic - Tetec), hyaluronic acid (HYALOFAST® - Anika) and decellularized hyaline cartilage (DeNovo® NT – Zimmer and Biocartilage ® - Arthrex) are currently available for cartilage regeneration and allograft-derived osteochondral scaffold (Chondrofix ® - Zimmer biomet) for osteochondral defects.

1.4.2. Bioactive molecules

Bioactive molecules represent a powerful strategy to improve tissue regeneration by promoting cell differentiation towards intended cell type (osteoblast/chondrocyte etc.) or attract cells either i) upon implantation by functionalization of scaffolds or ii) during *in vitro* culture of TE constructs. The choice of bioactive molecules is commonly based on knowledge gained from development and repair where multiple growth factors are active as described in 1.2 and 1.2.2. BMPs, which are part of the TGF-β superfamily, are present during both bone development and fracture healing in a sequential manner and represent a major part of bioactive molecules used for skeletal TE [27]. BMPs have the capacity to differentiate progenitor cells towards the osteochondral lineage *in vivo* and have been shown to generate bone upon implantation in combination with CaP/collagen scaffolds [118]. Among BMPs, BMP-2 has been proven crucial for initiation of fracture healing in mice and has also gained focus in bone TE as well as in the clinics with the commercialized product Infuse® Bone Graft (Medtronic, Inc.) which combines rhBMP-2 with a collagen type I scaffold [119,120].

Growth factors from the FGF and WNT-family are present during the early phases of development and have been applied to induce proliferation alone or in combinations to prime progenitor cells before differentiation [121–123]. For example, priming human BMSCs with FGF2 and WNT3A resulted in improved chondrogenic potential during TGFβ1 driven differentiation [123]. Chondrogenic differentiation is indeed commonly induced by adding TGFβ1/3 which links

to the importance of the TGFβ-signaling pathway in cartilage development and homeostasis [13]. However, the addition of TGFβ1 to induce chondrogenic differentiation have demonstrated varying results to achieve hyaline-like cartilage where onset of hypertrophy and presence of fibrous tissue have been reported [124–126]. Strategies to combine multiple growth factors and pharmacologically inhibit/activate specific signaling pathways during *in vitro* differentiation are therefore gaining more interest [123,124,127–130].

1.4.3. Cell source

Cells derived from adult tissues, e.g. osteoblasts and chondrocytes, have been applied for bone and cartilage TE respectively. However, the most common cell type studied for bone TE is so called mesenchymal stromal cells (MSCs) due to their multipotency [131]. MSCs were originally isolated from bone marrow and bone marrow stromal cells (BMSCs) are still the most widely applied cells for TE. The minimum criteria for MSCs have been defined *in vitro* as plastic adherence, expression of specific surface markers (CD105+, CD73+, CD90+, and CD45-, CD34-, CD14-) and potency to differentiate into osteoblasts, chondrocytes and adipocytes *in vitro* [132]. Although MSCs were first identified in bone marrow, multipotent progenitor cells have been identified and used in TE from a number of tissues including adipose tissue [133], synovial membrane [134,135] and periosteum [136–139]. However, progenitor cells from different donors and tissues demonstrated varying differentiation potential which indicated that they were not identical and the "MSC" cell populations used in TE are indeed heterogeneous and contain multiple cell types instead of one specific stem cell population [140,141]. The definition of "MSCs" is and has therefore been controversial along with novel identification of "true" stem cells in different skeletal tissues *in vivo* (see 1.2.5) defined as skeletal stem cells (SSCs) [71,73]. In contrary to SSCs, tissue-derived "MSCs" represent a heterogenous cell population, possibly including stem cells but also more specified progenitor cells. **This thesis focused on human periosteum-derived cells (hPDCs)** because of the importance of periosteum during fracture healing (see 1.2.4). Recent identification of SSCs in the periosteum have further increased the interest in periosteum as a cell source for bone TE [38,61–63]. Furthermore, direct comparison of adult murine periosteum derived cells (mPDCs) with murine BMSCs, demonstrated improved clonogenic and regenerative potential for mPDCs [38,61].

Pluripotent stem cells derived from human embryo (hESCs) possess great proliferation and differentiation capacity and have therefore value for skeletal tissue engineering [142]. However, their application remains challenging because of ethical considerations related to their origin.

In addition, clinical application of allogeneic hESCs entails a risk of immune rejection [143]. Human induced pluripotent stem cells (hiPSCs) derived from adult somatic cells have therefore gained significant interest in skeletal tissue engineering [144–146].

1.5. Developmental engineering - towards biological manufacturing

Despite decades of research applying a top-down approach with seeding cells onto scaffolds and adding bioactive molecules, few tissue engineered constructs have reached the market (1.3.3). The limited clinical translation has been associated with a lack of robust manufacturing processes leading to inhomogeneous *in vitro* constructs as well as to the biological hurdles of mimicking the complex composition of cells, extracellular matrix as well as retaining viability during *in vitro* culture and after implantation[147]. These hurdles have been linked to the approach of combining distinct fields (biology and engineering) with isolated specific knowledge in cells, bioactive molecules or scaffolds with a trial-and-error method instead of developing a novel *in vitro* process using the fields combined knowledge [148].

R. Langer and J. P. Vacanti described tissue engineering as the merging of biology and engineering principles[113] but the "top-down" approach of seeding single cells onto scaffolds have dominated the bone TE field with limited success for clinical translation [149]. Consequently, researchers reconsidered the approach of generating constructs that mimic the final tissue structure to instead observe the process of tissue development, and coined the term "developmental engineering" [148,150]. Importantly, the three components described above (scaffolds 1.4.1, bioactive molecules 1.4.2 and cell source 1.4.3) are still crucial for the development of bioartificial tissues but the "developmental engineering" approach have generated a **paradigm shift in tissue engineering where engineering strategies are applied to recapitulate developmental processes** [148,151].

"**Developmental engineering**" **aims to create *in vitro* intermediate tissues that remodel into functional tissues upon implantation *in vivo* by mimicking developmental stages of native tissues** [151]. This concept suggests the application of an engineering perspective with focus on process design to mimic developmental events as described in developmental biology. Since the development of tissues has been studied during centuries, considerable knowledge of the developmental stages already exists (see 1.2). This knowledge generates a template to both follow and use as "quality control" during the *in vitro* process as well as for the final intermediate provisional tissue. By following the sequential stages of tissue development or repair, progression of the intermediate tissue is expected to reach a stage of semi-autonomy allowing successful maturation and host integration upon implantation [152,153].

1.5.1. Bone developmental engineering - recapitulate endochondral ossification

The principal development and repair of long bones occur through endochondral ossification (1.2.1 and 1.2.2). Accordingly, recapitulation of EO has been suggested for creation of cell-based cartilage intermediate constructs to heal long bone defects [150,154–156]. The inherent autonomy of EO has previously been described by ectopic implantation of whole and dissociated murine cartilage anlage, resulting in continuous limb growth and formation of growth plate-like structures [157]. Hence, recapitulation of the initial stages of EO (**Figure 1.5**a-c) is hypothesized to direct cells in a synchronized manner to produce appropriate ECM and growth factors required for bone formation upon implantation [148]. Accordingly, the extensive knowledge in the growth plate and its molecular regulation (1.2.6) represents robust process guidelines and quality controls for an EO *in vitro* process (**Figure 1.11**).

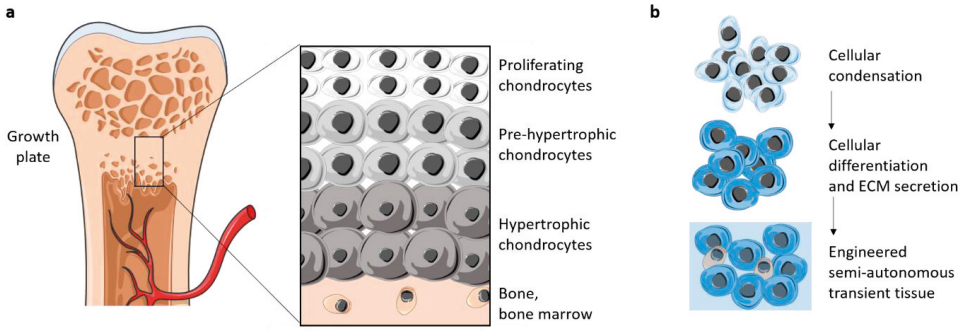

Figure 1.11. Knowledge from in vivo development represents guidelines and quality control for the in vitro process. *a) The growth plate contributing to longitudinal growth during long bone development contain a hierarchical structure of chondrocytes going through endochondral ossification (EO). b) Cellular and molecular knowledge from initial cellular condensation and growth plate advancement during bone development can guide the in vitro process to create engineered semi-autonomous transient tissues. The schematic was produced using Servier Medical Art (https://smart.servier.com). Servier Medical Art by Servier is licensed under a Creative Commons Attribution 3.0 Unported License (https://creativecommons.org/licenses/by/3.0/).*

The advantage of the EO approach as compared to the intramembranous ossification (direct bone formation) strategy has been demonstrated by chondrogenic differentiation of BMSCs seeded on calcium and/or phosphate-based scaffolds [158–160]. However, the presence of mineralized scaffolds has later been shown to impede the EO ossification *in vivo* [161,162]. In addition, recapitulation of the initial stages of EO during skeletal development (1.2.1) requires cellular condensation [16]. To mimic this mesenchymal condensation, a common approach has been to seed hundred thousand of cells on non-adherent surfaces leading to aggregation which generates scaffold-free pellets or micromasses [124,125,161,163–167]. Subsequent chondrogenic differentiation and ectopic/orthotopic implantation in mice have resulted in the formation of

complete ossicles (small bone) and fracture bridging. The newly formed bone organs contained mature bone as well as bone marrow compartments with multilineage murine hematopoietic cells and progenitors [165,166,168,169]. However, despite demonstration of bone organ formation, pellet structures and large cell constructs often contained fibrotic/necrotic areas. Presence of fibrotic/necrotic areas *in vitro* has been linked with diffusion limitations, and resulted in bone structures with fibrous areas also after implantation [124,170–172]. In addition, it has been stated that adjacent chondrogenic pellets do not integrate with each other which will impede further scale-up [173].

The differentiation of progenitor cells to create a cartilage intermediate is of importance and the extent of chondrogenic differentiation required for bone formation has been, and is still under investigation. Current culture media strategies involve differentiation with only chondrogenic media[161,174–176] or in combination with hypertrophic/osteogenic media[171,177,178] formulations to reach pre-hypertrophy or hypertrophy prior to implantation. Although there is a consensus that a hypertrophic stage should be reached, the level of maturation is still debated *i.e.* presence of mineralization or not [171,176]. Nevertheless, in addition to knowledge from developmental biology[179], some differentiation protocols have linked markers to the *in vivo* capacity of bone organ formation making it possible to define the required *in vitro* maturity [125]. However, optimal *in vitro* maturity will need optimization and depends on both culture setup and cell type used.

1.5.2. Osteochondral developmental engineering

Analogous concepts apply for developmental engineering of osteochondral tissues. While adult articular cartilage is healing poorly, early fetal cartilage defects repair spontaneously [180]. Hence, a developmental engineering strategy to mimic joint development (0) and create an early intermediate tissue presents a promising strategy for osteochondral repair. Accordingly, the subchondral bone zone is suggested to be generated through EO forming bone and a mineralized cartilage zone with an overlying zone of non-mineralized hyaline-like cartilage.

A plethora of tissue engineered osteochondral constructs exist and many include a mineralized scaffold to represent mature bone and cell-based constructs to represent cartilage. However, the direct combination of a mineralized scaffold and hydrogel/cells for cartilage have resulted in limited integration between the two zones and less attention has been paid on the interface between bone and cartilage [181]. By mimicking joint development and create a cell-based osteochondral tissue intermediate, it is anticipated that the gradual cartilage-bone interface can

mature and stabilize upon implantation. The creation of such zonal structure requires controlled stimulation of cellular differentiation *in vitro* in addition to modulation of construct architecture. These are parameters which can be met by a modular developmental engineering approach.

1.6. Assembly of developmentally engineered modules

Developmental engineering for skeletal tissue engineering has enabled the formation of cell-based constructs which form bone organs in a biologically robust manner, mimicking the developmental pathway endochondral ossification (1.5.1). However, these *in vitro* cultures have a size restraint since diffusion limitations hinder the creation of larger homogeneous constructs with high cell density [182]. The proposed solution to this limitation includes the generation of smaller cellular building blocks which subsequently are assembled into a defined spatial structure, a so-called bottom-up approach. Cellular building blocks range from cell fibers, cell spheroids to more complex structures such as organoids which can be assembled either alone or in combinations with biomaterials (**Figure 1.12**) [183–185]. The concepts of a modular bottom-up approach have previously been well described and *in vitro* studies have demonstrated building block fusion but the translation towards *in vivo* functional bioartificial tissues is still limited [185,186]. This thesis includes a bottom-up strategy using cellular spheroids that undergo chondrogenic differentiation prior to assembly.

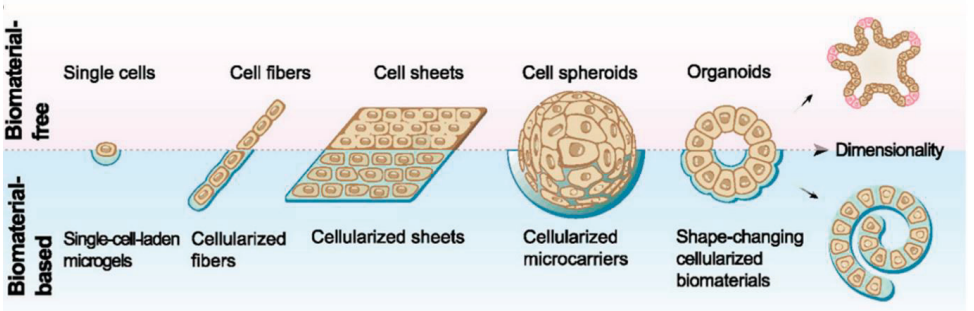

Figure 1.12. *Schematic visualization of different living building blocks to be applied for assembly into larger tissues. Figure adapted from Ouyang et.al 2020* [185].

1.6.1. 3-dimensional spheroid culture

The inherent capacity of cells to self-assemble allows the formation of 3D scaffold-free *in vitro* cellular aggregates when cells are seeded onto non-adherent surfaces[187]. Survival and growth of aggregated cells *in vitro* was demonstrated early[188] using different cells types *i.e.* chick chondrogenic and limb-bud cells[189], and cancer cells[190]. These cell cultures provide cell-cell interaction and possibility for ECM secretion to generate a microenvironment that resembles their native counterpart. The 3D structure generates diffusion gradients from the outer border to the central core, where a decrease in oxygen tension as well as nutrients has been described

[191]. Although a certain gradient may be beneficial, depletion of oxygen and nutrients in the central aggregate regions leads to dying cells and the formation of necrotic cores. Necrotic cores can be avoided by creating aggregates with a limited diameter length corresponding to the mass transfer limitations of the specific cell type which frequently represents a few hundreds of micrometers [192,193]. In this thesis, small aggregates are named microspheroids.

Cellular aggregation in multi-well plates (96, 384 and 1536 wells/plate) or microwells (200-2000 microwells/well) have enabled high-throughput formation of microspheroids [194]. Along with these emerging high throughput platforms, 3D cultures, such as spheroids, microtissues and organoids, have gained great interest scientifically (**Figure 1.13**). Developmentally inspired differentiation of stem and progenitor cells in micrometer to millimeter sized spheroids have resulted in the formation of microtissues, containing "cells + ECM", and more complex organoids characterized by cellular architecture and function (**Figure 1.12**).

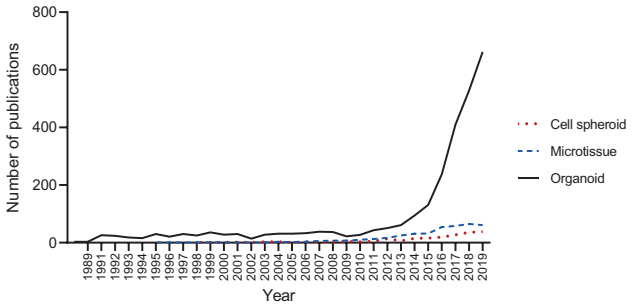

Figure 1.13. *Number of publications containing the key words "cell spheroid", "microtissue" or "organoid" have increased the last decade. Certain data included herein are derived from Clarivate Web of Science. © Copyright Clarivate 2019. All rights reserved.*

Microtissues and organoids represent modules of increased maturity as compared to microspheroids and resemble therefore their native counterpart tissue/organ regarding presence of ECM and cellular organization as well as function. Microspheroids or microtissues have previously been investigated for cardiovascular, respiratory as well as musculoskeletal system (cartilage[186,195,196] and bone[197]) either alone or in combination with biomaterials [198]. The more complex, adult human stem cell-derived organoids have been created by mimicking the native stem cell environment and/or repair process of intestine, liver and pancreas among others and PSC-derived organoids have been generated by recapitulation of organ development of *e.g.* kidney, heart, optic cup and brain compartments [199,200].

Up till now, applications for microtissues and organoids have mostly included disease modeling and drug screening while the use as building blocks for tissue regeneration has been limited [199]. Nevertheless, these 3D structures have great promise for developmental engineering since they i) mimic native tissue/organ structures and ii) function, iii) circumvent diffusion limitations *in vitro* and iv) are able to fuse through cell-cell/ECM interactions [185,194,199]. Nonetheless, the knowledge in how mature building blocks assemble and if the building blocks are able to create larger functional tissues/organs is restricted.

2

CHAPTER 2.

Hypothesis, objectives and methodology

2.1. General hypothesis and project aim

Tissue engineered constructs for bone and cartilage regeneration have shown promise in research but only a limited number of Advanced therapy medicinal products (ATMPs) have reached clinical translation [111]. This indicates inappropriate strategies and requires new approaches. Tissue engineering is therefore more and more leaving the concept of *seeding single cells onto a scaffold of defined size*, to instead mimicking the process of tissue development and build from the "bottom-up" by creating building blocks (modules) which subsequently are assembled into larger intermediate tissues. This concept has been defined as "**developmental engineering**" and is hypothesized to allow the generation of intermediate tissues *in vitro* that upon implantation can regenerate damaged tissues.

Bone development (endochondral ossification) has previously been mimicked *in vitro* and shown promise by the formation of hypertrophic cartilaginous *in vitro* pellets (1-2 mm) which generate bone organs upon subcutaneous implantation [168,171]. However, diffusion and assembly limitations are prone to hamper translation towards scalable production. In this thesis, the developmental engineering concept was taken to the next level through assembly of smaller building blocks (100-200 μm) to create living implants. Despite description of bottom-up approaches and their *in vitro* functionality [194], few research groups have reported functional regeneration of tissues or organs. **The aim of this PhD-project was to develop a developmentally inspired micromodule-based process for bone and cartilage repair.**

2.2. Specific objectives and hypotheses

This thesis was divided into three chapters (**Figure 2.1**) and the specific objectives were to:

CHAPTER 3: Develop a blueprint for micromodule-based healing of long-bone defects including building block characterization. Based on the process of endochondral ossification which starts with mesenchymal condensation, a culture system allowing cellular condensation was applied to recapitulate the events of endochondral ossification. The use of microspheroids (~100 μm) was hypothesized to overcome diffusion limitations which are seen in the commonly applied chondrogenic differentiation assay pellet culture. Next, transcriptomic analysis of the *in vitro* differentiated microspheroids was compared to the developmental process endochondral ossification, and subcutaneous implantations were performed to enable identification of a chondrogenic maturity level that is required to generate bone organs *in vivo* and heal a critically-sized murine long bone defect.

CHAPTER 4: Demonstrate modular capacity by assembly of distinct cellular building blocks for the generation of osteochondral tissues *in vivo* (ectopically). The inherent capacity of cellular spheroids to fuse was hypothesized to also allow assembly of cellular building blocks with different cellular phenotype to create an osteochondral tissue unit. Adult progenitor cells, hPDCs, were used to generate the osteogenic part while either hPDCS or hiChon were studied for the chondrogenic part. The modular approach allowed specific differentiation culture for each building block phenotype, followed by assembly shortly before implantation. With defined cell type and controlled pre-differentiation, each phenotype was anticipated to retain their specific capacity to further mature towards either bone or cartilage upon implantation.

CHAPTER 5: Investigate the design limitations of the developed micromodule-based approach. The first aim was to investigate how chondrogenic maturity affects micromodule assembly. A dual spheroid fusion assay and a spheroid spreading assay on adherent surface was applied as a mean to quantify differences. Next, the impact of "time-of-assembly" as well as "size of construct" of the final tissue engineered construct was studied to identify optimal parameters. These investigations are of importance to define design limitations for future scale-up and automation of spheroid-based tissue engineering.

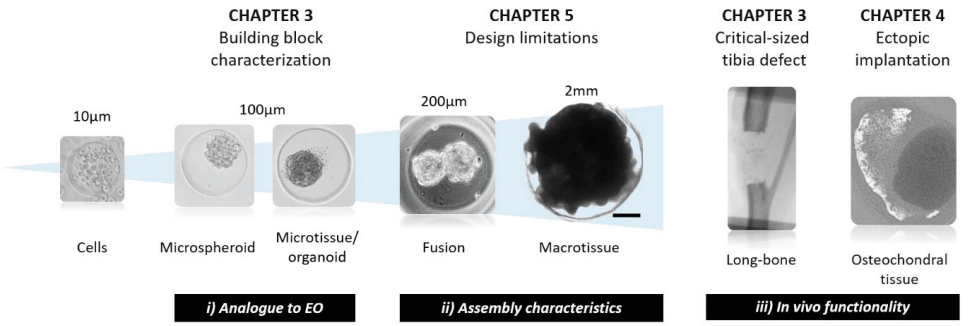

***Figure 2.1. Thesis CHAPTER overview**. The three chapters will cover a modular developmental engineering approach using differentiated cell spheroids. The following parameters were defined: i) building block maturation analogous to endochondral ossification (EO), ii) assembly characteristics to define design limitations and iii) the in vivo functionality of engineered constructs.*

2.3. Experimental methodology

The general experimental methodology used to reach the described aim and objectives of this dissertation are presented below. For detailed description of materials and methods, see CHAPTER 3-5.

2.3.1. Cell types

Adult progenitor cells were derived from periosteum of multiple human donors (9 donors of ages between 10-47 years). Biopsies were expanded in FBS-based expansion media and combined to create **human periosteum-derived cell (hPDC)** pools. hPDC cell pools were evaluated for spheroid formation and subsequent chondrogenic differentiation. (CHAPTER 3-5)

Human induced pluripotent stem cells (hiPSCs) were induced towards mesoderm followed by chondrogenic differentiation to generate cartilage-like nodules. The nodules were enzymatically digested to isolate **hiPSC derived chondrocytes (hiChon)**. hiChon were assessed for spheroid formation and cartilage formation. (CHAPTER 5)

2.3.2. Cell culture set-up

Cell expansion of hPDCs was performed in tissue culture flasks at a density of 5700 cells/cm^2. (CHAPTER 3-5)

Microspheroid formation was achieved using micro-well platforms created from agarose. The non-adherent agarose hampers cell adhesion to its surface leading to cellular aggregation within each micro-well (200-400 μm in diameter). (CHAPTER 3-5)

Building-block assembly was done in agarose macro-wells of defined size depending on application. (CHAPTER 3-5)

2.3.3. Media formulation

hPDC spheroids were differentiated in a serum-free chemically-defined chondrogenic media containing developmentally relevant growth factors presented in **Table 1**. The cell culture was previously optimized for high cell density cultures of hPDCs [128].

Table 1. *List of growth factors present in the differentiation media and their knockout phenotype.*

Growth factor	Knockout phenotype
BMP2	Limb specific (*Prx1*): spontaneous fractures and impaired fracture healing [119] Cartilage specific (*Col2a1*): impaired fracture healing[201]
GDF5	Brachypodism; altered joint and bone formation[202]
TGFβ1	Limb specific (*Prx1*) deletion of *Tgfbr2*: short limbs and fusion of the joints [27]
BMP6	Reduced growth plate function and decreased cortical cross-sectional area[203]
FGF2	Decreased bone mass[204]

2.3.4. *In vitro* assays

Cellular identity and purity of microspheroids, microtissues and organoids was characterized with gene expression analysis (real-time quantitative PCR and RNAseq), immunostaining and histological staining. Cell viability and proliferation was assessed using fluorescent staining and DNA quantification. Image analysis was performed with ImageJ software[205] to quantify features of bright field and histological microscope pictures.

2.3.5. *In vivo* assays

The potency of intermediate tissue constructs to form bone/cartilage was assessed in ectopic (subcutaneous) and orthotopic long-bone critically-sized defect (4 mm, tibia) mouse models. Neo-tissue formation was characterized using *in vivo* computed x-ray tomography (CT), nano-CT, histological staining, immunostaining and histomorphometry.

CHAPTER 3.

Developmentally engineered callus organoid bioassemblies exhibit predictive *in vivo* long bone healing

3

Gabriella Nilsson Hall[1], Luís Freitas Mendes[1], Charikleia Gklava[1], Liesbet Geris[1,2,3], Frank P. Luyten[1,] and Ioannis Papantoniou[1,‡,*]*

* These authors share senior authorship

[1]Prometheus Division of Skeletal Tissue Engineering and Skeletal Biology and Engineering Research Center, Department of Development and Regeneration, KU Leuven, Belgium. [2]GIGA in silico medicine, Université de Liège, Belgium. [3]Biomechanics Section, KU Leuven
Belgium. ‡ Current address: Institute of Chemical Engineering Sciences (ICE-HT) Foundation for Research and Technology, Hellas (FORTH), Greece.

Manuscript adapted from *Advanced Science* (2020) 1-16; doi:10.1002/advs.201902295.

Open access article distributed under the terms of the Creative Commons CC BY license

Abstract

Clinical translation of cell-based products is hampered by their limited predictive in vivo performance. To overcome this hurdle, engineering strategies advocate to fabricate tissue products through processes that mimic development and regeneration, a strategy applicable for the healing of large bone defects, an unmet medical need. Natural fracture healing occurs through the formation of a cartilage intermediate, termed “soft callus,” which is transformed into bone following a process that recapitulates developmental events. The main contributors to the soft callus are cells derived from the periosteum, containing potent skeletal stem cells. Herein, cells derived from human periosteum are used for the scalable production of microspheroids that are differentiated into callus organoids. The organoids attain autonomy and exhibit the capacity to form ectopic bone microorgans *in vivo*. This potency is linked to specific gene signatures mimicking those found in developing and healing long bones. Furthermore, callus organoids spontaneously bioassemble *in vitro* into large engineered tissues able to heal murine critical-sized long bone defects. The regenerated bone exhibits similar morphological properties to those of native tibia. These callus organoids can be viewed as a living “bio-ink” allowing bottom-up manufacturing of multimodular tissues with complex geometric features and inbuilt quality attributes.

3.1. Introduction

Tissue-engineered advanced therapy medicinal products (TE-ATMPs) are poised to revolutionize health care by replacing or restoring the function of damaged organs. Although major advances in the field of cell therapy manufacturing have been witnessed, only a small fraction of TE-ATMPs exhibit quality attributes that could guarantee predictive performance *in vivo* and hence support clinical translation.[1-3] To tackle these hurdles, a conceptual and technical merging of developmental biology and engineering principles is taking place within regenerative medicine. These "developmental engineering" strategies strive to mimic developmental events while guaranteeing robustness and predictive outcomes in a clinical setting.[4-7] According to this strategy, cellular self-assemblies and condensations of the appropriate length scale are key initiators for the formation of transient tissue structures capable of executing developmental programs with a high level of independence leading to organogenesis processes.[8, 9] These processes are regulated through the activation of tissue-specific genes and pathways characterized by a high degree of autonomy resulting in tissues that are able to undergo a similar cascade of processes even *ex vivo*.[10] This type of recapitulation of developmental events has previously been demonstrated with human adult stem cells, for example, for the formation of epithelial1 and liver [11] organoids.

In the context of bone tissue engineering, fracture healing of long bones includes the formation of a cartilaginous "soft callus" that subsequently is transformed into bone,[12] a process that resembles the well-described and tightly synchronized process of endochondral ossification in the growth plate during development.[13-15] The autonomy of the growth plate cartilage in embryonic cartilage anlagen was previously reported, and even when the cartilage anlage was decomposed into single cells and re-implanted subcutaneously, re-organization occurred and a growth plate-like structure was formed.[4, 10] Furthermore, investigations inspired by "developmental engineering" demonstrated recapitulation of endochondral ossification in ectopic environments using embryonic stem cells[16] or bone marrow mesenchymal stromal cells (BM-MSCs)[17, 18] and orthotopically using rat[19] or human[20] BM-MSCs. However, only partially successful results have been demonstrated due to scalability challenges and uncontrolled complexity in 3D cell culture formats currently used for inducing chondrogenic differentiation.[18, 21] The use of scaffold-free microspheroid cultures could provide a more homogeneous 3D culture format to precisely engineer soft callus-like microenvironments.[22-25] The ability to produce populations of small functional modules will constitute a major step toward the incorporation of design principles in skeletal living implant manufacturing.[2]

The formation of high-throughput cell microspheroid populations of defined size and their use as building modules for bottom-up tissue formation strategies is gaining momentum for various TE applications.[22, 26-28] However, the construction of complex engineered tissues possessing multicomponent tissue architecture is still elusive. Although bottom-up approaches have been suggested in recent years in order to build larger tissue structures from micromodules, the majority of these studies used cell microspheroids with minimal cell-secreted extracellular matrix (ECM).[26] Regarding long bone defect regeneration, there is scarce literature on the potential of modular bioengineering strategies to generate larger implants while there is no understanding yet of how this architecture dictates whole tissue function after implantation. Ideally, modules for regeneration of long bone defects should possess an autonomy that would guarantee that the repeated functional units can synergistically contribute to the regenerative process, resulting in a predictive clinical outcome.

In this work, we present a developmental bioengineering strategy based on self-assembly of human-periosteum-derived cells (hPDCs). hPDCs have great promise for regeneration of long bone defects, since the majority of cells forming the "soft callus" during fracture healing are derived from the periosteum.[14, 15, 29] In addition, recently published studies demonstrated the presence of skeletal stem cells within the periosteum with improved capacity to regenerate bone as compared to BM-MSCs.[15, 30] Herein, self-assembly of hPDCs allowed scalable production of semiautonomous callus organoids that formed bone microorgans upon implantation. The *in vitro* maturation toward callus organoids was linked to gene expression patterns encountered in the embryonic growth plate and during fracture healing. Furthermore, an assembly of multiple callus organoids resulted in multimodular constructs that formed large bone organs ectopically and healed critical-sized long bone defects in mice. In both cases, bone organs were formed in the absence of contaminating fibrotic tissue and exhibited a well-developed bone marrow compartment, thus demonstrating the potential of this modular approach (Figure 1a) for future clinical applications.

3.2 Results

3.2.1 Long-Term Culture of Microspheroids Follows Early Pattern of Endochondral Ossification

Endochondral ossification is initiated with cell aggregation and condensation, followed by chondrocyte specification, differentiation, and formation of a cartilage tissue intermediate that

subsequently is replaced by bone.[31] Here, cell aggregation, condensation, and differentiation of hPDC microspheroids were studied over a period of 4 weeks (Figure 1b, c). The self-aggregation process comprised two steps. Initially, over a course of 5 h (day 0), hPDCs self-assembled to form a stack of cells until a spheroid shape was attained (Figure 1c, d; Movie S1, Supporting Information). Filamentous-actin (F-actin) staining demonstrated changes in the actin cytoskeleton by formation of stress fibers during the first week as well as compaction of microspheroids with a more confined cortical actin network over time and its thinning after 3 weeks (Figure 1d).

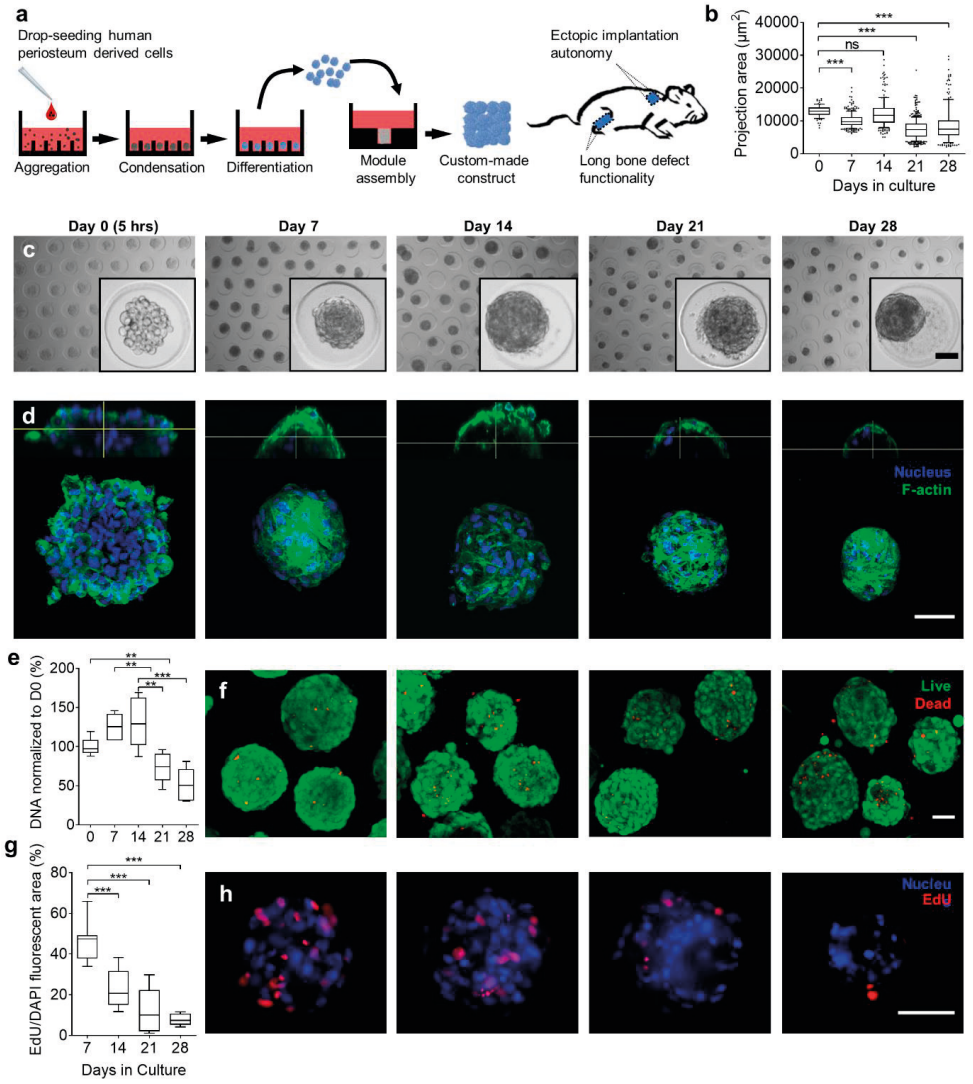

Figure 3.1. Long-term culture of periosteal microspheroids*. a) Schematic overview of the bioengineering process starting with cellular aggregation, condensation, and differentiation followed by callus organoid assembly and implantation in ectopic and orthotopic environment. b) Projection area of microspheroids over time (87–400 microspheroids, 10–90 percentiles). c) Representative bright-field images of microspheroids over time. d) Representative 3D renderings of confocal images of stained with DAPI (nucleus) and Phalloidin (F-actin) over time. e) DNA quantification of microspheroids over time, normalized to day 0 (5 h) (n = 6, 10–90 percentiles). f) Representative confocal z-projection images of LIVE (green)/ DEAD (red) staining over time. g) Semiquantification of cell proliferation in microspheroids over time. EdU fluorescent area was normalized to DAPI fluorescent area (10–15 microspheroids per condition, 10–90 percentiles). h) Representative fluorescent images of proliferating cells (EdU, red) in microspheroids over time, blue represents the nucleus. **p < 0.01; ***p < 0.001; one-way analysis of variance (ANOVA) followed by Tukey's multiple comparison test. Scale bars: c,d,f,h) 50 µm.*

3D visualization of cell nuclei showed the presence of nuclear condensation and fragmentation indicating occurrence of apoptosis in some cells starting from day 14 [32] (Figure S1a, white arrows, Supporting Information). Furthermore, DNA quantification suggested a stable number of cells during 2 weeks followed by a 44% decrease after 3 weeks (Figure 1e). The majority of cells in the microspheroids were viable; however, an increase in dead cells was observed during the last week of the culture period (Figure 1f). Messenger ribonucleic acid (mRNA) transcripts of the marker of proliferation Ki-67 (*MKI67*) declined after 21 days (Figure S1d, Supporting Information) and 5-ethynyl-2′-deoxyuridine (EdU) staining confirmed this trend by revealing a high number of proliferating cells (46%) during the first weeks, which subsequently decreased and was almost absent after 4 weeks in culture (Figure 1g, h). This decrease in proliferation is also seen during endochondral ossification [31] indicating chondrocyte differentiation and maturation of the microspheroid cells.

To further define the differentiation stages of the microspheroids, gene expression of relevant markers was analyzed (Figure 2a). The early chondrogenic transcription factor sex-determining region Y box (*SOX*)9 was upregulated (5-fold) the first 14 days in culture followed by a downregulation while the cartilage matrix marker collagen type II alpha 1 (*COL2A1*) was highly upregulated (6100-fold) after 21 days in culture. The early osteogenic and pre-hypertrophic marker runt-related transcription factor 2 (*RUNX2*) was upregulated after 7 (10-fold) and 14 days (16-fold) where after a downregulation was seen. The transcription factor osterix (*OSX* or *SP7*), which is directly regulated by *RUNX2* and expressed in pre-hypertrophic chondrocytes and osteoblasts, followed a similar expression trend.[33, 34] Distinct upregulation of the hypertrophic markers collagen type X alpha 1 chain (*COL10A1*) (1340-fold) and Indian hedgehog signaling molecule (*IHH*) (33-fold) was detected at day 21. In addition, alkaline phosphatase (*ALP*) gene expression was upregulated (19-fold) at day 14 and integrin binding sialoprotein (*BSP* or *IBSP*), linked to matrix mineralization and osteoblast differentiation,[35-37] was upregulated 8400-fold, after 21 days in culture. No significant

upregulation of the analyzed genes (*SOX9, COL2A1, RUNX2, OSX, COL10A1, IHH, ALP*, and *BSP*) was detected between day 21 and day 28 (Figure S2a, Supporting Information). Therefore, the following analyses were performed until day 21. In summary, the above results demonstrated a proliferation phase that was interchanged with cellular differentiation and maturation defined by genes associated with both hypertrophic chondrocyte and osteogenic differentiation.

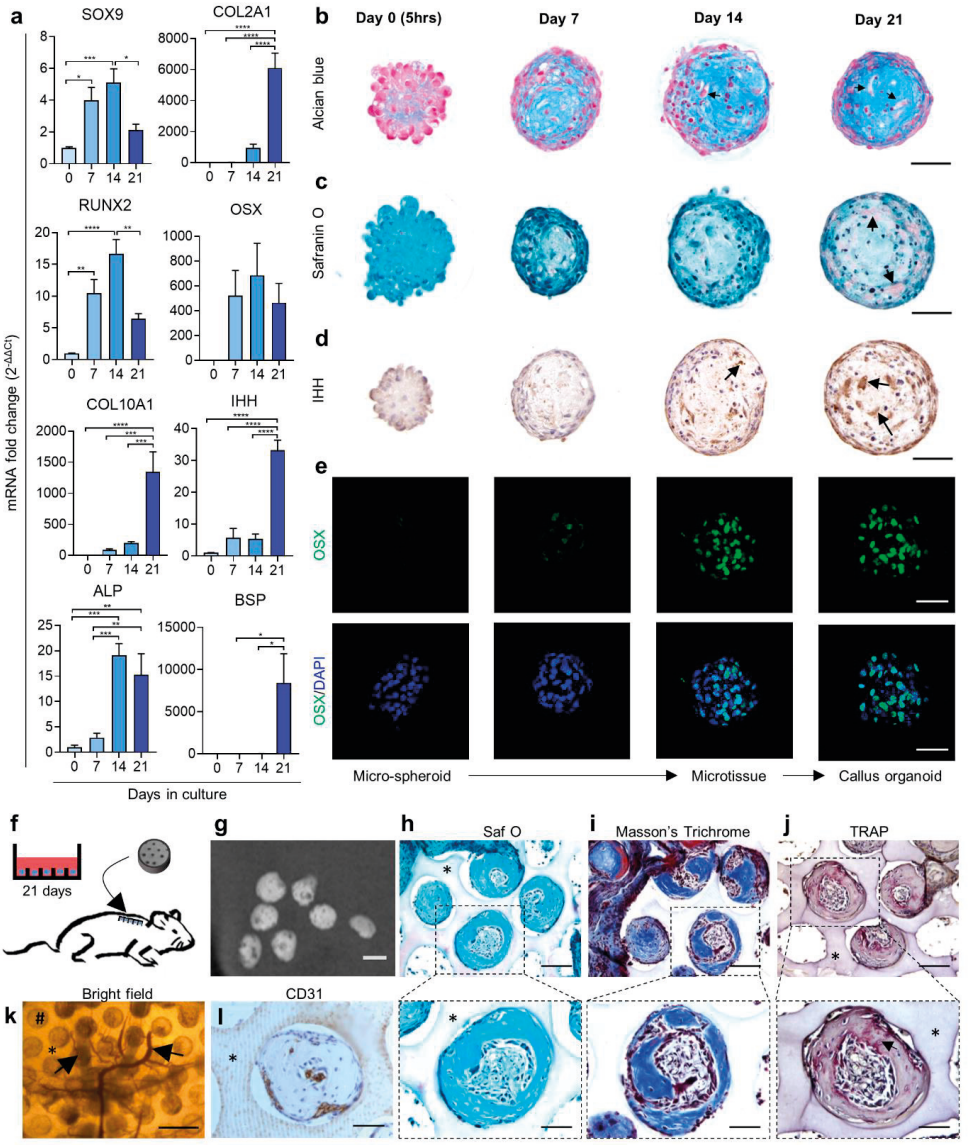

***Figure 3.2. Microspheroids follow endochondral ossification patterns toward pre-hypertrophic callus organoids able to form bone* in vivo**. *a) Quantification of mRNA transcript of chondrogenic and pre-hypertrophic/hypertrophic gene markers was performed and normalized to D0 (n = 6 mean value ± SEM). *p < 0.05; **p < 0.01; ***p < 0.001; one-way ANOVA followed by Tukey's multiple comparison test. b–e) Representative sections of: b) Alcian Blue, c) Safranin O, d) IHH immunostaining, and e) confocal z-projection image of OSX immunostaining over time. f) Schematic view of individual callus organoid implantation. g) 3D rendering of nano-CT images after 4 weeks* in vivo *implantation. h) Safranin O, i) Masson's Trichrome, and j) TRAP staining after 4 weeks* in vivo*. k) Bright-field image of invading blood vessels (black arrow, #: microwell) and l) CD31 immunostaining 4 weeks after implantation (* represents the agarose mold). Scale bars: b–e) 50 µm; g) 100 µm; h–j) the upper row represents 100 µm and the lower row 50 µm; k) 400 µm; and l) 50 µm.*

3.2.2 Microspheroids Mature toward Pre-Hypertrophic Callus Organoids That Form Bone Microorgans In Vivo

The gene expression analysis indicated chondrogenic differentiation toward hypertrophy in combination with osteogenic differentiation at day 21 (Figure 2a). Furthermore, Alcian Blue staining at low pH, specific for glycosaminoglycan (GAG), confirmed an increased presence of cartilage-like ECM within the microspheroids, and pre-hypertrophic like cells were visible after 3 weeks in culture (Figure 2b, black arrows). Safranin O staining demonstrated slight presence of cartilage-specific sulfated GAGs after 21 days in culture (Figure 2c) and immunostaining confirmed the presence of IHH, OSX, and COL2 protein after 14 days in culture (Figure 2d,e; Figure S1b,d,e, Supporting Information). The gene expression and histological analysis demonstrated that the microspheroids, containing ≈250 aggregated cells (day 0, Figure 2b,c), matured into microtissues with differentiated cells and ECM (day 14, Figure 2b,c).

Based on the upregulation of hypertrophic gene markers (Figure 2a) and the presence of pre-hypertrophic cells (Figure 2b), day 21 microtissues were chosen to be implanted subcutaneously to evaluate their capacity to mature into bone *in vivo*. Implantation of whole agarose microwell platforms with a diameter of 5 mm was carried out in immunodeficient mice to ensure that microtissues would remain entrapped in their microwells (Figure 2f). After 4 weeks of ectopic implantation, nano-computed tomography (nano-CT) scans demonstrated the formation of distinct mineralized spheres (Figure 2g) with a volume of (5.4 ± 3.54) × 105 µm3 and an average diameter of 209 ± 41 µm (24 spheres quantified from three explants). Histological sections further demonstrated the presence of bone matrix (Figure 2h, i) surrounding a marrow compartment with osteoclast activity (Figure 2j) and blood vessels (Figure 2k, l). These data demonstrated the development of microtissues with proteoglycan-rich ECM positive for IHH and COL2. Furthermore, these microtissues were able to form bone microorgans *in vivo* (Figure 2g), confirming that these implants behaved as single semiautonomous bone-forming modules *in vivo* acting as callus organoids. This defines a

maturation process from microspheroids (day 0) to microtissues (day 14) and finally callus organoids (day 21) (Figure 2e).

3.2.3 Callus Organoids Fuse into Larger Constructs In Vitro

In order to demonstrate that the above-mentioned microtissues and callus organoids can be used as building modules to form larger constructs, we initially studied the fusion process of two callus organoids. Despite long-term culture as microtissues, creating a substantial amount of secreted ECM, the callus organoids spontaneously fused over 24 h (Movie S2, Supporting Information). Subsequently, ≈3000 modules were flushed out of their microwells and assembled in an agarose well (2 mm diameter and depth) for fusion into a multimodule construct (Figure 3a; Figure S2b, Supporting Information). 14- (microtissues) and 21-day (callus organoids) modules were chosen for further analysis based on chondrogenic (*SOX9* and *COL2A1*) and hypertrophic (*COL10A1*, *IHH*, and *ALP*) gene markers (Figure 2a, d, e), as well as cell morphology (Figure 2b–d). Both 14 day and 21 day modules fused into larger constructs that could be handled and transported (Figure 3a); however, single callus organoid structures were still visually discernible in 21 day constructs. As a control to these structures, a macropellet formed with the same number of cells and cultured for 3 weeks in the same media formulation was introduced (Figure 3a, Macropellet).

Alcian Blue staining demonstrated increased module fusion within the day 14 constructs as compared to day 21 constructs (Figure 3b), albeit both module constructs contained positive staining thoughout their structures. In contrast, the macropellet, not assembled with modules, did only show Alcian Blue staining at the periphery (Figure 3b). Safranin O staining corresponded to the Alcian Blue staining seen in macropellets. In contrast, Safranin O positive areas were found throughout the day 21 constructs (Figure S3a, Supporting Information). None of the constructs demonstrated positive staining for Alizarin red or von Kossa (Figure S3b,c, Supporting Information), indicating that mineralization was not present in the constructs. In conclusion, these results demonstrated the formation of larger constructs through assembly of micromodules resulting in more homogenously distributed GAG-rich ECM as compared to macropellets (Figure 3b).

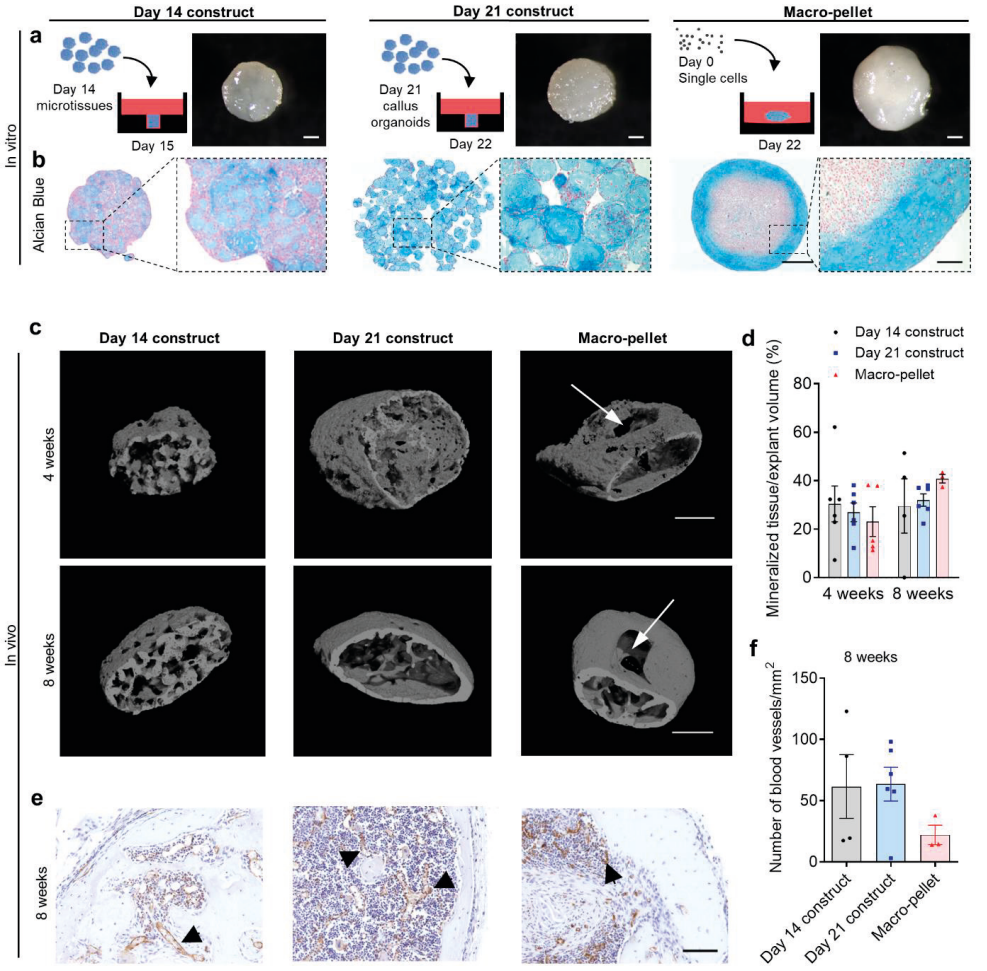

Figure 3.3. Assembly of cartilage intermediate microtissues into larger bone forming constructs. *a) Schematic drawing demonstrating module assembly into an agarose macrowell (left) and representative photographs of the day 14, day 21 constructs, and Macropellet (right). b) Alcian Blue staining of fused constructs and Macropellet. c) 3D rendering of nano-CT images 4 and 8 weeks after implantation. d) Quantification of mineralized tissue 4 and 8 weeks after implantation (mean value ± SEM, n = 3–6). e) Representative images of CD31 immunostaining (black arrows demonstrate blood vessels), and f) quantification 8 weeks after implantation (mean value ± SEM, n = 3–6). ANOVA followed by Tukey's multiple comparison test. Scale bars: a) 500 µm, b) 500 and 100 µm, c) 500 µm, and d) 100 µm.*

3.2.4 Assembled Callus Organoids Form Single Large Bone Organs In Vivo

Next, day 7, 14, and 21 constructs, as well as the macropellets were implanted ectopically in immunodeficient mice to investigate their capacity to form bone *in vivo* (4 and 8 weeks). None of the day 7 constructs were retrieved (n = 4). However, mineralization was detected with nano-CT in the other three conditions after 4 week implantation (Figure 3c). No significant difference

in mineralization percentage was seen between the conditions after 4 or 8 weeks. However, a nonmineralized core was detected in the macropellet at both timepoints (Figure 3c, white arrows). Furthermore, after 8 weeks' ectopic implantation, the day 21 constructs and macropellets contained a mineralized cortex, while the mineralized tissue in the day 14 constructs appeared porous hence less mature. The number of blood vessels was quantified with CD31 immunostaining, and no significant difference between the constructs was detected although a larger number of day 21 constructs (5/6) contained a high amount (>50 blood vessels mm−2) of blood vessels as compared to day 14 constructs (2/4) and macropellets (0/3) (Figure 3e, f; Figure S3d, Supporting Information).

Safranin O and Massons's Trichrome staining on histology sections after 4 weeks' implantation revealed that day 21 constructs contained bone, bone marrow, as well as remodeling cartilage indicating the occurrence of endochondral ossification (Figure 4a; Figure S3f, Supporting Information). Although no significant difference was detected, limited bone marrow compartments were seen in the day 14 constructs and macropellets in contrast to the day 21 constructs (Figure 4a, b, e). Strikingly, significant areas of fibrotic tissue were detected in both day 14 constructs and macropellets as compared to day 21 constructs (Figure 4f). Furthermore, tartrate-resistant acid phosphatase (TRAP) staining (Figure 4c) demonstrated osteoclast activity in all constructs although more prominent in day 21 constructs. Human osteocalcin (hOCN) staining demonstrated that implanted cells contributed to the bone formation in all constructs (day 14 construct: 74 ± 10%, day 21 construct: 58 ± 18%, and macropellet: 72 ± 2%) (Figure 4d, g; Figure S3e, Supporting Information).

Furthermore, hematoxylin–eosin (H&E), safranin O, and Masson's Trichrome staining revealed mature bone in all conditions after 8 weeks' implantation, but the day 14 constructs and macropellets still contained domains of fibrotic tissue which were absent in the day 21 constructs (Figure 4h–j). In addition, OCN positive cells of human origin were present also after 8 weeks' implantation (Figure 4k). Although mineralized, some of the day 21 constructs maintained a hypertrophic chondrocyte phenotype after both four (three of six implants) and eight (one of six implants) weeks *in vivo* implantation (Figure S3f, Supporting Information). Taken together, these results supported that callus organoids fused into larger day 21 constructs *in vitro* and further developed into bone organs *in vivo*.

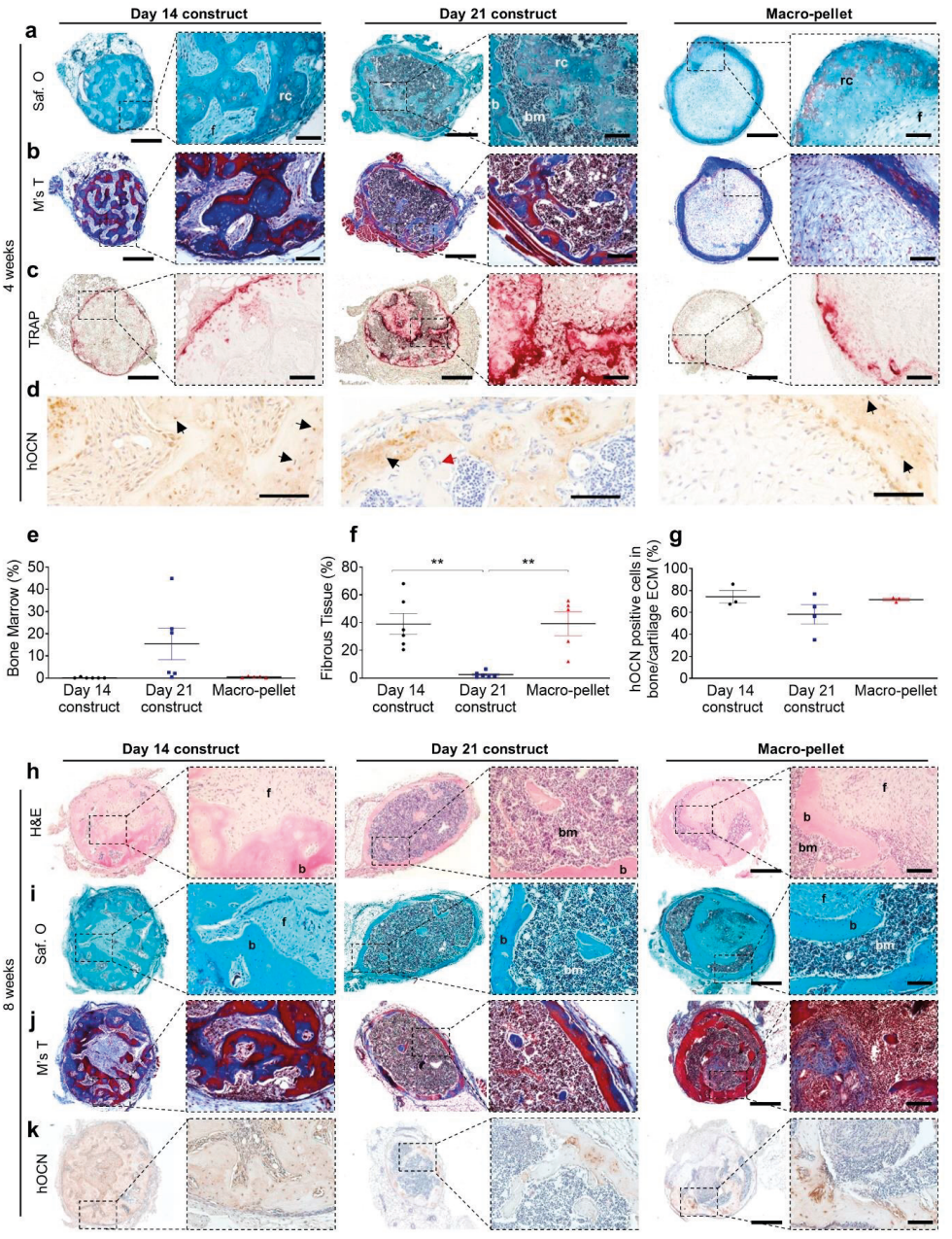

Figure 3.4. Histological assessment after ectopic implantation. *a) Safranin O, b) Masson's Trichrome, c) TRAP, and d) hOCN staining of day14, day 21 constructs, and Macropellet 4 weeks after* in vivo *implantation. e–g) Quantification (mean value ± SEM) of: e) bone marrow compartment (n = 5–6), f) fibrous tissue area (n = 5–6), and g) hOCN positive cells (n = 3–4) 4 weeks after implantation. h) Hematoxylin and eosin (H&E), i) Safranin O, j) Masson's Trichrome (M's T), and k) hOCN staining after 8 weeks* in vivo *implantation. *p < 0.05; **p < 0.01; ***p < 0.001; one-way ANOVA followed by Tukey's multiple comparison test. Scale bars: a–c,h–j) 500 µm (left) and 100 µm (right) and d) 100 µm.*

3.2.5 Temporal Gene Expression Patterns during Callus Organoid Formation Follow the Endochondral Ossification Process toward a Niche for Matrix Remodeling and Bone Organ Formation

To better explain the differentiation pathway of the callus organoids, an RNA sequencing analysis of D0 (5 h), D7, D14, and D21 modules was performed demonstrating a similar trend as the limited gene expression analysis (Figure 2a; Figure S4a,b Supporting Information). Furthermore, the number of significant ($p < 0.05$ and log2-fold > 1) differentially expressed genes decreases over time from 3949 (D0–D7) and 847 (D7–D14) to 55 (D14–D21) and 84 (D21–pellet) (Figure 5a) indicating that the most dramatic changes occurred at the early stages of differentiation.

Pathway analysis using Enrichr [38, 39] with WikiPathway (2016) grouped upregulated genes (D0–D21) into endochondral ossification (WP474, adj. p-value 1.0e-13) and embryonic skeletal system development (Gene Ontology (GO): 00 48706, adj. p-value 1.379e-8) from GO Biological Process (BP) (Data File S1, Supporting Information).[38-40] Next, unsupervised clustering was performed on the 400 most variable genes in order to gain a holistic overview of signaling action during the callus organoid maturation process and the GO enrichment for each cluster was defined (Data Files S2 and S3, Supporting Information). The first cluster with a continuously upgoing trend included genes enriched to skeletal and cartilage development and regulation of mitogen-activated protein kinases (MAPK) and ERK1/2 signaling (where ERK = extracellular signal-regulated kinase) involving the wingless-INT (WNT), bone morphogenetic protein (BMP), and fibroblast growth factor (FGF) signaling (Figure 5b). These are crucial signaling pathways driving endochondral ossification working in a converging manner toward chondrocyte hypertrophy.[41] Interestingly, genes related to WNT signaling were also present in the transient downregulated cluster 3. This cluster included genes related to transforming growth factor beta (TGF-β)/BMP related SMAD and WNT signaling motivating a converging crosstalk during callus organoid maturation. In addition, Notch, which is important for stem cell maintenance, suppression of chondrocyte differentiation, and proliferation,[42] was represented in the downregulated cluster 3. These two clusters (clusters 1 and 3) indicate cell signaling regulation analogous to the molecular cascade of events present during endochondral ossification.[41]

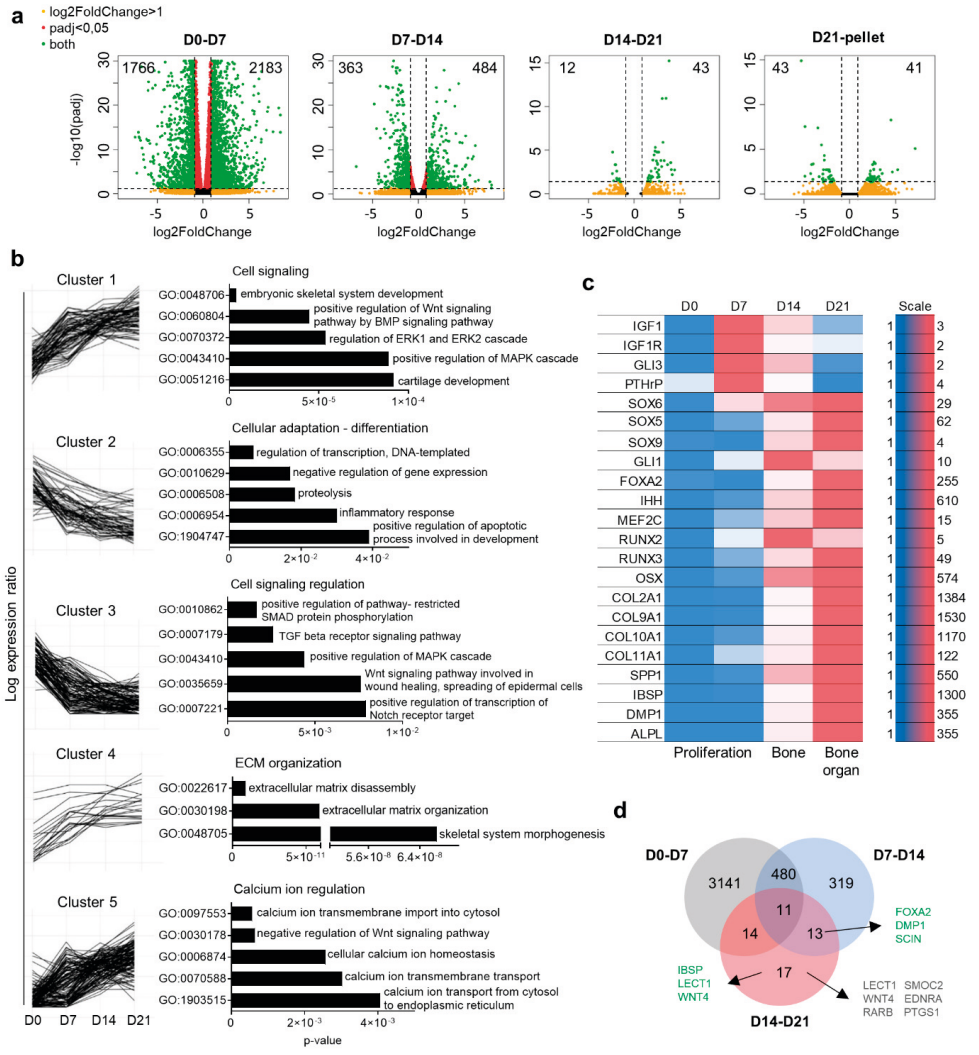

Figure 3.5. RNA sequencing analyses of spheroids and Macropellet (n = 3–4). *a) Volcano plots of differentially expressed genes from RNA-seq data between the different spheroids and Macropellet. X- and Y-axes represent log2fold change and log10p-value, respectively, and green dots represent genes with log2FoldChange > 1 and padj < 0.05. b) Gene Ontology (GO) Biological Processes (2017b) of genes within the five different clusters of the 400 most variable genes (log2FoldChange > 1 and padj < 0.05). c) Heat map of spheroid mRNA transcript levels of genes regulating endochondral ossification (relative expression value for each gene). d) Venn diagram of the number of significant differentially expressed genes (green dots in (a)) for the different spheroid maturations. Green text represents genes associated with endochondral ossification and gray text genes associated with angiogenesis.*

Cluster 2, with constant downregulation, included genes associated with DNA transcriptional activity correlating with the decrease in cell proliferation occurring during the transition from proliferative to hypertrophic chondrocytes43 which was indicative also in our data (Figure 1g, h). Genes associated with ECM disassembly (*MMP13*) and produced by hypertrophic

chondrocytes (*COL10A*, *COL9*, and *SPP1*) were grouped in the constantly upregulated cluster 4 supporting maturation toward hypertrophic callus organoids that exhibited a high turnover and capacity to remodel the surrounding matrix. In addition, genes linked to calcium-ion regulation were highly represented in the upregulated cluster 5, suggesting a gradual transition to a pre-hypertrophic niche favoring mineralization, although no *in vitro* mineralization was detected (Figure S3b, c, Supporting Information).[44]

The GO enrichment of the unsupervised clusters demonstrated that the callus organoid maturation followed signaling pathways regulating endochondral ossification. This was further supported by analysis of well-known regulators. During the first phase (D7), important regulators of chondrocyte proliferation, differentiation, and organization were upregulated, including *IGF1* and its receptor *IGF1R*,[45] *GLI3* ,[46-48] *PTHrP* ,[49] and the SOX trio (*SOX* 5 /6 /9)[50] (Figure 5c). From day 14 onward, the *PTHrP* positive state converted into an *IHH* positive state, followed by increased expression of chondrocyte hypertrophy activators, such as *GLI1, FOXA2, MEF2C, OSX, RUNX2*, and *RUNX3* [48, 51] (Figure 5c). This pattern was mirrored in the gene expression of matrix proteins and regulators involved in endochondral ossification with a distinct upregulation of collagens (*COL2A1*, *COL9A1*, *COL10A1*, and *COL11A1*) and signaling factors correlated to pre-hypertrophic/hypertrophic chondrocytes and osteoblasts (*SPP1, IBSP, DMP1*, and *ALPL*).[48, 51]

These data demonstrate a regulatory “switch” between D7 and D14 plausibly crucial for bone formation *in vivo*. Genes significantly upregulated between both D7–D14 and D14–D21 included *FOXA2, DMP1*, and *SCIN* which are crucial for chondrocyte hypertrophy,[52] cartilage–bone transition,[53] and bone resorption,[54] respectively, indicating their significant role in bone formation and also in the current manufacturing approach (Figure 5d). Subsequently, comparison from D14 to D21 indicated further maturation linking to the *in vivo* formation of a bone organ with matrix remodeling and the presence of bone marrow (Figure 4). Since only a limited number of genes were significantly changed (55 up/downregulated genes, Figure 5a) during this period, individual analysis was performed for these genes (Figure S4c, Supporting Information). Around 15 of the 43 differentially upregulated genes (Figure S4c, Supporting Information) have been associated with endochondral ossification and pre-hypertrophic/hypertrophic chondrocytes (Table S1, Supporting Information) whereof *IBSP*,[36, 37] chondromodulin (*CNMD* or *LECT1*),[55, 56] and *WNT4* [57] were exclusively significant for D14–D21 (Figure 5d). Interestingly, 15 of the 55 significantly changed genes D14–D21 (Figure S4c, Supporting Information) have been associated with regulation of

angiogenesis (Table S2, Supporting Information), a pivotal event during the transition from cartilage to bone in endochondral ossification. Of these angiogenic genes, six were exclusively differentially expressed between D14 and D21 (Figure 5d). Conclusively, the RNA-seq analysis demonstrated endochondral maturation from initial microspheroids (aggregated cells) to callus organoids (cells and ECM) exhibiting pre-hypertrophic characteristics and active remodeling of the secreted ECM resulting in bone organ formation *in vivo*.

3.2.6 Assembled Callus Organoids Heal Critical-Sized Long Bone Defects

Based on the ectopic implantation and RNA sequencing results, day 21 modules were defined as "callus organoids" and selected as modules for the formation of larger constructs and orthotopic implantation in a murine, critical-sized long bone defect.[58] An agarose mold based on the dimensions of the critical-sized defect and with the decrease in size during fusion of callus organoids accounted for was fabricated (Figure 6a). Next, ≈6000 callus organoids were seeded into the agarose mold (Figure 6b) and fused during 24 h resulting in a construct (≈4.5 mm length and 2 mm wide) (Figure 6c) that was fitted into the tibia defects of immunodeficient mice (Figure 6d).

X-ray images and 3D renderings of *in vivo* CT scans demonstrated occurrence of mineralization after 2 weeks, and bridging of defects was detected after 4 weeks followed by increased corticalization until week 8 (Figure 6e, h; Figure S5a, Supporting Information). No bridging was detected in the empty defects after 8 weeks (Figure 6f) while quantification of *in vivo* CT images confirmed the increase in mineralized tissue over time in experimental conditions (Figure 6g). Cross section of the nano-CT 3D rendering from week 8 demonstrated the presence of cortical bone in the defect with a nonmineralized compartment in the center, suggesting a defined bone marrow cavity (Figure 6i). Structure thickness increased significantly from week 2 to 4 correlating to the time of defect bridging (Figure 6j; Figure S5a, Supporting Information). Furthermore, the number of structures decreased from week 4 to 8 indicating remodeling from a trabecular to a more cortical structure, which was also visible on *in vivo* CT images (Figure 6k, l).

Next, the healed defects at week 8 were compared to native tibia at the same location as the defect, in mice of the same age and gender. No significant differences were found regarding mineralized percentage, volume (Figure 6m; Figure S5b, Supporting Information), structure linear density (Figure 6p), or medullary cavity occupancy (Figure 6n), while the medullary volume in healed defects was significantly larger than in native bone (Figure S5c, Supporting

Information). In addition, structure thickness was lower in the healed defects as compared to native bone indicating that longer healing time may be necessary for full regeneration (Figure 6o).

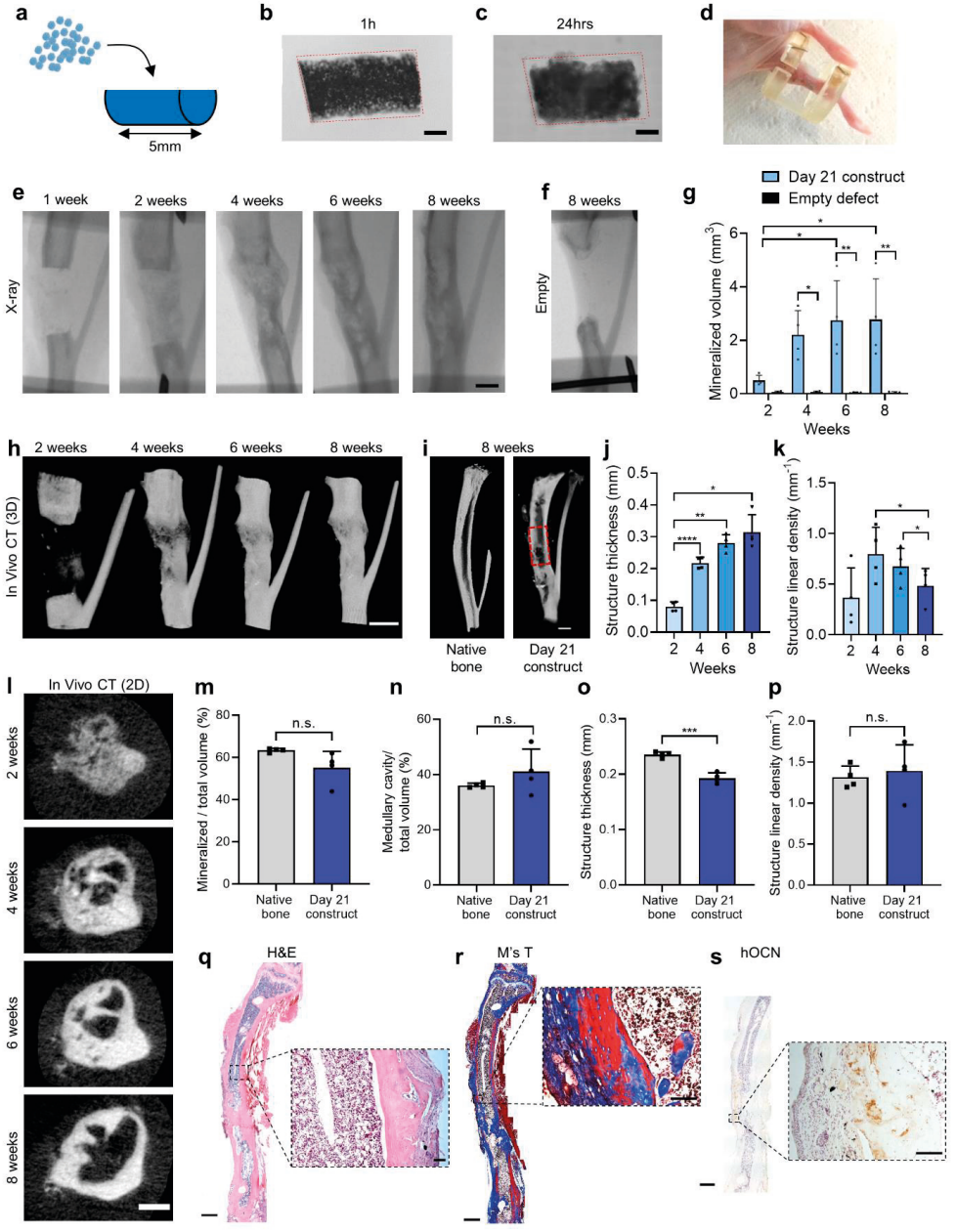

Figure 3.6. Healing of murine critical-sized long bone defect. *a) Schematic visualization of implant formation. b,c) Bright-field image 1 h (b) and 24 h (c) after callus organoid assembly. d) Photograph of a 4 mm tibia defect*

after healing. e) X-ray images of tibia defect with a day 21 construct. f) Negative control: X-ray of empty defect after 8 weeks. g) Quantification of mineralized volume in defects with day 21 construct and empty defects (n = 4 animals for each condition, two-way ANOVA followed by Tukey's multiple comparison test). h) Nano-CT 3D rendering images over time of defect with day 21 construct. i) Cross section of 3D rendering of native tibia and defect 8 weeks after day 21 construct implantation. j–l) In vivo *CT quantification of structure: j) thickness, and k) linear density over time visualized with l)* in vivo *CT 2D images. m–p) Comparison between native tibia and healed defect 8 weeks after construct implantation was demonstrated by ex vivo nano-CT quantification of: m) mineralized tissue (%), n) medullary cavity (%), o) structure thickness, and p) structure linear density (n = 4, unpaired t-test). q) H&E, r) Masson's Trichrome, and s) hOCN immunohistological staining of defect 8 weeks after day 21 construct implantation. *p < 0.05; **p < 0.01; ****p < 0.0001. Scale bars: b,c,e,h,i) 1 mm, l) 500 µm, q–s) overview 1 mm and zoom-in 100 µm.*

H&E and Masson's Trichrome staining after 8 weeks confirmed full bridging (3/4) with the presence of mature bone and bone marrow (Figure 6q, r; Figure S5d, e, Supporting Information), and hOCN staining (Figure 6s) revealed the contribution of donor cells to the bone formation process. In conclusion, the assembly of multiple callus organoids into an easy-to-handle scaffold-free implant resulted in full bridging of a critical-sized long bone defect by the formation of cortical-like bone tissue with a medullary cavity containing bone marrow with the absence of fibrous tissue. In addition, structural characterization of the regenerated defect showed high similarities to native tibia.

3.3 Discussion

In this work, we developed a bottom-up modular strategy for scalable biofabrication of cartilage intermediate tissues that were able to form ossicles without contaminating tissue compartments while exhibiting a unique capacity to heal critical-sized long bone defects. During native fracture healing, cells from the periosteum are the main contributors of the callus.[14, 29] These cells have recently been shown to possess a higher regenerative capacity than bone marrow mesenchymal cells and contain a skeletal stem cell population with distinct functions during endogenous bone repair.[15, 30] Moreover, it was recently reported that periosteum contains not only renewable skeletal stem cells forming membranous, cortical bone, but also endochondral bone upon damage.[59] Hence, this understudied progenitor cell source possesses critical advantages in terms of clinical application for the design of engineered ATMPs aiming to heal large long bone defects.

To date, the formation of cartilage intermediates *in vitro* was obtained through the use of pellets containing large amount of cells (>2 × 105 cells).[17, 18, 60, 61] However, the use of such methods has resulted in diffusion-related challenges such as the formation of undifferentiated tissue compartments *in vitro* which hinder the concerted progression of tissue maturation to their final phenotype upon implantation.[18] This was also detected in our study by the large

fibrotic compartments encountered within macropellet explants (Figure 3). In addition, when chondrogenic [61] and hypertrophic [62] pellets were fused into larger structures, limited remodeling *in vivo* was shown. Hence, we designed cell microspheroids (comprised of 250 cells) that would not exceed 150 μm in diameter to match with the length scale that diffusible signals can be transported and to mimic the initial developmental event of growth plate formation (condensation) whereby only a few hundred cells are needed.[63] During differentiation, we observed that cells underwent a cascade of molecular and cellular events that reflect endochondral ossification allowing them to transform from cellular spheroids to semiautonomous microtissue structures, callus organoids, capable of undergoing organogenesis (Figures 1-3). In addition, the assembly of callus organoids into larger tissue structures resulted in implants containing active regenerative components throughout their structure. Ultimately, the populations of callus organoids described in our study could be viewed as a living "bio-ink" that also allows the formation of scaffold-free tissue structures with intricate geometric features (Figure S6, Supporting Information).[64]

In order to obtain quality attributes that could be linked to the functionality of the callus organoids, high-depth transcriptomic profiling was carried out. Sets of genes were determined to provide signatures to identify whether engineered microtissue niches have attained the degree of autonomy required for bone organ formation. These were compared to recent studies focused on the identification of transcription factor panels that control differentiation transitions from one zone to the other in the growth plate.[48, 51] With this comparison, we were able to discern similar temporal gene regulation kinetics and link the phenotypic state and semiautonomous function of our microtissues to that of an "early pre-hypertrophic" stage for day 14 modules (microtissues) and that of "late pre-hypertrophic" stage for day 21 modules (callus organoids). In addition, GO term analysis of the 400 most variable genes revealed additional etiologies (Figure 5b) for the striking bone organ formation observed in our study. Upregulated clusters indicated gradual transition to pre-hypertrophy, favoring mineralization as well as ECM disassembly and organization (Figure 5b). Apart from the relevance of ECM disassembly and organization in the transition from hypertrophic cartilage to bone,[65] this property could also be key in regulating the orchestrated transition of the multimodular constructs into a single ossicle by facilitating ECM reorganization and vascular invasion across the implant. This could also explain the rapid vascularization and bone marrow formation of day 21 constructs observed as early as 4 week postimplantation (Figure 4) as well as host integration in the long bone defect (Figure 6). Chan et al.[66] have previously demonstrated

the importance of endochondral ossification for the formation of hematopoietic stem-cell (HSC) niches, and here we provide a set of metrics that would allow fine tuning and robust bone organ formation.

Although scaffold-free constructs are beneficial for mimicking native tissue morphology, a combination of the callus organoids with suitable biomaterials could further enable upscaling into centimeter-sized implants and even enhance their performance.[67-69] Functionalized biomaterials possessing molecular signatures relevant to the timescales of the differentiation cascades and the proper length scale could interact and support endochondral ossification events. Petersen et al. recently demonstrated that the architecture of collagen scaffolds can direct endochondral fracture healing *in vivo*.[70] They showed that scaffold pores oriented along the defect resulted in ECM alignment and controlled invasion of progenitor cells and blood vessels leading to the onset of endochondral ossification. In the present work, we observed rapid vascularization and bone formation which was attributed to active ECM remodeling, a dynamic property that could further be supported by properly designed scaffolds through the delivery of relevant enzymes.[71]

Localized delivery of growth factors through tailored biomaterials could further direct tissue maturation *in vivo* while avoiding release of supraphysiological levels, which for BMP-2 has been proven to cause severe side effects including swelling and heterotopic bone formation.[72] Herberg et al. demonstrated that a combination of BMP-2 and TGF-β1 releasing microparticles in cell-based constructs resulted in mineralized bridging in tibia defects which was further enhanced by mechanical stimulation of the defect.[73] Furthermore, nanoscale fibronectin coatings on polycaprolactone scaffolds were shown to allow incorporation of ultralow dose BMP-2 (100 ± 8 ng cm−2) resulting in bone formation *in vivo*.[74] However, it is of note that the use of biomaterials could also have adverse effects for tissue regeneration when their properties are not coupled to the precise regenerative context. For example, collagen I scaffolds used in both clinical and research applications for bone regeneration were recently shown to impede osteogenic differentiation and fracture healing.[75] This highlights the importance of thorough understanding of the interaction between the scaffold material and the biology for a specific application.

There are still a number of technical challenges that need to be addressed for future biomanufacturing of callus organoids for mass production. The transition of the static process developed in this study to bioreactor systems where thousands of organoids could be generated

could aid in its full automation and enhance its capability. In addition, the transfer of this process to stirred bioreactor systems could potentially allow increased flexibility in terms of achievable scale.[76] At the same time, already available technologies for isolating single microtissue modules for at-line quality controls could provide an ideal method for real-time evaluation of their degree of autonomy[77] allowing the implementation of real-time potency monitoring as envisaged in the quality by design paradigm for cell therapy. Bioprinting technologies with the capacity to manipulate single spheroids have been developed through laser-induced forward transfer, a high-resolution method using laser pulses.[78] Finally, robotic devices have been shown to possess the capacity to manipulate single spheroids and positioning them in preordered grids allowing them to fuse [79, 80] or depositing them in printed scaffolds.[78]

Another technical bottleneck that will need to be addressed is the vascularization of multicentimeter-sized implants. Although chondrocytes possess resistance to stress conditions found at the implantation site such as hypoxia and low nutrient availability, it is expected that vascularization will be a prerequisite for cell survival in large implants.[81] Recently, vascularized structures based on the concomitant use of mesenchymal condensations, of similar dimensions to the ones presented here and endothelial cells, exhibited improved *in vivo* functionality.[8] Moreover, sacrificial writing into functional tissue (SWIFT) bioprinting with direct fabrication of vasculature in organoid suspensions could also be employed for introducing vasculature patterns when upscaling to larger callus-organoid-based implants.[82] In addition, using purified stem cell populations recently described by Chan et al.[83] could substantially enhance the potential and efficiency of the strategy described in this work.

3.4 Conclusion

In conclusion, the described callus organoids provide an engineering approach for predictive design of large-scale living implants. The callus organoids exhibited a deterministic behavior by reaching autonomy thresholds attributed to synchronized activation of molecular pathways providing robustness and potentially facilitating regulatory approval and safety. Furthermore, this process is scalable both in terms of production of single callus organoids and in terms of tissue implant size and at the same time allowing the design of intricate geometric features. Importantly, the *in vivo* functional assessment of orthotopic bone formation with bridging of the long bone defect took place within the timelines of natural fracture healing and resulted in a bone structure highly resembling native long bone.[12] With these advancements, we believe

that future biofabrication of skeletal implants using callus organoids will follow design principles resulting in achieving “bone by design”. This will eventually pave the way for the biomanufacturing of clinically relevant implants possessing robust functionality and causal connection with the clinical outcome. This can revolutionize the mitigation of currently unmet clinical challenges such as healing of critical-size long bone defects.

3.5 Experimental Section

Cell Expansion : hPDCs were isolated from periosteal biopsies of nine different donors, and two different cell pools were created (ages of 29 ± 12 and 14 ± 3 years) as previously described.[84] The hPDC pools were expanded (5700 cells cm−2) until passage 7 (*in vivo*, RNA-seq) and 10 (*in vitro*) at 37 °C, 5% CO2, and 95% humidity in Dulbecco's modified Eagle medium (DMEM, Life Technologies, UK) with 10% fetal bovine serum (HyClone FBS, Thermo Scientific, USA), 1% antibiotic–antimycotic (100 units mL−1 penicillin, 100 mg mL−1 streptomycin, and 0.25 mg mL−1 amphotericin B), and 1 × 10−3 m sodium pyruvate (Life Technologies, UK). Medium was changed every 2–3 days, and cells were harvested with TrypLE Express (Life Technologies, UK) at a confluence of 80–90%. TrypLE Express was used for all passaging and harvesting steps during cell handling. The ethical committee for Human Medical Research (Katholieke Universiteit Leuven) approved all procedures, and patients' informed consent forms were obtained (ML7861).

Formation of Microspheroids : Agarose microwell inserts for formation of a high number of microspheroids with homogeneous size distribution were created as previously described by Leijten et al.[85] Briefly, 3 % (w/v) Agarose (Invitrogen, Belgium) was poured onto a polydimethylsiloxaan (PDMS, Dow Corning Sylgard 184 elastomer, MAVOM Chemical Solutions) master mould containing pillars with a diameter of 200 μm. The agarose was let to solidify where after microwell inserts with an area of ≈1.8 cm2 were punched out, placed in 24-well plates, 1 mL of phosphate-buffered saline (PBS; Lonza, Verviers, Belgium) was added and the wells were sterilized under UV for 30 min. Each well insert contained ≈2000 microwells. hPDCs were harvested and seeded with a concentration of 500 000 cells per well to obtain ≈250 cells per spheroid after self-aggregation. Microspheroids were differentiated into microtissues in a serum-free chemically defined chondrogenic medium (CM) containing LG-DMEM (Gibco) supplemented with 1% antibiotic–antimycotic (100 units mL−1 penicillin, 100 mg mL−1 streptomycin, and 0.25 mg mL−1 amphotericin B), 1 × 10−3 m ascorbate-2 phosphate, 100 × 10−9 m dexamethasone, 40 μg mL−1 proline, 20 × 10−6 m of Rho-kinase

inhibitor Y27632 (Axon Medchem), ITS+ Premix Universal Culture Supplement (Corning) (including 6.25 µg mL−1 insulin, 6.25 µg mL−1 transferrin, 6.25 µg mL−1 selenious acid, 1.25 µg mL−1 bovine serum albumin (BSA), and 5.35 µg mL−1 linoleic acid), 100 ng mL−1 BMP-2 (INDUCTOS), 100 ng mL−1 growth/differentiation factor 5 (GDF5) (PeproTech), 10 ng mL−1 TGF-β1 (PeproTech), 1 ng mL−1 BMP-6 (PeproTech), and 0.2 ng mL−1 basic FGF-2 (R&D systems).[86] Half of the media volume was changed every 3–4 days.

Viability Assay : Cell viability in microspheroids was assessed qualitatively with LIVE/DEAD Viability/Cytotoxicity Kit (Invitrogen, USA) for mammalian cells by following the manufacturer's protocol. Briefly, microspheroids were rinsed with PBS, where after they were incubated in 2 × 10−6 m Calcein AM and 4 × 10−6 m ethidium homodimer-1 for 30 min at 37 °C, 5% CO2, and 95% humidity. Stained microspheroids were visualized with a confocal microscope ZEISS LSM 510 META (Cell imaging core facility of KU Leuven) with 4 µm thick slices.

Cell Proliferation Assay : Cell proliferation during microspheroid differentiation was visualized with Click-iT EdU Imaging Kit (Life Technologies, USA) according to the manufacturer's protocol. Briefly, 10 × 10−6 m EdU was added to the microspheroids during 4 days for each time point. Next, samples were fixed in 4% paraformaldehyde (PFA), EdU was detected with Alexa Fluor azide, stained with Hoechst 33 342 (5 µg mL−1) followed by visualization with a Leica M165 FC microscope (Microsystems, Belgium). The percentage of EdU/Hoechst (proliferating per all cells) stained area was quantified using ImageJ software[87] for 10–15 microspheroids per time point.

Cytoskeleton and Nuclei Visualization : Cell nucleus and F-actin distribution within microspheroids was visualized by staining with 2.5 µg mL−1 4′,6-diamidino-2-phenylindole (DAPI) (Invitrogen) and 0.8 U mL−1 Alexa Fluor 488 phalloidin (Invitrogen) during 1 h at room temperature. Stained spheroids were imaged with an inverted laser scanning fluorescence confocal microscope ZEISS LSM 510 META (Cell imaging core facility of KU Leuven) with 1 µm thick slices using an argon ion 488 nm and MaiTai laser.

DNA Quantification, Total RNA Extraction, and Quantitative Reverse Transcription–Polymerase Chain Reaction Analysis : Quantitative real-time polymerase chain reaction (qRT-PCR) was used to quantify mRNA of markers relevant for endochondral ossification. Pooled microspheroids (≈2000 microspheroids represent n = 1) were washed in PBS followed by cell lysis in 350 µL RLT lysis buffer (Qiagen, Germany) and 3.5 µL β-mercaptoethanol (Sigma

Aldrich, Germany), vortexed and stored at −80 °C. DNA assay kit QuantiT dsDNA HS kit (Invitrogen) was used to quantify the DNA content for each condition. Cell lysate was spun down and the DNA assay was performed according to the manufacturer's protocol. RNeasy Mini Kit (Qiagen) was used to isolate the total amount of RNA from lysed cells. After RNA extraction, the RNA concentration was quantified with NanoDrop 2000 (Thermo Scientific), and sample purity was evaluated at A260/A280 (protein purity; ≈2.0+) and A260/A230 (salt purity; 2.0–2.2). RevertAid H Minus First Strand cDNA Synthesis Kit (Thermo Scientific, USA) was used for reverse transcription; 500 ng of RNA was mixed with 1 µg of oligo(dT18) for each reaction (5 min at 65 °C). The reaction mixture (4 µL 5× reaction buffer, 1 µL ribolock ribonuclease inhibitor, 2 µL dNTPmix (10×10^{-3} M), and 1 µL RevertAid H Minus M-MuL VRT) was added to the samples and run in Applied Biosystems Veriti 96-Well Fast Thermal Cycler (60 min at 42 °C followed by 10 min at 70 °C). qRT-PCR was further performed with the cDNA, SYBR Green (Life Technologies) and primers designed for the specific human markers in cycling: 95 °C, 3 s; 60 °C, 20 s. Glyceraldehyde 3-phosphate dehydrogenase (*GAPDH*) was used as house-keeping gene and relative differences in expression were calculated using the 2−ΔΔCt method.88

RNA Sequencing : RNA isolation from samples (n = 3–4) was performed as described above. The Genomics Core Leuven performed the sequencing and the RNA-seq expression analysis as follows. Library preparation was performed with the Illumina TruSeq Stranded mRNA Sample Preparation Kit, according to the manufacturer's protocol. Denaturation of RNA was performed at 65 °C in a thermocycler and cooled down to 4 °C. Samples were indexed to allow for multiplexing. Sequencing libraries were quantified using the Qubit fluorometer (Thermo Fisher Scientific, MA, USA). Library quality and size range were assessed using the Bioanalyzer (Agilent Technologies) with the DNA 1000 kit (Agilent Technologies, CA, USA) according to the manufacturer's recommendations. Each library was diluted to a final concentration of 2×10^{-9} M and sequenced on Illumina HiSeq4000 according to the manufacturer's recommendations generating 50 bp single-end reads. A minimum of 14M reads per sample were produced. Quality control of raw reads was performed with FastQC v0.11.5. Adapters were filtered with ea-utils v1.2.2.18. Splice-aware alignment was performed with TopHat v2.0.13 against the human hg19. The number of allowed mismatches was 2. Reads that mapped to more than one site to the reference genome were discarded. The minimal score of alignment quality to be included in count analysis was 10. Resulting sequence alignment map (SAM) and binary alignment map (BAM) alignment files were handled with Samtools

v0.1.19.24. Quantification of reads per gene was performed with HT-Seq count v0.5.3p3. Count-based differential expression analysis was done with R-based (The R Foundation for Statistical Computing, Vienna, Austria) Bioconductor package DESeq. Reported p-values were adjusted for multiple testing with the Benjamini–Hochberg procedure, which controls false discovery rate (FDR). A list of differentially expressed genes was selected at an FDR of 0.05.

Formation of Microtissue Constructs : Macrowells with a diameter and a depth of 2 mm (ectopic implantation) and a length of 5 mm, a width of 3 mm, and a depth of 2 mm (orthotopic implantation) were created with 3% w/v agarose (Invitrogen, Belgium) and sterilized under UV. Microtissues were recuperated from their microwells by gently pipetting up and down several times. The microtissue suspension was concentrated with centrifugation to a volume corresponding to the macrowells. Next, the microtissues were added into the macrowells (≈3000 for ectopic and ≈6000 for large bone defect implantation) and incubated for 1 h to sediment, where after CM was added and constructs were incubated for additional 23 h to fuse into constructs.

In Vivo Implantation of Microtissue Constructs : Subcutaneous implantation was used to validate the construct's autonomy to form cartilage and bone tissue. Bone and cartilage do not naturally form in this location and chondro- and osteo-inductive signals must therefore arise from the construct itself. After 24 h fusion, the microtissue constructs were implanted subcutaneously in immune compromised mice (Rj :NMRInu/nu). Explants were taken out 4 and 8 weeks after *in vivo* implantation and fixed in 4% PFA for subsequent nano-CT and histological analysis. A large bone defect mouse model, described elsewhere,[58] was used to assess the impact of the environment and mechanical loading on the bone forming potential of the day 21 microtissue constructs. Briefly, a custom-made Ilizarov fixator was fixed to the tibia using 27 G steel needles. The tibia was exposed, and a 4 mm mid-diaphyseal segment was removed with a diamond saw. Custom-made constructs (≈6000 callus organoids per construct, n = 4) were placed into the defect, and the skin was sutured to close the wound. An empty defect was used as control (n = 4). Defects were monitored with *in vivo* micro-CT (SkyScan 1076, Bruker micro-CT, BE) 1, 2, 4, 6, and 8 weeks after surgery (voxel size of 9 µm). Animals were sacrificed after 8 weeks; the tibia was fixed in 4% PFA and analyzed with ex vivo nano-CT and processed for histology. All procedures on animal experiments were approved by the local ethical committee for Animal Research, KU Leuven. The animals were housed according to the regulations of the Animalium Leuven (KU Leuven).

Quantification of Mineralized Tissue from In Vivo Micro-CT and Ex Vivo Nano-CT : Ex vivo nano-CT (Pheonix Nanotom M, GE Measurement, and Control Solutions) was used for 3D quantification of mineralized tissue in each explant. Explants were scanned with a diamond target, mode 0, 500 ms exposure time, 1 frame average, 0 image skip, 2400 images, and a 0.2 mm aluminum filter. Subcutaneous explants were scanned at a voltage of 60 kV and a current of 140 µA resulting in a voxel size of 2 µm. Large bone defect explants and native tibia were scanned at a voltage of 60 kV and a current of 390 µA resulting in a voxel size of 5.6 µm. CTAn (Bruker micro-CT, BE) was used for all image processing and quantification of mineralized tissue based on automatic Otsu segmentation, 3D space closing, and despeckle algorithm. Percentage of mineralized tissue was calculated with respect to the total explant volume. CTvox (Bruker micro-CT, BE) was used to create 3D visualization.

Histochemistry and Immuno-Histochemistry : Retrieved subcutaneous explants were fixed in 4% PFA overnight and decalcified in ethylenediaminetetraacetic acid (EDTA)/PBS (pH 7.5) for 10 days at 4 °C followed by paraffin embedding. Tibias were fixed in 2% PFA overnight and decalcified in EDTA/PBS (pH 7.5) for 3 weeks then dehydrated and embedded in paraffin. Ectopic samples were sectioned at 5 µm and tibias at 6 µm. Histology was performed according to previously reported methods of H&E, Alcian Blue, Masson's Trichrome, and Safranin O staining.[10] Immuno-histochemistry was performed on PFA-fixed microtissues (Osterix), paraffin-embedded PFA-fixed microtissues (Indian Hedgehog), and paraffin-embedded EDTA-decalcified explants (human osteocalcin, CD31). Epitope retrieval was performed with Uni-Trieve (INNOVEX Bioscience, USA) for 30 min at 70 °C. Quenching of endogenous peroxidase activity was performed with 3% H2O2 for 10 min. Next, sections were blocked in serum for 30 min and incubated overnight at 4 °C with the primary antibodies human osterix (R&D Systems, MAB7547: dilution 1:300), human osteocalcin29 (a gift from E. Van Herck, Legendo, KU Leuven, BE; dilution 1:5000), rabbit polyclonal anti-Ihh antibody–N-terminal (Abcam, ab80191; dilution 1:50), rabbit anticollagen type II (Merck Millipore, AB761; dilution 1:50), or purified rat antimouse CD31 (BD Biosciences, USA, 550 274; dilution 1:50). Next, slides were blocked and incubated with the secondary antibodies Alexa 488 antimouse (Thermo Fisher Scientific, A11001; dilution 1:500), horseradish peroxidase (HRP) conjugated goat anti-guineaPig or—rabbit (Jackson ImmunoResearch, UK; dilution 1:500) for 30 min and peroxidase activity was determined using 3,3′-diaminobenzidine (DAB) (K3468, Dako, USA). For detection of CD31, the secondary antibody Biotin conjugated Goat-anti-Rat Ig (BD Biosceinces, USA, 559 286) and a tyramide signal amplification (TSA) Biotin detection system

(PerkinElmer, USA) were used. Stained histology sections were visualized with a Leica M165 FC microscope (Microsystems, Belgium) or an inverted laser scanning fluorescence confocal microscope ZEISS LSM 510 META (Cell imaging core facility of KU Leuven). Histomorphometry was performed in ImageJ software using ROI manager[87] on three to four nonconsecutive sections per sample, and mean values from these sections were used as data point for one sample.

Transcriptomics Analysis : An unsupervised analysis of the RNA-seq data and subsequently gene visualization was performed. For this, a [gene × experimental condition] matrix was obtained from the bulk RNA-seq data. First genes were ranked based on variance, and then the gene expression profile of 400 most variable genes across four time points was selected for downstream analysis. Gene expression values were mean and log2-normalized. Then, k-means clustering was used to computationally cluster these genes based on their expression profiles.

In order to select the number of clusters, the elbow method was applied and determined that k = 5 was the optimal parameter for achieving the most robust partition. Clustering results were visualized in order to provide insight into the patterns of correlation between samples and expression levels. A profile plot, also known as parallel coordinate plot was plotted using ggplot2—a package for data visualization within the R-statistical computing environment (http://www.r-project.org/) in order to visualize the expression levels of a total of 400 gene transcripts across all four time points including k-means cluster information. Subsequently, Gene Ontology enrichment of Biological Processes (2017b) for each cluster was performed with Enrichr.[38, 39]

Statistical Analysis : All experiments were performed with at least three replicates per condition. Data were represented as mean ± standard error of the mean (SEM) or box-plot with 10–90 percentiles, if otherwise not stated. Data were compared with one-way or two-way ANOVA and Tukey's Multiple Comparison test or Student's t test. Results were considered statistically different for p- values lower than 0.05 (*$p < 0.05$, **$p < 0.01$, ***$p < 0.001$). Statistical analysis was performed with GraphPad Prism 8 (GraphPad Software, Inc., USA) unless otherwise stated.

3.6 Acknowledgements

F.P.L. and I.P. contributed equally to this work. Kathleen Bosmans is thanked for performing *in vivo* experiments, and Melanie Van den Broeck and Inge Van Hoven for their experimental

assistance. Research was funded by the Research Foundation Flanders (FWO) G.N.H: 1S05116N, I.P.: 12O7916N, and CARTiPLEX: G0A4718N, the European Research Council under the European Union's Seventh Framework Program (FP/2007-2013)/ERC (249191) and Horizon 2020 Framework Program (H2020/2014-2021)/ERC (772418) and the special research fund of the KU Leuven (GOA/13/016 and C24/17/077). This work was supported by the partners of Regenerative Medicine Crossing Borders (http://www.regmedxb.com). Powered by Health—Holland, and Top Sector Life Sciences & Health. Confocal images were recorded on a Zeiss LSM 510 and 880—Airyscan, Cell and Tissue Imaging Cluster (CIC), Supported by Hercules AKUL/15/37_GOH1816N and FWO G.0929.15 to Pieter Vanden Berghe, KU Leuven. RNA sequencing and a part of the RNA-seq expression analysis were performed by the Genomics Core Leuven, KU Leuven. The micro (or nano)-CT images were generated on the X-ray computed tomography facility of the Department of Development and Regeneration of the KU Leuven, financed by the Hercules Foundation (project AKUL/13/47). The funders had no role in study design, data collection and analysis, decision to publish, or preparation of the manuscript. This work was part of Prometheus, the KU Leuven R&D division for skeletal tissue engineering (http://www.kuleuven.be/prometheus).

3.7 Conflict of Interest

The authors declare no conflict of interest.

3.8 Supporting Information

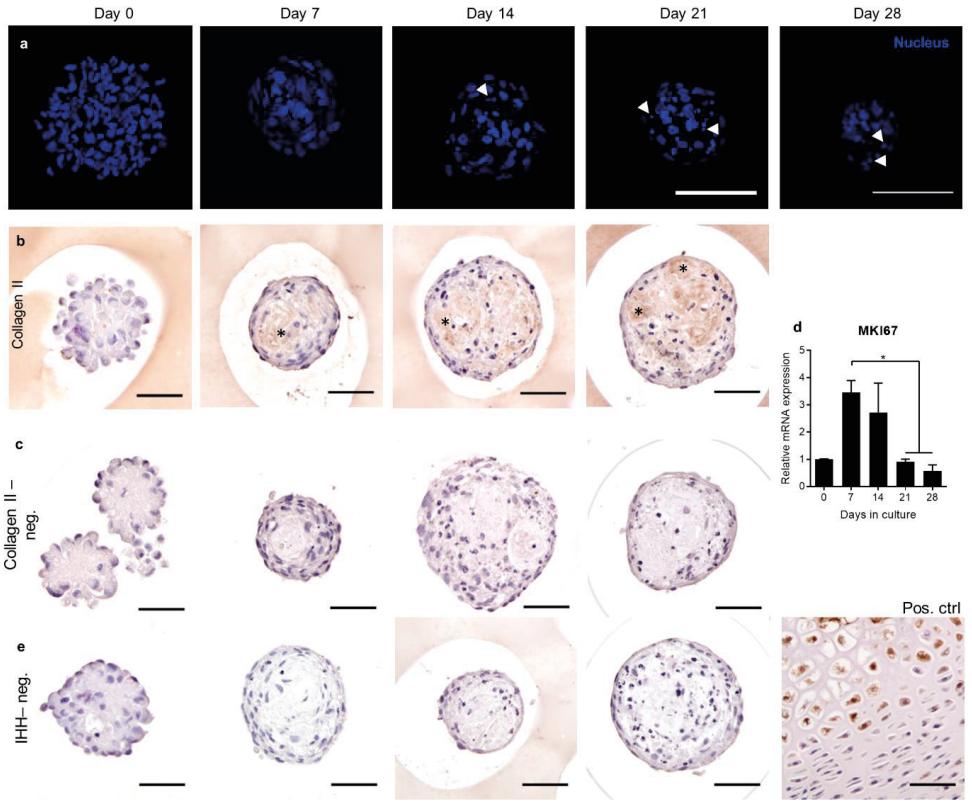

Figure S1. Characterization of cartilage intermediate microtissues. *a) 3D renderings of confocal images of micro-spheroids stained with DAPI (nucleus) over time (white arrows represent apoptotic-like nuclei). b) Representative sections of collagen II immunostaining with c) negative control (excluding primary antibody). d) Quantification of MKI67mRNA transcript (n = 3, mean value ± SEM). *p < 0.05; ANOVA and Tukey's multiple comparisons test. e) Negative control (excluding primary antibody, left panels D0, 7, 14 and 21) and positive control (E14.5 mouse limb, right panel) for IHH immunostaining. Scale bar a: 100 µm; b, d-e: 50 µm.*

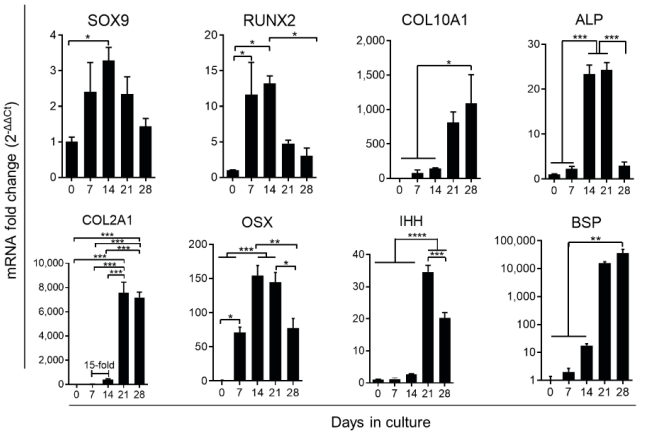

Figure S2. *Gene expression analysis of spheroids overtime until D28. mRNA transcript quantification normalized to D0 (n = 3). *p < 0.05; **p < 0.01; ***p < 0.001; ****p < 0.0001; ANOVA and Tukey's multiple comparisons test.*

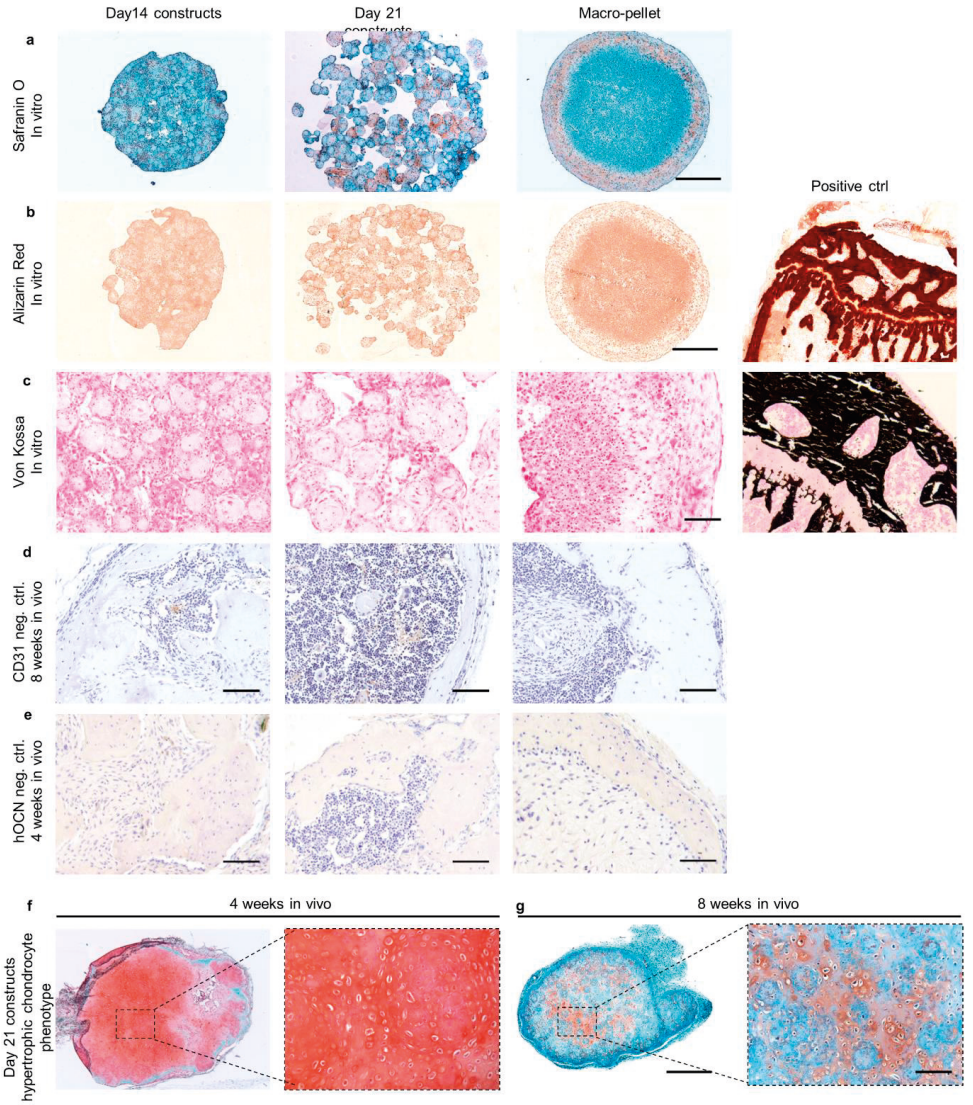

Figure S3. Assembly of callus organoids results in homogenous constructs able to form bone in vivo. *a) Safranin O staining of constructs analyzed: Day 14, day 21 constructs and Macro-pellet. b) Alizarin Red staining and c) Von Kossa staining with positive control demonstrated lack of mineralization in fused constructs and Macro-pellet in vitro. d) Negative control (excluding primary antibody) of CD31 immunostaining after 8 weeks in vivo and e) hOCN immunostaining after 4 weeks in vivo. f-g) Safranin O staining of day 21 constructs after 4 and 8 weeks in vivo, representing a hypertrophic phenotype. Scale bars a-b: 500 µm, c-e: 100 µm, f-g: 500 µm (left) and 100 µm (right).*

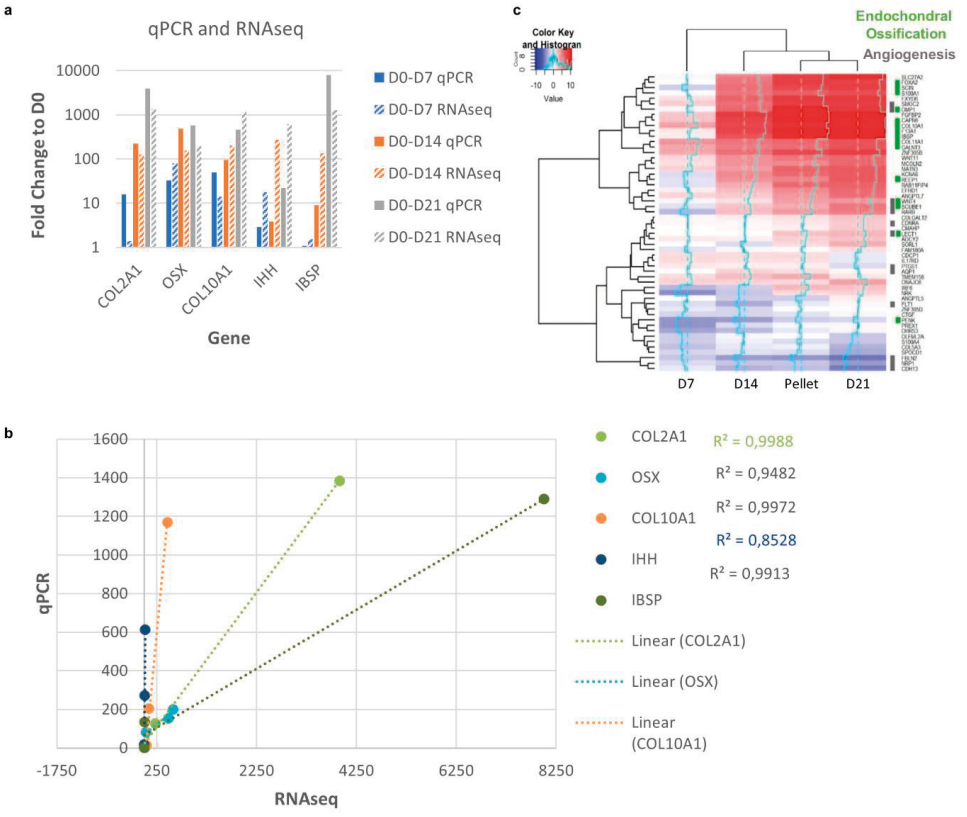

***Figure S4**. **RNA sequencing analysis of callus organoid maturation**. a) Comparison of key mRNA transcripts quantified with qPCR and RNA-seq demonstrating b) high linear fit for the two methods. c) Heat map of the 55 differentially expressed genes between D14 and D21 spheroids (green dots, Figure 5a) represented overtime and associated with endochondral ossification (green bar) and/or angiogenesis (grey bar).*

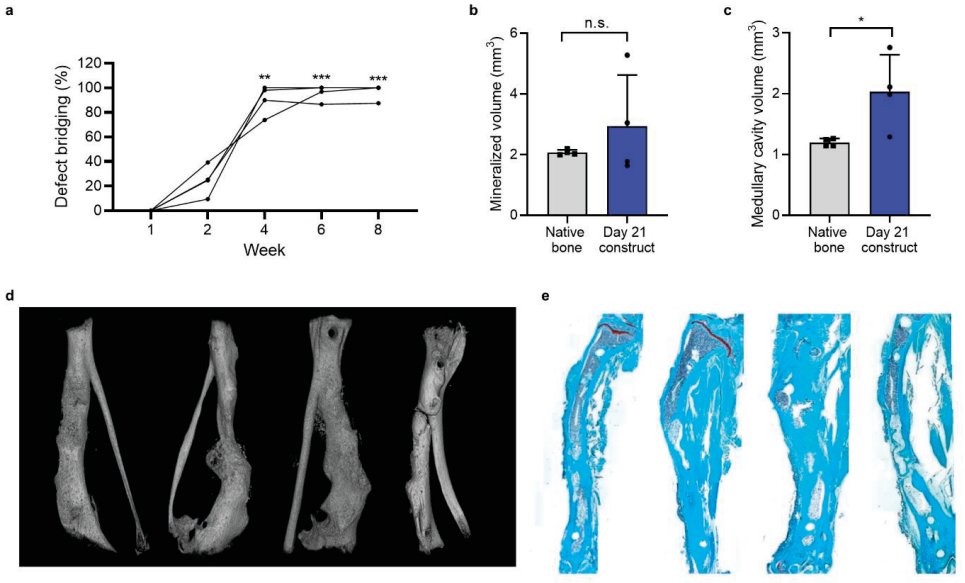

Figure S5. Fused callus organoids (Day 21 construct) heal critical-sized long bone defects in mice (n = 4 animals). *a) X-ray analysis of bone bridging over time defined by mineral bridging of the defect on two sides of the defect. ANOVA and Tukey's multiple comparisons test. **p < 0.01; ***p < 0.001 compared to Week 1. b) Comparison between native tibia and healed defect 8 weeks after construct implantation demonstrated by ex vivo nano-CT quantification of b) mineralized volume (mm^3) and c) medullary cavity volume (mm^3); unpaired t-test; *p < 0.05. d) 3D reconstruction of nano-CT scans and e) histological Safranin O staining for all four animals 8 weeks after construct implantation.*

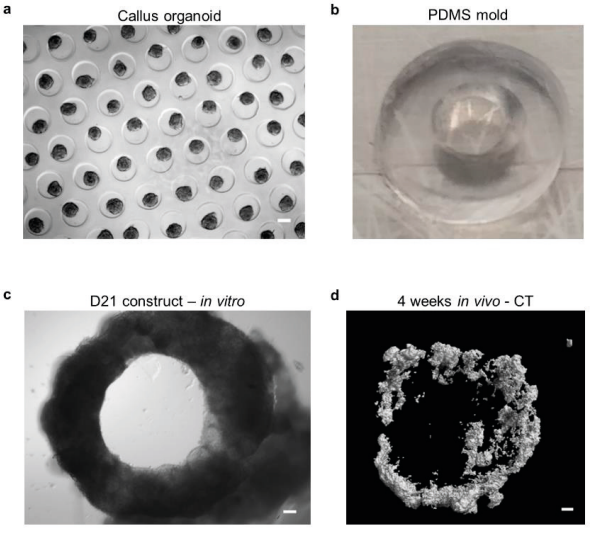

Figure S6. Formation of a ring-shaped mineralized tissue. *a) callus organoids cultured in micro-wells for seeding in a ring-shaped agarose well made from b) an in-house designed PDMS mold. c) Mature callus organoids (D21) were assembled in the agarose well and fused for 24h resulting into a ring-shaped construct. d) A mineralized ring was formed after 4 weeks ectopic implantation. Scale bars a, c-d: 100 µm.*

Table S1. Genes significantly up-regulated D14-21 and associated with endochondral ossification.

Gene	Fold Change	Adj.p-value	Full name	Description	Localization
IBSP	9,64	0,00017	Bone Sialoprotein	Regulates both chondrocyte proliferation and apoptosis as well as transition from cartilage to bone during development of endochondral bone. [206]	Extracellular
LECT1	7,47	0,00015	Chondromodulin (CNMD)	Expressed in the avascular zone of prehypertrophic cartilage and its expression decreases during chondrocyte hypertrophy and vascular invasion. The mature protein likely plays a role in endochondral bone development by permitting cartilaginous anlagen to be vascularized and replaced by bone. [207]	Extracellular
WNT4	6,65	0,03795	Wnt Family Member 4	Wnt4 accelerates chondrocyte differentiation. [208]	Plasma membrane, extracellular
RARB	6,50	0,012	Retinoic Acid Receptor Beta	Retinoid signaling crucial for chondrocyte maturation and endochondral ossification. [209]	Nucleus
FOXA2	6,41	0,00181	Forkhead Box A2	Detected in hypertrophic zone and mice engineered to lack expression of both FoxA2 and FoxA3 in their chondrocytes display defects in chondrocyte hypertrophy. [210]	
REEP1	6,35	0,00002	Receptor Accessory Protein 1	Increased expression in growth plate cartilage as compared to articular cartilage. [211]	endoplasmic reticulum
F13A1	6,23	0,00626	Coagulation Factor XIII A Chain	Increased expression in the hypertrophic zone compared to the proliferative/resting zone of the growth plate. [212]	extracellular
COL10A1	5,81	0,00045	Collagen Type X Alpha 1 Chain	ECM component secreted by hypertrophic chondrocytes. [213]	Extracellular, endoplasmic reticulum
DMP1	5,61	0,00002	Dentin Matrix Acidic Phosphoprotein 1	Critical for proper mineralization of bone. [214,215]	Extracellular, endoplasmic reticulum
SCIN	5,31	0,00017	Scinderin	Restricted to hypertrophic chondrocytes of the embryonic growth plate. Crucial for bone resorption. [216]	Extracellular
PENK	4,89	0,00000	Proenkephalin	Opioid. Expressed in the skeletal tissues, bone, and cartilage. Inhibit ALP expression in osteoblasts. [217]	Extracellular, endoplasmic reticulum
CAPN6	4,48	0,00004	Calpain 6	Calcium-dependent cysteine protease. Involved in proteoglycan degradation during bone development and fracture healing (rat). [218]	Cytoskeleton, cytosol
S100A1	4,10	0,00014	S100 Calcium Binding Protein A1	Transcriptional target of SOX trio and is present in late proliferative and prehypertrophic chondrocytes of mice growth plate. [219]	Extracellular, nucleus, endoplasmic reticulum
GALNT3	3,56	0,00262	Polypeptide N-Acetylgalactosaminyltransferase 3	Runx2 target gene in chondrocytes. Galnt3 is also likely to regulate chondrocyte maturation by modifying the glycosylation of Acan. [220]	Extracellular, golgi apparatus
COL11A1	2,91	0,01385	Collagen Type XI Alpha 1 Chain	A fibrillar collagen gene, critically involved in spatial organization of growth plate chondrocytes. [221]	Extracellular, endoplasmic reticulum

Table S2. Genes significantly up-regulated D14-21 and associated with angiogenesis.

Gene	Fold Change	Adj.p-value	Full name	Description	Localization
IRF6	17,55	0,0065	Interferon regulatory factor 6	Transcription factor that plays a role in late endothelial progenitor cells. [222]	Nucleus, cytoplasm, extracellular
ANGPTL7	13,87	5,16E-16	Angiopoietin Like 7	Stimulate endothelial cell proliferation *in vitro* and vascularization *in vivo*. [223]	Extracellular
FLT1 (VEGFR-1)	12,38	0,00046	Vascular Permeability Factor Receptor	Receptor for vascular endothelial growth factor (VEGF), an essential mediator of angiogenesis. [224]	Plasma membrane, extracellular, cytoskeleton, endosome
SCUBE1	8,76	1,29E-06	Signal Peptide, CUB Domain and EGF Like Domain Containing 1	Cell surface glycoprotein associated to vascular biology. [225]	Plasma membrane, extracellular
LECT1 (CNMD)	7,47	0,00015	Chondromodulin	Expressed in the avascular zone of prehypertrophic cartilage. The mature protein likely plays a role in endochondral bone development by permitting cartilaginous anlagen to be vascularized and replaced by bone. [207]	Extracellular
WNT4	6,65	0,038	Wnt Family Member 4	Promote MSC-mediated angiogenesis. [226]	Plasma membrane, extracellular
RARB	6,50	0,012	Retinoic Acid Receptor Beta		Nucleus
SMOC2	5,76	0,00032	SPARC Related Modular Calcium Binding 2	Angiogenic factor that potentiates angiogenic effects of growth factors. [227]	Extracellular
DMP1	5,61	0,00002	Dentin Matrix Acidic Phosphoprotein 1	Suggested as an inhibitor of VEGF-induced angiogenesis. [228]	Extracellular, endoplasmic reticulum
EDNRA	3,12	0,0081	Endothelin Receptor Type A	EDNRA is involved in the inhibition of angiogenesis in the retina. [229]	Plasma membrane
AQP1	0,36	0,045	Aquaporin 1	Targeted AQP1 gene disruption in mice reduces angiogenesis *in vivo*. [230]	Plasma membrane, extracellular, nucleus
FBLN2	0,34	0,041	Fibulin 2	Suppress angiogenesis in tumors *in vivo*. [231]	Extracellular
NRP1	0,27	0,017	Neuropilin 1	Stimulates angiogenesis in endothelial cells *in vitro*. [232]	Plasma membrane, extracellular
PTGS1 (COX-1)	0,25	0,00047	Prostaglandin-Endoperoxide Synthase 1	Regulates angiogenesis in endothelial cells *in vitro*. [233]	Extracellular, nucleus, ER, golgi
CDH13	0,23	0,00046	Cadherin 13	Code for T-cadherin involved in vascular homeostasis. [234]	Plasma membrane, extracellular

References

[1] S. Dimmeler, S. Ding, T. A. Rando, A. Trounson, Nat. Med. 2014, 20, 814.
[2] Y. Y. Lipsitz, N. E. Timmins, P. W. Zandstra, Nat. Biotechnol. 2016, 34, 393.
[3] D. C. Kirouac, P. W. Zandstra, Cell Stem Cell 2008, 3, 369.
[4] P. Lenas, Regen. Med. 2018, 13, 7.
[5] P. Lenas, M. Moos, F. P. Luyten, Tissue Eng., Part B 2009, 15, 381.
[6] P. Lenas, F. P. Luyten, Ind. Eng. Chem. Res. 2011, 50, 482.
[7] R. S. Marcucio, L. Qin, E. Alsberg, J. D. Boerckel, J. Orthop. Res. 2017, 35, 2356.
[8] T. Takebe, M. Enomura, E. Yoshizawa, M. Kimura, H. Koike, Y. Ueno, T. Matsuzaki, T. Yamazaki, T. Toyohara, K. Osafune, H. Nakauchi, H. Y. Yoshikawa, H. Taniguchi, Cell Stem Cell 2015, 16, 556.
[9] N. C. Rivron, J. Frias-Aldeguer, E. J. Vrij, J. C. Boisset, J. Korving, J. Vivié, R. K. Truckenmüller, A. Van Oudenaarden, C. A. Van Blitterswijk, N. Geijsen, Nature 2018, 557, 106.
[10] W. A. Fernando, I. Papantoniou, L. F. Mendes, G. Nilsson Hall, K. Bosmans, W. L. Tam, L. M. Teixeira, M. Moos, L. Geris, F. P. Luyten, J. Tissue Eng. Regener. Med. 2017, 12, 794.
[11] M. Huch, H. Gehart, R. Van Boxtel, K. Hamer, F. Blokzijl, M. M. A. Verstegen, E. Ellis, M. Van Wenum, S. A. Fuchs, J. De Ligt, M. van de Wetering, N. Sasaki, S. J. Boers, H. Kemperman, J. de Jonge, J. N. Ijzermans, E. E. Nieuwenhuis, R. Hoekstra, S. Strom, R. R. Vries, L. J. van der Laan, E. Cuppen, H. Clevers, Cell 2015, 160, 299.
[12] T. a. Einhorn, L. C. Gerstenfeld, Nat. Rev. Rheumatol. 2014, 11, 45.
[13] H. Kronenberg, Nature 2003, 423, 332.
[14] C. Colnot, J. Bone Miner. Res. 2009, 24, 274.
[15] O. Duchamp de Lageneste, A. Julien, R. Abou-Khalil, G. Frangi, C. Carvalho, N. Cagnard, C. Cordier, S. J. Conway, C. Colnot, Nat. Commun. 2018, 9, 773.
[16] J. M. Jukes, S. K. Both, A. Leusink, L. M. T. Sterk, C. A. van Blitters wijk, J. de Boer, Proc. Natl. Acad. Sci. USA 2008, 105, 6840.
[17] C. Scotti, B. Tonnarelli, A. Papadimitropoulos, A. Scherberich, S. Schaeren, A. Schauerte, J. Lopez-Rios, R. Zeller, A. Barbero, I. Martin, Proc. Natl. Acad. Sci. USA 2010, 107, 7251.
[18] C. Scotti, E. Piccinini, H. Takizawa, A. Todorov, P. Bourgine, A. Papadimitropoulos, A. Barbero, M. G. Manz, I. Martin, Proc. Natl. Acad. Sci. USA 2013, 110, 3997.
[19] N. Harada, Y. Watanabe, K. Sato, S. Abe, K. Yamanaka, Y. Sakai, T. Kaneko, T. Matsushita, Biomaterials 2014, 35, 7800.
[20] A. M. McDermott, S. Herberg, D. E. Mason, J. M. Collins, H. B. Pearson, J. H. Dawahare, R. Tang, A. N. Patwa, M. W. Grinstaff, D. J. Kelly, E. Alsberg, J. D. Boerckel, Sci. Transl. Med. 2019, 11, eaav7756.
[21] A. Atala, F. K. Kasper, A. G. Mikos, Sci. Transl. Med. 2012, 4, 160rv12.
[22] M. W. Laschke, M. D. Menger, Trends Biotechnol. 2017, 35, 133.
[23] K. Jakab, A. Neagu, V. Mironov, R. R. Markwald, G. Forgacs, Proc. Natl. Acad. Sci. USA 2004, 101, 2864.
[24] V. Mironov, R. P. Visconti, V. Kasyanov, G. Forgacs, C. J. Drake, R. R. Markwald, Biomaterials 2009, 30, 2164.
[25] K. Futrega, J. S. Palmer, M. Kinney, W. B. Lott, M. D. Ungrin, P. W. Zandstra, M. R. Doran, Biomaterials 2015, 62, 1.
[26] A. Leferink, D. Schipper, E. Arts, E. Vrij, N. Rivron, M. Karperien, K. Mittmann, C. van Blitterswijk, L. Moroni, R. Truckenmüller, Adv. Mater. 2014, 26, 2592.
[27] E. Fennema, N. Rivron, J. Rouwkema, C. van Blitterswijk, J. De Boer, Trends Biotechnol. 2013, 31, 108.
[28] A. D. Dikina, D. S. Alt, S. Herberg, A. McMillan, H. A. Strobel, Z. Zheng, M. Cao, B. P. Lai, O. Jeon, V. I. Petsinger, C. U. Cotton, M. W. Rolle, E. Alsberg, Adv. Sci. 2018, 5, 1700402.
[29] C. De Bari, F. Dell'Accio, J. Vanlauwe, J. Eyckmans, I. M. Khan, C. W. Archer, E. a. Jones, D. McGonagle, T. a. Mitsiadis, C. Pitzalis, F. P. Luyten, Arthritis Rheum. 2006, 54, 1209.
[30] K. M. Pineault, J. Y. Song, K. M. Kozloff, D. Lucas, D. M. Wellik, Nat. Commun. 2019, 10, 3168.
[31] E. J. Mackie, Y. a. Ahmed, L. Tatarczuch, K.-S. Chen, M. Mirams, Int. J. Biochem. Cell Biol. 2008, 40, 46.

[32] D. Kobayashi, T. Oike, A. Shibata, A. Niimi, Y. Kubota, M. Sakai, N. Amornwhichet, Y. Yoshimoto, Y. Hagiwara, Y. Kimura, Y. Hirota, H. Sato, M. Isono, Y. Yoshida, T. Kohno, T. Ohno, T. Nakano, Sci. Rep. 2017, 7, 40588.
[33] L. Yang, K. Y. Tsang, H. C. Tang, D. Chan, K. S. E. Cheah, World Rev. Nutr. Diet. 2014, 111, 13.
[34] X. Zhou, Z. Zhang, J. Q. Feng, V. M. Dusevich, K. Sinha, H. Zhang, B. G. Darnay, B. de Crombrugghe, Proc. Natl. Acad. Sci. USA 2010, 107, 12919.
[35] C. S. Bahney, D. P. Hu, T. Miclau, R. S. Marcucio, Front. Endocrinol. 2015, 6, 4.
[36] J. Park, M. Gebhardt, S. Golovchenko, F. Perez-Branguli, T. Hattori, C. Hartmann, X. Zhou, B. deCrombrugghe, M. Stock, H. Schneider, K. von der Mark, Biol. Open 2015, 4, 608.
[37] E. Holm, J. E. Aubin, G. K. Hunter, F. Beier, H. A. Goldberg, Bone 2015, 71, 145.
[38] E. Y. Chen, C. M. Tan, Y. Kou, Q. Duan, Z. Wang, G. V. Meirelles, N. R. Clark, A. Ma'ayan, BMC Bioinformatics 2013, 14, 128.
[39] M. V. Kuleshov, M. R. Jones, A. D. Rouillard, N. F. Fernandez, Q. Duan, Z. Wang, S. Koplev, S. L. Jenkins, K. M. Jagodnik, A. Lachmann, M. G. McDermott, C. D. Monteiro, G. W. Gundersen, A. Ma'ayan, Nucleic Acids Res. 2016, 44, W90.
[40] M. Kutmon, A. Riutta, N. Nunes, K. Hanspers, E. L. Willighagen, A. Bohler, J. Mélius, A. Waagmeester, S. R. Sinha, R. Miller, S. L. Coort, E. Cirillo, B. Smeets, C. T. Evelo, A. R. Pico, Nucleic Acids Res. 2016, 44, D488.
[41] W. E. Samsa, X. Zhou, G. Zhou, Semin. Cell Dev. Biol. 2017, 62, 3.
[42] T. J. Mead, K. E. Yutzey, Proc. Natl. Acad. Sci. USA 2009, 106, 14420.
[43] K. Yeung Tsang, S. Wa Tsang, D. Chan, K. S. E. Cheah, Birth Defects Res., Part C 2014, 102, 52.
[44] J. P. Iannotti, C. T. Brighton, J. Orthop. Res. 1989, 7, 511.
[45] A. R. Guntur, C. J. Rosen, BoneKEy Rep. 2013, 2, 437.
[46] M. Barna, P. P. Pandolfi, L. Niswander, Nature 2005, 436, 277.
[47] M. B. Goldring, K. Tsuchimochi, K. Ijiri, J. Cell. Biochem. 2006, 97, 33.
[48] Z. Tan, B. Niu, K. Y. Tsang, I. G. Melhado, S. Ohba, X. He, Y. Huang, C. Wang, A. P. McMahon, R. Jauch, D. Chan, M. Q. Zhang, K. S. E. Cheah, PLoS Genet. 2018, 14, 1007346.
[49] H. M. Kronenberg, Ann. N. Y. Acad. Sci. 2006, 1068, 1.
[50] P. Smits, P. Dy, S. Mitra, V. Lefebvre, J. Cell Biol. 2004, 164, 747.
[51] J. Li, H. Luo, R. Wang, J. Lang, S. Zhu, Z. Zhang, J. Fang, K. Qu, Y. Lin, H. Long, Y. Yao, G. Tian, Q. Wu, Cell Rep. 2016, 15, 1467.
[52] A. Ionescu, E. Kozhemyakina, C. Nicolae, K. H. Kaestner, B. R. Olsen, A. B. Lassar, Dev. Cell 2012, 22, 927.
[53] L. Ye, Y. Mishina, D. Chen, H. Huang, S. L. Dallas, M. R. Dallas, P. Sivakumar, T. Kunieda, T. W. Tsutsui, A. Boskey, L. F. Bonewald, J. Q. Feng, J. Biol. Chem. 2005, 280, 6197.
[54] M. K. Song, Z. H. Lee, H. H. Kim, Exp. Mol. Med. 2015, 47, e199.
[55] Y. Nakamichi, C. Shukunami, T. Yamada, K.-i. Aihara, H. Kawano, T. Sato, Y. Nishizaki, Y. Yamamoto, M. Shindo, K. Yoshimura, T. Nakamura, N. Takahashi, H. Kawaguchi, Y. Hiraki, S. Kato, Mol. Cell. Biol. 2003, 23, 636.
[56] S. Miura, J. Kondo, A. Takimoto, H. Sano-Takai, L. Guo, C. Shukunami, H. Tanaka, Y. Hiraki, PLoS One 2014, 9, 3.
[57] H. H. Lee, R. R. Behringer, PLoS One 2007, 2, 450.
[58] N. Van Gastel, S. Stegen, I. Stockmans, K. Moermans, J. Schrooten, D. Graf, F. P. Luyten, G. Carmeliet, Stem Cells 2014, 32, 2407.
[59] S. Debnath, A. R. Yallowitz, J. McCormick, S. Lalani, T. Zhang, R. Xu, N. Li, Y. Liu, Y. S. Yang, M. Eiseman, J.-H. Shim, M. Hameed, J. H. Healey, M. P. Bostrom, D. A. Landau, M. B. Greenblatt, Nature 2018, 562, 133.
[60] C. S. Bahney, D. P. Hu, A. J. Taylor, F. Ferro, H. M. Britz, B. Hallgrimsson, B. Johnstone, T. Miclau, R. S. Marcucio, J. Bone Miner. Res. 2014, 29, 1269.
[61] J. van der Stok, M. K. E. Koolen, H. Jahr, N. Kops, J. H. Waarsing, H. Weinans, O. P. van der Jagt, Eur. Cells Mater. 2014, 27, 137.
[62] C. Epple, A. Haumer, T. Ismail, A. Lunger, A. Scherberich, D. J. Schaefer, I. Martin, Biomaterials 2018, 192, 118.

[63] P. Li, J. S. Markson, S. Wang, S. Chen, V. Vachharajani, M. B. Elowitz, Science 2018, 360, 543.
[64] J. Groll, J. A. Burdick, D.-W. Cho, B. Derby, M. Gelinsky, S. C. Heilshorn, T. Jüngst, J. Malda, V. A. Mironov, K. Nakayama, A. Ovsianikov, W. Sun, S. Takeuchi, J. J. Yoo, T. B. F. Woodfield, Biofabrication 2018, 11, 013001.
[65] A. Page-McCaw, A. J. Ewald, Z. Werb, Nat. Rev. Mol. Cell Biol. 2007, 8, 221.
[66] C. K. F. Chan, C.-C. Chen, C. A. Luppen, J.-B. Kim, A. T. DeBoer, K. Wei, J. A. Helms, C. J. Kuo, D. L. Kraft, I. L. Weissman, Nature 2009, 457, 490.
[67] A. Ovsianikov, A. Khademhosseini, V. Mironov, Trends Biotechnol. 2018, 36, 348.
[68] A. C. Daly, P. Pitacco, J. Nulty, G. M. Cunniffe, D. J. Kelly, Biomaterials 2018, 162, 34.
[69] L. Moroni, J. A. Burdick, C. Highley, S. J. Lee, Y. Morimoto, S. Takeuchi, J. J. Yoo, Nat. Rev. Mater. 2018, 3, 21.
[70] A. Petersen, A. Princ, G. Korus, A. Ellinghaus, H. Leemhuis, A. Herrera, A. Klaumünzer, S. Schreivogel, A. Woloszyk, K. Schmidt-Bleek, S. Geissler, I. Heschel, G. N. Duda, Nat. Commun. 2018, 9, 4430.
[71] F. Qu, J. L. Holloway, J. L. Esterhai, J. A. Burdick, R. L. Mauck, Nat. Commun. 2017, 8, 1780.
[72] A. W. James, G. LaChaud, J. Shen, G. Asatrian, V. Nguyen, X. Zhang, K. Ting, C. Soo, Tissue Eng., Part B 2016, 22, 284.
[73] S. Herberg, A. M. McDermott, P. N. Dang, D. S. Alt, R. Tang, J. H. Dawahare, D. Varghai, J.-Y. Shin, A. McMillan, A. D. Dikina, F. He, Y. B. Lee, Y. Cheng, K. Umemori, P. C. Wong, H. Park, J. D. Boerckel, E. Alsberg, Sci. Adv. 2019, 5, eaax2476.
[74] Z. A. Cheng, A. Alba-Perez, C. Gonzalez-Garcia, H. Donnelly, V. Llopis-Hernandez, V. Jayawarna, P. Childs, D. W. Shields, M. Cantini, L. Ruiz-Cantu, A. Reid, J. F. C. Windmill, E. S. Addison, S. Corr, W. G. Marshall, M. J. Dalby, M. Salmeron-Sanchez, Adv. Sci. 2019, 6, 1800361.
[75] A. Lang, M. Kirchner, J. Stefanowski, M. Durst, M. C. Weber, M. Pfeiffenberger, A. Damerau, A. E. Hauser, P. Hoff, G. N. Duda, F. Buttgereit, K. Schmidt-Bleek, T. Gaber, Acta Biomater. 2019, 86, 171.
[76] H. Fonoudi, H. Ansari, S. Abbasalizadeh, M. R. Larijani, S. Kiani, S. Hashemizadeh, A. S. Zarchi, A. Bosman, G. M. Blue, S. Pahlavan, M. Perry, Y. Orr, Y. Mayorchak, J. Vandenberg, M. Talkhabi, D. S. Winlaw, R. P. Harvey, N. Aghdami, H. Baharvand, Stem Cells Transl. Med. 2015, 4, 1482.
[77] S. Sart, R. F. X. Tomasi, G. Amselem, C. N. Baroud, Nat. Commun. 2017, 8, 469.
[78] S. V. Murphy, A. Atala, Nat. Biotechnol. 2014, 32, 773.
[79] N. I. Moldovan, N. Hibino, K. Nakayama, Tissue Eng., Part B 2017, 23, 237.
[80] N. V. Mekhileri, K. S. Lim, G. C. J. Brown, I. Mutreja, B. S. Schon, G. J. Hooper, T. B. F. Woodfield, Biofabrication 2018, 10, 024103.
[81] J. Rouwkema, A. Khademhosseini, Trends Biotechnol. 2016, 34, 733.
[82] M. A. Skylar-Scott, S. G. M. Uzel, L. L. Nam, J. H. Ahrens, R. L. Truby, S. Damaraju, J. A. Lewis, Sci. Adv. 2019, 5, eaaw2459.
[83] C. K. F. Chan, G. S. Gulati, R. Sinha, J. V. Tompkins, M. Lopez, A. C. Carter, R. C. Ransom, A. Reinisch, T. Wearda, M. Murphy, R. E. Brewer, L. S. Koepke, O. Marecic, A. Manjunath, E. Y. Seo, T. Leavitt, W.-J. Lu, A. Nguyen, S. D. Conley, A. Salhotra, T. H. Ambrosi, M. R. Borrelli, T. Siebel, K. Chan, K. Schallmoser, J. Seita, D. Sahoo, H. Goodnough, J. Bishop, M. Gardner, R. Majeti, D. C. Wan, S. Goodman, I. L. Weissman, H. Y. Chang, M. T. Longaker, Cell 2018, 175, 43.
[84] J. Eyckmans, S. J. Roberts, J. Schrooten, F. P. Luyten, J. Cell. Mol. Med. 2010, 14, 1845.
[85] J. Leijten, L. S. Moreira Teixeira, J. Bolander, W. Ji, B. Vanspauwen, J. Lammertyn, J. Schrooten, F. P. Luyten, Sci. Rep. 2016, 6, 36011.
[86] L. F. Mendes, W. L. Tam, Y. C. Chai, L. Geris, F. P. Luyten, S. J. Roberts, Tissue Eng., Part C 2016, 22, 473.
[87] C. A. Schneider, W. S. Rasband, K. W. Eliceiri, Nat. Methods 2012, 9, 671.
[88] K. J. Livak, T. D. Schmittgen, Methods 2001, 25, 402.

CHAPTER 4.

Patterned, organoid-based osteochondral implants result in zone-specific functionality *in vivo*

4

Gabriella Nilsson Hall[1], Wai Long Tam, Leire Casas-Fraile[2], Liesbet Geris[1,3,4], Frank P. Luyten[1,], Ioannis Papantoniou[1,‡,*]*

* These authors share senior authorship

[1]Prometheus Division of Skeletal Tissue Engineering and Skeletal Biology and Engineering Research Center, Department of Development and Regeneration, KU Leuven, Belgium. [2]Laboratory of Tissue Homeostasis and Disease, Skeletal Biology and Engineering Research Center, Department of Development and Regeneration, KU Leuven, Belgium. [3]GIGA in silico medicine, Université de Liège, Belgium. [4]Biomechanics Section, KU Leuven Belgium. [‡] Current address: Institute of Chemical Engineering Sciences (ICE-HT) Foundation for Research and Technology, Hellas (FORTH), Greece.

Manuscript submitted

Abstract

Current clinical treatments for deep osteochondral defects are limited and associated with donor-site morbidity and tissue shortage. Tissue engineered constructs, such as cell-based osteochondral grafts, have the potential to respond to this unmet medical need. In this work, a developmentally-inspired modular approach is applied whereby distinct cartilaginous organoids are used as living building blocks. An implant is assembled into a hierarchical construct composed of three layers consisting of cartilaginous tissue intermediates of progressive maturity with (i) early, (ii) mature and (iii) (pre)hypertrophic organoids. Upon ectopic implantation in nude mice, the formation of a hybrid tissue with a bone, mineralized cartilage and fibrocartilage was observed. To engineer a more stable articular cartilage, iPSC-derived hyaline cartilage microtissues were introduced in combination with the pre-hypertrophic cartilage organoids to create dual structures. Both tissue zones revealed their biological potency upon ectopic implantation, corresponding to the pre-engineered zonal pattern. The assembly of functional building blocks as presented in this work, opens possibilities for the production of complex tissue engineered implants by embedding zone-specific functionality through the use of properly pre-programmed living building blocks.

4.1 Introduction

An osteochondral defect is a local injury of the joint surface affecting the articular cartilage and the underlying subchondral bone.[1] These defects can result in substantial functional disability, pain, swelling and when left untreated lead inevitably to osteoarthritis. Osteoarthritis (OA) is a joint disease affecting the whole joint but in particular the osteochondral unit.[2] OA poses a major socioeconomic challenge also in view of the ageing population.[3] To prevent the onset of OA, treatment of deep osteochondral defects (>8 mm) require implants that represent the full osteochondral unit of articular cartilage and subchondral bone.[4] Currently, these treatment methods include osteochondral autograft/allograft transplantation and autologous bone grafting in combination with autologous chondrocyte implantation (ACI), named "ACI sandwich technique".[4–6] These techniques are associated with donor-site morbidity and/or limited tissue availability. Novel advancements in tissue engineering (TE) could provide better solutions for efficient and synchronized regeneration of the articular cartilage and subchondral bone, irrespective of the size of the defect.

TE constructs developed to date for osteochondral defect regeneration have employed scaffolds created from hydrogels,[7] polymers in combination with ceramics[8] and native cartilage extracellular matrix (ECM)[9] either alone or seeded with chondrocytes and/or adult progenitor cell types.[10,11] A majority of efforts employed single cell populations which upon implantation as large implants have shown impaired cell viability and regenerative potential.[12] In addition, the large volumetric presence of foreign material has recently been shown to affect the regenerative processes in an *in vivo* setting.[13] At the same time, the use of calcium phosphate (CaP) components has been shown to trigger immune reactions from the host with detrimental effects on the implanted cells.[14] Moreover, many of these TE constructs are biphasic and composed of two considerably different zones either in terms of biology (for example using terminal differentiated cells), or in terms of material (using high volumes of polymers and CaP) which have very different properties from the native tissue. These implants not only fail biomechanically, but do not heal properly with full tissue integration.[4,15]

Recent advances in the field of TE demonstrate that *in vitro* recapitulation of processes during skeletal development can lead to the development of functional intermediate tissues that upon implantation *in vivo* mature into full organs.[16–20] Regarding osteochondral tissue, a distinct engineered cartilage intermediate *in vitro* could further mature into non-mineralized, mineralized cartilage or bone upon implantation *in vivo*. Cartilage intermediate tissues from

lapine bone marrow-derived mesenchymal stromal cells (BMSC) or human periosteum derived cells (hPDC) have been demonstrated to contribute to the regeneration of osteochondral defects, illustrating the power of a developmentally inspired approach.[21,22] However, the cartilage quality was not optimal and the constructs failed to capture the zonal nature of the native joint containing several zones being articular cartilage, mineralized cartilage and subchondral bone. In addition, articular cartilage and subchondral bone develops through different processes which makes it a challenge to create osteochondral grafts *in vitro* using a single cell type under the same culture condition.[23] Efforts have been made to allow gradient maturation within one tissue by applying different media from the top to the bottom of the constructs[24] but this makes the process complex and may limit the future possibility for upscaling.

Therefore, the zonal complexity of osteochondral tissues implicates that a bottom-up approach, where different building blocks are assembled into a multi-layered structure, is more attractive.[25–27] A developmentally inspired bottom-up approach was recently demonstrated by us for healing of long-bone defects through assembly of prehypertrophic microtissues ("callus organoids") which upon implantation mimicked the function of the soft callus during fracture healing. Furthermore, gene signatures attained from transcriptomic analysis demonstrated that the differentiation into "callus organoids" followed the developmental process of endochondral ossification from a proliferative to a prehypertrophic stage.[19] Hence, the sequentially differentiated building blocks have potential for the formation of a hierarchical osteochondral tissue.

To generate cell-based constructs, a major challenge for the use of adult mesenchymal stromal cells (MSCs) is the formation of hyaline-like cartilage rich in collagen type II. Instead, mostly fibrocartilage rich in collagen type I is formed and because of its suboptimal mechanical properties, clinical success is limited.[28,29] Articular chondrocytes (ACs) isolated from the articular surface have shown promising results for the healing of full thickness cartilage defects but isolation and extended expansion leads to dedifferentiation.[30] For these reasons, induced pluripotent stem cells (iPSCs) are emerging as a promising cell source for cartilage TE and hyaline-like cartilage tissue has successfully been produced from human iPSCs.[31–33] Additionally, the iPSC-derived engineered cartilage tissue demonstrated phenotypic stability in both rat and mini-pig cartilage defect models.[32]

Successful treatment of osteochondral defects should aim at the synchronized regeneration with integration of both the damaged articular cartilage and the underlying subchondral bone. In the current study, we applied a bottom-up strategy to create patterned osteochondral constructs. In order to obtain best performance for both layers, distinct cartilaginous microtissue populations derived from human adult progenitors (periosteum-derived cells; hPDCs) or human induced pluripotent stem cells (iPSCs) were developed to regenerate the subchondral and articular cartilage zone respectively. We hypothesized that cartilage microtissues (iCMTs) from hiPSC-derived chondrocytes (hiChon) in combination with bone forming "callus organoids" (COs) from hPDCs could be engineered into osteochondral implants that possess zone specific functionality resulting in bone and hyaline-like cartilage upon implantation.

4.2 Results

4.2.1 Human periosteum derived cells form microtissues with cartilaginous and hypertrophic cell phenotype

Human periosteum-derived cells (hPDCs) were seeded into non-adherent microwells to form microspheroids of homogenous size (107 ± 12 µm dimeter, 2700 microspheroids quantified day 1). The microspheroids were differentiated in chemically defined chondrogenic media for 21 days leading to accumulation of extracellular matrix (**Figure 1a** and **Figure S1**, Supporting Information). Gene expression analysis was performed to define the maturity of microspheroids over time. mRNA expression of the early chondrogenic marker *SOX9* was up-regulated 7-folds after 7 days in culture without significant change on day 14 followed by a 3-fold down-regulation at day 21 (Figure 1b). The mRNA of the gene *COL2A1,* encoding the alpha-1 chain of type II collagen present in cartilage, was significantly up-regulated a 1600-fold by day 14, and a 5200-fold after 21 days in culture. Up-regulation of the (pre)hypertrophic gene markers *IHH* and *COLX* was detected after 21 days in culture (Figure 1c). These results indicate the formation of chondrogenic microtissues after 7 to 14 days which attain a (pre)hypertrophic phenotype after 21 days in culture corroborating our previously attained data within the same culture platform.[19]

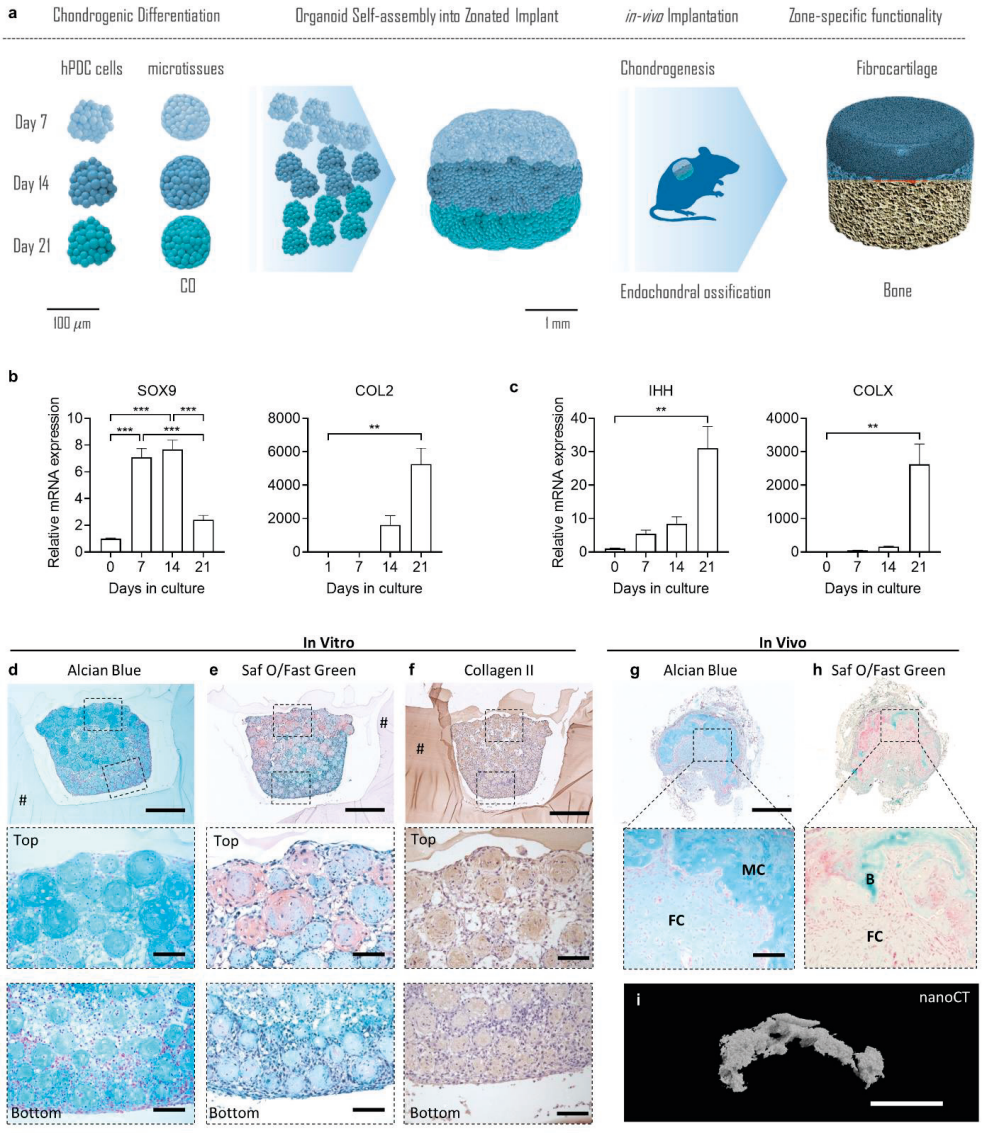

Figure 4.1. Hierarchical micromodule implant derived from adult hPDCs. *a) Schematic overview of building block assembly into tri-layered constructs. b) Gene expression analysis of chondrogenic and c) hypertrophic markers (mean ± SEM three samples). d)* In vitro *constructs stained with alcian blue, e) Safranin O/Fast Green and f) collagen type II immunostaining. Samples four weeks after implantation stained with g) alcian blue, h) Safranin O/Fast Green and i) 3D visualization of mineralized tissue imaged with nanoCT. #: agarose, FC: fibrocartilage, MC: mineralized cartilage, B: bone. Scale bars a-e: top-images represent 500 µm, zoom-in images 100 µm and f: 500 µm.*

4.2.2 Building blocks from adult progenitor cells form hierarchical structures for gradient cartilaginous tissue

The osteochondral tissue is defined by layers of tissues with different properties going from avascular cartilage, mineralized cartilage to subchondral bone. To create a hierarchical intermediate tissue that upon implantation would create these layers, building blocks of different maturity were sequentially assembled in a non-adherent macrowells of 2 mm diameter (Figure 1a). Day 7 and day 14 microtissues were added to represent the hyaline-like chondrogenic part followed by the prehypertrophic day 21 microtissues expected to continuously mature and mineralize *in vivo* to represent the bone part. The macrowell was placed in a Thincert™ to allow media diffusion from both the top and bottom of the construct during the 24 hours fusion period. Histological characterization of the *in vitro* construct showed a gradient increase in Alcian Blue staining, Saf O and collagen type II (Figure 1d-f). Day 7 microtissues in the bottom layer contained a higher number of cells per area (4062 ± 463 cells/mm^2) compared to the top layer with day 21 microtissues (2538 ± 521 cells/mm^2) while the top layer contained increased sulfated glycosaminoglycans (sGAG) and collagen type II positive areas confirming the formation of a hierarchical construct (Figure 1d-f).

Next, the constructs were implanted subcutaneously in immunocompromised mice for 4 weeks to evaluate their *in vivo* tissue formation/maturation potency. Alcian blue staining indicated formation of two distinct layers, a fibrocartilage-like layer which was non-mineralized and a second layer containing mature hypertrophic chondrocyte-like cells (Figure 1g). NanoCT demonstrated that the top layer was mineralized and certain areas were fast green positive indicating presence of bone formation (Figure 1h-i). Although a layered structure was created after ectopic *in vivo* implantation, the cartilaginous part showed a fibrous phenotype indicating that the day 7 and 14 microtissues were insufficient for regeneration of hyaline-like articular cartilage at an ectopic implantation site.

4.2.3 Chondroprogenitors from human induced pluripotent stem cells form hyaline-like cartilage microtissues in vitro

Since the day 7 and 14 microtissues formed fibrous cartilage *in vivo*, an alternative cell source for creation of the hyaline cartilaginous part was introduced. Human induced pluripotent stem cells (iPSCs) were differentiated into chondrogenic nodules highly positive for Safranin O (Saf O) (**Figure 2a**).[32] The human iPSC derived chondroprogenitors (hiChon) were subsequently isolated by enzymatic digestion of the chondrogenic nodules resulting in a yield of 256 500 ±

37 590 cells per nodule (140 nodules from 4 independent digestions). Gene expression of three independent hiChon batches were compared to human articular chondrocytes (hACs) from three donors to assess their chondrogenic phenotype. hiChon had increased mRNA expression of the early chondrogenic marker *SOX9* and *COL2* but no significant difference was seen for *ACAN* and *COL1* (Figure 2b). These data demonstrate that hiPSCs were successfully differentiated into chondrocytes which secreted sGAG-rich cartilaginous matrix and isolated hiChon.

Next, the isolated chondroprogenitors (hiChon) were seeded into non-adherent micro-wells. The entrapped chondroprogenitors underwent self-aggregation and subsequently condensation into microspheroids at day 7 (Figure 2c) followed by an increase in size over time (Figure 2d). Alcian blue and Saf O staining demonstrated presence of extracellular matrix already day 7 (Figure 2e-f). A down-regulation of the early chondrogenic marker *SOX9* was detected in the building blocks as compared to the isolated iPSC derived chondrocytes (Day 0), indicating an effect of the aggregation. However, the chondrogenic marker *COL2* remained stable over time (Figure 2g) suggesting that ECM secretion has remained stable as confirmed by histological staining (Figure 2e-f). No significant difference in gene expression of the hypertrophic marker *IHH* or *COL2* was detected until day 14, *COLX* was significantly up-regulated day 21 (Figure 2g). In conclusion, isolated hiChon were able to form cartilage-like microtissues with increasing size over time.

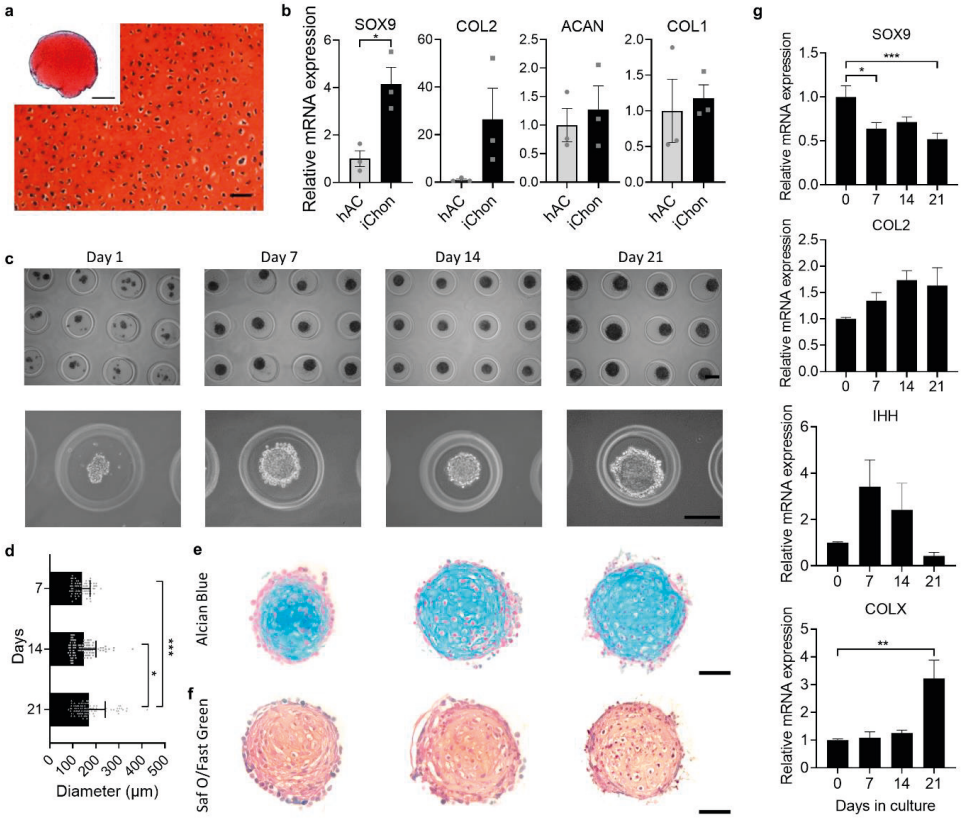

Figure 4.2. Formation of cartilage microtissues from hiPSC derived chondrocytes (hiChon). *a) Safranin O /Fast Green staining of mature chondrogenic nodules derived from iPSCs. b) Gene expression comparison of cells isolated from hiPSC derived chondrogenic nodules (hiChon) and human articular chondrocytes (hAC) (mean ± SEM, each data point represents one hAC donor/ iPSC batch). c) Bright field images of building blocks created from hiChon in non-adherent microwells. d) Projection area of hiChon building blocks over time (mean ± SD, each data point represents one individual building block, data pooled from 3 independent iPSC experiments). Histological sections of cartilaginous building blocks stained with e) alcian blue and f) Safranin O/Fast Green. g) Gene expression analysis of hiChon building blocks over time (mean ± SEM of three samples). Scale bars represent a: 50 µm (zoom-in) and 500 µm (insert), c: 200 µm and e-f: 50 µm.*

4.2.4 Chondrogenic and prehypertrophic building blocks assemble into integrated constructs in vitro

The presented results indicate that the day 21 hPDC-derived "callus organoids" (COs) (Figure 1b) and day 21 hiChon-derived chondrogenic microtissues (iCMTs) (Figure 2) have characteristics suitable to create a dual construct from the bottom up with one part (iCMTs) representing hyaline-like cartilage and the second part (COs) more hypertrophic cartilage potentially serving as a template for the subchondral bone. Indeed, gene expression was

analyzed to further assess the cellular phenotype of the building blocks. No significant difference of the chondrogenic gene markers (*SOX9*, *COL2*) was detected between day 21 hPDC- and hiChon- derived building blocks (**Figure 3a**) while the hypertrophic gene markers (*IHH*, *COLX*) were significantly up-regulated in the hPDC-derived building blocks and absent to low in hiChon derived cartilage (Figure 3b).

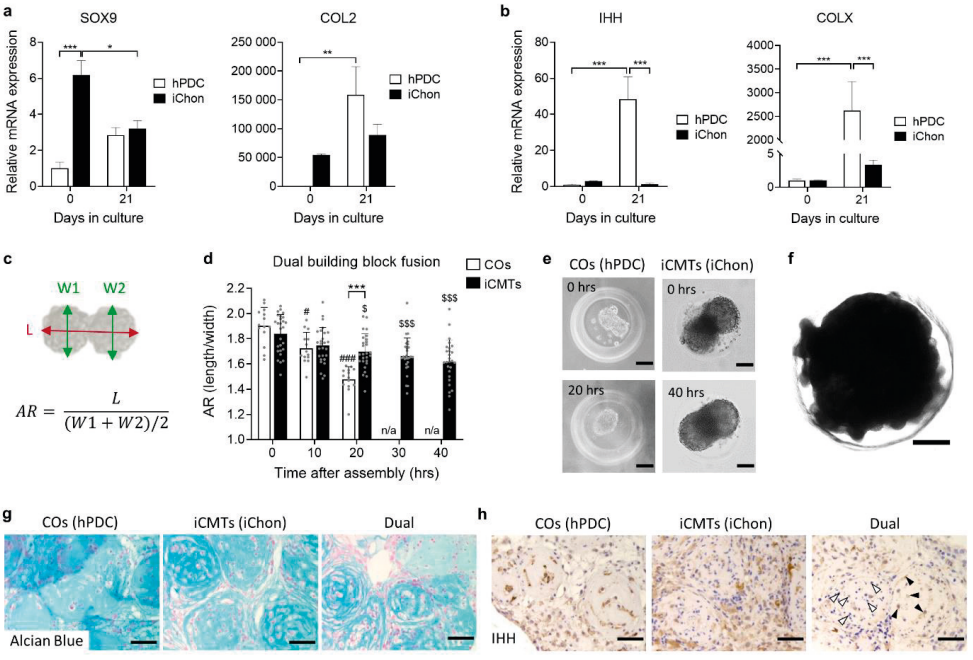

Figure 4.3. Creation of integrated osteochondral tissues through assembly of hPDC- and hiChon-derived building blocks. *a) Chondrogenic and b) hypertrophic gene expression analysis of hPDC- and hiChon derived building blocks at day 0 and 21 (mean ± SEM of three samples). c) Equation for the aspect ratio (AR). d) Aspect ratio (AR) quantification for dual building block fusion over time for callus organoids (COs) and cartilage microtissues (iCMTs) separately (mean ± SD, each data point represents one dual fusion; two-way ANOVA and Tukey's post-hoc test; #: compared to COs 0hrs; $: compared to iCMTs 0hrs). e) Representative images of fusing building blocks. f) Bright field image of a fused construct. Histological sections of* in vitro *constructs stained with g) alcian blue and h) indian hedgehog (IHH) immunostaining (white arrows: cells negative for IHH; black arrows: cells positive for IHH). L: length, W: width, COs: callus organoids, iCMTs: cartilage microtissues, IHH: Indian hedgehog. Scale bars represent e: 100 µm, f: 500 µm, c-d: 50 µm.*

Since formation of larger constructs require fusion of building blocks, quantification of fusion capacity was assessed by fusion of two building blocks of each tissue type (Figure 3c). 24 hours fusion was previously shown to work well for callus organoids which was confirmed by the significantly lower aspect ratio (AR) already after 10 hrs and continue to decrease (Figure 3d). Markedly, iCMTs fuse (Supplemental Movie 1) but significantly slower and consequently a longer fusion time for iCMTs was used. The iCMTs were assembled in a non-adherent macrowell (2 mm diameter) which resulted in a thin layer (**Figure S2a**, Supporting

Information). After 24 hrs, COs were added on top for an additional 24 hrs of fusion into a dual construct (Figure 3f, Figure S2b, Supporting Information). Hence, to correlate with the AR quantification iCMTs were fused for 48 hrs in total while the COs were fused for 24 hrs.

Alcian blue staining of fused constructs demonstrated presence of ECM although no or small differences were detected between COs and iCMTs (Figure 3g) while IHH immunostaining hinted towards more increased staining of cells within COs as compared to cells within iCMTs (Figure 3h). Nevertheless, although gene expression analysis demonstrated a distinct difference between hPDC and hiChon building blocks on day 21 (Figure 3b), only limited differences were detected on histological sections.

4.2.5 Integrated constructs maintain maturation properties in vivo and form osteochondral-like tissues

The fused constructs (only COs or iCMTs and Dual) were implanted ectopically for 4 weeks to evaluate their capacity to mature *in vivo* (**Figure 4a)**. Mineralization was detected in both dual and osteogenic (COs) constructs but not in chondrogenic (iCMTs) constructs (Figure 4b and **Figure S3a**, Supporting Information). As expected, the dual constructs contained significantly less mineralization (18 ± 6 %) as compared to the hPDC constructs (29 ± 3 %) (Figure S3c, Supporting Information). To enable visualization of cartilaginous tissue with nanoCT, the contrast agent Hexabrix (ioxaglate meglumine & ioxaglate sodium) was used. Ionic Hexabrix is detected by nanoCT and repelled by negatively charged tissue, such as sGAG-rich cartilage, resulting in decreased gray values for cartilaginous tissues.[34] Cartilaginous tissue was detected in both the iCMTs (3/3 samples) and dual constructs (3/6 samples). 3D rendering of mineralized and cartilaginous tissue demonstrated that the two parts formed a dual tissue (Figure 4b). H&E staining of the dual constructs indicated areas of integration between the distinct building blocks (Figure 4b, black arrow) although non-mineralized fibrous regions were also discerned between the two parts (Figure 4c, white arrow and Figure S3d, Supporting Information). The presence of two distinct zones was further demonstrated with positive Saf O staining in three of six dual samples (Figure 4d and Figure S3d, Supporting Information) as well as collagen type II positive areas in the iCMT construct/part (Figure 4e). However, COs in dual samples with advanced maturation into bone ossicles appeared to subdue the iCMTs (Figure S3e, Supporting Information). Moreover, human osteocalcin (hOCN) positive areas in the CO construct/part provided evidence that at least some of the implanted human cells were contributing to bone formation (Figure 4f). These

data demonstrated that the different building blocks integrated into dual constructs with preserved maturation properties upon implantation. Hence, the assembled COs and iCMTs can maintain their zonal stability to form integrated osteochondral-like tissues *in vivo*.

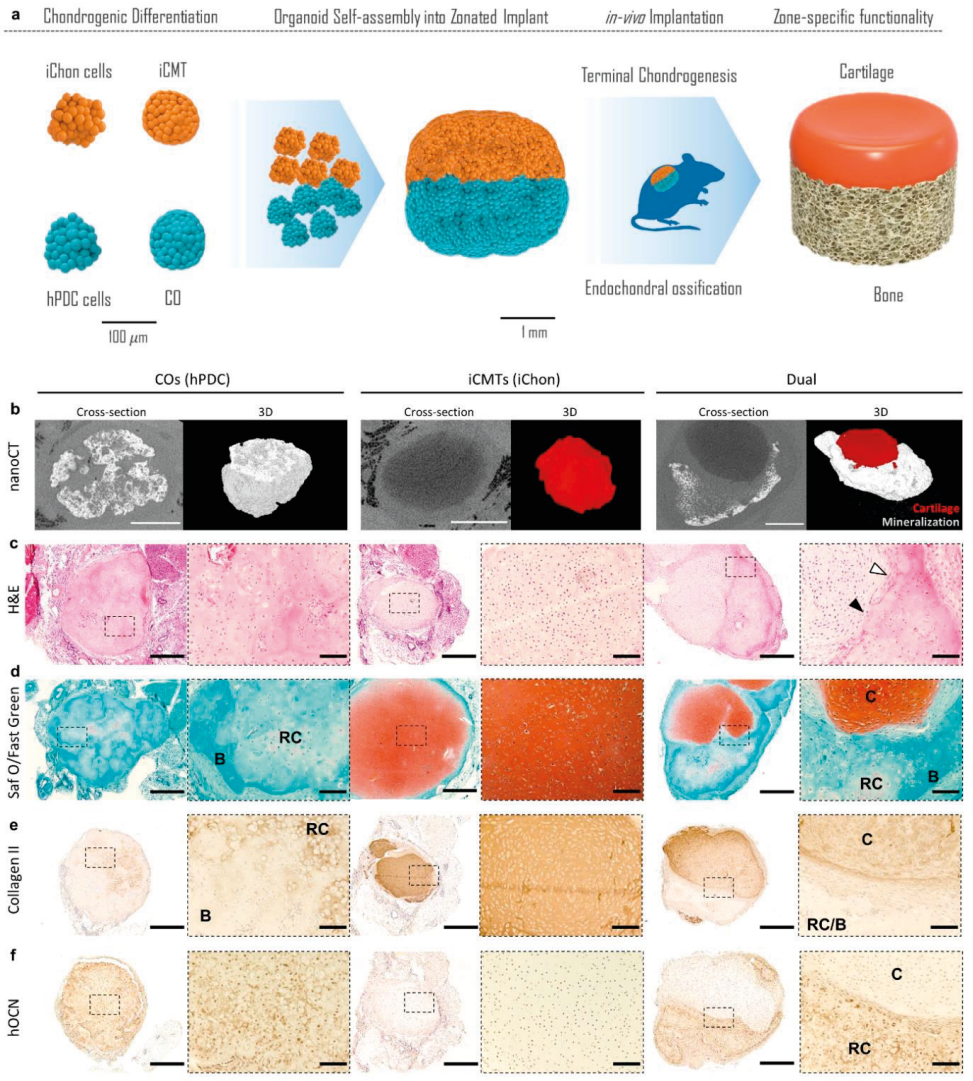

Figure 4.4.* In vivo *functionality of integrated dual constructs after 4 weeks implantation. *a) Schematic illustration of building block assembly into zonal constructs. b) Cross-section and 3D rendering of nanoCT demonstrating mineralized (white) and cartilaginous tissue (dark grey in cross-section and red in 3D rendering). Histological sections of samples after 4 weeks ectopic implantation stained with c) H&E (arrows: zone interface), d) Safranin O/Fast Green (Figure S3d-e, Supporting Information), e) collagen type II and f) human osteocalcin (hOCN) immunostaining. 5 of 5 COs, 3 of 4 iCMTs and 6 of 6 Dual constructs were recuperated in total from two separate experiments. B: bone, RC: remodeling cartilage, C: cartilage, COs: callus organoids, iCMTs: cartilage microtissues. Scale bars represent 500 µm and zoom-ins (dashed border) 100 µm.*

4.3 Discussion

In this study, we aimed to engineer a patterned osteochondral tissue using distinct cartilaginous building blocks which allowed the progressive formation of an osteochondral unit upon *in vivo* implantation. The native osteochondral tissue consists of a gradient with multiple cell types, which maintain a stability of the full depth joint surface including non-mineralized hyaline cartilage, mineralized cartilage to subchondral bone and the current one-module culture set-up is limiting the complexity of TE constructs.[35] A multimodular approach using microtissues and organoids[25,36] was therefore proposed here, to allow the assembly of multiple building blocks into designed gradients corresponding to the native requirements for regeneration. By generating a hierarchical tissue assembly from building blocks of defined developmental stages (proliferation to hypertrophy) we aimed to create an engineered implant able to form an osteochondral unit *in vivo*. However, although mineralized tissue was detected, the hPDC derived microtissues with chondrogenic gene expression phenotype (*SOX9*, *COL2A1* up-regulated mRNA expression) resulted rather in fibrocartilage upon ectopic implantation (Figure 1g-h). The use of multipotent MSCs have been shown to result in fibrocartilage or onset of hypertrophy leading to mineralization after long term implantation, even at orthotopic sites [21,29], indicating that adult MSCs either do not have the intrinsic capacity to form stable cartilage or that current chondrogenic differentiation protocols are not appropriate. For further improvement, developmentally-inspired expansion and differentiation protocols have been presented to obtain more stable cartilage from adult progenitor cells.[37,38]

In order to address this limitation, we aimed at using human iPSCs as cell source for the generation of cartilage microtissues that could result in stable hyaline-like cartilage *in vivo*. In contrast to hACs, chondrocytes derived from iPSCs can be produced in large amounts without the need of making additional cartilage defects for obtaining biopsies, making iPSCs potentially attractive for clinical translation.[39] Additionally, iPSC-derived microtissues can be produced through protocols assuring homogeneity and purity[31,32,40] and their production have scale-up potential by applying bioreactors.[41] We demonstrated that cells isolated from chondrogenic nodules derived from hiPSCs (hiChon) attained comparable gene expression levels of *ACAN* and *COL1A1* as hACs while *SOX9* and *COL2* mRNA transcript levels were higher in hiChon (Figure 2b). The relatively high *SOX9* and *COL2* mRNA expression in hiChon compared to hACs may be linked to a younger cell phenotype of hiChon or be an effect of the well-known event of dedifferentiation during monolayer culture.[42,43]. Subsequent

aggregation of hiChon into microspheroids allowed the formation of cartilage microtissues (iCMTs) permitting bottom-up formation of larger constructs. Upon implantation, the iCMT constructs formed uniform cartilaginous tissue demonstrating building block integration (Figure 4). This is in contrast to previously published data of assembled iPSC cartilage nodules[32] and the improved building block integration could be related to the relatively short culture time for hiChon as microtissues (3 weeks) compared to nodules (6-8 weeks). This time-dependent fusion capacity is a phenomenon previously described for sheep articular chondrocytes.[44]

Although iPSCs demonstrate promise for cartilage regeneration, few studies have to our knowledge applied iPSC-derived chondrocytes to tissue engineer zonal osteochondral grafts. Lin et.al. demonstrated the formation of an osteochondral unit *in vitro* using iPSCs for the purpose of drug screening but no *in vivo* functionality was reported.[45] Our approach involved the combination of hiChon derived iCMTs for the cartilage part to overcome limitations using hACs and adult progenitor cell (hPDC) derived COs for the bone part to take advantage of their robust endochondral bone forming potency.[19] Subcutaneous implantation demonstrated tissue maturation and the two different zones showed the development of a tissue interface that appeared to have areas of integration (Figure 4b, black arrow), quite critical for its potential biomechanical and biological behavior *in vivo* when implanted in a deep osteochondral defect. The native cartilage-bone interface of the joint surface is defined by the tidemark, a tissue junction between mineralized and non-mineralized cartilage which plays an important role in the maintenance of a balanced osteochondral unit.[46,47] Attempts to recreate an *in vitro* cartilage-bone interface using combinations of biomaterials and cells have been presented as well as scaffold-free approaches to recreate the crucial mineralized cartilage zone between the non-mineralized cartilage and bone substitute [8,48,49] However, the formation of the tidemark is hypothesized to be linked to mechanical stimulation[50,51] and orthotopic implantation is therefore probably necessary to evaluate this point. Hence, orthotopic implantation in an osteochondral defect model is also required to assess whether the interface between iCMTs and OCs could possess a functional role corresponding to that of the tidemark. Moreover, the building block approach applied in our work provide the possibility to model cartilage-bone integration by detailed analysis of building block fusion as previously described for hepato-biliary-pancreatic organoids.[52] The *in vitro* building block fusion could further be combined with novel microwell platform designs which might elicit improvements in micro-engineering of osteochondral niches *in vitro*.[53] Additionally, the development of dual constructs with an

iPSC-derived bone part[31,54,55] is envisaged to create an osteochondral graft entirely derived from iPSCs.

The modular approach suggested in this work is amenable to the use of recently developed biofabrication technologies for a more automated and guided bioassembly process.[8,36,56–58] The use of large spheroids for bioprinting has been exhibited[58] also for the formation of spatially organized tissues,[57] in the presence of scaffolds. The intrinsic design of scaffolds could also be designed to further promote a gradient tissue formation[59] in addition to deposition of spheroids. Recently, aspiration assisted bioprinting showed that single microspheroids, of equivalent size to our study, could be picked-up and transferred at desired locations.[56] Currently, the throughput of these strategies is low and considerable time would be needed for the biomanufacturing of clinically relevant tissue volumes. However, it is plausible that through parallelization and further intensification of these processes it could be possible to automate the production of complex patterned osteochondral tissues as developed in the present study.

4.4 Conclusion

Organoids engineered *in vitro* possess the capacity to semi-autonomously undergo maturation and developmental events *in vivo* leading to functional tissues. This provides the unique opportunity to build complex living implants within which a quasi-deterministic behavior can be embedded. In this study, we embedded spatially distinct populations of cartilaginous tissue intermediates within a single implant in order to create an osteochondral tissue unit. Hyaline-like cartilage microtissues (iCMTs) derived from iPSCs were assembled with hPDC-derived "callus organoids" (COs) to engineer a zonal structure. Upon implantation, the different zones (iCMTs and COs) of the implant, resulted in the formation of a dual structure of cartilage and bone corresponding to the preimplantation design. Additional studies at orthotopic sites will be needed to explore the capacity of these implants to gradually integrate at the defect site and result in a fully regenerated functional joint surface.

4.5 Materials and methods

Periosteal cell isolation and culture: Human periosteum-derived cells (hPDCs) were isolated from periosteal biopsies of five female donors of age 14 ± 3 years old (n=5) from which a single cell pool was created as previously described.[60] Cells were seeded at a density of 5700 cells/cm^2 for expansion until passage 9 (*in vitro* experiment) and 7 (in vivo experiments) at

37°C, 5% CO_2 and 95% humidity in Dulbecco′s modified Eagle′s medium (DMEM, Life Technologies, UK) with 10% fetal bovine serum (HyClone FBS, Thermo Scientific, USA), 1% antibiotic-antimycotic (100units/mL penicillin, 100mg/mL streptomycin and 0.25mg/mL amphotericin B) and 1mM sodium pyruvate (Life Technologies, UK). Expansion medium was changed every 2-3 days and cells were harvested with TrypLE™ Express (Life Technologies, UK) at a confluence of 90%. TrypLE™ Express was used for all passaging and harvesting steps during cell handling. All procedures were approved by the ethical committee for Human Medical Research (Katholieke Universiteit Leuven) and patients' informed consent forms were obtained (ML7861).

Formation of agarose microwells and "callus organoids": Polydimethylsiloxane (PDMS, Dow Corning Sylgard 184 elastomer, MAVOM Chemical Solutions) molds were fabricated as described elsewhere.[61] Briefly, an SU8 wafer was fabricated to produce a PDMS mold containing pillars with a diameter of 200 µm and height of 153 µm. Next, 3% agarose (Thermo Fisher) was carefully poured over the PDMS mold and let to cool down to form agarose microwells (153 µm depth, 200 µm diameter). The agarose microwells were punched into a size (1.8 cm^2) to fit in a 24-well plate resulting in approximately 2000 microwells per 24 well plate well. Agarose microwells were sterilized under UV before seeding 500 000 hPDCs per well resulting in microspheroids with approximately 250 cells/spheroid. Microspheroids were cultured in xeno-free chemically defined chondrogenic medium (CM1) (LG-DMEM (Gibco) supplemented with 1% antibiotic-antimycotic (100units/mL penicillin, 100mg/mL streptomycin and 0.25mg/mL amphotericin B), 1 mM ascorbate-2 phosphate, 100 nM dexamethasone, 40 µg/mL proline, 20 µM of Rho-kinase inhibitor Y27632 (Axon Medchem), ITS+ Premix Universal Culture Supplement (Corning) (including 6.25 µg/mL insulin, 6.25 µg/mL transferrin, 6.25 µg/mL selenious acid, 1.25 µg/mL bovine serum albumin (BSA), and 5.35 µg/mL linoleic acid), 100 ng/mL BMP-2 (INDUCTOS®), 100 ng/mL GDF5 (PeproTech), 10 ng/mL TGFβ1 (PeproTech), 1 ng/mL BMP-6 (PeproTech) and 0.2 ng/mL FGF-2 (R&D systems))[62] for three weeks with media changes 2 times per week to reach a pre-hypertrophic state.

Isolation and expansion of human articular chondrocytes: Human articular chondrocytes (hACs) were obtained from patients undergoing hip replacement for osteoporotic or malignancy-associated fractures (female: 82, male: 54 and male 84 years old). The University Hospitals Leuven Ethics Committee and Biobank Committee approved the study. For chondrocytes isolation, cartilage was dissected from the joint explant surfaces and then rinsed

with saline. The tissue was cut into small pieces, using a sterile surgical blade. Cartilage explants were incubated with 2 mg/ml pronase solution (Roche) for 90 min at 37 °C under continuous agitation and digested overnight at 37 °C in 1.5 mg/ml collagenase B solution (Roche). The preparation was filtered through a 70 μM strainer and cells were plated in culture flasks and cultured in a humidified atmosphere at 37 °C, 5% CO_2 with a density of 16 000 cells cm^{-2}. Culture medium consisted of DMEM/F12 (Gibco), 10% fetal bovine serum (FBS) (Gibco), 1% (vol/vol) antibiotic/antimycotic (Gibco) and 1% L-glutamine (Gibco). Experiments were performed with passage 2 cells in triplicate.

Generation of iPSC derived chondrocytes : The human pluripotent stem cell (hiPSC) line CY2 (Rutgers University Cell and DNA Repository) was cultured as previously described.[32] In summary, hiPSCs were maintained on mitomycin-c (Sigma) treated SNL feeder cells in human embryonic stem cell medium (Dulbecco's modified eagle medium (DMEM) Ham's F12 nutrient mix (F12) (Sigma) supplemented with 20% knockout serum replacement, 2mM Glutamax, 1% sodium pyruvate (SP), 1% non-essential amino acids (NEAA), 0.1 mM 2-mercaptoethanol (2ME), 50 U and 50 mg/ml penicillin/streptomycin (Pen/Strep) and 10 ng/ml human basic fibroblast growth factor (FGF-2, R&D systems)) at 37°C and 5% CO_2. Medium refreshment was performed daily and cells were passaged once a week onto fresh feeder cells. hiPSCs were transferred and maintained in feeder-free conditions using Essential 8 and Matrigel (Becton Dickinson) coated well plates followed by chondrogenic differentiation according to a previously described protocol.[32] Primitive streak and mesoderm induction was carried out for 72 hours by using 8 μM canonical wingless related integration protein (Wnt) agonist CHIR99021 (GSK3 inhibitor, Axon Medchem), 8-20 ng/ml FGF-2 and 1 μM retinoic acid (RA). Subsequently, chondrogenic differentiation was performed until day 14 using chondrogenic medium (CM2) (DMEM supplemented with 1% Fetal Bovine Serum (FBS, Hyclone), 1% L-Glutamine, 1% NEAA, 1% SP, 1% Insulin-Transferrin-Selenite X (ITS-X), 50 μg/ml ascorbic acid (AA, Sigma), 0.1 mM 2ME, 10 ng/ml FGF-2, 10 ng/ml TGF- β1, 10 ng/ml BMP2, 10 ng/ml GDF5 (Prospec), 50 U and 50 mg/ml Pen/Strep). After 14 days, cartilage-like nodules were cultured in suspension using CM2 without FGF-2 for 8 weeks. Next, cartilage-like nodules were digested to release and isolate hiPSC derived chondrocytes (hiChon). The nodules were incubated with rotation for 4 hrs at 37°C and 5% CO_2 in digestion medium (DMEM: F12 (Gibco) supplemented with 1.5 mg/mL Collagenase B (Roche), 1% Antibiotics-Antimycotics: Gibco, 10% FBS: Hyclone SV30160.03).

Formation of hiPSC derived cartilage microtissues: Agarose microwells were created using MicroTissues® 3D Petri Dish® micro-molds (Sigma) for 12-well plates according to manufacturer's description. Briefly, 500 µL of melted 2% agarose (Thermo Fisher) was pipetted into the precision micro-molds containing 256 pillars (800 µm depth, 400 µm dimeter). After the agarose was gelled, it was removed and transferred to a 12 well and an additional of 500 µL agarose (2%) was added around the insert for immobilization. The microwells were sterilized under UV before use. hiChon were resuspended in CM2 to a concentration of 128 000 cell/100µL and 100µL was seeded into the microwell. Cells were let to sediment for 20 minutes where after 1mL CM2 was added and cultured for 3 weeks at 37°C, 5% CO_2 and 95%.

Dual building block fusion assay: Microtissues were carefully flushed out from their microwells and added onto another micro-well insert already containing microtissues. Wells containing two microtissues were imaged with 10x magnification over time in a well plate incubator (OKOlab Top Stage Incubator with insert H301-EC-24MW) using an inverted microscope (Olympus IX53) previously described [63]. The length of the duplets and width of each microtissue was manually measured and the aspect ratio (AR) was defined as length divided by the average widths (**Figure** 3c).

Formation of zonal constructs: PDMS cylinders (2mm diameter, 5mm depth) were placed in a petri-dish and 3% agarose was carefully poured to cover the PDMS cylinders. The agarose was left to gel where after a 6mm agarose part was punched out, the PDMS pillar was removed and the now created macro-well was placed in a ThinCert™ Cell Culture Inserts (Greiner Bio-One) for 24 well plates. The macro-wells were sterilized under UV before use. Next, approximately 1000 building blocks were carefully flushed out from their micro-wells, centrifuged and resuspended in 20µL fresh media and pipetted into the macro-well to sediment at 37°C, 5% CO_2 and 95% for 1 hour followed by addition of media. For dual constructs, cartilage microtissues were added and incubated during 24 hours where after prehypertrophic microtissues were added and fused for additional 24 hours.

Gene expression analysis: Total RNA from hAC was extracted using the Nucleospin RNA II kit (Macherey-Nagel). Microspheroids from one well were pooled together and total RNA was isolated using QIAshredder (Qiagen) followed by RNeasy Mini Kit (Qiagen). RNA concentration and quality were assessed with NanoDrop 2000 (Thermo Scientific) and PrimeScript™ RT reagent kit (Takara) was used for cDNA synthesis. Quantitative real-time polymerase chain reaction (qRT-PCR) was performed using SYBR® Green (Life

Technologies) on Rotor Gene® 6000 (Qiagen) and relative differences in expression were calculated using the $2^{-\Delta\Delta Ct}$ method normalized to the housekeeping gene Glyceraldehyde-3-Phosphate Dehydrogenase (GAPDH).[64] All protocols were performed according to the manufacturer's protocol.

Ectopic implantation: The zonal constructs were implanted subcutaneously in immune compromised mice (Rj:NMRInu/nu). After 4 weeks implantation, explants were taken out and fixed in 4% paraformaldehyde (PFA) for subsequent nanoCT scan and histological analysis. All procedures on animal experiments were approved by the local ethical committee for Animal Research, KU Leuven (P36/2016 ECD) and the animals were housed according to the regulations of the Animalium Leuven (KU Leuven).

NanoCT imaging and quantification: After PFA fixation, the explants were washed in Phosphate buffered saline (PBS) and immersed in 20% Hexabrix® 320 (Guerbet Nederland BV) overnight. Hexabrix® 320 contains negatively charged ioxaglate molecules which are locally repelled by the negatively charged sulfated glycosaminoglycans (sGAG) containing cartilage enabling visualization of the cartilage tissues [34]. Samples were scanned with nano-CT (Pheonix Nanotom M®, GE Measurement and Control Solutions) at a voltage of 60 kV and a current of 140 µA resulting in an isotropic voxel size of 2 µm using diamond target, mode 0, 500ms exposure time, 1 frame average, 0 image skip, 2400 images and a 0.2 mm aluminum filter. Region of interest (ROI) was drawn to define total explant volume followed by mineralization quantification using CTAn (Bruker micro-CT, BE) based on automatic Otsu segmentation, 3D space closing and despeckle algorithm. CTvox (Bruker micro-CT, BE) was used to create 3D visualizations.

Histological analysis: After nanoCT imaging, explants were decalcified in ethylenediaminetetraacetic acid (EDTA)/PBS (pH 7.5) for 10 days at 4˚C followed by paraffin embedding overnight. Explants were sectioned into 5 µm slices and de-paraffinized in HistoclearTM (Laborimpex, Brussels, Belgium) followed by histological staining Haematoxylin-eosin (H&E), Alcian Blue and Safranin O (Saf O) as previously described [42]. Immunostaining of Collagen type II (Col2) was performed by antigen retrieval (1 mg/mL pepsin in 0.02 M HCl), washes, quenching in 3% H2O2 and blocking followed by primary anti-Col2 antibody (dilution 1:50, AB761, Merck Millipore) incubation overnight at 4°C. Next, slides were blocked and incubated with secondary anti-rabbit antibody (dilution 1:500, 111-035-003, Jackson ImmunoResearch, UK) followed by visualization with DAB (K3468, Dako,

US) and counterstaining with haematoxylin. Stained sections were imaged with Leica M165 FC microscope (Microsystems, BE).

4.6 Acknowledgements

F.P.L. and I.P. contributed equally to this work. Kathleen Bosmans is thanked for performing *in vivo* experiments; Inge Van Hoven, Samuel Ribeiro Viseu and Tim Reekmans for their experimental assistance. Research was funded by the Research Foundation Flanders (FWO) G.N.H: 1S05116N, I.P.: 12O7916N, and CARTiPLEX: G0A4718N, the European Research Council under the European Union's Seventh Framework Program (FP/2007-2013)/ERC (249191) and Horizon 2020 Framework Program (H2020/2014-2021)/ERC (772418), the special research fund of the KU Leuven (GOA/13/016 and C24/17/077) and BONE Interreg North West Europe (NWE 497), European Regional Development Fund. This work was supported by the partners of Regenerative Medicine Crossing Borders (http://www.regmedxb.com). Powered by Health—Holland, and Top Sector Life Sciences & Health. The micro (or nano)-CT images were generated on the X-ray computed tomography facility of the Department of Development and Regeneration of the KU Leuven, financed by the Hercules Foundation (project AKUL/13/47). The funders had no role in study design, data collection and analysis, decision to publish, or preparation of the manuscript. This work was part of Prometheus, the KU Leuven R&D division for skeletal tissue engineering (http://www.kuleuven.be/prometheus).

4.7 Supporting Information

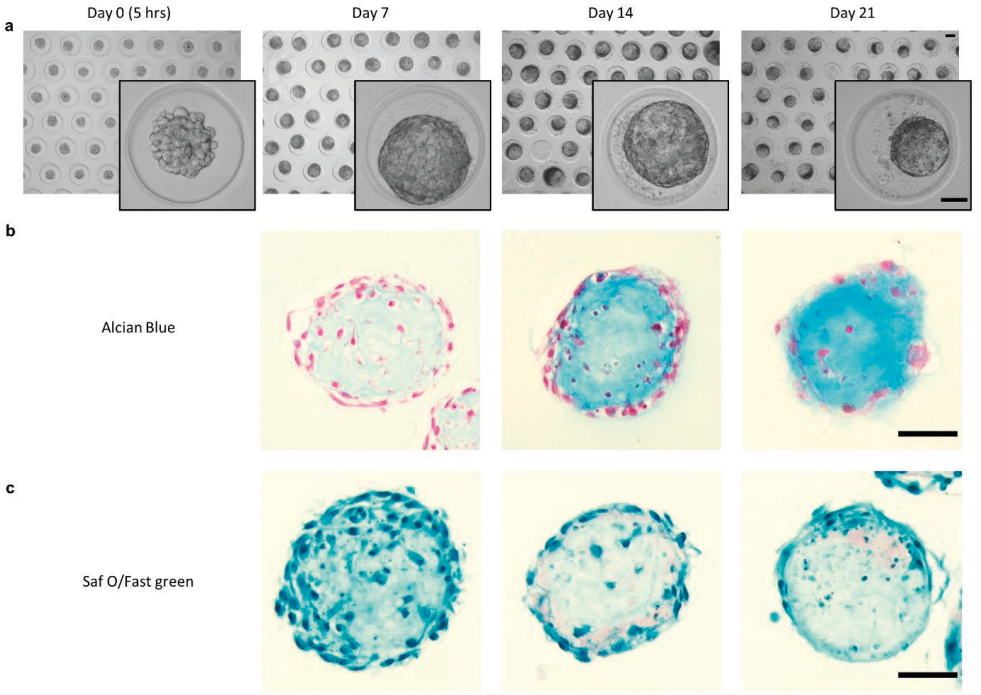

Figure S1. Formation of cartilaginous and prehypertrophic building blocks from adult hPDCs*. a) Bright field images of spheroids over time. b) Alcian blue and c) Safranin O (Saf O) staining of building block sections at day 7, 14 and 21.*

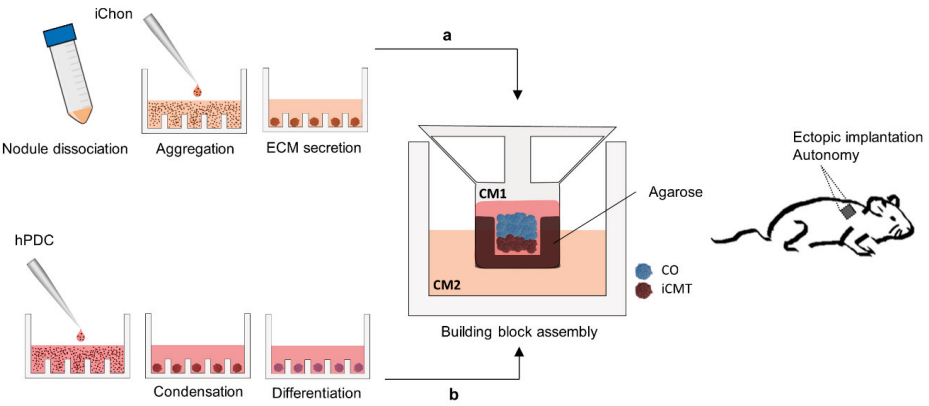

Figure S2. Schematic image of building block assembly into dual constructs. hPDC: human periosteum-derived cells, *hiChon: hiPSC-derived chondroprogenitors, CM: chondrogenic medium, COs: callus organoids, iCMTs: cartilage microtissues.*

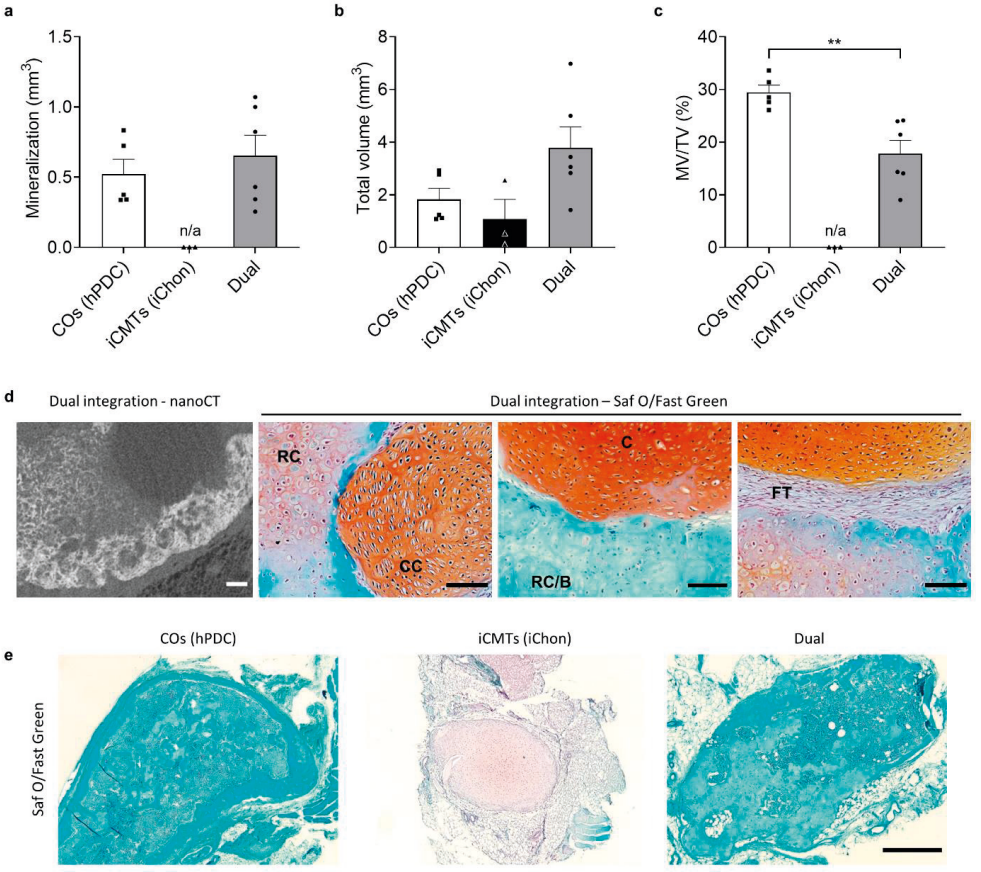

Figure S3. *NanoCT analysis after 4 weeks implantation to define a) total explant volume, b) total mineralized volume and c) percentage mineralized tissue (mineralized volume/tissue volume: MV/TV). Graphs show two individual experiments; each data point represents one sample. d) nanoCT section and Saf O/Fast Green staining of three types of dual integration detected. e) Saf O/Fast green staining of alternative in vivo outcome. COs forming full ossicle (2/5), iCMTs with weak Saf O staining (2/3) and Dual constructs without Saf O positive areas (3/6). RC: remodeling cartilage, CC: columnar chondrocytes, B: bone, FT: fibrous tissue, hiChon: hiPSC-derived chondroprogenitors, COs: callus organoids, iCMTs: cartilage microtissues.*

References

[1] T. Gorbachova, Y. Melenevsky, M. Cohen, B. W. Cerniglia, *Radiographics* **2018**, *38*, 1478.

[2] R. J. Lories, F. P. Luyten, *Nat. Rev. Rheumatol.* **2011**, *7*, 43.

[3] S. Chubinskaya, M. A. Wimmer, *Cartilage* **2013**, *4*, 13S.

[4] T. Ogura, G. Merkely, T. Bryant, C. S. Winalski, T. Minas, *Orthop. J. Sport. Med.* **2019**, *7*, 232596711984717.

[5] T. Minas, T. Ogura, J. Headrick, T. Bryant, *Am. J. Sports Med.* **2018**, *46*, 322.

[6] A. E. Gross, W. Kim, F. Las Heras, D. Backstein, O. Safir, K. P. H. Pritzker, *Clin. Orthop. Relat. Res.* **2008**, *466*, 1863.

[7] J. Visser, D. Gawlitta, K. E. M. Benders, S. M. H. Toma, B. Pouran, P. R. van Weeren, W. J. A. Dhert, J. Malda, *Biomaterials* **2015**, *37*, 174.

[8] P. Diloksumpan, M. de Ruijter, M. Castilho, U. Gbureck, T. Vermonden, P. R. van Weeren, J. Malda, R. Levato, *Biofabrication* **2020**, *12*, 025014.

[9] R. A. Vindas Bolaños, S. M. Cokelaere, J. M. Estrada McDermott, K. E. M. Benders, U. Gbureck, S. G. M. Plomp, H. Weinans, J. Groll, P. R. van Weeren, J. Malda, *Osteoarthr. Cartil.* **2017**, *25*, 413.

[10] E. J. Sheehy, T. Vinardell, C. T. Buckley, D. J. Kelly, *Acta Biomater.* **2013**, *9*, 5484.

[11] C. Stüdle, Q. Vallmajó-Martín, A. Haumer, J. Guerrero, M. Centola, A. Mehrkens, D. J. Schaefer, M. Ehrbar, A. Barbero, I. Martin, *Biomaterials* **2018**, *171*, 219.

[12] P. J. Stiers, S. Stegen, N. van Gastel, R. Van Looveren, S. Torrekens, G. Carmeliet, *J. Bone Miner. Res.* **2019**, *34*, 333.

[13] A. Lang, M. Kirchner, J. Stefanowski, M. Durst, M. C. Weber, M. Pfeiffenberger, A. Damerau, A. E. Hauser, P. Hoff, G. N. Duda, et al., *Acta Biomater.* **2019**, *86*, 171.

[14] H. Katagiri, L. F. Mendes, F. P. Luyten, *J. Tissue Eng. Regen. Med.* **2019**, *13*, 846.

[15] G. Filardo, L. Andriolo, F. Soler, M. Berruto, P. Ferrua, P. Verdonk, F. Rongieras, D. C. Crawford, *Knee Surgery, Sport. Traumatol. Arthrosc.* **2019**, *27*, 1726.

[16] P. Lenas, M. Moos, F. P. Luyten, *Tissue Eng. Part B. Rev.* **2009**, *15*, 381.

[17] P. Lenas, F. P. Luyten, *Ind. Eng. Chem. Res.* **2011**, *50*, 482.

[18] C. Scotti, E. Piccinini, H. Takizawa, A. Todorov, P. Bourgine, A. Papadimitropoulos, A. Barbero, M. G. Manz, I. Martin, *Proc. Natl. Acad. Sci. U. S. A.* **2013**, *110*, 3997.

[19] G. Nilsson Hall, L. F. Mendes, C. Gklava, L. Geris, F. P. Luyten, I. Papantoniou, *Adv. Sci.* **2020**, *7*, 1.

[20] E. Farrell, S. K. Both, K. I. Odörfer, W. Koevoet, N. Kops, F. J. O'Brien, R. J. B. De Jong, J. A. Verhaar, V. Cuijpers, J. Jansen, et al., *BMC Musculoskelet. Disord.* **2011**, *12*, 31.

[21] L. F. Mendes, H. Katagiri, W. L. Tam, Y. C. Chai, L. Geris, S. J. Roberts, F. P. Luyten, *Stem Cell Res. Ther.* **2018**, *9*, 1.

[22] S. Critchley, G. Cunniffe, A. O'Reilly, P. Diaz-Payno, R. Schipani, A. McAlinden, D. Withers, J. Shin, E. Alsberg, D. J. Kelly, *Tissue Eng. - Part A* **2019**, *25*, 159.

[23] I. Gadjanski, G. Vunjak-Novakovic, *Expert Opin. Biol. Ther.* **2015**, *15*, 1583.

[24] E. Kunisch, A. K. Knauf, E. Hesse, U. Freudenberg, C. Werner, F. Bothe, S. Diederichs, W. Richter, *Biofabrication* **2019**, *11*, 015001.

[25] B. K. Babur, K. Futrega, W. B. Lott, T. J. Klein, J. Cooper-White, M. R. Doran, *Cell Tissue Res.* **2015**, *361*, 755.

[26] L. Ouyang, J. P. K. Armstrong, M. Salmeron-Sanchez, M. M. Stevens, *Adv. Funct. Mater.* **2020**, *1909009*, 1.

[27] S. Bhumiratana, R. E. Eton, S. R. Oungoulian, L. Q. Wan, G. a Ateshian, G. Vunjak-Novakovic, *Proc. Natl. Acad. Sci. U. S. A.* **2014**, *111*, 6940.

[28] K. Mithoefer, T. Mcadams, R. J. Williams, P. C. Kreuz, B. R. Mandelbaum, *Am. J. Sports Med.* **2009**, *37*, 2053.

[29] S. Wakitani, M. Nawata, K. Tensho, T. Okabe, H. Machida, H. Ohgushi, *J. Tissue Eng. Regen. Med.* **2007**, *1*, 74.

[30] H. S. McCarthy, S. Roberts, *Osteoarthr. Cartil.* **2013**, *21*, 2048.

[31] A. M. Craft, J. S. Rockel, Y. Nartiss, R. A. Kandel, B. A. Alman, G. M. Keller, *Nat. Biotechnol.* **2015**, *33*, 638.
[32] A. Yamashita, M. Morioka, Y. Yahara, M. Okada, T. Kobayashi, S. Kuriyama, S. Matsuda, N. Tsumaki, *Stem cell reports* **2015**, *4*, 404.
[33] A. Yamashita, Y. Tamamura, M. Morioka, P. Karagiannis, N. Shima, N. Tsumaki, *Inflamm. Regen.* **2018**, *38*, 1.
[34] G. Kerckhofs, J. Sainz, M. Marechal, M. Wevers, T. Van de Putte, L. Geris, J. Schrooten, *Cartilage* **2013**, *5*, 55.
[35] J. J. Ng, Y. Wei, B. Zhou, J. Bernhard, S. Robinson, A. Burapachaisri, X. E. Guo, G. Vunjak-Novakovic, *Proc. Natl. Acad. Sci. U. S. A.* **2017**, *114*, 2556.
[36] M. A. Skylar-Scott, S. G. M. Uzel, L. L. Nam, J. H. Ahrens, R. L. Truby, S. Damaraju, J. A. Lewis, *Sci. Adv.* **2019**, *5*, eaaw2459.
[37] P. Occhetta, S. Pigeot, M. Rasponi, B. Dasen, A. Mehrkens, T. Ullrich, I. Kramer, S. Guth-Gundel, A. Barbero, I. Martin, *Proc. Natl. Acad. Sci. U. S. A.* **2018**, *115*, 4625.
[38] L. Ling, X. Ren, X. Cao, A. B. M. Hassan, S. Mah, P. Sathiyanathan, R. A. A. Smith, C. L. L. Tan, M. Eio, R. M. Samsonraj, et al., *Stem cell reports* **2019**, *14*, 1.
[39] R. Castro-Viñuelas, C. Sanjurjo-Rodríguez, M. Piñeiro-Ramil, T. Hermida-Gómez, I. M. Fuentes-Boquete, F. J. de Toro-Santos, F. J. Blanco-García, S. M. Díaz-Prado, *Eur. Cells Mater.* **2018**, *36*, 96.
[40] S. Diederichs, F. A. M. Klampfleuthner, B. Moradi, W. Richter, *Front. Cell Dev. Biol.* **2019**, *7*, 270.
[41] Y. Li, L. Li, Z. N. Chen, G. Gao, R. Yao, W. Sun, *Biofabrication* **2017**, *9*, 032001.
[42] M. Schnabel, S. Marlovits, G. Eckhoff, I. Fichtel, L. Gotzen, V. Vécsei, J. Schlegel, *Osteoarthr. Cartil.* **2002**, *10*, 62.
[43] F. P. Luyten, F. Dell'Accio, C. De Bari, *Best Pract. Res. Clin. Rheumatol.* **2001**, *15*, 759.
[44] N. P. Omelyanenko, P. A. Karalkin, E. A. Bulanova, E. V. Koudan, V. A. Parfenov, S. A. Rodionov, A. D. Knyazeva, V. A. Kasyanov, I. I. Babichenko, T. Z. Chkadua, et al., *Cartilage* **2018**, DOI 10.1177/1947603518798890.
[45] Z. Lin, Z. Li, E. N. Li, X. Li, C. J. Del Duke, H. Shen, T. Hao, B. O'Donnell, B. A. Bunnell, S. B. Goodman, et al., *Front. Bioeng. Biotechnol.* **2019**, *7*, 1.
[46] S. R. Goldring, M. B. Goldring, *Nat. Rev. Rheumatol.* **2016**, *12*, 632.
[47] C. D. Hoemann, C. H. Lafantaisie-Favreau, V. Lascau-Coman, G. Chen, J. Guzmán-Morales, *J. Knee Surg.* **2012**, *25*, 085.
[48] H. Da, S. J. Jia, G. L. Meng, J. H. Cheng, W. Zhou, Z. Xiong, Y. J. Mu, J. Liu, *PLoS One* **2013**, *8*, e54838.
[49] W. D. Lee, M. B. Hurtig, R. M. Pilliar, W. L. Stanford, R. A. Kandel, *Osteoarthr. Cartil.* **2015**, *23*, 1307.
[50] I. Kiviranta, J. Jurvelin, M. Tammi, A. -M SääMäunen, H. J. Helminen, *Arthritis Rheum.* **1987**, *30*, 801.
[51] J. Ng, Y. Wei, B. Zhou, S. Bhumiratana, A. Burapachaisri, E. Guo, G. Vunjak-Novakovic, *J. Tissue Eng. Regen. Med.* **2018**, *12*, 468.
[52] H. Koike, K. Iwasawa, R. Ouchi, M. Maezawa, K. Giesbrecht, N. Saiki, A. Ferguson, M. Kimura, W. L. Thompson, J. M. Wells, et al., *Nature* **2019**, *574*, 112.
[53] P. Samal, C. van Blitterswijk, R. Truckenmüller, S. Giselbrecht, *Adv. Mater.* **2019**, *31*, DOI 10.1002/adma.201805764.
[54] G. M. De Peppo, I. Marcos-Campos, D. J. Kahler, D. Alsalman, L. Shang, G. Vunjak-Novakovic, D. Marolt, *Proc. Natl. Acad. Sci. U. S. A.* **2013**, *110*, 8680.
[55] C. Jacobsen, A. M. Craft, *Nat. Biomed. Eng.* **2019**, *3*, 504.
[56] B. Ayan, D. N. Heo, Z. Zhang, M. Dey, A. Povilianskas, C. Drapaca, I. T. Ozbolat, *Sci. Adv.* **2020**, *6*, 1.
[57] A. C. Daly, D. J. Kelly, *Biomaterials* **2019**, *197*, 194.
[58] N. V. Mekhileri, K. S. Lim, G. C. J. Brown, I. Mutreja, B. S. Schon, G. J. Hooper, T. B. F. Woodfield, *Biofabrication* **2018**, *10*, 024103.
[59] A. Di Luca, I. Lorenzo-Moldero, C. Mota, A. Lepedda, D. Auhl, C. Van Blitterswijk, L. Moroni, *Adv. Healthc. Mater.* **2016**, *5*, 1753.
[60] J. Eyckmans, S. J. Roberts, J. Schrooten, F. P. Luyten, *J. Cell. Mol. Med.* **2010**, *14*, 1845.

[61] J. Leijten, L. S. Moreira Teixeira, J. Bolander, W. Ji, B. Vanspauwen, J. Lammertyn, J. Schrooten, F. P. Luyten, *Sci. Rep.* **2016**, *6*, 1.
[62] L. F. Mendes, W. L. Tam, Y. C. Chai, L. Geris, F. P. Luyten, S. J. Roberts, *Tissue Eng. Part C Methods* **2016**, *22*, 473.
[63] T. Deckers, T. Lambrechts, S. Viazzi, G. N. Hall, I. Papantoniou, V. Bloemen, J. M. Aerts, *PLoS One* **2018**, DOI 10.1371/journal.pone.0199092.
[64] K. J. Livak, T. D. Schmittgen, *Methods* **2001**, *25*, 402.

CHAPTER 5.

Design considerations for spheroid-based implants for endochondral ossification: towards robotic-driven biomanufacturing

*Gabriella Nilsson Hall[1, 2], Iene Rutten[3], Jeroen Lammertyn[3], Jeroen Blommaert, Jens Eberhardt[4], Liesbet Geris[1, 5, 6], Frank P. Luyten[1, 2, †, *], Ioannis Papantoniou[1, 2, 7 †, *]*

* These authors share senior authorship

[1]Prometheus Division of Skeletal Tissue Engineering, KU Leuven, O&N1, Herestraat 49, PB 813, 3000 Leuven, Belgium. [2]Skeletal Biology and Engineering Research Center, Department of Development and Regeneration, KU Leuven, O&N1, Herestraat 49, PB 813, 3000 Leuven, Belgium. [3] Department of Biosystems, KU Leuven, Willem de Croylaan 42, Box 2428, 3001, Leuven, Belgium. [4]ALS automated lab solutions, Jena, Germany. [5]GIGA in silico medicine, Université de Liège, Avenue de l'Hôpital 11 – BAT 34, 4000 Liège 1, Belgium. [6]Biomechanics Section, KU Leuven, Celestijnenlaan 300C, PB 2419, 3001 Leuven, Belgium. [7]Institute of Chemical Engineering Sciences, Foundation for Research and Technology-Hellas, Stadiou 26504, Platani, Patras, Greece

Manuscript in preparation

Abstract

Modular tissue engineering strategies using microspheroids as building blocks are currently gaining momentum for biofabrication of tissues and organs. Direct or gradual assembly of microspheroids generates opportunities to fabricate scalable and complex tissues. In this work, assembly of cartilaginous micropsheroids for endochondral bone formation was studied to outline relevant design considerations for a scaffold-free modular approach. Fusion capacity of two or thousands of assembled microspheroids as well as individual microspheroid spreading capacity decreased with increased maturity. Module assembly followed by *in vitro* culture resulted in the formation of non-differentiated central regions if the final size/thickness was not limited to ≤ 1 mm. Four weeks implantation of constructs assembled at different time-points but with a total culture time of 3 weeks, resulted in bone formation independent on the time of assembly. Finally, a robotics driven biomanufacturing method for image-guided spheroid aspiration and deposition was described demonstrating a prospect for automated manufacturing of spheroid-based implants.

5.1 Introduction

During recent years, modular tissue engineering strategies through the use of scaffold-free building blocks have emerged as a novel paradigm for engineering functional tissue implants [1,2]. Different building block configurations have been explored, such as cell sheets [3], tissue strands [4] and spheroids [5]. Formation of these cellular structures is based on the capacity of cells to aggregate into dense structures allowing them to undergo crucial biological events such as condensation followed by extracellular matrix (ECM) production forming a native-like microenvironment [2]. Through controlled differentiation, these living building blocks mature *in vitro* into microtissues and organoids which resemble native organs, also after assembly [6,7]. Additionally, cellular spheroids can be integrated via hybrid biofabrication strategies with printed scaffolds [8,9] or used in scaffold-free tissue implants following bottom-up strategies [10]. For the scaffold-free case, the innate self-assembly properties of three-dimensional spheroids can be used to increase tissue size in a stepwise manner from microspheroid to mesotissue to final macrotissue [11]. Through this strategy, complex shapes can be produced by assembly of microspheroids as building blocks in prefabricated non-adherent molds [12–14]. Formation of smaller building blocks followed by direct or gradual assembly generates opportunities to fabricate scalable complex tissues [15,16].

Even though microtissues and organoids may function as mini-organs it is not obvious how the fusion process may affect tissue functionality upon assembly. Therefore, the use of microtissues and organoids as "raw biological material" requires dedicated studies providing further insights and defined parameters on the events occurring during spheroid assembly. These parameters should support the decision of spheroid preculture time before assembly or combination with a scaffold [2,10]. Previous studies demonstrated that spheroid fusion kinetics depends on cell type (*e.g.* human chondrocytes or human breast cancer cells), disturbance in their cytoskeleton [17], preculture time in spheroid format [14] and number of cells per spheroid [18]. For example, spheres of sheep articular chondrocytes fused slower if matured longer individually before fusion [19]. Furthermore, the degree of matrix integration between the building blocks was shown to be affected by the time human bone marrow derived stromal cells (hBMSC) were cultured as spheroids in chondrogenic media before assembly [20].

Typically, the size of spheroids ranges from 100-300 µm operating in dimensions that prevent the presence of detrimental diffusion limitations during lengthy differentiation protocols [3–5]. We recently demonstrated that by employing 100 µm sized "callus organoid" bioassemblies, it

was possible to obtain bone organs upon implantation at ectopic and orthotopic sites in a murine model. During spheroid differentiation, progressive formation and maturation of cartilaginous extracellular matrix (ECM) was observed with cells reaching a prehypertrophic phenotype after 21 days in culture [7].

In this study, we explored the assembly of cartilaginous spheroids derived from human periosteum-derived cells (hPDCs) to investigate the influence of spheroid fusion on the final tissue outcome in terms of time (how early is the fusion occurring) and in terms of dimension (how large can a mesotissue become using this strategy). We provide information on two key events that might dictate how subsequent biofabrication strategies can be tailored around this paradigm. Finally, we provide proof-of-concept on the feasibility of image-driven robotics biomanufacturing of such implants.

5.2 Results

5.2.1 Microspheroids form cartilaginous microtissues

Human periosteum-derived cells (hPDCs) were seeded onto non-adherent microwells (200µm Ø), leading to cell-cell attachment, aggregation and subsequent condensation. Chondrogenic differentiation was induced for 21 days to reach a pre-hypertrophic state as previously reported [7]. Microspheroids were formed after one day in culture, although single cells were still discernible on the spheroid-surface (**figure 1A**). Over time, the spheroid surface became more even, eliminating visible single cells. The spheroids grew slightly in size until day 14 (based on projection diameter) where after a decrease in size was monitored at day 21 (**figure 1B**). RNA-sequencing analysis of spheroids over time, previously reported by us [7], demonstrated up-regulation of chondrogenic transcription factors (TFs) (*SOX5*, *6* and *9*) day 14 and day 21 and hypertrophic TFs distinctly up-regulated day 21 (*RUNX3* and *MEF2C*) (**figure 1C**) [26]. Genes which encode collagens related to chondrogenesis (*COL2A1, COL9A1*) and more mature tissues (*COL10A1*) were significantly up-regulated day 21. Furthermore, matrix regulators (DMP1, *SPP1* and *IBSP*) associated with hypertrophic chondrocytes and osteogenic cells were up-regulated from day 14 and 21 (**figure 1C**). Alcian blue staining, specific for glycosaminoglycan-rich extracellular matrix (ECM) demonstrated an expected increase in ECM overtime (**figure 1D**). These data indicated gradual maturation of microspheroids into microtissues and callus organoids through both hypertrophic chondrocyte and osteogenic differentiation as described previously [7]. The gradual maturation allowed analysis of

spheroids consisting of only cells (day 1 microspheroids), combination of cells and ECM (day 7-14 microtissue) and with abundant ECM (day 21 "callus organoids"). From here on in the results, all stages of spheroids will be described as spheroids.

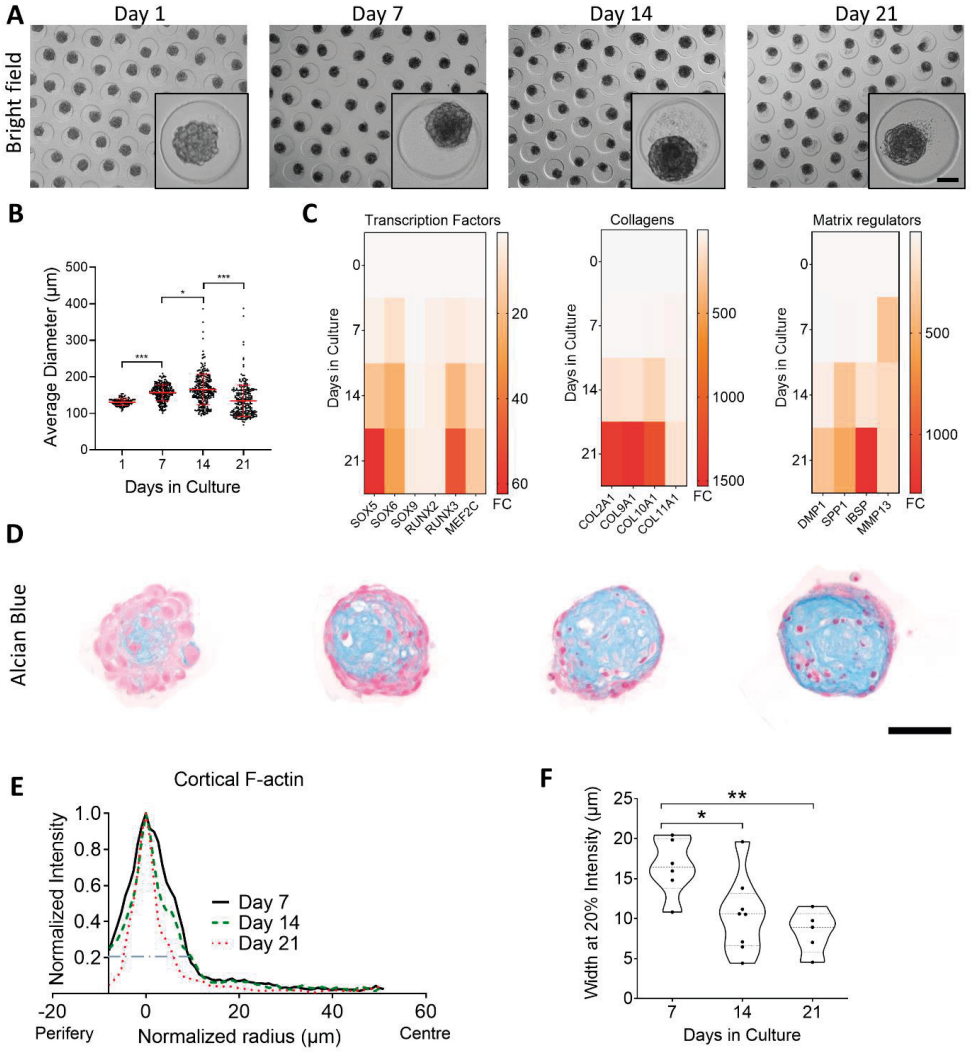

Figure 5.1. Chondrogenic maturation of cellular building-blocks. *(A) Bright field images of spheroids over time. (B) Average spheroid diameter over time. Each data point represents individual spheroids, data pooled from four individual experiments, red bars show mean ± SD. (C) Heat map demonstrating fold-change transcription of chondrogenic and hypertrophic biomarkers (average of triplicates). (D) Histological sections of spheroids stained with alcian blue. (E) Average normalized intensity of phalloidin (F-actin) confocal images. (F) Width of normalized phalloidin intensity at 20% of maximal intensity. Graph show violin plot with median and quartiles, each data point represent one spheroid. Scale bars represent 50 µm.*

To better define the change in spheroid surface over time that was detected with brightfield images, the cortical F-actin thickness was quantified for day 7, 14 and 21 spheroids (**figure 1E**). Day 1 spheroids were excluded since single cells were clearly present on the spheroid surface and no distinct cortical spheroid actin was present. A significantly thinner F-actin layer was detected between day 7 and 14 spheroids as well as between day7 and day 21 (**figure 1F**).

5.2.2 Fusion and spreading capacity of cartilaginous spheroids is affected by time in culture

To assess the fusion capacity of chondrogenic spheroids, spheroids from each maturation stage (day 1, 7, 14 and 21) were dually assembled in agarose wells (400 μm in diameter). Attachment between all modules was detected after 1 hour where after they gradually fused to form close to spherical or oval shapes (**figure 2A**). Day 1 modules fused into a round sphere while day 21 modules resulted in an oval shape after 24 hours of fusion. Viability staining demonstrated viable cells and that the dead cells were dispersed, hence indicating absence of necrotic cores within the fused spheroids (supplementary figure S1A). The fusion kinetics were defined by measuring the aspect ratio (AR) of the major and minor axis (**figure 2B**) and no significant difference in AR was detected between day 1, 7 and 14 modules. Nevertheless, day 1 modules continued to fuse towards a sphere after 15 hours while day 7 and 14 modules attained a steady state after approximately 15 hours (**figure 2C**). Interestingly, day 21 modules fused with a slower rate and reached a steady state even before forming a sphere demonstrating a significant difference after 20 hours fusion as compared to day 1 spheroid duplets (**figure 2D**). The normalized duplet length after 20 hours further indicated a significant difference between day 1 and 7 modules (**supplementary figure S1B**).

Moreover, alcian blue staining, specific for glycosaminoglycan rich ECM, revealed interior differences between fusions of different time-points (**figure 2E**). The two day 1 modules were barely visible after 24 hours fusion while two different cores were clearly noticeable for day 7 and 14 modules and even more distinct in day 21 fusions. Sirius Red staining, specific for collagen fibers, demonstrated gradual collagen fiber maturation over time with two distinct module cores present already for day 7 modules (**figure 2F** and **supplementary figure S1C**). Although bright field images showed a close to spherical state after 24 hours for day 1, 7 and 14 modules (**figure 2A**), the histological staining reveals that the mature ECM of the two modules was not fully fused (**figure 2E-F**). These data conclude that the chondrogenic maturation affect their fusion kinetics and 21 days of maturation seem to delay fusion significantly although the modules were still attached to each other to form one tissue.

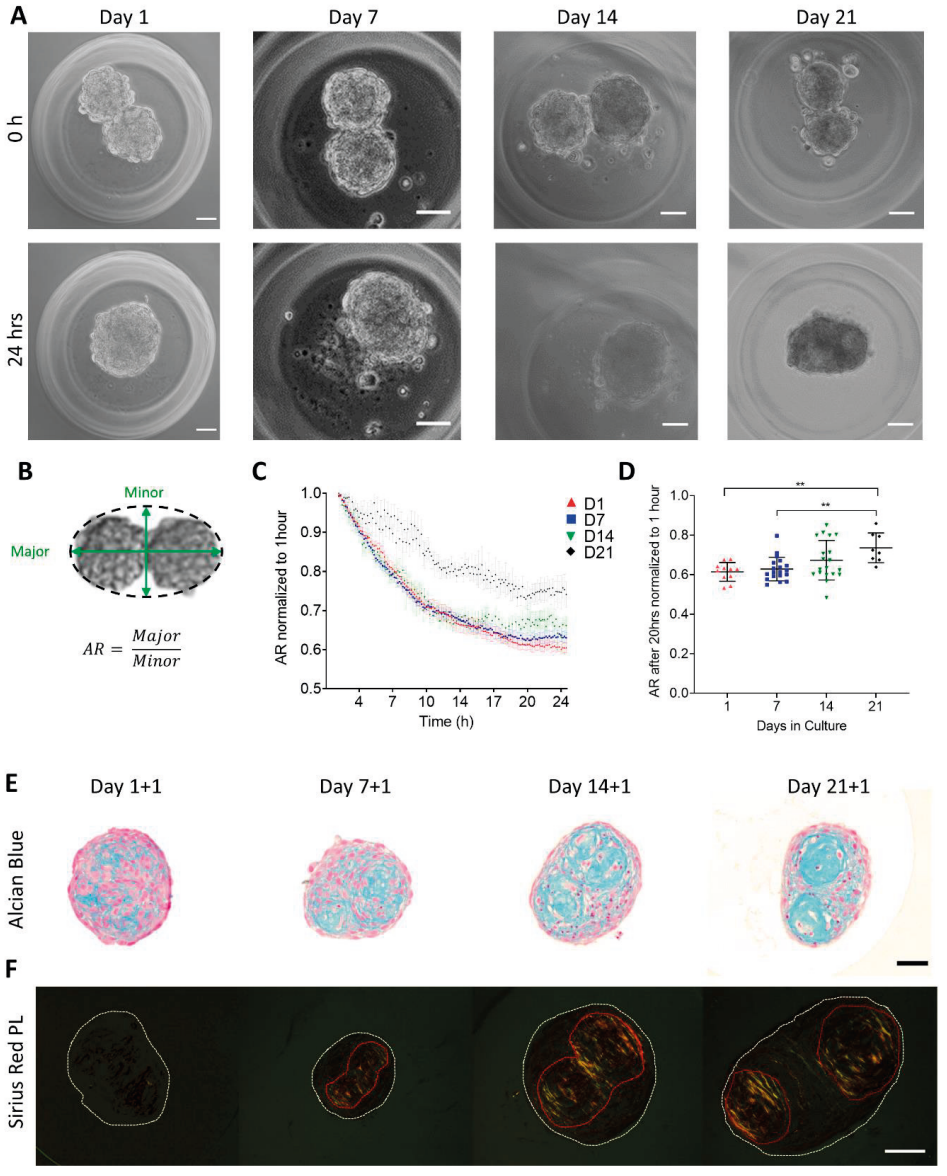

Figure 5.2. Dual fusion of building-blocks with different maturity*. (A) Representative bright field images after 1 and 24 hours of fusion of spheroids cultures in chondrogenic media for 1, 7, 14 or 21 days. (B) The aspect ratio was calculated as major/minor length of duplets. (C) Aspect ratio (AR) normalized to 1 hour quantified over 24 hours. Graph show average ± SEM of 8-19 spheroids per condition, pooled from two individual experiments. (D) Aspect ratio after 20 hours of fusion normalized to 1 hour. Each data point represents individual spheroids, data pooled from two individual experiments, mean ± SD. (E) Alcian blue staining of spheroids fused for 24 hours. (F) Picrosirius red staining of spheroids fused for 24 hours, visualized under polarized light. Scale bars represent 50 μm.*

An important driving force during fusion of cellular spheroids is the capacity of cells to attach and migrate in between the modules. Additionally, cell contractility is expected to have an impact and the culture media used in this study contained the Rho kinase inhibitor Y27632 which suppress cytoskeletal rearrangements [30]. Absence of Y27632 in the culture media resulted in a larger AR after 20 hours fusion of small spheroids (100 cells) indicating decreased fusion capacity (supplementary figure S1D). All other experiments were performed with addition of Y27632. Next, the area of cells able to migrate out from the modules was characterized with a spreading assay. Spheroids of different maturity were seeded onto a cell adherent surface and imaged after 20 hours to quantify the area that cells had spread from the initial spheroid (**figure 3A**). The spreading area as compared to initial spheroid size was calculated to quantify the spread. As expected, day 1 spheroids exhibited largest spread area with more than 27-fold increase in area compared to their initial projection area (**figure 3B**). The spreading capacity decreased over time with 16-, 8- and 5-fold spread area for day 7, 14 and 21 spheroids respectively. This would be expected since the spheroids day 7-21 contain a higher amount of ECM as compared to day 1. To address changes with regard to cellular migration, the maximum displacement rate over the 20 hrs of spreading was calculated (**figure 3C**). A continuous decrease in maximum displacement rate was detected for the following weeks. Taken together, the spreading assay demonstrates that the capacity of cells to spread from spheroids decrease over time in culture.

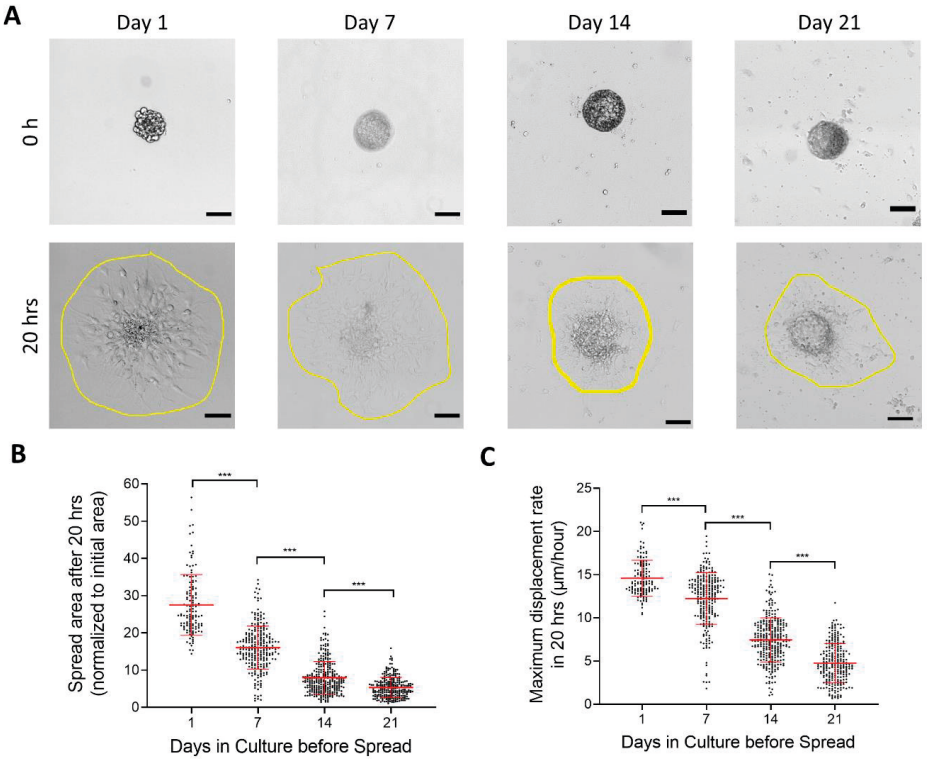

Figure 5.3. Spreading assay on adherent surface. *(A) Representative bright field images of spheroids cultures in chondrogenic media for 1, 7, 14 or 21 days followed by spreading on an adherent surface for 20 hours. The yellow rings represent quantified spread area. (B) Quantified spread area after 20 hours normalized to 0 hours. (C) Maximum displacement rate defined from the widest spread after 20 hours. Each data point represents individual spheroids, data pooled from four individual experiments, red bars show mean ± SD. Scale bars represent 50 µm.*

5.2.3 Time-of-assembly to direct mesotissue formation

Previous data demonstrated that spheroid maturation affects both fusion and spreading kinetics and that more mature modules fuse and spread slower (**figure 2-3**). These data indicate that the time of module assembly also will affect the characteristics of a final construct or mesotissue. To study this, thousands of spheroids (~2000) were assembled after 1, 7 or 14 days in 24-well plates covered with agarose (**supplementary figure S1E** and **S2A**). However, limited assembly was observed with a gradual decrease in fusion capacity from day 1, 7 to 14 modules after 1 week of fusion (**supplementary figure S2B**). To confine spheroids and promote active contact during post-culture until day 22, a smaller non-adherent agarose well (2mm in diameter) was constructed (**figure 4A** and **supplementary figure S2C**).

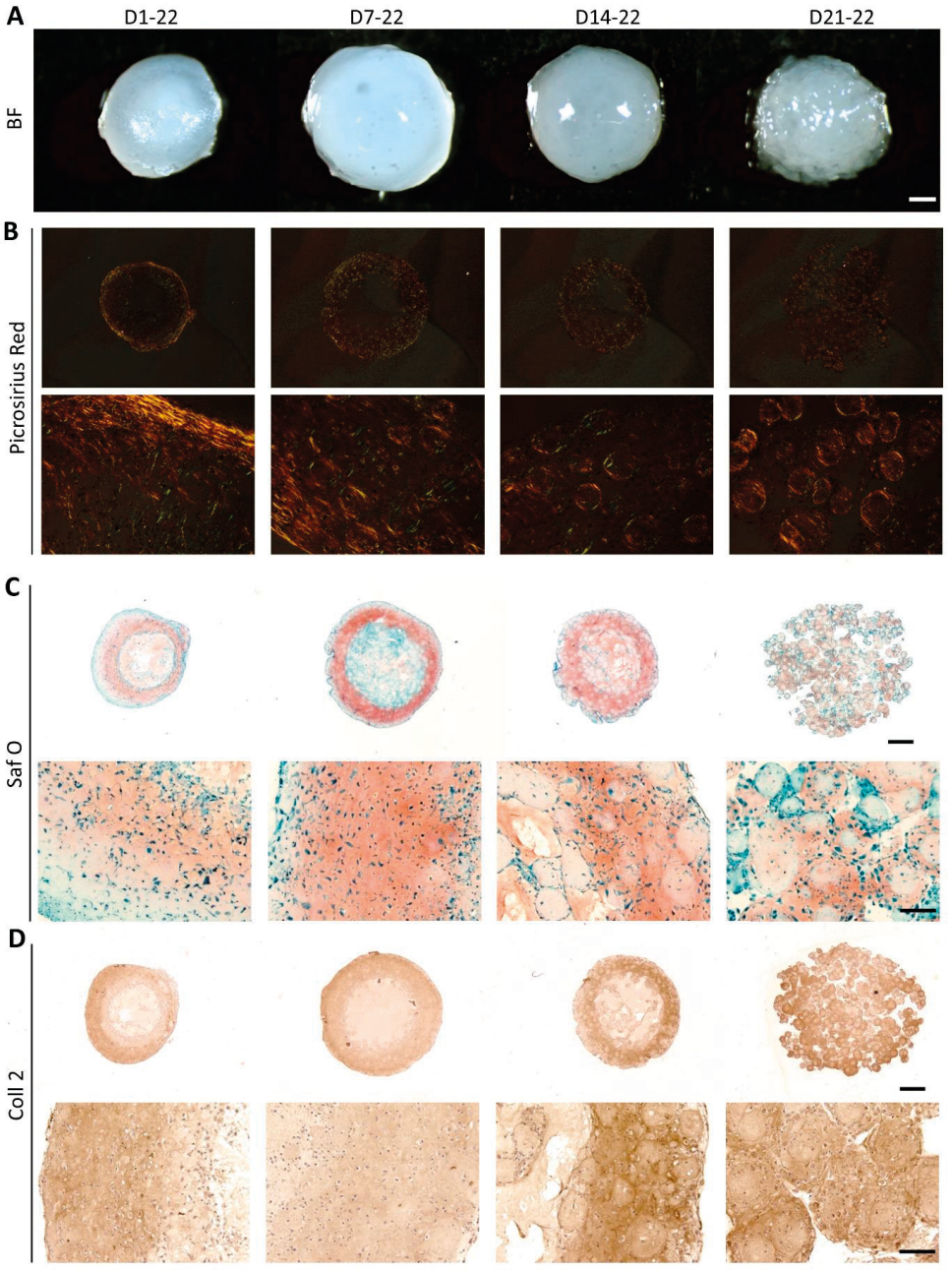

Figure 5.4. Assembly of building-blocks of different chondrogenic maturity into mesotissues with a total culture time of 22 days. *Condition titles define fusion time. (A) Bright field image of each mesotissue at day 22. (B) Picrosirius red staining of mesotissues on day 22, visualized under polarized light. (C) Safranin O and (D) collagen type 2 (Coll 2) immunostaining of mesotissues at day 22. Scale bars represent 500 µm and 100 µm.*

Polarized light of Sirius Red staining demonstrated a cortical collagen layer aligning the surface of D1-22 mesotissues and no spheroid shapes were detected within the constructs (**figure 4B**). In contrary, spheroid shaped patterns were seen at the border of D7- and D14-22 constructs, indicating limited spheroid fusion as depicted in the spreading assay. No or limited amount of collagen fibers were detected in the center of the D1-, D7- and D14-22 constructs while spheroid shaped collagen fibers were present throughout the D21-22 construct.

Safranin O staining (**figure 4B**) revealed a sGAG rich periphery with absence of or limited safranin O positive area in the center for the D1-, D7-, and D14-22 and Collagen type 2 (Coll 2) immunostaining demonstrated the same patterns (**figure 4C**). This indicates lack of differentiation, probably because of diffusion limitations and no significant difference in the thickness of the safranin O positive areas of D1-, D7- nor D14-22 constructs (456, 564 and 487 µm respectively, **Supplementary figure S2F**), was detected. In contrast, D21-22 constructs were fused only 1 day and had safranin O positive area distributed throughout. These data depict that the constructs were too large for homogenous differentiation during long-term *in vitro* culture. The quantification of safranin O positive area resulted in an average thickness of 492 ± 92 µm for all samples, hence a mesotissue diameter of approximately 1 mm would be expected to allow differentiation throughout the constructs.

To avoid the consequences of diffusion limitations, smaller mesotissues (~ 1000 spheroids / construct) were prepared (**figure 5A**). This resulted in mesotissues with an average diameter between 1.3-1.9 mm and average thickness of 0.78-0.96 mm (**figure 5B-C**). Histological staining showed safranin O positive staining throughout the majority of the construct confirming that diffusion limitations were restricted (**figure 5D**). D1-22, D7-22 and D21-22 constructs were implanted ectopically which resulted in mineralization and bone formation after four weeks *in vivo* (**figure 5E-F**).

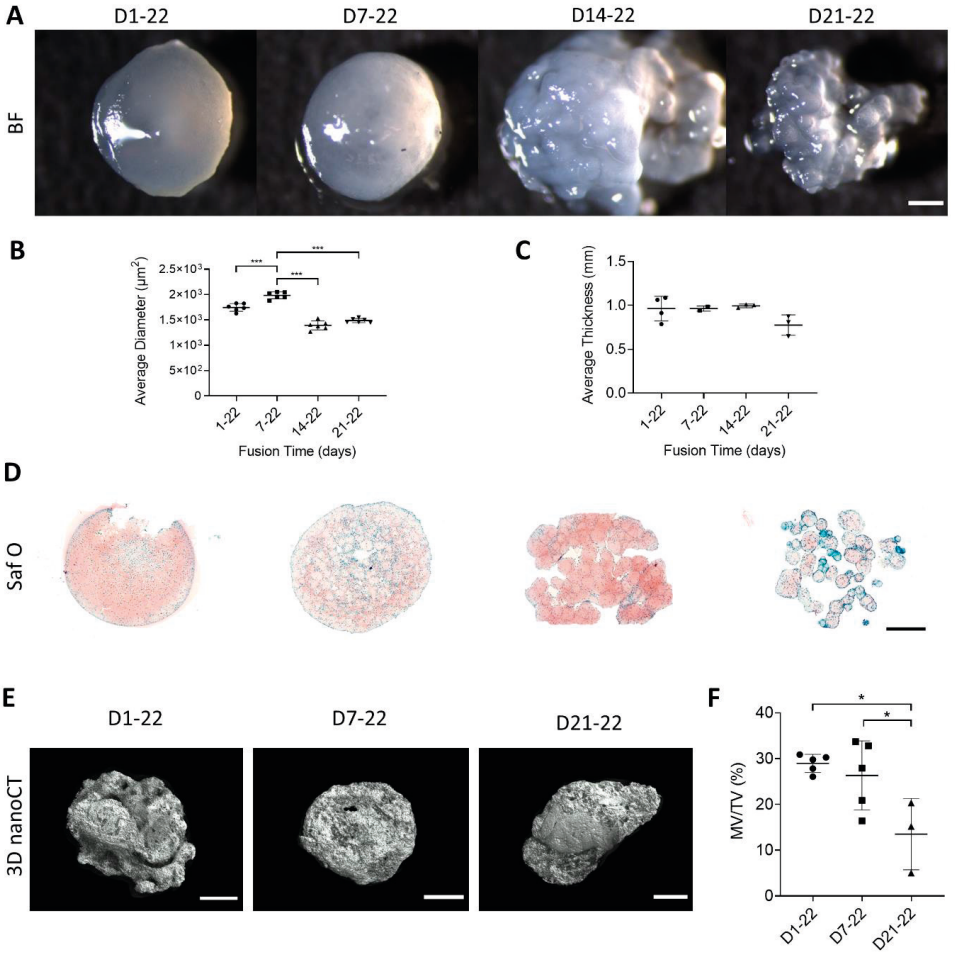

Figure 5.5. Assembly of building-blocks of different chondrogenic maturity into mesotissues without necrotic core. *(A) Bright field image of each mesotissue at day 22. Quantification of the mesotissue (B) diameter and (C) thickness. Each data point represents one mesotissue from one experiment, lines depicts mean ± SD. (D) Safranin O staining of mesotissues at day 22. (E) 3D rendering of nanoCT images of explants after 4 weeks implantation. (F) nanoCT quantification of mineralized volume (MV) normalized to tissue volume (TV). Each data point represents one explant, data pooled from two individual experiments, lines depicts mean ± SD. Scale bars represent 500 µm.*

5.2.4 Image-driven robotic spheroid assembly

The method for spheroid assembly, that was described above, comprised manual bulk pipetting of thousands of modules simultaneously resulting in fusion of modules with varying characteristics. To allow automation and controlled assembly, the automated aspiration system CellCelector™ [27] was applied to select and transfer spheroids in a controlled manner (**figure 6A and supplementary figure S3A**). Overview bright field pictures were captured over the agarose microwell inserts and spheroids were manually selected with the software to be aspirated (**figure 6B and supplementary figure 3C-E**). Next, aspirated spheroids were deposited in a defined receiver microwell (**figure 6C**). Parameters for each spheroid were logged to identify source well, position, shape characteristic and size allowing characterization of *e.g.* projection area of each individual spheroid as well as the whole spheroid population (**figure 6D, Supplementary figure 3F**). Based on the spheroid identification and characterization, a programmed selection of microwells containing only one spheroid ("singlets") was done to avoid picking doublets (**figure 6E**). Fluorescent imaging further enabled evaluation of viability for each spheroid (**figure 6F**). The presented robotic setup demonstrated high throughput characterization of spheroids which were designated based on defined parameters (*e.g.* shape, size, viability) for selective picking and deposition in a pre-defined receiver well.

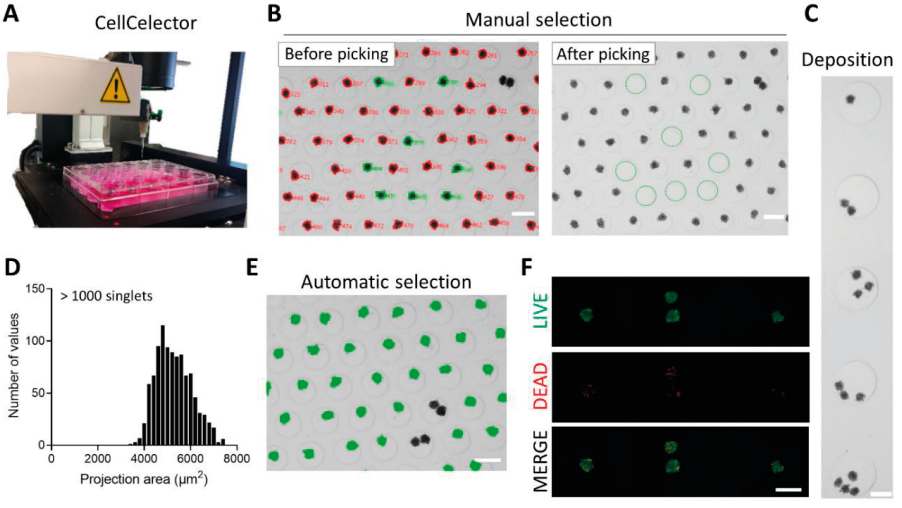

Figure 5.6. Image-driven robotic spheroid handling. *(A) CellCelector™ setup with 24 well plate containing micro-wells with cellular spheroids. (B) Individual spheroids were manually selected in the software (green) and selectively picked by aspiration. (C) Spheroids deposited in a specific microwell of another 24wp well. (D) Distribution of spheroid projection area quantified in software. (E) Single spheroids were selected (green) based on shape characteristics. (F) Viability staining of spheroids. Scale bars represent B and E: 200 µm; F and C: 100 µm.*

5.3 Discussion

In this study, we investigated the influence and limitations of bottom-up strategies for engineering modular spheroid-based cartilaginous implants for endochondral ossification. This approach holds great promise from both a biological perspective, as it provides a robust mechanism of action [7,28], but also from the manufacturing perspective as it allows scalability and precision to be inbuilt in the final product. Finally, we provided evidence for the capacity to adopt fully automated bioprocesses tailored for the range of tissue dimensions investigated in this approach.

5.3.1 Cartilaginous Spheroid fusion potential

We observed that the fusion capacity of cartilaginous spheroids decreased with increased maturation *in vitro* time. This was seen across scale with the aspect ratio of doublet spheroids as well as for assembly of thousands of spheroids (**figure 2** and **Supplementary figure 2B**). We attribute this to two reasons. (i) First, increased amounts of ECM per spheroid could contribute to this phenomenon and a decrease in fusion capacity correlated with increasing accumulation of ECM has previously been shown in a study of fusing spheroids from sheep articular chondrocytes [19]. Interestingly, in our study, apart from the day 1 spheroids, it seems that when spheroid fusion was carried out between spheroids containing ECM, the spheroids distinct structure was maintained even for prolonged subsequent culture times (**figure 4B**). This data correlates with previous work which described integration of GAG-rich ECM between day 5 spheroids while fused day 7 spheroids had maintained boundaries between the spheroids [29].

(ii) Second, spheroid self-assemblies are driven by highly contractile cells found at the periphery of spheroids [30,31]. The thickness of the outer layer of cells in our study, defined by F-actin, per spheroid dropped during chondrogenic differentiation which could reflect the diminished power of fusion. We further assessed the cells capable of migrating out from spheroids by spreading of spheroids on flat adherent surface [32]. A continuous decrease in maximum displacement rate (figure 3C) with increased spheroid maturation demonstrated a comparable trend as the normalized AR from the dual fusion assay (figure 2D) and the gradual fusion capacity during fusion of thousands of spheroids (Supplementary figure S2B). Accordingly, the spreading assay could potentially serve as real-time prediction regarding the fusion capacity of differentiated cartilaginous spheroids. As described in our study and others

[33], the amount of ECM has an effect on building-block fusion but as in embryonic morphogenesis, presence of both cadherin and integrins and their communication with F-actin are also involved in tissue self-assembly [18,34–36]. Better understanding of the effect of these different parameters could be further addressed by using computational models of cellular aggregation and spheroid fusion [37].

5.3.2 Size limitations for cartilaginous templates

Spheroids sizes typically ranges from 100-300 µm in diameter to prevent the formation of detrimental diffusion limitations during lengthy differentiation protocols. We can expect two adverse outcomes related to diffusion: (i) detrimental outcomes such as increased cell apoptosis due to lack of nutrients or oxygen and (ii) inadequate cell function or presence of ECM due to local lack of proper growth and differentiation factors [38,39]. Moreover, these dimensions are highly dependent on the transient properties of differentiating cells and may vary from the type of tissue formed. In large bone marrow derived stromal cell (BMSC) spheroids, containing 60 000 cells, no hypoxic conditions were seen in the center while a hypoxic core was detected in spheroids containing at least 250 000 MSCs [40], correlating with the number of cells to create mesotissues without fibrotic cores in our study (1000 spheroids = 250 000 seeded cells) (figure 5). Regarding diffusion of growth factors, a more complex mechanism including active binding by cells through specific receptors and diffusion coefficients in cartilage can be envisioned. For BMSC-derived cartilaginous tissues, such inhomogeneities have been encountered in pellets and micromasses [7,41,42]. In our study, we defined a maximum diameter of progenitor derived cartilaginous tissue to 1000 µm that could be reached without compromising *in vitro* quality characteristics such as homogenous positivity for cartilaginous ECM markers. Homogeneous differentiation is of importance since it has been reported that domains that are not positive of cartilaginous markers do not participate in the bone forming process leading to the presence of fibrous tissue structures [7,28]. Further studies should be done to elucidate if the fusion process itself affects chondrogenic differentiation [43]. However, we observed that using the aforementioned design specifications, fused cartilage intermediate structures were able to form mineralized tissues upon implantation independently of their culture and fusion prehistory.

5.3.3 Image-driven robotic biomanufacturing

For a viable and compliant clinical translation of cell-based products, the adoption of automated technologies has been acknowledged as a prerequisite [44]. Given the high promise

of the recent *in vivo* outcomes observed through endochondral ossification, biomanufacturing technologies able to handle these tissue building blocks are required. Extrusion-based bioprinting [45–47] can be employed, however results to date indicate that structures with low cellular densities are obtained through this methodology while only low control over spheroid deposition can be achieved. A further disadvantage described for this approach is nozzle clogging when spheroids are bioprinted [11]. Robotics approaches such as the "Kenzan" method [48], and "biogripper" [49,50] have been explored for scaffold-free handling of spheroids. However, the "Kenzan" method requires homogenous spheroid sizes to enable proper fit onto the needle array [48] while the "biogripper" is developed to handle larger building blocks (600 – 3400 μm) [49,50]. Moreover, the existing techniques described to date suffered from the positional accuracy of spheroid deposition. Ayan *et. al.* recently demonstrated the use of aspiration for pick-up and positioning of spheroids [15]. While this enabled gentle manipulation of spheroids, it was performed in a semi-automated fashion. We demonstrated successful image-driven picking of spheroids through aspiration with an automated single cell and colony picking system [27]. Image analysis allowed precise selection of spheroids for picking followed by transfer into a designated microwell. Further application of automated picking systems for module-based tissue engineering will permit creation of complex tissues with both automation and precision.

5.4 Conclusion

We explored the design limitations of a scaffold-free, bottom-up biofabrication strategy in the context of endochondral ossification using cartilaginous spheroids. Design considerations related to the fusion of spheroids at different maturation degrees was investigated with regard to capacity and assembly time-point. Fusion and spreading capacity of spheroids decreased with prolonged differentiation time and a maximum *in vitro* tissue size was defined to 1 mm, independent on time of assembly. Additionally, bone formation *in vivo* was observed independent on the time of assembly. Finally, a robotics driven biomanufacturing method for image-guided spheroid aspiration and deposition was described illustrating a way forward for fully automated manufacturing of spheroid-based implants.

5.5 Materials and methods

Cell expansion: Periosteal biopsies from nine donors were digested for cell isolation and two cell pools were created (29 ± 12 and 14 ± 3 years old) as previously described [21]. Briefly,

the periosteal biopsies were washed and digested in type IV collagenase (440 units/mg, Invitrogen, BE) in growth medium (high-glucose Dulbecco's modified Eagle's medium (DMEM, Invitrogen, BE) supplemented with 10% fetal bovine serum (FBS, Hyclone), and an antibiotic–antimycotic solution (100 µg/ml streptomycin, 100 units/ml penicillin and 0.25 µg/ml amphotericin B, Invitrogen, BE). Next, the digested cells having similar growth kinetics and bone formation capacity were pooled together to create a cell pool. The cell pool was expanded until passage 9 in growth medium at 37℃, 5% CO_2 and 95% humidity. Growth medium was changed three times per week until 90% confluency when the cells were harvested with TrypLE™ Express (Life Technologies, UK). All procedures were approved by the ethical committee for Human Medical Research (Katholieke Universiteit Leuven) and patients' informed consent forms were obtained (ML7861).

Microspheroid formation: Microwells were created in 3% UltraPure™ agarose (Thermo Fisher) as described elsewhere [22]. 500 000 cells were seeded per well containing 2000 microwells resulting in microspheroids with approximately 250 cells/spheroid. Microspheroids were differentiated towards microtissues in a chemically defined chondrogenic medium (CM) composed of LG-DMEM (Gibco) supplemented with 1% antibiotic-antimycotic (100units/mL penicillin, 100mg/mL streptomycin and 0.25mg/mL amphotericin B), 1 mM ascorbate-2 phosphate, 100 nM dexamethasone, 40 µg/mL proline, 20 µM of Rho-kinase inhibitor Y27632 (Axon Medchem), ITS+ Premix Universal Culture Supplement (Corning) (including 6.25 µg/mL insulin, 6.25 µg/mL transferrin, 6.25 µg/mL selenious acid, 1.25 µg/mL bovine serum albumin (BSA), and 5.35 µg/mL linoleic acid), 100 ng/mL BMP-2 (INDUCTOS®), 100 ng/mL GDF5 (PeproTech), 10 ng/mL TGFβ1 (PeproTech), 1 ng/mL BMP-6 (PeproTech) and 0.2 ng/mL FGF-2 (R&D systems) [23]. Half of the media was carefully exchanged every 3-4 days.

Confocal imaging and semi quantification of f-actin: Spheroids were flushed out from their microwells and fixed in 4% paraformaldehyde (PFA) for 1 hour at room temperature. Next, cell nuclei and filamentous actin (F-actin) were stained with 2.5 µg/mL 4′,6-diamidino-2-phenylindole (DAPI) (Invitrogen) and 0.8U/mL Alexa Fluor 488® phalloidin (Invitrogen) during 1 hour at room temperature. Stained spheroids were imaged with an inverted laser scanning fluorescence confocal microscope ZEISS LSM 510 META (Cell imaging core facility of KU Leuven) with 1 µm thick slices using an argon ion 488 nm and MaiTai® laser.

Dual fusion and spreading assay: Dual spheroid fusion was performed in MicroTissues® 3D Petri Dish® (Sigma-Aldrich, BE) for 12-well plate. The manufacturer's instructions were

followed to create 256 agarose microwells with 400 µm diameter and 800 µm depth. Next, approximately 500 microspheroids were seeded into the 12-well plate that was placed in a well-plate incubator for imaging [24]. Microwells containing two microspheroids were selected and imaged (10x magnification) for 24 hours taking one picture every 10 minutes. The projection area and Aspect Ratio of the fusing spheroids of each frame was quantified using "Find edges" and "Analyze Particles" in ImageJ [25].

Spheroids of different maturity (1, 7, 14 or 21 days) were flushed out and 2 mL fresh CM was added. Next, the spheroid suspension was distributed in adherent 12 well plate (1mL per well) and placed in a Live cell monitoring system (LiMSy) including a microscope and well plate incubator (OKOlab Top Stage Incubator) as described elsewhere [24]. The microspheroids were imaged with a SC30 Colour Camera (Olympus) and 10x magnification during 20 hours. The first time-point was used to define the projection area of the microspheroids using Thresholding and "Analyzing Particles" in ImageJ while the 20 hours' time-point was used to quantify the spreading area using manual drawing and the ROI manager in ImageJ [25]. The spreading capacity was defined as the fold change of the area after 20 hrs divided by initial microspheroid projection area and the maximum displacement rate in 20 hours (µm/hour) was calculated according to $\frac{major(20hrs)\mu m - major(0hrs)\mu m}{2}/20hrs$.

Multifusion of microspheroids into pellets: Macrowells with a diameter of 2 mm were produced in-house with 3% UltraPure™ agarose (Thermo Fisher) and sterilized under UV. Approximately 2000 or 1000 microspheroids of 1-, 7-, 14- or 21-days maturity were pipetted into the macro-well with 40 uL of CM, let to sediment for 30 minutes at 37°C where after 1mL CM was added. Half of the media was changed every 3-4 days until a total culture time of 22 days.

In vivo implantation and quantification of mineralized tissue: The construct's autonomy to form bone tissue was evaluated with a subcutaneous mice model. Pellets (1000 fused microtissues per pellet) were implanted subcutaneously in immune compromised mice (Rj:NMRInu/nu). Explants were taken out 4 weeks after implantation and fixed in 4% PFA for subsequent nano-computed tomography (nano-CT). Samples were scanned with e*x vivo* nano-CT (Pheonix Nanotom M®, GE Measurement and Control Solutions) for 3D quantification of mineralized tissue. Scans were performed at 60 kV, 140 µA and with diamond target, mode 0, 1 frame average, 0 image skip, 500ms exposure time, 2400 images and a 0.2 mm aluminum filter resulting in a voxel size of 2 µm. CTAn (Bruker micro-CT, BE) was used for image

processing and quantification of mineralized tissue based on automatic Otsu segmentation, 3D space closing and despeckle algorithm. Percentage of mineralized tissue was calculated with respect to the total explant volume (MV/TV). CTvox (Bruker micro-CT, BE) was used to create 3D visualizations of the mineralized tissue. All procedures on animal experiments were approved by the local ethical committee for Animal Research, KU Leuven and the animals were housed according to the regulations of the Animalium Leuven (KU Leuven).

Histochemistry and immunohistochemistry: After nano-CT analysis, the explants were decalcified in ethylenediaminetetraacetic acid (EDTA)/PBS (pH 7.5) for 10 days at 4˚C followed by paraffin embedding. Samples were sectioned at 5 μm for subsequent alcian blue and Safranin O staining according to previously described protocols [7]. Picrosirius red staining was performed by deparaffinization in Histo-Clear (national diagnostics, USA) and hydration followed by nuclei staining with Weigert's haematoxylin, washing in tap water, picrosirius red staining (0.1%, Sigma-Aldrich) for 1h, washed in acidified water, dehydration and mounting. The stained slides were imaged with Leica M165 FC microscope (Microsystems, BE) with bright-field and polarized light.

Statistical analysis: Statistical data was analyzed using GraphPad Prism 8 software (GraphPad Software, Inc., La Jolla, CA) and represented as mean ± S.D. if nothing else was noted. Analysis of Variance followed by Tukey post hoc test was used to find the significant differences between the means of the different groups with $p<0.05$: *, $p<0.01$: ** and $p<0.001$: ***.

5.6 Acknowledgment

F.P.L. and I.P. contributed equally to this work. Kathleen Bosmans is thanked for performing *in vivo* experiments; Inge Van Hoven for experimental assistance. Research was funded by the Research Foundation Flanders (FWO) G.N.H: 1S05116N, I.P.: 12O7916N, and CARTiPLEX: G0A4718N, the European Research Council under the European Union's Seventh Framework Program (FP/2007-2013)/ERC (249191) and Horizon 2020 Framework Program (H2020/2014-2021)/ERC (772418), the special research fund of the KU Leuven (GOA/13/016 and C24/17/077) and BONE Interreg North West Europe (NWE 497), European Regional Development Fund. This work was supported by the partners of Regenerative Medicine Crossing Borders (http://www.regmedxb.com). Powered by Health—Holland, and Top Sector Life Sciences & Health. Confocal images were recorded on a Zeiss LSM 510 and 880 – Airyscan, Cell and Tissue Imaging Cluster (CIC), Supported by Hercules AKUL/15/37_GOH1816N and FWO G.0929.15 to Pieter Vanden Berghe, KU Leuven. The micro (or nano)-CT images were generated on the X-ray computed tomography facility of the Department of Development and Regeneration of the KU Leuven, financed by the Hercules Foundation (project AKUL/13/47). The funders had no role in study design, data collection and analysis, decision to publish, or preparation of the manuscript. This work was part of Prometheus, the KU Leuven R&D division for skeletal tissue engineering (http://www.kuleuven.be/prometheus).

5.7 Author contributions

GNH, IR, JL, LG, IP and FPL designed research; GNH, IR, JB and JE performed research; IR performed fabrication of microwells; JE and GNH performed image-driven robotic experiments; GNH, JB and IP analysed data; GNH and IP wrote the manuscript draft and FPL revised the manuscript.

5.8 Supporting Information

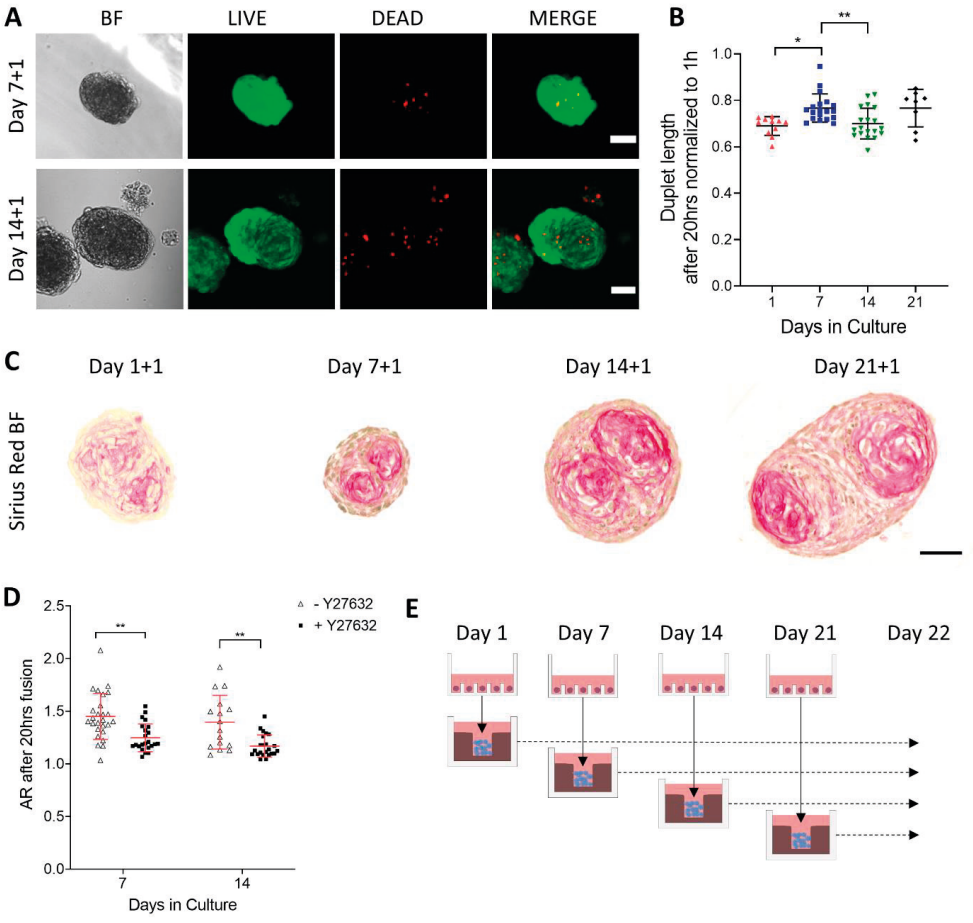

Supplementary Figure S1. *Dual fusion and assembly of spheroids with different maturation. (A) Confocal images of fused spheroids stained with LIVE/DEAD™ Viability/Cytotoxicity kit. Live cells: green (calcein-AM), dead cells: red (ethidium homodimer-1). (B) Quantification of duplet length after 20 hours normalized to 1 hour. Each data point represents individual spheroids, data pooled from two individual experiments, mean ± SD. (C) Bright field images of sections stained with Picrosirius Red staining. (D) Quantified aspect ratio (AR) after 20 hours fusion of spheroids cultured in media with + or without – Y27631. (E) Schematic illustration of spheroid assembly into mesotissues. Scale bar represents 50 µm.*

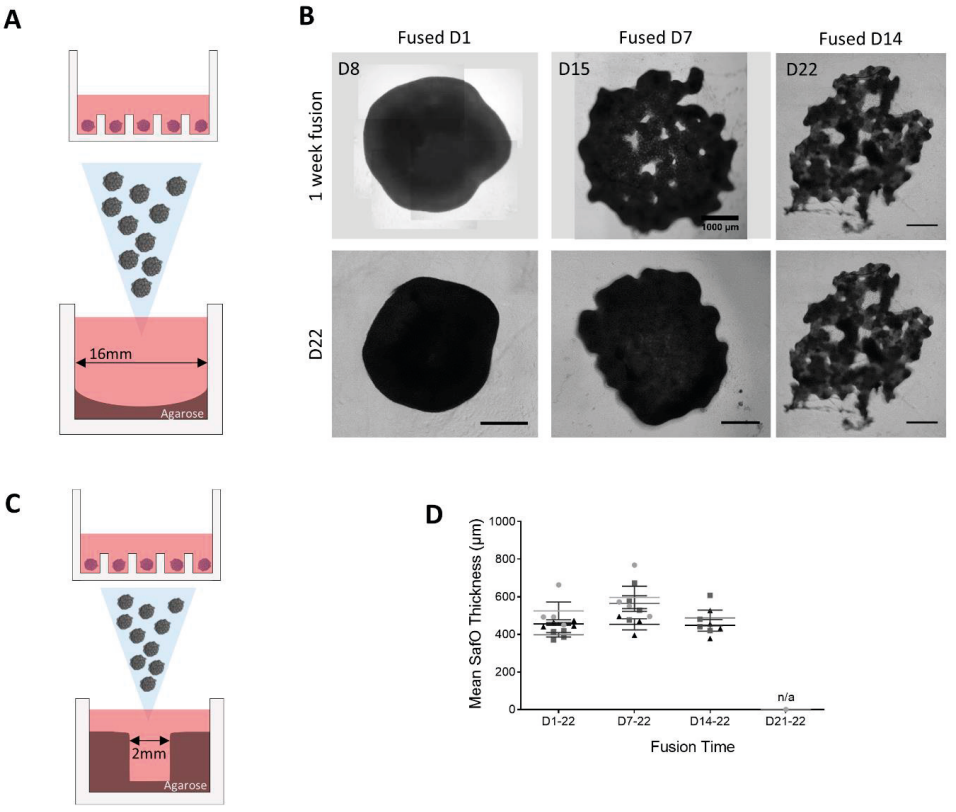

Supplementary Figure S2. *Spheroid assembly into mesotissues. (A) Spheroids were assembled into non-adherent 16mm wide surface. (B) Bright field images of mesotissues after 1 week of fusion and after a total culture time of 22 days. (C) Spheroids were assembled into non-adherent 2mm wide macrowells. (D) Quantified thickness of safranin O positive area in mesotissues fused in 2mm macrowells. Each data point represents one section. Scale bars represent 1000 µm.*

A



C

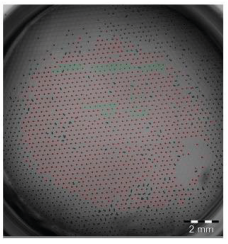

D

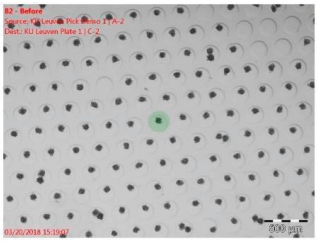

E

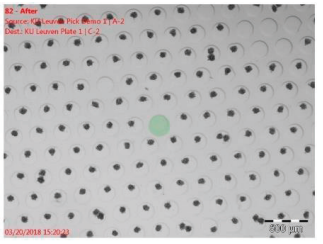

F

SourcePlate	Source Well	ID	PickStatus	DestinationWell	PickDate	Area (um^2)	Diameter (um)	Elongation	Nearest Neighbour Distance (um)	Shape Factor	ScanDate
KU Leuven Pick	A-2	94	Picked	C-2	2018/03/20 15:31:50	5518.01	97.19	1.17	259.2622427	0.88	2018/03/20 14:39:42
KU Leuven Pick	A-2	95	Picked	C-2	2018/03/20 15:32:02	4484.68	88.66	1.23	265.0037443	0.79	2018/03/20 14:39:42
KU Leuven Pick	A-2	96	Picked	C-2	2018/03/20 15:32:14	5483.57	94.07	1.17	259.2622427	0.85	2018/03/20 14:39:42
KU Leuven Pick	A-2	97	Picked	C-2	2018/03/20 15:32:59	5208.01	99.75	1.11	279.0094674	0.81	2018/03/20 14:39:42
KU Leuven Pick	A-2	98	Unpicked			5642.01	111.18	1.45	280.7193916	0.81	2018/03/20 14:39:42
KU Leuven Pick	A-2	99	Picked	A-1	2018/03/20 15:45:31	4498.45	82.79	1.08	273.704299	0.87	2018/03/20 14:39:42
KU Leuven Pick	A-2	100	Unpicked			5449.12	92.24	1.06	258.1364277	0.88	2018/03/20 14:39:42
KU Leuven Pick	A-2	101	Picked	A-1	2018/03/20 15:47:20	4374.45	91.5	1.22	266.8741286	0.83	2018/03/20 14:39:42
KU Leuven Pick	A-2	102	Picked	B-1	2018/03/20 15:51:07	4725.79	89.62	1.19	276.6076024	0.86	2018/03/20 14:39:42
KU Leuven Pick	A-2	103	Unpicked			5958.9	108.77	1.23	258.1364277	0.76	2018/03/20 14:39:42
KU Leuven Pick	A-2	104	Picked	A-1	2018/03/20 15:53:34	4374.45	85.17	1.03	281.7066504	0.84	2018/03/20 14:39:42
KU Leuven Pick	A-2	105	Unpicked			6048.46	118.92	1.49	262.3339866	0.67	2018/03/20 14:39:42
KU Leuven Pick	A-2	106	Picked	A-1	2018/03/20 15:57:46	4526.01	87.48	1.04	252.4302363	0.81	2018/03/20 14:39:42
KU Leuven Pick	A-2	107	Picked	B-1	2018/03/20 15:59:21	4581.12	92.24	1.33	270.3509018	0.86	2018/03/20 14:39:42
KU Leuven Pick	A-2	108	Unpicked			5263.12	94.82	1.11	262.3339866	0.85	2018/03/20 14:39:42
KU Leuven Pick	A-2	109	Picked	B-1	2018/03/20 16:01:21	4718.9	94.79	1.33	270.0106696	0.9	2018/03/20 14:39:42
KU Leuven Pick	A-2	110	Picked	C-1	2018/03/20 16:02:19	5283.79	95.98	1.14	267.7311136	0.85	2018/03/20 14:39:42
KU Leuven Pick	A-2	111	Picked	C-1	2018/03/20 16:02:31	4429.56	91.19	1.28	258.0415796	0.89	2018/03/20 14:39:42

Supplementary Figure S3. *Image-driven robotic spheroid handling. (A) CellCelector™ setup. (C) Full well with microwells with identified spheroids. (D) Before picking of one selected spheroid. (E) After picking of the selected spheroid. Adjoining spheroids stayed in their microwells. (F) Information sheet listing data for each spheroid.*

References

[1] Ouyang L, Armstrong J P K, Salmeron-Sanchez M and Stevens M M 2020 Assembling Living Building Blocks to Engineer Complex Tissues *Adv. Funct. Mater.* **1909009** 1–22

[2] Laschke M W and Menger M D 2017 Life is 3D: Boosting Spheroid Function for Tissue Engineering *Trends Biotechnol.* **35** 133–44

[3] McDermott A M, Herberg S, Mason D E, Collins J M, Pearson H B, Dawahare J H, Tang R, Patwa A N, Grinstaff M W, Kelly D J, Alsberg E and Boerckel J D 2019 Recapitulating bone development through engineered mesenchymal condensations and mechanical cues for tissue regeneration *Sci. Transl. Med.* **11**

[4] Yu Y, Moncal K K, Li J, Peng W, Rivero I, Martin J A and Ozbolat I T 2016 Three-dimensional bioprinting using self-assembling scalable scaffold-free "tissue strands" as a new bioink *Sci Rep* **6** 28714

[5] Kim T G, Park S H, Chung H J, Yang D Y and Park T G 2010 Hierarchically assembled mesenchymal stem cell spheroids using biomimicking nanofilaments and microstructured scaffolds for vascularized adipose tissue engineering *Adv. Funct. Mater.* **20** 2303–9

[6] Skylar-Scott M A, Uzel S G M, Nam L L, Ahrens J H, Truby R L, Damaraju S and Lewis J A 2019 Biomanufacturing of organ-specific tissues with high cellular density and embedded vascular channels *Sci. Adv.* **5** eaaw2459

[7] Nilsson Hall G, Mendes L F, Gklava C, Geris L, Luyten F P and Papantoniou I 2020 Developmentally Engineered Callus Organoid Bioassemblies Exhibit Predictive In Vivo Long Bone Healing *Adv. Sci.* **7** 1–16

[8] Leferink a, Schipper D, Arts E, Vrij E, Rivron N, Karperien M, Mittmann K, van Blitterswijk C, Moroni L and Truckenmüller R 2014 Engineered micro-objects as scaffolding elements in cellular building blocks for bottom-up tissue engineering approaches. *Adv. Mater.* **26** 2592–9

[9] Yajima Y, Yamada M, Utoh R and Seki M 2017 Collagen Microparticle-Mediated 3D Cell Organization: A Facile Route to Bottom-up Engineering of Thick and Porous Tissues *ACS Biomater. Sci. Eng.* **3** 2144–54

[10] Ovsianikov A, Khademhosseini A and Mironov V 2018 The Synergy of Scaffold-Based and Scaffold-Free Tissue Engineering Strategies *Trends Biotechnol.* **36** 348–57

[11] Mironov V, Visconti R P, Kasyanov V, Forgacs G, Drake C J and Markwald R R 2009 Organ printing: Tissue spheroids as building blocks *Biomaterials* **30** 2164–74

[12] Livoti C M and Morgan J R 2010 Self-Assembly and Tissue Fusion of Toroid-Shaped Minimal Building Units *TISSUE Eng. Part A* **16**

[13] Dikina A D, Alt D S, Herberg S, McMillan A, Strobel H A, Zheng Z, Cao M, Lai B P, Jeon O, Petsinger V I, Cotton C U, Rolle M W and Alsberg E 2018 A Modular Strategy to Engineer Complex Tissues and Organs *Adv. Sci.* **5** 1700402

[14] Rago A P, Dean D M and Morgan J R 2009 Controlling cell position in complex heterotypic 3D microtissues by tissue fusion *Biotechnol. Bioeng.* **102** 1231–41

[15] Ayan B, Heo D N, Zhang Z, Dey M, Povilianskas A, Drapaca C and Ozbolat I T 2020 Aspiration-assisted bioprinting for precise positioning of biologics *Sci. Adv.* **6** 1–17

[16] Fonoudi H, Ansari H, Abbasalizadeh S, Larijani M R, Kiani S, Hashemizadeh S, Zarchi A S, Bosman A, Blue G M, Pahlavan S, Perry M, Orr Y, Mayorchak Y, Vandenberg J, Talkhabi M, Winlaw D S, Harvey R P, Aghdami N and Baharvand H 2015 A Universal and Robust Integrated Platform for the Scalable Production of Human Cardiomyocytes From Pluripotent Stem Cells *Stem Cells Transl. Med.* **4** 1482–94

[17] Susienka M J, Wilks B T and Morgan J R 2016 Quantifying the kinetics and morphological changes of the fusion of spheroid building blocks *Biofabrication* **8** 045003

[18] Olsen T R, Mattix B, Casco M, Herbst A, Williams C, Tarasidis A, Simionescu D, Visconti R P and Alexis F 2015 Manipulation of cellular spheroid composition and the effects on vascular tissue fusion *Acta Biomater.* **13** 188–98

[19] Omelyanenko N P, Karalkin P A, Bulanova E A, Koudan E V., Parfenov V A, Rodionov S A, Knyazeva A D, Kasyanov V A, Babichenko I I, Chkadua T Z, Khesuani Y D, Gryadunova A A and Mironov V A 2018 Extracellular Matrix Determines Biomechanical Properties of Chondrospheres during Their Maturation In Vitro *Cartilage*

[20] Bhumiratana S, Eton R E, Oungoulian S R, Wan L Q, Ateshian G a and Vunjak-Novakovic G 2014 Large, stratified, and mechanically functional human cartilage grown in vitro by mesenchymal condensation. *Proc. Natl. Acad. Sci. U. S. A.* **111** 6940–5

[21] Eyckmans J, Roberts S J, Schrooten J and Luyten F P 2010 A clinically relevant model of osteoinduction: A process requiring calcium phosphate and BMP/Wnt signalling *J. Cell. Mol. Med.* **14** 1845–56

[22] Leijten J, Moreira Teixeira L S, Bolander J, Ji W, Vanspauwen B, Lammertyn J, Schrooten J and Luyten F P 2016 Bioinspired seeding of biomaterials using three dimensional microtissues induces chondrogenic stem cell differentiation and cartilage formation under growth factor free conditions *Sci. Rep.* **6** 1–12

[23] Mendes L F, Tam W L, Chai Y C, Geris L, Luyten F P and Roberts S J 2016 Combinatorial Analysis of Growth Factors Reveals the Contribution of Bone Morphogenetic Proteins to Chondrogenic Differentiation of Human Periosteal Cells *Tissue Eng. Part C Methods* **22** 473–86

[24] Deckers T, Lambrechts T, Viazzi S, Hall G N, Papantoniou I, Bloemen V and Aerts J M 2018 High-throughput image-based monitoring of cell aggregation and microspheroid formation *PLoS One*

[25] Schneider C A, Rasband W S and Eliceiri K W 2012 NIH Image to ImageJ: 25 years of image analysis *Nat. Methods* **9** 671–5

[26] Li J, Luo H, Wang R, Lang J, Zhu S, Zhang Z, Fang J, Qu K, Lin Y, Long H, Yao Y, Tian G and Wu Q 2016 Systematic Reconstruction of Molecular Cascades Regulating GP Development Using Single-Cell RNA-Seq *Cell Rep.* **15** 1467–80

[27] Nelep C and Eberhardt J 2018 Automated rare single cell picking with the ALS cellcelector™ *Cytom. Part A* **93** 1267–70

[28] Scotti C, Piccinini E, Takizawa H, Todorov A, Bourgine P, Papadimitropoulos A, Barbero A, Manz M G and Martin I 2013 Engineering of a functional bone organ through endochondral ossification. *Proc. Natl. Acad. Sci. U. S. A.* **110** 3997–4002

[29] Bhumiratana S, Eton R E, Oungoulian S R, Wan L Q, Ateshian G a and Vunjak-Novakovic G 2014 Large, stratified, and mechanically functional human cartilage grown in vitro by mesenchymal condensation. *Proc. Natl. Acad. Sci. U. S. A.* **111** 6940–5

[30] Dean D M and Morgan J R 2008 Cytoskeletal-mediated tension modulates the directed self-assembly of microtissues *Tissue Eng. - Part A* **14** 1989–97

[31] Youssef J, Nurse A K, Freund L B and Morgan J R 2011 Quantification of the forces driving self-assembly of three-dimensional microtissues *Proc. Natl. Acad. Sci. U. S. A.* **108** 6993–8

[32] Beaune G, Stirbat T V, Khalifat N, Cochet-Escartin O, Garcia S, Gurchenkov V V, Murrell M P, Dufour S, Cuvelier D and Brochard-Wyart F 2014 How cells flow in the spreading of cellular aggregates *Proc. Natl. Acad. Sci. U. S. A.* **111** 8055–60

[33] Hajdu Z, Mironov V, Mehesz A N, Norris R A, Markwald R R and Visconti R P 2010 Tissue spheroid fusion-based in vitro screening assays for analysis of tissue maturation 659–64

[34] McMillen P and Holley S A 2015 Integration of cell-cell and cell-ECM adhesion in vertebrate morphogenesis *Curr. Opin. Cell Biol.* **36** 48-53

[35] Foty R A and Steinberg M S 2005 The differential adhesion hypothesis: A direct evaluation *Dev. Biol.* **278** 255–63

[36] Munjal A and Lecuit T 2014 Actomyosin networks and tissue morphogenesis *Dev.* **141** 1789–93

[37] Smeets B, Pešek J, Deckers T, Hall G N, Cuvelier M, Ongenae S, Bloemen V, Luyten F P, Papantoniou I and Ramon H 2020 Compaction dynamics during progenitor cell self-assembly reveal granular mechanics *Matter* **2** 1283–95

[38] Albro M B, Nims R J, Durney K M, Cigan A D, Shim J J, Vunjak-Novakovic G, Hung C T and Ateshian G A 2016 Heterogeneous engineered cartilage growth results from gradients of media-supplemented active TGF-β and is ameliorated by the alternative supplementation of latent TGF-β *Biomaterials* **77** 173–85

[39] Sarem M, Otto O, Tanaka S and Shastri V P 2019 Cell number in mesenchymal stem cell aggregates dictates cell stiffness and chondrogenesis 1–18

[40] Murphy K C, Hung B P, Browne-Bourne S, Zhou D, Yeung J, Genetos D C and Leach J K 2017 Measurement of oxygen tension within mesenchymal stem cell spheroids *J. R. Soc. Interface* **14** 20160851

[41] Mendes L F, Katagiri H, Tam W L, Chai Y C, Geris L, Roberts S J and Luyten F P 2018 Advancing

osteochondral tissue engineering: Bone morphogenetic protein, transforming growth factor, and fibroblast growth factor signaling drive ordered differentiation of periosteal cells resulting in stable cartilage and bone formation in vivo *Stem Cell Res. Ther.* **9** 1–13

[42] Scotti C, Tonnarelli B, Papadimitropoulos A, Scherberich A, Schaeren S, Schauerte A, Lopez-Rios J, Zeller R, Barbero A and Martin I 2010 Recapitulation of endochondral bone formation using human adult mesenchymal stem cells as a paradigm for developmental engineering. *Proc. Natl. Acad. Sci. U. S. A.* **107** 7251–6

[43] Lehmann M, Martin F, Mannigel K, Kaltschmidt K, Sack U and Anderer U 2013 Three-dimensional scaffold-free fusion culture: The way to enhance chondrogenesis of in vitro propagated human articular chondrocytes *Eur. J. Histochem.* **57** 206–16

[44] Moutsatsou P, Ochs J, Schmitt R H, Hewitt C J and Hanga M P 2019 Automation in cell and gene therapy manufacturing: from past to future *Biotechnol. Lett.* **41** 1245–53

[45] Bulanova E A, Koudan E V., Degosserie J, Heymans C, Pereira F D A S, Parfenov V A, Sun Y, Wang Q, Akhmedova S A, Sviridova I K, Sergeeva N S, Frank G A, Khesuani Y D, Pierreux C E and Mironov V A 2017 Bioprinting of a functional vascularized mouse thyroid gland construct *Biofabrication* **9** 034105

[46] Mekhileri N V., Lim K S, Brown G C J, Mutreja I, Schon B S, Hooper G J and Woodfield T B F 2018 Automated 3D bioassembly of micro-tissues for biofabrication of hybrid tissue engineered constructs *Biofabrication* **10** 024103

[47] De Moor L, Merovci I, Baetens S, Verstraeten J, Kowalska P, Krysko D V., De Vos W H and Declercq H 2018 High-throughput fabrication of vascularized spheroids for bioprinting *Biofabrication* **10**

[48] Moldovan N I, Hibino N and Nakayama K 2017 Principles of the *Kenzan* Method for Robotic Cell Spheroid-Based Three-Dimensional Bioprinting <sup/> *Tissue Eng. Part B Rev.*

[49] Ip B C, Cui F, Tripathi A and Morgan J R 2016 The bio-gripper: A fluid-driven micro-manipulator of living tissue constructs for additive bio-manufacturing *Biofabrication* **8**

[50] Blakely A M, Manning K L, Tripathi A and Morgan J R 2015 Bio-Pick, Place, and Perfuse: A New Instrument for Three-Dimensional Tissue Engineering *Tissue Eng. - Part C Methods* **21** 737–46

[51] Gutzweiler L, Kartmann S, Troendle K, Benning L, Finkenzeller G, Zengerle R, Koltay P, Stark G B and Zimmermann S 2017 Large scale production and controlled deposition of single HUVEC spheroids for bioprinting applications *Biofabrication* **9**

CHAPTER 6.

General discussion,

Future perspective and applications

6

6.1. Project strategy and results overview

The term "Tissue engineering" emerged in the late 80's and although the initial engineered cell-based constructs demonstrated cell viability in 3D, they lacked biological functionality required for the creation of bioartificial tissues and organs [113,150]. As a consequence, the concept of creating bioartificial tissues by mimicking developmental processes named "Developmental Engineering" was proposed in 2009 [148]. Ten years later, the field is seeing research that enables the engineering of *in vitro* structures that to a certain degree resemble developing native organs, *i.e.* microtissues and organoids. Subsequent assembly of these *in vitro* engineered living modules (building blocks) is predicted to generate clinically relevant tissue implants and organs *in vivo*. This modular tissue engineering strategy is currently gaining momentum along with an increase in technical tools for both building block formation and their automated assembly [153,185,235,236].

In this thesis, bottom-up assembly of cartilaginous cellular building blocks (micromodules) for bone and cartilage regeneration was hypothesized to overcome previously encountered issues of creating larger *in vitro* tissues, *e.g.* diffusion limitations and tissue complexity [147]. To promote bone healing capacity, the establishment of living building blocks ("callus organoids") was based on differentiation cascades by recapitulating endochondral ossification.

In CHAPTER 3, the differentiation cascade from microspheroid to microtissues and finally "callus organoids" was characterized and these living implants were able to generate bone organs *in vivo* either individually or assembled. The regeneration capacity of assembled "callus organoids" was demonstrated through healing of murine critically-sized long bone defects.

In CHAPTER 4, the "callus organoids" were combined with iPSC-derived cartilage microtissues resulting in osteochondral tissues *in vivo*, demonstrating biofabrication of more complex tissues.

The design limitations, in terms of module size and timing of module fusion, of such a scaffold-free modular approach using spheroids for endochondral bone formation was outlined in CHAPTER 5. A decreased spheroid fusion over time and size restriction for long-term *in vitro* assembly was defined and represents the limits of a design window in which intermediate *in vitro* tissues can be created.

Each CHAPTER contains separate discussions and a general discussion is presented below.

6.2. Biological autonomy depicts functionality

Fracture healing of long bone defects with successful outcome includes the formation of a cartilaginous callus which bridges the defect and subsequently mineralizes and remodels into bone [39]. Generation of a bioartificial "fracture callus" may therefore be a suitable strategy to treat non-unions, fractures that fail to heal. Since periosteum has been shown to possess a crucial role in callus formation during native fracture healing[45,46], it was used as the main cell source in this PhD project to generate cartilaginous intermediate tissues *in vitro*. An alternative cell source would be bone marrow stromal cells (BMSCs) which have extensively been used within tissue engineering and are able to differentiate towards the chondrogenic lineage *in vitro*[123]. BMSCs have previously been applied for endochondral ossification of cartilaginous pellets[165]. However, cells from the bone marrow were shown to mainly contribute to intramembranous bone formation during fracture healing and may therefore not be optimal for generation of cartilage intermediates [45]. In addition, Duchamp de Lageneste *et. al*. demonstrated that murine periosteum derived cells (PDCs) have higher bone regenerative potential in mice compared to murine BMSCs [61]. Hence, studies regarding the molecular mechanisms of PDC activation during fracture healing is also suggested to guide improvements in PDC *in vitro* cultures for tissue engineering of a bioartificial fracture callus.

In CHAPTER 3, ectopic bone organ formation without fibrous tissue was presented. This data highlights an improved outcome by applying a modular strategy with microspheroids compared to using large pellet cultures [165,172]. This may be attributed to improved diffusion of nutrients as well as growth factors. For example, more rapid TGFβ1-driven chondrogenic differentiation has been reported in hBMSC microspheroids compared to large pellets [237]. Transcriptomic analysis of hPDC spheroids (CHAPTER 3) differentiated into "callus organoids" (day 21) indicated that a prehypertrophic cell state was reached and required for bone organ formation [172]. Previous studies using pellet culture have demonstrated that longer culture time (4 weeks) and/or addition of a "hypertrophic medium" for differentiation towards a late hypertrophic state, resulting in presence of mineralization *in vitro*, is beneficial for ectopic bone formation with bone marrow compartments [165,177]. However, the *in vitro* mineral deposition in these studies was mainly detected in the pellet periphery [165,171]. Nevertheless, despite the difference in *in vitro* mineralization, a common factor which appear crucial for bone marrow formation *in vivo* was ECM remodeling upon implantation [165,172,177]. In CHAPTER 4, implantation of assembled "callus organoids" demonstrated bone organ formation after 4 weeks *in vivo*. This relatively fast bone organ formation was linked with an increase in ECM

turnover observed *in vivo* which was further associated with the transcriptional profile of day 21 “callus organoids” that included up-regulation of genes associated with ECM organization.

While the data in this dissertation presented building block characterization that indicated presence of cells with a prehypertrophic phenotype, the exact cellular composition within the maturing spheroids was not elucidated. Linked with the heterogeneous nature of periosteum, the initial cell population of hPDCs may contain multiple progenitor cells[238] and is therefore also expected to generate different cellular phenotypes within each micromodule. scRNAseq would allow better identification of different cell populations within the micromodules over time resulting in quantitative correlation of cellular subpopulation structure with *in vivo* bone forming capacity. Recent advances in single cell transcriptomics of bone tissue and development will enable identification of specific cell types and association with developmental stages [71,75]. Nevertheless, there are still difficulties in defining late hypertrophic chondrocytes from early osteoblasts and the mechanism of hypertrophic chondrocyte transdifferentiation into osteoblasts is not fully elucidated [77]. However, multiple reports indicate that hypertrophic chondrocytes transdifferentiate towards osteoblasts during endochondral ossification[35,47,239] and hence it could be credible that transdifferentiation occurs also within the hPDC derived “callus organoids” either *in vitro* or *in vivo*.

The size of building blocks presented in this dissertation was defined in order to avoid diffusion limitations during differentiation. Additionally, 250 cells per spheroid was previously defined to result in up-regulation of hypertrophic genes (*COL10A1*, *RUNX2* and *DLX5*) during early chondrogenic differentiation, compared to 50 and 100 cells per spheroid [195]. In another study, the number of BMSCs per aggregate (70-, 150-, 150-, 350- and 500 thousand) was shown to dictate chondrogenic differentiation, with the lower cell number resulting in up-regulation of chondrogenic and hypertrophic gene markers [240]. Hence, the cellular microenvironment within spheroids is affected by cell number but also position within each spheroid. Quantification of mechanical stress within ~ 800 μm sized spheroids demonstrated a difference in stress depending on position within the spheroid and a gradient molecular signaling pattern along the spheroid radius has been observed in hMSC spheroids [241,242]. Additionally, molecular signaling as well as cellular patterning within spheroids has been observed to change depending on microwell design [243]. Hence, correlation with internal stresses mapped in the limb bud[244] and directed design of microwells[245] could further aid in improving the generation of functional building blocks and their fusion for bone and cartilage regeneration.

In conclusion, in depth micromodule characterization with regard to cellular population within each module will increase the understanding of the cellular and molecular basis required for successful *in vivo* tissue formation. This knowledge would aid in further improvements to generate functional micromodules by adapting parameters throughout the biomanufacturing process including cell expansion, micromodule differentiation and assembly.

6.3. Cellular building blocks as "bioink" – alone or with biomaterial?

Generation of micromodules with biological functionality offers the possibility of applying them as living "bioink" for biofabrication of functional tissues [236,246,247]. This thesis demonstrated bone organ formation by assembly of "callus organoids" and osteochondral-like tissues by combining two distinct micromodule populations (iPSC derived cartilage microtissues and "callus organoids"). The inherent fusion capacity of multicellular spheroids permitted the creation of multimodular constructs but the difference in fusion capacity regarding both spheroid maturity and cell type should be considered when designing multimodular tissues (CHAPTER 4-5) [248]. Assembly of spheroid populations containing various cell phenotypes will enable creation of even more complex tissues. For example, integrated vascularization in cartilage intermediates for bone regeneration could be generated by including human umbilical vein endothelial cell (HUVEC) spheroids [249]. In addition, integrated vasculature could aid in the transition towards centimeter sized constructs *in vivo*, however *in vitro* assembly of modules will still be limited in size if multiple days are required for fusion (CHAPTER 5). To resolve this problem, bioprinting strategies have established the creation of channels within *in vitro* tissues which may allow for longer *in vitro* assembly periods of larger structures [246,250].

A challenge that scaffold-free *in vitro* constructs may face is the lack sufficient mechanical stability for applications in load-bearing tissues. Inclusion of suitable biomaterials in combination with cellular micromodules could improve these properties. To do so, it is important to select and adapt the biomaterials for the intended application, *i.e*. bone or cartilage. The integration of biomaterials into *in vitro* engineered cartilage intermediates has previously demonstrated successful bone formation upon ectopic implantation by relying on a high initial cell density (20-70 x 10^6 cells/mL [171,251,252]) which allows cell-cell contact and appropriate chondrogenic differentiation. The main biomaterials used for *in vivo* EO bone formation include hydrogels such as alginate[251,253], GelMA[254], fibrin[174] and collagen type I scaffolds alone[171,177,255,256] or in combination with hyaluronic acid[257] to render mechanical support and

at the same time allow cellular maturation. A more recent approach for cell-based EO constructs, involves the use of biomaterials as delivery of growth factors via hydrogel functionalization[252] or gelatin microsphere incorporation[258]. Hence, if chosen carefully, biomaterials can be beneficial for *in vivo* functionality and scaffolds alone have been demonstrated to promote EO in long bone defects through collagen fiber alignment[259]. Ultimately, the development of novel biomaterials suitable for chondrogenesis and endochondral bone formation is evolving and has potential to create hybrid constructs in combination with cellular micromodules such as spheroids and organoids [260–264].

Bioprinting shows promise for robust biofabrication of tissues and organs with a higher degree of structural organization[265]. In addition to extrusion bioprinting of spheroid in hydrogel[266], combination with other biofabrication techniques such as extrusion thermoplastic polymer dispensing [267,268], electrospinning [269] or melt electrowriting (MEW)[270] have been presented for controlled deposition of spheroids. Spheroid interaction with the biomaterial in question is therefore of importance and should be considered when designing a biofabrication setup. For example, the spreading capacity of hPDC spheroids on flat adherent surfaces decreased with prolonged chondrogenic differentiation (CHAPTER 4) and the attachment and integration with a scaffold would therefore also be expected to decrease. Furthermore, geometric features such as pore size, filament spacing and fiber alignment are shown to affect cellular behavior [271,272] and a smaller fiber spacing of 500 µm, as compared to 1100 µm, was shown to influence chondrogenic differentiation of hBMSCs resulting in higher GAG content [273].

Conclusively, generation of bioartificial tissues with cellular building blocks require considerations regarding fusion behavior as well as interaction with biomaterials. Further development in tissue complexity as well as assembly precision is expected to be supported by the fast development in novel biofabrication techniques.

6.4. Applicability for clinical translation

Cell-based constructs and the emergence of developmental engineering strategies have rendered the formation of *in vitro* tissues with improved resemblance to native tissues and ability to regenerate tissues in a semi-autonomous fashion. Despite promising *in vivo* data in a research setting, only a limited number of cell-based products have reached market authorization[106]. Currently, cell-based clinical trials for bone defects mainly include combinations of ceramic-based scaffolds and BMSCs used either naive or after osteogenic

differentiation[96,274] demonstrating that the endochondral developmental engineering paradigm has not yet reached clinical trials.

Implantation of cartilage intermediates has yielded successful outcomes in orthotopic environments with bridging of critical-sized long bone defects in small animal models using different adult progenitor cells (hBMSCs[168,258,275], hASCs[160] and hPDCs[138,172]). The modular approach presented in this thesis demonstrated biological robustness and show promise for scalable manufacturing of cartilage intermediates for healing of bone. Nevertheless, the defect environment affect healing capacity and implantation in compromised defects should be studied to represent a situation closer to the clinical reality [276]. Furthermore, donors of different age and sex should be screened to characterize the donor variability of the process and old age is often linked with decreased regenerative capacity [168,174]. An alternative to adult progenitor cells is the application of hiPSCs, which were described in CHAPTER 4 for generation of hyaline-like cartilage. hiPSCs opens the possibility to generate cells with "younger phenotype" and therefore also with greater regenerative capacity. This will be of great importance for tissues where adult progenitor cells have shown varying clinical results *i.e.* articular cartilage[277] and cardiac tissues[278]. In addition, relatively easy accessibility to and capacity to expand iPSCs will be beneficial for manufacturing of larger tissues. A number of clinical trials using cells derived from hiPSCs are ongoing and regulatory guidelines are developing[279]. However, considerations regarding purity, mutations and tumorgenicity are aspects which still represent obstacles for clinical translation of hiPSCs [145,280].

Additionally, current quality controls during a donor screening would include destructive analysis methods *i.e.* gene expression and histological analyses. Development of non-destructive and affordable quality controls, *i.e.* biomarkers identified in the cell culture media would enable more efficient monitoring throughout the manufacturing process [281]. Since biomarkers in media are non-destructive, they would also facilitate future translation of an autologous process towards clinical applications. Nevertheless, high donor-variability may be an issue for clinical translation and devitalization of cellular constructs could pose as an alternative to avoid immune reaction and allow use of allogeneic cells. Even so, variable *in vivo* results have been observed using devitalized cartilage pellets for endochondral bone formation [282,283]. Hence, additional advancements are required to enable large animal studies and future translation toward a cell-based advanced therapy medicinal product (ATMP).

6.5. Towards building block manufacturing and assembly

The application of micro-scale cellular building blocks for scaffold-free regeneration of osteochondral (>1 cm ø) or bone (>3 cm) defects will require production and maintenance of hundreds of thousands to millions of modules. Adaptations with regard to automation and up-scaling of the process is therefore of great importance to move from a laboratory-scale towards industrial manufacturing [284]. In this thesis, microspheroids were generated in microwell platforms with a protocol that would be feasible to scale-out using robotic systems as previously described for organoid drug screening systems [285]. Nevertheless, the microwell system has limitations regarding scale-up, hence dynamic suspension cultures could be a solution to allow a substantial volumetric increase of spheroid culture and differentiation [286,287]. Next, automation of subsequent building block handling is required for controlled assembly into larger constructs. Deposition of individual microspheroids as presented in CHAPTER 5 and by Ayan *et. al*.[249] allow for precision which is important for creation of complex structures. Integrated bioprinting platforms adapted for spheroid or other cellular modules have been developed based on needles [288] as well as aspiration/fluidics [289,290] among others. These platforms will be important for robust manufacturing of modular tissue constructs and should be adapted for each application with careful consideration to defined design windows regarding both micromodule maintenance as well as assembly. Finally, the manufacturing cost is not to be neglected when designing a manufacturing process for clinical translation [291].

6.6. Disease model and drug screening platform

The resemblance of human organoids and microtissues to native organs and tissues, motivate their application for disease modeling as well as drug screening [199]. Disease modeling of cystic fibrosis (genetic disease) have already been applied in personalized medicine by using patient-derived intestinal organoids and additional organoids have been commercialized [292,293]. Application of iPSCs has also opened the possibility for generation of patient- and disease-specific 3D models for drug screening and disease modelling[294]. In the case of the hPDC-derived building blocks presented in this thesis, they could be developed for disease modelling or drug screening of joint diseases such as osteoarthritis (OA) [295]. In addition, the presence of bone marrow within the "callus organoids" after implantation open the possibility to model hematopoietic diseases in a micro-format [296]. Enhanced cellular characterization within the maturing microspheroids will be a step towards drug screening platform by improving the understanding of the differentiation cascade at a single cell level. High-throughput monitoring of the supposed drug response could be permitted by integration with recently described image analysis platforms dedicated for microspheroids [243,297–299]. Automation regarding microspheroid formation and media change would further advance these assays towards fully automated processes of *in vitro* drug screening [285,300]. Next, biocompatible implantation devices adapted for microspheroids would allow controlled *in vivo* evaluation for each individual microspheroid [301].

CHAPTER 7.

General Conclusions

7

A modular tissue engineering approach with assemblies of developmentally engineered cartilaginous building blocks was presented in this thesis. The approach was proven successful in a small animal model (mouse) and demonstrated a proof-of-concept for the possibility of scalable spheroid-based constructs for regeneration of bone and cartilage.

CHAPTER 3 demonstrated that assemblies of microtissues formed more homogenously differentiated *in vitro* constructs as compared to the traditional large pellet cultures. In addition, temporal transcriptome analysis of the hPDC-derived microtissues displayed differentiation patterns similar to those of endochondral ossification. The temporal gene profile was linked to the *in vivo* outcome concluding that a differentiation stage of prehypertrophic chondrocytes should be reached for successful bone organ formation and healing of murine critically-sized long bone defects (**Figure 7.1**). The defined gene signatures linked with *in vivo* functionality, generated plausible gene markers allowing quality control for future manufacturing processes.

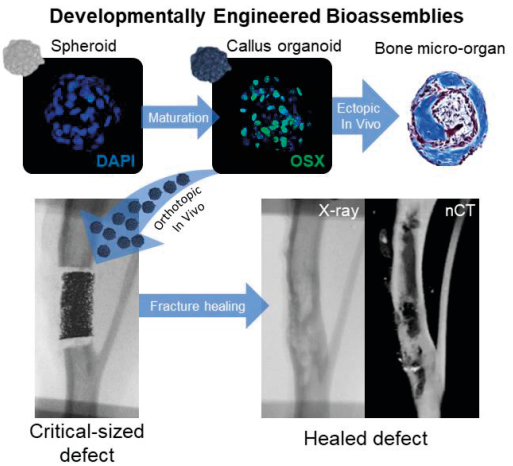

Figure 7.1. *Developmentally engineered bioassemblies for healing of critical-sized murine defect. Figure from Nilsson Hall et.al.* [172].

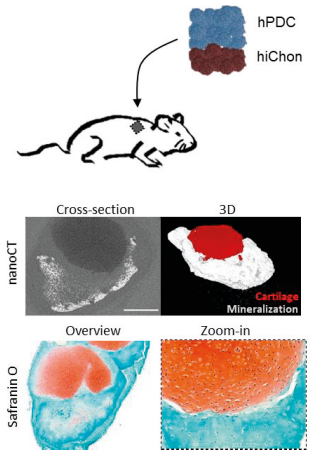

Figure 7.2. *Assembly of distinct cellular building blocks in vitro matured into osteochondral-like tissues in vivo.*

CHAPTER 4 aimed to demonstrate the formation of a cartilage intermediate by assembly of distinct microtissue building blocks which formed either endochondral bone or cartilage. hiChon-derived cartilage microtissues exhibited hyaline-like cartilage upon implantation, while hPDC-derived microtissues formed fibrous-like cartilage. Therefore, hPDC-derived "callus organoids" were assembled with hiChon-derived cartilage microtissues which resulted in the formation of osteochondral-like tissue units upon implantation (**Figure 7.2**). Hence, the assembly of two distinct microtissues from different cell types were able to further mature towards their intended tissue type upon implantation. This opens the

possibility to design *in vitro* constructs according to native tissue complexity.

CHAPTER 5 describes two assays to quantify spheroid assembly behavior (**Figure 7.3**). Both fusion and spreading capacity of hPDC-derived microtissues decreased with prolonged chondrogenic differentiation. Furthermore, assembly of microtissues at an early time-point resulted in the formation of non-differentiated central regions if the final size/thickness was not limited to ≤1mm. Conclusively, assembly of fully mature microtissues, as studied in CHAPTER 3 and 4, may be a preferred option, although limited fusion and spreading capacity could hamper assembly and integration with biomaterials. Finally, an aspiration-based robotic system with image-based spheroid recognition was presented as a proof-of-concept for future automation of spheroid picking and deposition.

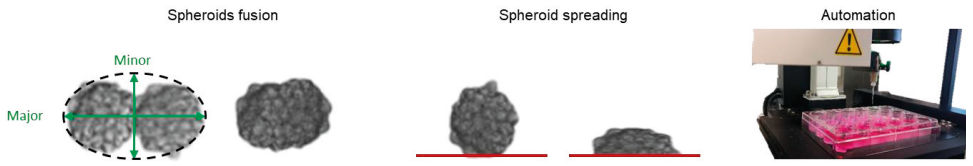

Figure 7.3. *Spheroid assays to quantify fusion and spreading capacity of cellular building blocks to define design limitations for future robotic manufacturing of spheroid-based tissue engineering.*

The described modular approach shows promise in generating functional cell-based constructs for bone and cartilage but many hurdles must be overcome to enable translation towards large animal studies and a future clinical setting. These hurdles include donor variability, assembly approaches, scale-up as well as automation.

Project summary

Tissue engineered constructs for bone and cartilage regeneration have shown promise in research but only a limited number of Advanced therapy medicinal products (ATMPs) have reached clinical translation. In this thesis, a developmental engineering approach was applied through assembly of cartilaginous building blocks (100-200 µm) to create living implants for regeneration of bone or osteochondral tissue. Description of spheroid-based bottom-up approaches and their *in vitro* characteristics has been reported but few research groups have demonstrated functional regeneration of tissues or organs.

Results obtained during this PhD-project present a novel developmental engineering approach for biofabrication of cartilage intermediate tissues from the bottom-up that are able to regenerate murine long-bone defects and form osteochondral tissue units subcutaneously. CHAPTER 3 demonstrated that assemblies of microtissues formed more homogenously differentiated *in vitro* constructs as compared to the traditional large pellet cultures. In addition, temporal transcriptome analysis of the hPDC-derived microtissues displayed differentiation patterns similar to those of endochondral ossification. The temporal gene profile was linked to the *in vivo* outcome concluding that a differentiation stage of prehypertrophic chondrocytes should be reached for successful bone organ formation. Hence the micro-modules were defined to differentiate from spheroids (only cells), microtissues (cells and ECM) to "callus organoids" (prehypertrophic cells and ECM). The defined gene signatures linked with *in vivo* functionality, generated plausible gene markers allowing quality control for future manufacturing processes.

Assembly of smaller building-blocks (100-200 µm), as described in CHAPTER 3, enables creation of more complex structures regarding both geometric shape as well as tissue type. In CHAPTER 4, the combination of hPDC-derived "callus organoids" with hiChon-derived cartilage microtissues resulted in the formation of osteochondral-like tissue units upon implantation. Hence, demonstrating the integration of two distinct microtissue assemblies which upon implantation further matured towards their intended tissue type which opens the possibility to design *in vitro* constructs according to native tissue complexity.

Although single building-blocks are functional, it is critical to assemble thousands of modules to enable healing of larger defects. CHAPTER 5 concludes that the spreading and fusion capacity of hPDC-derived microtissues decrease with prolonged differentiation. Additionally, assembly of microtissues at an early time-point risk the formation of non-differentiated central regions if the final size/thickness is not limited to ≤ 1 mm. Conclusively, assembly of fully mature microtissues, as studied in CHAPTER 3 and 4, may be a preferred option, although limited fusion and spreading capacity could hamper fusion and integration with biomaterials. This data demonstrated that diffusion limitation as well as spreading and fusion kinetics represent relevant screening parameters for bottom-up processes which include cell-based modules, *e.g*. spheroids, microtissues and organoids.

The developmental engineering approach described in this thesis was proven successful in a small animal model (mouse) and demonstrated a proof-of-concept for the possibility of scalable spheroid-based constructs for regeneration of bone and cartilage. Further actions with regard to scale-up and module characterization should be taken to enable large animal studies and future clinical translation.

References

Introduction, General discussion, Future perspective and applications

1. Villarreal, M. R. Axial skeleton diagram.svg. (2007). Available at: https://commons.wikimedia.org/wiki/File:Axial_skeleton_diagram.svg. (Accessed: 29th April 2020)
2. White, T. D., Black, M. T. & Folkens, P. A. *Human osteology: Third edition*. *Human Osteology: Third Edition* (2011).
3. OpenStax. *Anatomy & Physiology*. *Anatomy & Physiology* (2017). doi:10.5399/osu/1116
4. Colnot, C., Zhang, X. & Tate, M. L. K. Current insights on the regenerative potential of the periosteum: Molecular, cellular, and endogenous engineering approaches. *Journal of Orthopaedic Research* **30**, 1869–1878 (2012).
5. Reznikov, N., Shahar, R. & Weiner, S. Bone hierarchical structure in three dimensions. *Acta Biomater.* **10**, 3815–3826 (2014).
6. Hadjidakis, D. J. & Androulakis, I. I. Bone remodeling. *Ann. N. Y. Acad. Sci.* **1092**, 385–396 (2006).
7. Crockett, J. C., Rogers, M. J., Coxon, F. P., Hocking, L. J. & Helfrich, M. H. Bone remodelling at a glance. *J. Cell Sci.* **124**, 991–998 (2011).
8. Teitelbaum, S. L. Bone resorption by osteoclasts. *Science* (2000). doi:10.1126/science.289.5484.1504
9. Badawy, T. *et al.* Osteoblast lineage-specific cell-surface antigen (A7) regulates osteoclast recruitment and calcification during bone remodeling. *Lab. Investig.* **99**, 866–884 (2019).
10. Cappariello, A. *et al.* Osteoblast-Derived Extracellular Vesicles Are Biological Tools for the Delivery of Active Molecules to Bone. *J. Bone Miner. Res.* **33**, 517–533 (2018).
11. Sophia Fox, A. J., Bedi, A. & Rodeo, S. A. The basic science of articular cartilage: Structure, composition, and function. *Sports Health* **1**, 461–468 (2009).
12. Goldring, S. R. & Goldring, M. B. Changes in the osteochondral unit during osteoarthritis: Structure, function and cartilage bone crosstalk. *Nat. Rev. Rheumatol.* **12**, 632–644 (2016).
13. Chijimatsu, R. & Saito, T. Mechanisms of synovial joint and articular cartilage development. *Cell. Mol. Life Sci.* **76**, 3939–3952 (2019).
14. Di Luca, A., Van Blitterswijk, C. & Moroni, L. The osteochondral interface as a gradient tissue: From development to the fabrication of gradient scaffolds for regenerative medicine. *Birth Defects Res. Part C - Embryo Today Rev.* **105**, 34–52 (2015).
15. Luca, A. Di, Blitterswijk, C. Van & Moroni, L. The Osteochondral Interface as a Gradient Tissue : From Development to the Fabrication of Gradient Scaffolds for Regenerative Medicine. (2015). doi:10.1002/bdrc.21092
16. Hall, B. K. & Miyake, T. All for one and one for all: Condensations and the initiation of skeletal development. *BioEssays* **22**, 138–147 (2000).
17. Mackie, E. J., Tatarczuch, L. & Mirams, M. The skeleton: a multi-functional complex organ: the growth plate chondrocyte and endochondral ossification. *J. Endocrinol.* **211**, 109–121 (2011).
18. Ornitz, D. M. & Marie, P. J. FGF signaling pathways in endochondral and intramembranous bone development and human genetic disease. *Genes Dev.* **16**, 1446–1465 (2002).
19. Villarreal, M. R. Appendicular skeleton diagram.svg. *Wikimedia Commons, the free media repository* (2007). Available at: https://commons.wikimedia.org/wiki/File:Appendicular_skeleton_diagram_blank.svg. (Accessed: 29th April 2020)
20. Decker, R. S. Articular cartilage and joint development from embryogenesis to adulthood. *Semin. Cell Dev. Biol.* **62**, 50–56 (2017).
21. Yang, Y. Skeletal morphogenesis during embryonic development. *Crit. Rev. Eukaryot. Gene Expr.* **19**, 197–218 (2009).
22. Lefebvre, V., Angelozzi, M. & Haseeb, A. SOX9 in cartilage development and disease. *Curr. Opin. Cell Biol.* **61**, 39–47 (2019).
23. Akiyama, H. *et al.* Osteo-chondroprogenitor cells are derived from Sox9 expressing precursors. *Proc. Natl. Acad. Sci. U. S. A.* **102**, 14665–14670 (2005).

24. Ornitz, D. M. & Marie, P. J. Fibroblast growth factor signaling in skeletal development and disease. *Genes Dev.* **29**, 1463–1486 (2015).
25. Matsushita, Y. *et al.* Notch effector Hes1 marks an early perichondrial population of skeletal progenitor cells at the onset of endochondral bone development. *bioRxiv* (2020).
26. Kronenberg, H. M. The role of the perichondrium in fetal bone development. *Ann. N. Y. Acad. Sci.* **1116**, 59–64 (2007).
27. Salazar, V. S., Gamer, L. W. & Rosen, V. BMP signalling in skeletal development, disease and repair. *Nat. Rev. Endocrinol.* **12**, 203–221 (2016).
28. Li, J. *et al.* Systematic Reconstruction of Molecular Cascades Regulating GP Development Using Single-Cell RNA-Seq. *Cell Rep.* **15**, 1467–1480 (2016).
29. Arnold, M. A. *et al.* MEF2C Transcription Factor Controls Chondrocyte Hypertrophy and Bone Development. *Dev. Cell* **12**, 377–389 (2007).
30. Tan, Z. *et al.* Synergistic co-regulation and competition by a SOX9-GLI-FOXA phasic transcriptional network coordinate chondrocyte differentiation transitions. *PLoS Genet.* **14**, 1007346 (2018).
31. Zhang, X. *et al.* The critical role of the epidermal growth factor receptor in endochondral ossification. *J. Bone Miner. Res.* **26**, 2622–2633 (2011).
32. Walzer, S. M. *et al.* Vascularization of primary and secondary ossification centres in the human growth plate. *BMC Dev. Biol.* **14**, 1–12 (2014).
33. Maes, C. *et al.* Osteoblast precursors, but not mature osteoblasts, move into developing and fractured bones along with invading blood vessels. *Dev. Cell* **19**, 329–344 (2010).
34. Yang, L., Tsang, K. Y., Tang, H. C., Chan, D. & Cheah, K. S. E. Hypertrophic chondrocytes can become osteoblasts and osteocytes in endochondral bone formation. *World Review of Nutrition and Dietetics* **111**, 13 (2014).
35. Zhou, X. *et al.* Chondrocytes Transdifferentiate into Osteoblasts in Endochondral Bone during Development, Postnatal Growth and Fracture Healing in Mice. *PLoS Genet.* **10**, (2014).
36. Kindblom, J. M., Nilsson, O., Hurme, T., Ohlsson, C. & Sävendahl, L. Expression and localization of Indian hedgehog (Ihh) and parathyroid hormone related protein (PTHrP) in the human growth plate during pubertal development. *J. Endocrinol.* **174**, 2–7 (2002).
37. Vortkamp, A. *et al.* Regulation of rate of cartilage differentiation by Indian Hedgehog and PTH-related protein. *Science* (1996). doi:10.1126/science.273.5275.613
38. Debnath, S. *et al.* Discovery of a periosteal stem cell mediating intramembranous bone formation. *Nature* **562**, 133–139 (2018).
39. Bahney, C. S. *et al.* Cellular biology of fracture healing. *J. Orthop. Res.* **37**, 35–50 (2019).
40. Claes, L., Recknagel, S. & Ignatius, A. Fracture healing under healthy and inflammatory conditions. *Nat. Rev. Rheumatol.* **8**, 133–143 (2012).
41. Thompson, Z., Miclau, T., Hu, D. & Helms, J. A. A model for intramembranous ossification during fracture healing. *J. Orthop. Res.* **20**, 1091–1098 (2002).
42. Gerstenfeld, L. C., Cullinane, D. M., Barnes, G. L., Graves, D. T. & Einhorn, T. A. Fracture healing as a post-natal developmental process: Molecular, spatial, and temporal aspects of its regulation. *J. Cell. Biochem.* **88**, 873–884 (2003).
43. Einhorn, T. a & Gerstenfeld, L. C. Fracture healing: mechanisms and interventions. *Nat. Rev. Rheumatol.* **11**, 45–54 (2014).
44. Weiss, S., Zimmermann, G., Pufe, T., Varoga, D. & Henle, P. The systemic angiogenic response during bone healing. *Arch. Orthop. Trauma Surg.* **129**, 989–997 (2009).
45. Colnot, C. Skeletal cell fate decisions within periosteum and bone marrow during bone regeneration. *J. Bone Miner. Res.* **24**, 274–82 (2009).
46. Murao, H., Yamamoto, K., Matsuda, S. & Akiyama, H. Periosteal cells are a major source of soft callus in bone fracture. *J. Bone Miner. Metab.* **31**, 390–398 (2013).
47. Hu, D. P. *et al.* Cartilage to bone transformation during fracture healing is coordinated by the invading vasculature and induction of the core pluripotency genes. *Development* **144**, 221–234 (2017).
48. Shwartz, Y., Viukov, S., Krief, S. & Zelzer, E. Joint Development Involves a Continuous Influx of Gdf5-Positive Cells. *Cell Rep.* **15**, 2577–2587 (2016).
49. Decker, R. S. *et al.* Cell origin, volume and arrangement are drivers of articular cartilage formation, morphogenesis and response to injury in mouse limbs. *Dev. Biol.* **426**, 56–68 (2017).
50. Kozhemyakina, E. *et al.* Identification of a Prg4-expressing articular cartilage progenitor cell population in mice. *Arthritis Rheumatol.* **67**, 1261–1273 (2015).
51. Hsueh, M. F., Önnerfjord, P., Bolognesi, M. P., Easley, M. E. & Kraus, V. B. Analysis of 'old' proteins unmasks dynamic gradient of cartilage turnover in human limbs. *Sci. Adv.* **5**, 1–10 (2019).
52. Moore, S. R., Milz, S. & Knothe Tate, M. L. Periosteal thickness and cellularity in mid-diaphyseal cross-sections from human femora and tibiae of aged donors. *J. Anat.* **224**, 142–149 (2014).

53. Duchamp de Lageneste, O. & Colnot, C. Periostin in Bone Regeneration. in *Advances in Experimental Medicine and Biology - Periostin* **1132**, 49–61 (2019).
54. Rhee, Y. *et al.* PTH receptor signaling in osteocytes governs periosteal bone formation and intracortical remodeling. *J. Bone Miner. Res.* **26**, 1035–1046 (2011).
55. Gerbaix, M., Vico, L., Ferrari, S. L. & Bonnet, N. Periostin expression contributes to cortical bone loss during unloading. *Bone* **71**, 94–100 (2015).
56. Colnot, C. Skeletal cell fate decisions within periosteum and bone marrow during bone regeneration. *J. Bone Miner. Res.* **24**, 274–282 (2009).
57. Utvåg, S. E., Grundnes, O. & Reikeraos, O. Effects of periosteal stripping on healing of segmental fractures in rats. *J. Orthop. Trauma* **10**, 279–284 (1996).
58. Macnab, I. & de Haas, W. G. The Role of Periosteal Blood Supply in the Healing of Fractures of the Tibia. *Clin. Orthop. Relat. Res.* **105**, 27–33 (1974).
59. Choudry, U. H., Bakri, K., Moran, S. L., Karacor, Z. & Shin, A. Y. The Vascularized Medial Femoral Condyle Periosteal Bone Flap for the Treatment of Recalcitrant Bony Nonunions. *Ann. Plast. Surg.* **60**, (2008).
60. Hoikkai, V. E. J., Jaroma, H. J. & Ritsilä, V. A. Reconstruction of the patellar articulation with periosteal grafts: 4-year follow-up of 13 cases. *Acta Orthop.* **61**, 36–39 (1990).
61. Duchamp de Lageneste, O. *et al.* Periosteum contains skeletal stem cells with high bone regenerative potential controlled by Periostin. *Nat. Commun.* **9**, 773 (2018).
62. Pineault, K. M., Song, J. Y., Kozloff, K. M., Lucas, D. & Wellik, D. M. Hox11 expressing regional skeletal stem cells are progenitors for osteoblasts, chondrocytes and adipocytes throughout life. *Nat. Commun.* **10**, 3168 (2019).
63. Ortinau, L. C. *et al.* Identification of Functionally Distinct Mx1+αSMA+ Periosteal Skeletal Stem Cells. *Cell Stem Cell* **25**, 784-796.e5 (2019).
64. Retting, K. N., Song, B., Yoon, B. S. & Lyons, K. M. BMP canonical Smad signaling through Smad1 and Smad5 is required for endochondral bone formation. *Development* **136**, 1093–1104 (2009).
65. Yang, X. *et al.* TGF-β/Smad3 signals repress chondrocyte hypertrophic differentiation and are required for maintaining articular cartilage. *J. Cell Biol.* **153**, 35–46 (2001).
66. Joeng, K. S., Schumacher, C. A., Zylstra-Diegel, C. R., Long, F. & Williams, B. O. Lrp5 and Lrp6 redundantly control skeletal development in the mouse embryo. *Dev. Biol.* **359**, 222–229 (2011).
67. Karp, S. J. *et al.* Indian Hedgehog coordinates endochondral bone growth and morphogenesis via Parathyroid Hormone related-Protein-dependent and -independent pathways. *Development* **127**, 543–548 (2000).
68. Xing, W., Cheng, S., Wergedal, J. & Mohan, S. Epiphyseal chondrocyte secondary ossification centers require thyroid hormone activation of Indian hedgehog and osterix signaling. *J. Bone Miner. Res.* **29**, 2262–2275 (2014).
69. Creative Commons. Creative Commons Attribution 3.0 Unported License. Available at: https://creativecommons.org/licenses/by/3.0/. (Accessed: 10th May 2020)
70. Dodds, G. S. Row formation and other types of arrangement of cartilage cells in endochondral ossification. *Anat. Rec.* (1930). doi:10.1002/ar.1090460409
71. Chan, C. K. F. *et al.* Identification of the Human Skeletal Stem Cell. *Cell* **175**, 43-56.e21 (2018).
72. Chan, C. K. F. *et al.* Identification and specification of the mouse skeletal stem cell. *Cell* **160**, 285–298 (2015).
73. Mizuhashi, K. *et al.* Resting zone of the growth plate houses a unique class of skeletal stem cells. *Nature* (2018). doi:10.1038/s41586-018-0662-5
74. Newton, P. T. *et al.* A radical switch in clonality reveals the formation of a stem cell niche in the epiphyseal growth plate. doi:10.1038/s41586-019-0989-6
75. Kelly, N. H., Huynh, N. P. T. & Guilak, F. Single cell RNA-sequencing reveals cellular heterogeneity and trajectories of lineage specification during murine embryonic limb development. *Matrix Biol.* (2019). doi:10.1016/j.matbio.2019.12.004
76. Li, B., Balasubramanian, K., Krakow, D. & Cohn, D. H. Genes uniquely expressed in human growth plate chondrocytes uncover a distinct regulatory network. *BMC Genomics* **18**, 1–15 (2017).
77. Aghajanian, P. & Mohan, S. The art of building bone: emerging role of chondrocyte-to-osteoblast transdifferentiation in endochondral ossification. *Bone Res.* **6**, 19 (2018).
78. Bianco, P., Cancedda, F. D., Riminucci, M. & Cancedda, R. Bone formation via cartilage models: The 'Borderline' chondrocyte. *Matrix Biology* **17**, 185–192 (1998).
79. Thesingh, C. W., Groot, C. G. & Wassenaar, A. M. Transdifferentiation of hypertrophic chondrocytes into osteoblasts in murine fetal metatarsal bones, induced by co-cultured cerebrum. *Bone Miner.* **12**, 25–40 (1991).
80. Roach, H. I. Trans-differentiation of hypertrophic chondrocytes into cells capable of producing a

mineralized bone matrix. *Bone Miner.* **19**, 1–20 (1992).
81. Park, J. *et al.* Dual pathways to endochondral osteoblasts: a novel chondrocyte-derived osteoprogenitor cell identified in hypertrophic cartilage. *Biol. Open* **4**, 608–621 (2015).
82. Wang, L. *et al.* SHP2 Regulates the Osteogenic Fate of Growth Plate Hypertrophic Chondrocytes. *Sci. Rep.* **7**, 1–14 (2017).
83. Marsell, R. & Einhorn, T. A. The biology of fracture healing. *Injury* **42**, 551–555 (2011).
84. Calori, G., Albisetti, W., Agus, A., Iori, S. & Tagliabue, L. Risk factors contributing to fracture non-unions. *Injury* **38**, S11–S18 (2007).
85. study group. Recombinant Human BMP-2 for Treatment of Open Tibial Fractures. *J. Bone Jt. Surgey* **84**, 2123–2134 (2002).
86. Giannoudis, P. V. & Atkins, R. Management of long-bone non-unions. *Injury* **38**, S1–S2 (2007).
87. McEwan, J. K. *et al.* Regenerative medicine in lower limb reconstruction. *Regen. Med.* **13**, 477–490 (2018).
88. Zura, R., Mehta, S., Della Rocca, G. J. & Steen, R. G. Biological risk factors for nonunion of bone fracture. *JBJS Rev.* **4**, 1–12 (2016).
89. Chubinskaya, S. & Wimmer, M. A. Key Pathways to Prevent Posttraumatic Arthritis for Future Molecule-Based Therapy. *Cartilage* **4**, 13S-21S (2013).
90. Brown, T. D., Johnston, R. C., Saltzman, C. L., Marsh, J. L. & Buckwalter, J. A. Posttraumatic osteoarthritis: A first estimate of incidence, prevalence, and burden of disease. in *Journal of Orthopaedic Trauma* (2006). doi:10.1097/01.bot.0000246468.80635.ef
91. He, W., Goodkind, D. & Kowal, P. An Aging World : 2015 International Population Reports. *Aging (Albany. NY).* 165 (2016). doi:P95/09-1
92. Calori, G. M., Mazza, E., Colombo, M. & Ripamonti, C. The use of bone-graft substitutes in large bone defects: any specific needs? *Injury* **42 Suppl 2**, S56-63 (2011).
93. Flierl, M. A. *et al.* Outcomes and complication rates of different bone grafting modalities in long bone fracture nonunions: A retrospective cohort study in 182 patients. *J. Orthop. Surg. Res.* **8**, 1 (2013).
94. Fernandez de Grado, G. *et al.* Bone substitutes: a review of their characteristics, clinical use, and perspectives for large bone defects management. *J. Tissue Eng.* **9**, 1–18 (2018).
95. James, A. W. *et al.* A Review of the Clinical Side Effects of Bone Morphogenetic Protein-2. *Tissue Eng. - Part B Rev.* **22**, 284–297 (2016).
96. Ho-Shui-Ling, A. *et al.* Bone regeneration strategies: Engineered scaffolds, bioactive molecules and stem cells current stage and future perspectives. *Biomaterials* **180**, 143–162 (2018).
97. Gorbachova, T., Melenevsky, Y., Cohen, M. & Cerniglia, B. W. Osteochondral lesions of the knee: Differentiating the most common entities at MRI. *Radiographics* **38**, 1478–1495 (2018).
98. Iwamoto, M., Ohta, Y., Larmour, C. & Enomoto-Iwamoto, M. Toward regeneration of articular cartilage. *Birth Defects Res. Part C - Embryo Today Rev.* **99**, 192–202 (2013).
99. Cain, E. L. & Clancy, W. G. Treatment algorithm for osteochondral injuries of the knee. *Clin. Sports Med.* **20**, 321–342 (2001).
100. Lotz, M. K. & Kraus, V. B. Correction: Posttraumatic osteoarthritis: Pathogenesis and pharmacological treatment options. *Arthritis Res. Ther.* **12**, (2010).
101. Ogura, T., Merkely, G., Bryant, T., Winalski, C. S. & Minas, T. Autologous Chondrocyte Implantation "Segmental-Sandwich" Technique for Deep Osteochondral Defects in the Knee: Clinical Outcomes and Correlation With Magnetic Resonance Imaging Findings. *Orthop. J. Sport. Med.* **7**, 232596711984717 (2019).
102. Minas, T., Ogura, T., Headrick, J. & Bryant, T. Autologous Chondrocyte Implantation "Sandwich" Technique Compared With Autologous Bone Grafting for Deep Osteochondral Lesions in the Knee. *Am. J. Sports Med.* **46**, 322–332 (2018).
103. Gross, A. E. *et al.* Fresh osteochondral allografts for posttraumatic knee defects: Long-term followup. *Clin. Orthop. Relat. Res.* **466**, 1863–1870 (2008).
104. Luyten, F. P., Dell'Accio, F. & De Bari, C. Skeletal tissue engineering: opportunities and challenges. *Best Pract. Res. Clin. Rheumatol.* **15**, 759–69 (2001).
105. EUROPEAN, T. E. P. A. T. C. O. T. U. 10.12.2007. *Off. J. Eur. Union* **1**, 121–137 (2007).
106. European Medicines Agency. CAT monthly report of application procedures, guidelines and related documents on advanced therapies. 30 January 2020. **EMA**, EMA/CAT/54845/2020 (2020).
107. Seimetz, D., Heller, K. & Richter, J. Approval of First CAR-Ts: Have we Solved all Hurdles for ATMPs? *Cell Med.* **11**, 215517901882278 (2019).
108. Bethesda (MD): National Library of Medicine & (US). ClinicalTrials.gov. *Identifier: 'fractures, bone' 'cells'* (2000). Available at: https://clinicaltrials.gov/ct2/results?cond=Fractures%2C+Bone&term=cells&cntry=&state=&city=&dist=. (Accessed: 3rd March 2020)

109. Bethesda (MD): National Library of Medicine. ClinicalTrials.gov. *Identifier: 'cartilage defects' 'cells'* (2000). Available at: https://clinicaltrials.gov/ct2/results?term=cells&cond=Cartilage+defect. (Accessed: 3rd March 2020)
110. Cossu, G. *et al.* The Lancet Commissions: Stem cells and regenerative medicine. *Lancet* **6736**, 2–4 (2017).
111. O'Keefe, R. J. *et al.* American Society for Bone and Mineral Research-Orthopaedic Research Society Joint Task Force Report on Cell-Based Therapies. *J. Bone Miner. Res.* **35**, 3–17 (2020).
112. Heineken, F. G. & Skalak, R. Tissue engineering: A brief overview. *J. Biomech. Eng.* (1991). doi:10.1115/1.2891223
113. Langer, R. & Vacanti, J. P. Tissue Engineering. *Science (80-.).* **260**, 920–926 (1993).
114. Crane, G. M., Ishaug, S. L. & Mikos, A. G. Bone tissue engineering. *Nat. Med.* (1995). doi:10.1038/nm1295-1322
115. Hutmacher, D. W., Schantz, J. T., Lam, C. X. F., Tan, K. C. & Lim, T. C. State of the art and future directions of scaffold-based bone engineering from a biomaterials perspective. *J. Tissue Eng. Regen. Med.* **1**, 245–260 (2007).
116. Vega, S. L., Kwon, M. Y. & Burdick, J. A. Recent advances in hydrogels for cartilage tissue engineering. *Eur. Cells Mater.* **33**, 59–75 (2017).
117. Vega, S. L. *et al.* Combinatorial hydrogels with biochemical gradients for screening 3D cellular microenvironments. *Nat. Commun.* **9**, 1–10 (2018).
118. Bolander, J. *et al.* The combined mechanism of bone morphogenetic protein- and calcium phosphate-induced skeletal tissue formation by human periosteum derived cells. *Eur. Cells Mater.* **31**, 11–25 (2016).
119. Tsuji, K. *et al.* BMP2 activity, although dispensable for bone formation, is required for the initiation of fracture healing. *Nat. Genet.* **38**, 1424–1429 (2006).
120. Medtronic & A. InFuse Bone Graft/LT-Cage: Summary of Safety and Effectiveness. *Saf. Eff. Data* (2002).
121. Van Gastel, N. *et al.* Expansion of murine periosteal progenitor cells with fibroblast growth factor 2 reveals an intrinsic endochondral ossification program mediated by bone morphogenetic protein 2. *Stem Cells* **32**, 2407–2418 (2014).
122. Stevens, M. M., Marini, R. P., Martin, I., Langer, R. & Prasad Shastri, V. FGF-2 enhances TGF-??1-induced periosteal chondrogenesis. *J. Orthop. Res.* **22**, 1114–1119 (2004).
123. Narcisi, R. *et al.* Long-term expansion, enhanced chondrogenic potential, and suppression of endochondral ossification of adult human MSCs via WNT signaling modulation. *Stem Cell Reports* **4**, 459–472 (2015).
124. Mendes, L. F. *et al.* Advancing osteochondral tissue engineering: Bone morphogenetic protein, transforming growth factor, and fibroblast growth factor signaling drive ordered differentiation of periosteal cells resulting in stable cartilage and bone formation in vivo. *Stem Cell Res. Ther.* **9**, 1–13 (2018).
125. Pelttari, K. *et al.* Premature induction of hypertrophy during in vitro chondrogenesis of human mesenchymal stem cells correlates with calcification and vascular invasion after ectopic transplantation in SCID mice. *Arthritis Rheum.* **54**, 3254–3266 (2006).
126. Jakobsen, R. B., Østrup, E., Zhang, X., Mikkelsen, T. S. & Brinchmann, J. E. Analysis of the effects of five factors relevant to in vitro chondrogenesis of human mesenchymal stem cells using factorial design and high throughput mRNA-profiling. *PLoS One* **9**, (2014).
127. Occhetta, P. *et al.* Developmentally inspired programming of adult human mesenchymal stromal cells toward stable chondrogenesis. *Proc. Natl. Acad. Sci. U. S. A.* **115**, 4625–4630 (2018).
128. Mendes, L. F. *et al.* Combinatorial Analysis of Growth Factors Reveals the Contribution of Bone Morphogenetic Proteins to Chondrogenic Differentiation of Human Periosteal Cells. *Tissue Eng. Part C Methods* **22**, 473–486 (2016).
129. Hamamoto, S. *et al.* Enhancement of chondrogenic differentiation supplemented by a novel small compound for chondrocyte-based tissue engineering. *J. Exp. Orthop.* **7**, (2020).
130. Colombier, P. *et al.* TGF-β1 and GDF5 act synergistically to drive the differentiation of human adipose stromal cells toward nucleus pulposus-like cells. *Stem Cells* **34**, 653–667 (2016).
131. Pittenger, M. F. *et al.* Multilineage potential of adult human mesenchymal stem cells. *Science (80-.).* **284**, 143–147 (1999).
132. Lv, F.-J., Tuan, R. S., Cheung, K. M. C. & Leung, V. Y. L. Concise Review: The Surface Markers and Identity of Human Mesenchymal Stem Cells. *Stem Cells* **32**, 1408–1419 (2014).
133. Cowan, C. M. *et al.* Adipose-derived adult stromal cells heal critical-size mouse calvarial defects. *Nat. Biotechnol.* **22**, 560–567 (2004).
134. De Bari, C., Dell'Accio, F., Tylzanowski, P. & Luyten, F. P. Multipotent mesenchymal stem cells from adult human synovial membrane. *Arthritis Rheum.* **44**, 1928–1942 (2001).
135. Marsano, A. *et al.* Differential cartilaginous tissue formation by human synovial membrane, fat pad, meniscus cells and articular chondrocytes. *Osteoarthr. Cartil.* **15**, 48–58 (2007).

136. González-Gil, A. B. *et al.* Periosteum-derived mesenchymal progenitor cells in engineered implants promote fracture healing in a critical-size defect rat model. *J. Tissue Eng. Regen. Med.* **13**, 742–752 (2019).
137. De Bari, C. *et al.* Mesenchymal multipotency of adult human periosteal cells demonstrated by single-cell lineage analysis. *Arthritis Rheum.* **54**, 1209–21 (2006).
138. Bolander, J. *et al.* Healing of a Large Long-Bone Defect through Serum-Free In Vitro Priming of Human Periosteum-Derived Cells. *Stem Cell Reports* **8**, 758–772 (2017).
139. De Bari, C., Dell'Accio, F. & Luyten, F. P. Human periosteum-derived cells maintain phenotypic stability and chondrogenic potential throughout expansion regardless of donor age. *Arthritis Rheum.* **44**, 85–95 (2001).
140. da Silva Meirelles, L., Chagastelles, P. C. & Nardi, N. B. Mesenchymal stem cells reside in virtually all post-natal organs and tissues. *J. Cell Sci.* **119**, 2204–2213 (2006).
141. McLeod, C. M. & Mauck, R. L. On the origin and impact of mesenchymal stem cell heterogeneity: New insights and emerging tools for single cell analysis. *Eur. Cells Mater.* **34**, 217–231 (2017).
142. Jukes, J. M. *et al.* Endochondral bone tissue engineering using embryonic stem cells. *Proc. Natl. Acad. Sci. U. S. A.* **105**, 6840–6845 (2008).
143. Soldner, F. & Jaenisch, R. Stem Cells, Genome Editing, and the Path to Translational Medicine. *Cell* **175**, 615–632 (2018).
144. Tam, W. L., Luyten, F. P. & Roberts, S. J. From skeletal development to the creation of pluripotent stem cell-derived bone-forming progenitors. *Philos. Trans. R. Soc. B Biol. Sci.* **373**, (2018).
145. Shi, Y., Inoue, H., Wu, J. C. & Yamanaka, S. Induced pluripotent stem cell technology: A decade of progress. *Nat. Rev. Drug Discov.* **16**, 115–130 (2017).
146. Yamashita, A. *et al.* Generation of scaffoldless hyaline cartilaginous tissue from human iPSCs. *Stem cell reports* **4**, 404–18 (2015).
147. Cossu, G. *et al.* Lancet Commission: Stem cells and regenerative medicine. *Lancet* **6736**, 883–910 (2017).
148. Lenas, P., Moos, M. & Luyten, F. P. Developmental Engineering: A New Paradigm for the Design and Manufacturing of Cell-Based Products. Part II. From Genes to Networks: Tissue Engineering from the Viewpoint of Systems Biology and Network Science. *Tissue Eng. Part B Rev.* **15**, 395–422 (2009).
149. Ma, J. *et al.* Concise review: cell-based strategies in bone tissue engineering and regenerative medicine. *Stem Cells Transl. Med.* **3**, 98–107 (2014).
150. Ingber, D. E. *et al.* Tissue engineering and developmental biology: Going biomimetic. *Tissue Eng.* **12**, 3265–3283 (2006).
151. Lenas, P., Moos, M. & Luyten, F. P. Developmental engineering: a new paradigm for the design and manufacturing of cell-based products. Part I: from three-dimensional cell growth to biomimetics of in vivo development. *Tissue Eng. Part B. Rev.* **15**, 381–94 (2009).
152. Tonnarelli, B., Centola, M., Barbero, A., Zeller, R. & Martin, I. *Re-engineering Development to Instruct Tissue Regeneration*. *Current Topics in Developmental Biology* **108**, (Elsevier Inc., 2014).
153. Lenas, P. Developmental biology in bioartificial tissue design: Manufacturing and regulatory considerations. *Regenerative Medicine* (2018). doi:10.2217/rme-2017-0126
154. Lenas, P. & Luyten, F. P. An Emerging Paradigm in Tissue Engineering: From Chemical Engineering to Developmental Engineering for Bioartificial Tissue Formation through a Series of Unit Operations that Simulate the In Vivo Successive Developmental Stages †. *Ind. Eng. Chem. Res.* **50**, 482–522 (2011).
155. Thompson, E. M., Matsiko, A., Farrell, E., Kelly, D. J. & O'Brien, F. J. Recapitulating endochondral ossification: A promising route to in vivo bone regeneration. *Journal of Tissue Engineering and Regenerative Medicine* **9**, 889–902 (2015).
156. Freeman, F. E. & Mcnamara, L. M. Endochondral Priming : A Developmental Engineering Strategy for Bone Tissue Regeneration. **23**, 20–33 (2017).
157. Fernando, W. A. *et al.* Limb derived cells as a paradigm for engineering self-assembling skeletal tissues. *J. Tissue Eng. Regen. Med.* 1–14 (2017). doi:10.1002/term.2498
158. Oliveira, S. M. *et al.* Engineering endochondral bone: In vivo studies. *Tissue Eng. - Part A* **15**, 635–643 (2009).
159. Janicki, P., Kasten, P., Kleinschmidt, K., Luginbuehl, R. & Richter, W. Chondrogenic pre-induction of human mesenchymal stem cells on β-TCP: Enhanced bone quality by endochondral heterotopic bone formation. *Acta Biomater.* **6**, 3292–3301 (2010).
160. Bernhard, J. *et al.* Tissue-engineered hypertrophic chondrocyte grafts enhanced long bone repair. *Biomaterials* **139**, 202–212 (2017).
161. Weiss, H. E., Roberts, S. J., Schrooten, J. & Luyten, F. P. A Semi-Autonomous Model of Endochondral Ossification for Developmental Tissue Engineering. *Tissue Engineering Part A* **18**, 1334–1343 (2012).
162. Sarem, M., Heizmann, M., Barbero, A., Martin, I. & Shastri, V. P. Hyperstimulation of CaSR in human MSCs by biomimetic apatite inhibits endochondral ossification via temporal down-regulation of PTH1R.

Proc. Natl. Acad. Sci. **115**, E6135–E6144 (2018).
163. Farrell, E. *et al.* In-vivo generation of bone via endochondral ossification by in-vitro chondrogenic priming of adult human and rat mesenchymal stem cells. *BMC Musculoskelet. Disord.* **12**, 31 (2011).
164. Liu, Y., Kuang, B., Rothrauff, B. B., Tuan, R. S. & Lin, H. Robust bone regeneration through endochondral ossification of human mesenchymal stem cells within their own extracellular matrix. *Biomaterials* **218**, (2019).
165. Scotti, C. *et al.* Recapitulation of endochondral bone formation using human adult mesenchymal stem cells as a paradigm for developmental engineering. *Proc. Natl. Acad. Sci. U. S. A.* **107**, 7251–6 (2010).
166. Serafini, M. *et al.* Establishment of bone marrow and hematopoietic niches in vivo by reversion of chondrocyte differentiation of human bone marrow stromal cells. *Stem Cell Res.* **12**, 659–672 (2014).
167. Todorov, A. *et al.* Monocytes Seeded on Engineered Hypertrophic Cartilage Do Not Enhance Endochondral Ossification Capacity. *Tissue Eng. - Part A* **23**, 708–715 (2017).
168. van der Stok, J. *et al.* Chondrogenically differentiated mesenchymal stromal cell pellets stimulate endochondral bone regeneration in critical-sized bone defects. *Eur. Cells Mater.* **27**, 137–148 (2014).
169. Harada, N. *et al.* Bone regeneration in a massive rat femur defect through endochondral ossification achieved with chondrogenically differentiated MSCs in a degradable scaffold. *Biomaterials* **35**, 7800–7810 (2014).
170. Zhang, L. *et al.* Chondrogenic differentiation of human mesenchymal stem cells: A comparison between micromass and pellet culture systems. *Biotechnol. Lett.* **32**, 1339–1346 (2010).
171. Scotti, C. *et al.* Engineering of a functional bone organ through endochondral ossification. *Proc. Natl. Acad. Sci. U. S. A.* **110**, 3997–4002 (2013).
172. Nilsson Hall, G. *et al.* Developmentally Engineered Callus Organoid Bioassemblies Exhibit Predictive In Vivo Long Bone Healing. *Adv. Sci.* **7**, 1–16 (2020).
173. Bahney, C. S. *et al.* Stem cell-derived endochondral cartilage stimulates bone healing by tissue transformation. *J. Bone Miner. Res.* **29**, 1269–1282 (2014).
174. Knuth, C. A., Witte-Bouma, J., Ridwan, Y., Wolvius, E. B. & Farrell, E. Mesenchymal stem cell-mediated endochondral ossification utilising micropellets and brief chondrogenic priming. *Eur. Cells Mater.* **34**, 142–161 (2017).
175. Yang, W. *et al.* Effects of in vitro chondrogenic priming time of bone-marrow-derived mesenchymal stromal cells on in vivo endochondral bone formation. *Acta Biomater.* **13**, 254–265 (2015).
176. Le, B. Q., van Blitterswijk, C. & de Boer, J. An approach to in vitro manufacturing of hypertrophic cartilage matrix for bone repair. *Bioengineering* **4**, 1–18 (2017).
177. Osinga, R. *et al.* Generation of a Bone Organ by Human Adipose-Derived Stromal Cells Through Endochondral Ossification. *Stem Cells Transl. Med.* **5**, 1090–1097 (2016).
178. Farrell, E. *et al.* In-vivo generation of bone via endochondral ossification by in-vitro chondrogenic priming of adult human and rat mesenchymal stem cells. *BMC Musculoskelet. Disord.* **12**, 31 (2011).
179. Kozhemyakina, E., Lassar, a. B. & Zelzer, E. A pathway to bone: signaling molecules and transcription factors involved in chondrocyte development and maturation. *Development* **142**, 817–831 (2015).
180. Ribitsch, I. *et al.* Fetal articular cartilage regeneration versus adult fibrocartilaginous repair: Secretome proteomics unravels molecular mechanisms in an ovine model. *DMM Dis. Model. Mech.* **11**, (2018).
181. Jeon, J. E., Vaquette, C., Klein, T. J. & Hutmacher, D. W. Perspectives in multiphasic osteochondral tissue engineering. *Anat. Rec.* **297**, 26–35 (2014).
182. Albro, M. B. *et al.* Heterogeneous engineered cartilage growth results from gradients of media-supplemented active TGF-β and is ameliorated by the alternative supplementation of latent TGF-β. *Biomaterials* **77**, 173–185 (2016).
183. Rivron, N. C. *et al.* Tissue assembly and organization: Developmental mechanisms in microfabricated tissues. *Biomaterials* **30**, 4851–4858 (2009).
184. Nichol, J. W. & Khademhosseini, A. Modular tissue engineering: engineering biological tissues from the bottom up. *Soft Matter* **5**, 1312 (2009).
185. Ouyang, L., Armstrong, J. P. K., Salmeron-Sanchez, M. & Stevens, M. M. Assembling Living Building Blocks to Engineer Complex Tissues. *Adv. Funct. Mater.* **1909009**, 1–22 (2020).
186. Bhumiratana, S. *et al.* Large, stratified, and mechanically functional human cartilage grown in vitro by mesenchymal condensation. *Proc. Natl. Acad. Sci. U. S. A.* **111**, 6940–5 (2014).
187. Duguay, D., Foty, R. A. & Steinberg, M. S. Cadherin-mediated cell adhesion and tissue segregation: qualitative and quantitative determinants. *Dev. Biol.* **253**, 309–323 (2003).
188. Holtfreter, J. Experimental studies on the development of the pronephros. *Rev. Can. Biol.* **3**, 220–250 (1944).
189. Moscona, A. & Moscona, H. The dissociation and aggregation of cells from organ rudiments of the early chick embryo. *J. Anat.* **86**, 287–301 (1952).
190. Sutherland, R. M., McCredie, J. A. & Inch, W. R. Growth of multicell spheroids in tissue culture as a

model of nodular carcinomas. *J. Natl. Cancer Inst.* **46**, 113–120 (1971).
191. Mueller-Klieser, W. F. & Sutherland, R. M. Oxygen tensions in multicell spheroids of two cell lines. *Br. J. Cancer* **45**, 256–264 (1982).
192. Groebe, K. & Mueller-Klieser, W. On the relation between size of necrosis and diameter of tumor spheroids. *Int. J. Radiat. Oncol. Biol. Phys.* **34**, 395–401 (1996).
193. Glicklis, R., Merchuk, J. C. & Cohen, S. Modeling mass transfer in hepatocyte spheroids via cell viability, spheroid size, and hepatocellular functions. *Biotechnol. Bioeng.* **86**, 672–680 (2004).
194. Laschke, M. W. & Menger, M. D. Life is 3D: Boosting Spheroid Function for Tissue Engineering. *Trends Biotechnol.* **35**, 133–144 (2017).
195. Leijten, J. *et al.* Bioinspired seeding of biomaterials using three dimensional microtissues induces chondrogenic stem cell differentiation and cartilage formation under growth factor free conditions. *Sci. Rep.* **6**, 1–12 (2016).
196. Futrega, K. *et al.* The microwell-mesh: A novel device and protocol for the high throughput manufacturing of cartilage microtissues. *Biomaterials* **62**, 1–12 (2015).
197. Bolander, J. *et al.* Healing of a Large Long-Bone Defect through Serum-Free In Vitro Priming of Human Periosteum-Derived Cells. *Stem Cell Reports* **8**, 758–772 (2017).
198. Ong, C. S. *et al.* In vivo therapeutic applications of cell spheroids. *Biotechnol. Adv.* **36**, 494–505 (2018).
199. Rossi, G., Manfrin, A. & Lutolf, M. P. Progress and potential in organoid research. *Nat. Rev. Genet.* **19**, 671–687 (2018).
200. Clevers, H. Modeling Development and Disease with Organoids. *Cell* **165**, 1586–1597 (2016).
201. Mi, M. *et al.* Chondrocyte BMP2 signaling plays an essential role in bone fracture healing. *Gene* **512**, 211–218 (2013).
202. Storm, E. E. & Kingsley, D. M. Joint patterning defects caused by single and double mutations in members of the bone morphogenetic protein (BMP) family. *Development* **122**, 3969–3979 (1996).
203. Perry, M. J., McDougall, K. E., Hou, S. chen & Tobias, J. H. Impaired growth plate function in bmp-6 null mice. *Bone* **42**, 216–225 (2008).
204. Montero, A. *et al.* Montero A, Okada Y, Tomita M, Ito M, Tsurukami H, Nakamura T, et al. Disruption of the fibroblast growth factor-2 gene results in decreased bone mass and bone formation. The Journal of Clinical Investigation 2000;105(8):1085–93. *J. Clin. Invest.* **105**, 1085–1093 (2000).
205. Schneider, C. A., Rasband, W. S. & Eliceiri, K. W. NIH Image to ImageJ: 25 years of image analysis. *Nat. Methods* **9**, 671–675 (2012).
206. Holm, E., Aubin, J. E., Hunter, G. K., Beier, F. & Goldberg, H. A. Loss of bone sialoprotein leads to impaired endochondral bone development and mineralization. *Bone* **71**, 145–154 (2015).
207. Miura, S. *et al.* The n-terminal cleavage of chondromodulin-i in growth-plate cartilage at the hypertrophic and calcified zones during bone development. *PLoS One* **9**, 3–10 (2014).
208. Lee, H. H. & Behringer, R. R. Conditional expression of Wnt4 during chondrogenesis leads to dwarfism in mice. *PLoS One* **2**, 450 (2007).
209. Koyama, E. *et al.* Retinoid signaling is required for chondrocyte maturation and endochondral bone formation during limb skeletogenesis. *Dev. Biol.* **208**, 375–391 (1999).
210. Ionescu, A. *et al.* FoxA Family Members Are Crucial Regulators of the Hypertrophic Chondrocyte Differentiation Program. *Dev. Cell* **22**, 927–939 (2012).
211. Hissnauer, T. N. *et al.* Identification of molecular markers for articular cartilage. *Osteoarthr. Cartil.* **18**, 1630–1638 (2010).
212. Ulici, V., James, C. G., Hoenselaar, K. D. & Beier, F. Regulation of gene expression by PI3K in mouse growth plate chondrocytes. *PLoS One* **5**, e8866 (2010).
213. Mackie, E. J., Ahmed, Y. a, Tatarczuch, L., Chen, K.-S. & Mirams, M. Endochondral ossification: how cartilage is converted into bone in the developing skeleton. *Int. J. Biochem. Cell Biol.* **40**, 46–62 (2008).
214. Jing, Y. *et al.* Chondrogenesis and osteogenesis are one continuous developmental and lineage defined biological process. *Sci. Rep.* **7**, 10020 (2017).
215. Ye, L. *et al.* Dmp1-deficient mice display severe defects in cartilage formation responsible for a chondrodysplasia-like phenotype. *J. Biol. Chem.* **280**, 6197–6203 (2005).
216. Nurminsky, D., Magee, C., Faverman, L. & Nurminskaya, M. Regulation of chondrocyte differentiation by actin-severing protein adseverin. *Dev. Biol.* **302**, 427–437 (2007).
217. Rosen, H. & Bar-Shavit, Z. Dual role of osteoblastic proenkephalin derived peptides in skeletal tissues. *J. Cell. Biochem.* **55**, 334–339 (1994).
218. Yasuda, T. *et al.* m-Calpain in rat growth plate chondrocyte cultures: Its involvement in the matrix mineralization process. *Dev. Biol.* **170**, 159–168 (1995).
219. Saito, T., Ikeda, T., Nakamura, K., Chung, U. Il & Kawaguchi, H. S100A1 and S100B, transcriptional targets of SOX trio, inhibit terminal differentiation of chondrocytes. *EMBO Rep.* **8**, 504–509 (2007).
220. Yoshida, C. A. *et al.* Overexpression of Galnt3 in chondrocytes resulted in dwarfism due to the increase

of mucin-type O-glycans and reduction of glycosaminoglycans. *J. Biol. Chem.* **289**, 26584–26596 (2014).
221. Li, Y. *et al.* A fibrillar collagen gene, Col11a1, is essential for skeletal morphogenesis. *Cell* **80**, 423–430 (1995).
222. Cheng, C. C. *et al.* Distinct angiogenesis roles and surface markers of early and late endothelial progenitor cells revealed by functional group analyses. *BMC Genomics* **14**, 182 (2013).
223. Carbone, C. *et al.* Angiopoietin-like proteins in angiogenesis, inflammation and cancer. *Int. J. Mol. Sci.* **19**, 431 (2018).
224. Gerber, H. P. *et al.* VEGF couples hypertrophic cartilage remodeling, ossification and angiogenesis during endochondral bone formation. *Nat. Med.* **5**, 623–628 (1999).
225. Tu, C. F. *et al.* Domain and functional analysis of a novel platelet-endothelial cell surface protein, SCUBE. *J. Biol. Chem.* **283**, 12478–12488 (2008).
226. Xiao, Y. *et al.* Loss of Angiopoietin-like 7 diminishes the regeneration capacity of hematopoietic stem and progenitor cells. *J. Hematol. Oncol.* **8**, 7 (2015).
227. Rocnik, E. F., Liu, P., Sato, K., Walsh, K. & Vaziri, C. The novel SPARC family member SMOC-2 potentiates angiogenic growth factor activity. *J. Biol. Chem.* **281**, 22855–22864 (2006).
228. Pirotte, S. *et al.* Dentin matrix protein 1 induces membrane expression of VE-cadherin on endothelial cells and inhibits VEGF-induced angiogenesis by blocking VEGFR-2 phosphorylation. *Blood* **117**, 2515–2526 (2011).
229. Rattner, A., Yu, H., Williams, J., Smallwood, P. M. & Nathans, J. Endothelin-2 signaling in the neural retina promotes the endothelial tip cell state and inhibits angiogenesis. *Proc. Natl. Acad. Sci.* **110**, E3830–E3839 (2013).
230. Saadoun, S., Papadopoulos, M. C., Hara-Chikuma, M. & Verkman, A. S. Impairment of angiogenesis and cell migration by targeted aquaporin-1 gene disruption. *Nature* **434**, 786–792 (2005).
231. Law, E. W. L. *et al.* Anti-angiogenic and tumor-suppressive roles of candidate tumor-suppressor gene, Fibulin-2, in nasopharyngeal carcinoma. *Oncogene* **31**, 728–738 (2012).
232. Uniewicz, K. A., Cross, M. J. & Fernig, D. G. Exogenous recombinant dimeric neuropilin-1 is sufficient to drive angiogenesis. *J. Biol. Chem.* **286**, 12–23 (2011).
233. Tsujii, M. *et al.* Induced by Colon Cancer Cells. *Cell* **93**, 705–716 (1998).
234. Parker-Duffen, J. L. *et al.* T-cadherin is essential for adiponectin-mediated revascularization. *J. Biol. Chem.* **288**, 24886–24897 (2013).
235. Gaspar, V. M., Lavrador, P., Borges, J., Oliveira, M. B. & Mano, J. F. Advanced Bottom-Up Engineering of Living Architectures. *Adv. Mater.* **32**, 1–41 (2020).
236. Mironov, V. *et al.* Organ printing: Tissue spheroids as building blocks. *Biomaterials* **30**, 2164–2174 (2009).
237. Pamela, G., Travis, J., Ross, W. & Michael, R. Preprint article – Micro-pellet culture reveals that bone marrow mesenchymal stromal cell (BMSC) chondrogenic induction is triggered by a single day of TGF-b1 exposure. *bioRxiv* 1–23 (2019). doi:https://doi.org/10.1101/853556
238. Roberts, S. J., van Gastel, N., Carmeliet, G. & Luyten, F. P. Uncovering the periosteum for skeletal regeneration: The stem cell that lies beneath. *Bone* **70**, 10–18 (2015).
239. Yang, G. *et al.* Osteogenic fate of hypertrophic chondrocytes. *Cell Research* **24**, 1266–1269 (2014).
240. Sarem, M., Otto, O., Tanaka, S. & Shastri, V. P. Cell number in mesenchymal stem cell aggregates dictates cell stiffness and chondrogenesis. 1–18 (2019).
241. Lee, W. *et al.* Dispersible hydrogel force sensors reveal patterns of solid mechanical stress in multicellular spheroid cultures. *Nat. Commun.* **10**, 1–14 (2019).
242. Sart, S. *et al.* Mapping the structure and biological functions within mesenchymal bodies using microfluidics. *Sci. Adv.* **6**, (2020).
243. Samal, P., Maurer, P., van Blitterswijk, C., Truckenmüller, R. & Giselbrecht, S. A New Microengineered Platform for 4D Tracking of Single Cells in a Stem-Cell-Based In Vitro Morphogenesis Model. *Adv. Mater.* **1907966**, (2020).
244. Zhu, M. *et al.* Spatial mapping of tissue properties in vivo reveals a 3D stiffness gradient in the mouse limb bud. *Proc. Natl. Acad. Sci. U. S. A.* **117**, 4781–4791 (2020).
245. Samal, P., van Blitterswijk, C., Truckenmüller, R. & Giselbrecht, S. Grow with the Flow: When Morphogenesis Meets Microfluidics. *Adv. Mater.* **31**, (2019).
246. Skylar-Scott, M. A. *et al.* Biomanufacturing of organ-specific tissues with high cellular density and embedded vascular channels. *Sci. Adv.* **5**, eaaw2459 (2019).
247. Groll, J. *et al.* A definition of bioinks and their distinction from biomaterial inks. *Biofabrication* **11**, 013001 (2018).
248. Susienka, M. J., Wilks, B. T. & Morgan, J. R. Quantifying the kinetics and morphological changes of the fusion of spheroid building blocks. *Biofabrication* **8**, 045003 (2016).
249. Ayan, B. *et al.* Aspiration-assisted bioprinting for precise positioning of biologics. *Sci. Adv.* **6**, 1–17

(2020).
250. Haigh, J. N. *et al.* Hierarchically Structured Porous Poly(2-oxazoline) Hydrogels. *Macromol. Rapid Commun.* **37**, 93–99 (2016).
251. Sheehy, E. J., Mesallati, T., Vinardell, T. & Kelly, D. J. Engineering cartilage or endochondral bone: A comparison of different naturally derived hydrogels. *Acta Biomater.* **13**, 245–253 (2015).
252. Stüdle, C. *et al.* Spatially confined induction of endochondral ossification by functionalized hydrogels for ectopic engineering of osteochondral tissues. *Biomaterials* **171**, 219–229 (2018).
253. Weiss-Bilka, H. E., McGann, M. E., Meagher, M. J., Roeder, R. K. & Wagner, D. R. Ectopic models for endochondral ossification: comparing pellet and alginate bead culture methods. *J. Tissue Eng. Regen. Med.* **12**, e541–e549 (2018).
254. Visser, J. *et al.* Endochondral bone formation in gelatin methacrylamide hydrogel with embedded cartilage-derived matrix particles. *Biomaterials* **37**, 174–182 (2015).
255. Fritsch, K. *et al.* Engineered humanized bone organs maintain human hematopoiesis in vivo. *Exp. Hematol.* (2018). doi:10.1016/j.exphem.2018.01.004
256. Huang, R. L. *et al.* Dispersion of ceramic granules within human fractionated adipose tissue to enhance endochondral bone formation. *Acta Biomater.* **102**, 458–467 (2020).
257. Matsiko, A. *et al.* An endochondral ossification approach to early stage bone repair: Use of tissue-engineered hypertrophic cartilage constructs as primordial templates for weight-bearing bone repair. *J. Tissue Eng. Regen. Med.* **12**, e2147–e2150 (2018).
258. Herberg, S. *et al.* Combinatorial morphogenetic and mechanical cues to mimic bone development for defect repair. *Sci. Adv.* **5**, eaax2476 (2019).
259. Petersen, A. *et al.* A biomaterial with a channel-like pore architecture induces endochondral healing of bone defects. *Nat. Commun.* **9**, (2018).
260. Lienemann, P. S., Lutolf, M. P. & Ehrbar, M. Biomimetic hydrogels for controlled biomolecule delivery to augment bone regeneration. *Adv. Drug Deliv. Rev.* **64**, 1078–1089 (2012).
261. Gjorevski, N., Ranga, A. & Lutolf, M. P. Bioengineering approaches to guide stem cell-based organogenesis. *Dev.* **141**, 1794–1804 (2014).
262. Sheehy, E. J., Kelly, D. J. & O'Brien, F. J. Biomaterial-based endochondral bone regeneration: a shift from traditional tissue engineering paradigms to developmentally inspired strategies. *Mater. Today Bio* **3**, 100009 (2019).
263. Dalton, P. D., Woodfield, T. B. F., Mironov, V. & Groll, J. Advances in Hybrid Fabrication toward Hierarchical Tissue Constructs. *Adv. Sci.* 1902953 (2020). doi:10.1002/advs.201902953
264. Vinatier, C. & Guicheux, J. Cartilage tissue engineering: From biomaterials and stem cells to osteoarthritis treatments. *Ann. Phys. Rehabil. Med.* **59**, 139–144 (2016).
265. Mota, C., Camarero-Espinosa, S., Baker, M. B., Wieringa, P. & Moroni, L. Bioprinting: From Tissue and Organ Development to in Vitro Models. *Chem. Rev.* (2020). doi:10.1021/acs.chemrev.9b00789
266. De Moor, L. *et al.* Hybrid Bioprinting of Chondrogenically Induced Human Mesenchymal Stem Cell Spheroids. *Front. Bioeng. Biotechnol.* **8**, 1–20 (2020).
267. Daly, A. C. & Kelly, D. J. Biofabrication of spatially organised tissues by directing the growth of cellular spheroids within 3D printed polymeric microchambers. *Biomaterials* **197**, 194–206 (2019).
268. Ozbolat, I. T., Chen, H. & Yu, Y. Development of 'Multi-arm Bioprinter' for hybrid biofabrication of tissue engineering constructs. *Robot. Comput. Integr. Manuf.* **30**, 295–304 (2014).
269. Sankar, S., Sharma, C. S. & Rath, S. N. Enhanced osteodifferentiation of MSC spheroids on patterned electrospun fiber mats - An advanced 3D double strategy for bone tissue regeneration. *Mater. Sci. Eng. C* **94**, 703–712 (2019).
270. McMaster, R. *et al.* Tailored Melt Electrowritten Scaffolds for the Generation of Sheet-Like Tissue Constructs from Multicellular Spheroids. *Adv. Healthc. Mater.* **8**, (2019).
271. Abbasi, N., Ivanovski, S., Gulati, K., Love, R. M. & Hamlet, S. Role of offset and gradient architectures of 3-D melt electrowritten scaffold on differentiation and mineralization of osteoblasts. *Biomater. Res.* **24**, 1–16 (2020).
272. Gleadall, A., Visscher, D., Yang, J., Thomas, D. & Segal, J. Review of additive manufactured tissue engineering scaffolds: relationship between geometry and performance. *Burn. Trauma* **6**, 1–16 (2018).
273. Di Luca, A. *et al.* Influencing chondrogenic differentiation of human mesenchymal stromal cells in scaffolds displaying a structural gradient in pore size. *Acta Biomater.* (2016). doi:10.1016/j.actbio.2016.03.014
274. Perez, J. R. *et al.* Tissue Engineering and Cell-Based Therapies for Fractures and Bone Defects. *Front. Bioeng. Biotechnol.* **6**, 1–23 (2018).
275. McDermott, A. M. *et al.* Recapitulating bone development through engineered mesenchymal condensations and mechanical cues for tissue regeneration. *Sci. Transl. Med.* **11**, (2019).
276. Lammens, J. *et al.* A cell-based combination product for the repair of large bone defects. *Bone* 115511

(2020). doi:10.1016/j.bone.2020.115511
277. Yamashita, A. *et al.* Considerations in hiPSC-derived cartilage for articular cartilage repair. *Inflamm. Regen.* **38**, 1–7 (2018).
278. Hashimoto, H., Olson, E. N. & Bassel-Duby, R. Therapeutic approaches for cardiac regeneration and repair. *Nat. Rev. Cardiol.* **15**, 585–600 (2018).
279. Azuma, K. & Yamanaka, S. Recent policies that support clinical application of induced pluripotent stem cell-based regenerative therapies. *Regen. Ther.* **4**, 36–47 (2016).
280. Lee, A. S., Tang, C., Rao, M. S., Weissman, I. L. & Wu, J. C. Tumorigenicity as a clinical hurdle for pluripotent stem cell therapies. *Nat. Med.* **19**, 998–1004 (2013).
281. Kim, H. K. *et al.* A Subset of Paracrine Factors as Efficient Biomarkers for Predicting Vascular Regenerative Efficacy of Mesenchymal Stromal/Stem Cells. *Stem Cells* **37**, 77–88 (2019).
282. Bourgine, P. E. *et al.* Osteoinductivity of engineered cartilaginous templates devitalized by inducible apoptosis. *Proc. Natl. Acad. Sci. U. S. A.* **111**, 17426–17431 (2014).
283. McDermott, A. M. *et al.* Recapitulating bone development for tissue regeneration through engineered mesenchymal condensations and mechanical cues. *bioRxiv* **7756**, 157362 (2018).
284. Moutsatsou, P., Ochs, J., Schmitt, R. H., Hewitt, C. J. & Hanga, M. P. Automation in cell and gene therapy manufacturing: from past to future. *Biotechnol. Lett.* **41**, 1245–1253 (2019).
285. Brandenberg, N. *et al.* High-throughput automated organoid culture via stem-cell aggregation in microcavity arrays. *Nat. Biomed. Eng.* (2020). doi:10.1038/s41551-020-0565-2
286. Fonoudi, H. *et al.* A Universal and Robust Integrated Platform for the Scalable Production of Human Cardiomyocytes From Pluripotent Stem Cells. *Stem Cells Transl. Med.* **4**, 1482–1494 (2015).
287. Nadine, S., Patrício, S. G., Correia, C. R. & Mano, J. F. Dynamic microfactories co-encapsulating osteoblastic and adipose-derived stromal cells for the biofabrication of bone units. *Biofabrication* (2020). doi:10.1088/1758-5090/ab3e16
288. Moldovan, N. I., Hibino, N. & Nakayama, K. Principles of the *Kenzan* Method for Robotic Cell Spheroid-Based Three-Dimensional Bioprinting <sup/>. *Tissue Eng. Part B Rev.* (2017). doi:10.1089/ten.teb.2016.0322
289. Mekhileri, N. V. *et al.* Automated 3D bioassembly of micro-tissues for biofabrication of hybrid tissue engineered constructs. *Biofabrication* **10**, 024103 (2018).
290. Ip, B. C. *et al.* Perfused Organ Cell-Dense Macrotissues Assembled from Prefabricated Living Microtissues. *Adv. Biosyst.* **2**, 1–13 (2018).
291. Lipsitz, Y. Y. *et al.* A roadmap for cost-of-goods planning to guide economic production of cell therapy products. *Cytotherapy* **19**, 1383–1391 (2017).
292. Saini, A. Cystic Fibrosis Patients Benefit from Mini Guts. *Cell Stem Cell* **19**, 425–427 (2016).
293. Choudhury, D., Ashok, A. & Naing, M. W. Commercialization of Organoids. *Trends Mol. Med.* **26**, 245–249 (2020).
294. Rowe, R. G. & Daley, G. Q. Induced pluripotent stem cells in disease modelling and drug discovery. *Nat. Rev. Genet.* **20**, 377–388 (2019).
295. Thysen, S., Luyten, F. P. & Lories, R. J. U. Targets, models and challenges in osteoarthritis research. *DMM Dis. Model. Mech.* **8**, 17–30 (2015).
296. Dupard, S. J., Grigoryan, A., Farhat, S., Coutu, D. L. & Bourgine, P. E. Development of Humanized Ossicles: Bridging the Hematopoietic Gap. *Trends Mol. Med.* **26**, 552–569 (2020).
297. Sart, S., Tomasi, R. F. X., Amselem, G. & Baroud, C. N. Multiscale cytometry and regulation of 3D cell cultures on a chip. *Nat. Commun.* **8**, 469 (2017).
298. Deckers, T. *et al.* High-throughput image-based monitoring of cell aggregation and microspheroid formation. *PLoS One* **13**, (2018).
299. Tomasi, R. F. X., Sart, S., Champetier, T. & Baroud, C. N. Individual Control and Quantification of 3D Spheroids in a High-Density Microfluidic Droplet Array. *Cell Rep.* **31**, (2020).
300. Czerniecki, S. M. *et al.* High-Throughput Screening Enhances Kidney Organoid Differentiation from Human Pluripotent Stem Cells and Enables Automated Multidimensional Phenotyping. *Cell Stem Cell* **22**, 929-940.e4 (2018).
301. Buitinga, M. *et al.* Micro-fabricated scaffolds lead to efficient remission of diabetes in mice. *Biomaterials* **135**, 10–22 (2017).

Scientific acknowledgement

Research presented here was funded by the Research Foundation Flanders (FWO) G.N.H: 1S05116N, I.P.: 12O7916N, and CARTiPLEX: G0A4718N, the European Research Council under the European Union's Seventh Framework Program (FP/2007-2013)/ERC (249191) and Horizon 2020 Framework Program (H2020/2014-2021)/ERC (772418) and the special research fund of the KU Leuven (GOA/13/016 and C24/17/077) and BONE Interreg North West Europe (NWE 497), European Regional Development Fund. This work was supported by the partners of Regenerative Medicine Crossing Borders (http://www.regmedxb.com). Powered by Health—Holland, and Top Sector Life Sciences & Health.

Confocal images were recorded on a Zeiss LSM 510 and 880—Airyscan, Cell and Tissue Imaging Cluster (CIC), Supported by Hercules AKUL/15/37_GOH1816N and FWO G.0929.15 to Pieter Vanden Berghe, KU Leuven. RNA sequencing and a part of the RNA-seq expression analysis were performed by the Genomics Core Leuven, KU Leuven. The micro (or nano)-CT images were generated on the X-ray computed tomography facility of the Department of Development and Regeneration of the KU Leuven, financed by the Hercules Foundation (project AKUL/13/47). This work was part of Prometheus, the KU Leuven R&D division for skeletal tissue engineering (http://www.kuleuven.be/prometheus).Personal contribution

Personal contribution

The studies presented in this thesis manuscript were conceptualized by Ioannis Papantoniou, Frank P. Luyten, Liesbet Geris and Gabriella Nilsson Hall. The majority of i*n vitro* experiments were performed by Gabriella Nilsson Hall, with technical assistance from Inge van Hoven, Melanie Van den Broeck and Samuel Ribeiro Viseu (histological processing, cell culture). *In vivo* implantations were performed by Kathleen Bosmans. Data analysis and interpretation was performed by Gabriella Nilsson Hall, Liesbet Geris, Ioannis Papantoniou and Frank P. Luyten. The thesis manuscript was written by Gabriella Nilsson Hall and revised by Frank P. Luyten and Ioannis Papantoniou.

Conflicts of interest

A patent has been granted as a result of the work in this thesis.

Curriculum vitae

Personal information

Name:	Gabriella NILSSON HALL
Date of Birth:	December 19, 1987
Place of Birth:	Lund, Sweden
Address:	Blijde-Inkomststraat 115, bus 0203, 3000 Leuven, Belgium
Telephone:	+32 487 96 47 57 (cell phone)
E-mail:	gabriella.nilssonhall@kuleuven.be, gabriella.n.hall@gmail.com

Education

2014 – 2020 **Ph.D. in Biomedical Sciences** at KU Leuven, Belgium
Title: "Modular tissue engineering for regeneration of bone and cartilage - *Assemblies of developmentally engineered cartilaginous building blocks*"
Supported by a PhD Fellowship strategic basic research grant from the Research Foundation Flanders; Fonds voor Wetenschappelijk Onderzoek, Vlaanderen Flanders (FWO)

2011 – 2014 **Master in Bioengineering** at Chalmers University of Technology, Sweden
Master thesis: "*Priming human periosteum-derived stem cells in static and dynamic culture setups under the influence of Fibroblast Growth Factor 2: A bone tissue engineering approach*"

2008 – 2011 **Bachelor in Bioengineering** at Chalmers University of Technology, Sweden

Scientific training

2020	Systematic Reviews by Cochrane. KU Leuven, Belgium
2019	NextGenQBio platform. KU Leuven, Belgium
2018	Basics of Single Cell Analysis. VIB, Belgium
2014 – 2015	Laboratory Animals – FELASA Cat C. KU Leuven, Belgium

Bibliography

Articles published in internationally reviewed scientific journals

Smeets, B., Pešek, J., Deckers, T., **Nilsson Hall, G.**, Cuvelier, M., Ongenae, S., Bloemen, V., Luyten, F. P., Papantoniou, I., Ramon, H. (2020) "Compaction dynamics during progenitor cell self-assembly reveal granular mechanics", *Matter*, 2, pp. 1–13. doi: 10.1016/j.matt.2020.02.016.

Nilsson Hall, G., Mendes, L.F., Gklava, C., Geris, L., Luyten, F.P., Papantoniou, I. (2019). Developmentally Engineered Callus Organoid Bioassemblies Exhibit Predictive In Vivo Long Bone Healing. *Advanced Science*, 7 (2), Art.No. ARTN 1902295. doi: 10.1002/advs.201902295 Open Access

Gupta, P., **Nilsson Hall, G.**, Geris, L., Luyten, F.P., Papantoniou, I. (2019). Human Platelet Lysate Improves Bone Forming Potential of Human Progenitor Cells Expanded in Microcarrier-Based Dynamic Culture. *Stem Cells Translational Medicine*, 8 (8), 810-821. doi: 10.1002/sctm.18-0216 Open Access

Deckers, T., Lambrechts, T., Viazzi, S., **Nilsson Hall, G.**, Papantoniou, I., Bloemen, V., Aerts, J-M. with Aerts, J-M. (corresp. author) (2018). High-throughput image-based monitoring of cell aggregation and microspheroid formation. *PLoS One*, 13 (6), Art.No. e0199092. doi: 10.1371/journal.pone.0199092 Open Access

Fernando, W.A., Papantoniou, I., Freitas Mendes, L., **Nilsson Hall, G.**, Bosmans, K., Tam, W.L., Teixeira, L.M., Moos, M., Geris, L., Frank P. Luyten, F. (2018). Limb derived cells as a paradigm for engineering self-assembling skeletal tissues. *Journal of Tissue Engineering and Regenerative Medicine*, 12 (3), Art.No. 10.1002/term.2498, 794-807.

Patent

Luyten P., Freitas Mendes, L., **Nilsson Hall, G.**, Papantoniou, I., Geris, L., KU Leuven, 2018, Engineering functional bone organs, WO2018220051A1

Meeting abstracts presented at international conference or symposia

Nilsson Hall, G., Freitas Mendes, L., Gklava, C., Geris, L., Papantoniou, I., Luyten, F. (2019). Cartilage Micro-Tissues Mimic Bone Development And Regenerate Long-Bone Defects. Presented at the ISSCR International Symposium - Stem Cells & Organoids in Development & Disease, Amsterdam, Netherlands, 20 Feb 2019-22 Feb 2019.

Nilsson Hall, G., Geris, L., Luyten, F., Papantoniou, I. (2018). Complex Bioassemblies of Cartilage Intermediate μTissues Maintain Spatial Properties In Vivo. Presented at the International Society for Biofabrication Conference, Würzburg, Germany, 28 Oct 2018-31 Oct 2018.

Nilsson Hall, G., Freitas Mendes, L., Geris, L., Papantoniou, I., Luyten, F. (2018). Cartilage intermediate μTissue assemblies for healing of critical-sized long bone defects. (Abstract No. a91961), (178-178). Presented at the TERMIS World Congress, Kyoto, Japan, 04 Sep 2018-07 Sep 2018.

Nilsson Hall, G., Freitas Mendes, L., Geris, L., Frank P., F., Papantoniou, I. (2017). 3D cellular spheroids for formation of bone micro-organoids - through endochondral ossification. Presented at the World Preclinical Congress Europe, Lisbon, Portugal, 15 Nov 2017-17 Nov 2017. (professional oriented)

Nilsson Hall, G., Freitas Mendes, L., Geris, L., Luyten, F., Papantoniou, I. (2016). Bottom-up cell μ-aggregate assemblies for efficient endochondral bone tissue engineering. In: Towards Future Regenerative Therapies TERMIS-EU 2016 Conference, Uppsala, Sweden - Oral Abstracts: vol. 31. Presented at the TERMIS-EU, Uppsala, Sweden, 28 Jun 2016-01 Jul 2016.

Nilsson Hall, G., Papantoniou, I., Sonnaert, M., van Gastel, N., Carmeliet, G., Geris, L., Luyten, F. (2015). Fibroblast Growth Factor-2 Counteracts Osteogenic Priming during Expansion of Human Periosteum-Derived Cells in 3D Perfusion Bioreactors. In: Tissue Engineering Part A: vol. 21. Presented at the 4th TERMIS World Congress, Boston: MA, 08 Sep 2015-11 Sep 2015.

Nilsson Hall, G., Papantoniou, I., Sonnaert, M., van Gastel, N., Carmeliet, G., Geris, L., Frank P., F. (2015). Bone Tissue Engineering: The Effect of Fibroblast Growth Factor 2 on the Expansion of Human Periosteum-Derived Cells in 3D Perfusion Bioreactors. Presented at the Belgian Symposium on Tissue Engineering (BSTE), Leuven, Belgium, 19 Mar 2015-20 Mar 2015.



Depth map for stereogram image placed on the back cover. The femur is adapted from Isaza, Enrique & García, L & Salazar, E. (2013). *Determination of Mechanic Resistance of Osseous Element through Finite Element Modeling*.